# Study of combined effects of radiation and temperature on silica based material and optical fibers

Angela Guttilla

UNIVERSITÉ CÔTE D'AZUR

ÉCOLE DOCTORALE
SCIENCES FONDAMENTALES ET APPLIQUÉES


# THÈSE DE DOCTORAT

# Étude des effets combinés du rayonnement et de la température sur les matériaux à base de silice et les fibres optiques


## Angela GUTTILLA

Université Côte d'Azur – Institute de physique de Nice (INPHYNI)


**Présentée en vue de l'obtention du grade de docteur en** Physique **de l'**Université Côte d'Azur
**Dirigée par** : Mourad Benabdesselam, Sylvain Girard
**Soutenue le** : 30/06/2021

**Devant le jury, composé de** :
Mourad Benabdesselam, Professeur, Université Côte d'Azur.
Johan Bertrand, Ingénieur chercheur, ANDRA.
Marco Cannas, Professeur, DIFC, Università degli studi di Palermo.
Sylvain Girard, Professeur, Université Jean Monnet de Saint-Etienne.
Franck Mady, Professeur, Université Côte d'Azur.
Frédéric Wrobel, Professeur, IES-Institut d'électronique et des systèmes.

ANDRA IRSN INVESTIR L'AVENIR INPHYNI UNIVERSITÉ CÔTE D'AZUR cnrs UNIVERSITÉ DE LYON UNIVERSITÉ JEAN MONNET SAINT-ÉTIENNE

# Étude des effets combinés du rayonnement et de la température sur les matériaux à base de silice et les fibres optiques.

# Study of combined effects of radiation and temperature on silica based material and optical fibers.

**Jury:**

**Rapporteurs**

Frédéric Wrobel, Professeur, IES-Institut d'électronique et des systémes, UMR-CNRS 5214.

Marco Cannas, Professeur, DiFC, Università degli Studi di Palermo, via Archirafi 36, 90100 Palermo, Italie.

**Examinateurs**

Sylvain Girard, Professeur, Laboratoire Hubert Curien, Université Jean Monnet de Saint-Etienne, CNRS UMR 5516.

Bertrand Johan, Ingénieur de recherche, ANDRA.

Mourad Benabdesselam, Professeur, Université Côte d'Azur, CNRS UMR 7010, Parc Valrose, 06108 Nice, France.

Franck Mady, Professeur, Université Côte d'Azur, CNRS UMR 7010, Parc Valrose, 06108 Nice, France.

**Étude des effets combinés du rayonnement et de la température sur les matériaux à base de silice et les fibres optiques**.

**Résumé** Cette thèse s'inscrit dans le cadre du projet de recherche CERTYF dont l'objectif est l'amélioration des connaissances sur les processus de dégradation des fibres optiques à base de silice utilisées dans des environnements sévères combinant des contraintes d'irradiation, d'hydrogène et de température (R-H-T). Lorsqu'elle est exposée à un rayonnement, la fibre optique devient moins guidante en raison de la création de défauts. Ces défauts sont caractérisés par des niveaux d'énergie dans la bande interdite du matériau. Ainsi, lorsque la lumière est injectée à l'intérieur d'une fibre optique, la partie transmise de cette lumière diminue et inversement, l'atténuation radio-induite (ARI) augmente. Les objectifs du contrôle de l'ARI sont de développer des systèmes à base de fibres optiques tolérants aux radiations, capables de fonctionner dans les lieux de stockage de déchets radioactifs ou au contraire d'améliorer la sensibilité des fibres lors de leur utilisation pour la détection de la dose ou du débit de dose de rayonnement présent dans l'environnement radiatif. Ce travail est centré sur la construction d'un modèle physique capable de prédire l'ARI dans cet environnement sévère à travers une étude expérimentale basée sur la thermoluminescence (TL) et la spectroscopie d'absorption conduisant à la compréhension des mécanismes de création de défauts radio-induits. L'ARI qui en résulte est un processus complexe dépendant de plusieurs paramètres tels que la longueur d'onde, la dose, le débit de dose, la température et la composition des fibres. Tous ces paramètres qui doivent être pris en compte dans la modélisation reflètent les nombreux problèmes qui limitent l'intégration de la fibre dans des environnements combinés.

**Mots clés: Thermoluminescence, atténuation radio-induite, silice, fibres optiques, environnement radiatif**

---

**Study of combined effects of radiation and temperature on silica based material and optical fibers**.

**Abstract** This thesis is part of the CERTYF research project, acronym of Combined Effects of Radiation Temperature and hYdrogen in optical Fibers. The CERTYF project aims to improve knowledge on the degradation processes of silica-based material and optical fibers used in severe or harsh environments combining irradiation constraints, hydrogen and temperature (R-H-T), such as the one encountered by ANDRA (Agence nationale pour la gestion des déchets radioactifs). When exposed to radiation, the optical fiber becomes less guiding due to the creation of defects. These defects are characterized by energy levels within the bandgap of the material. Thus, when the light is injected inside an optical fiber the transmitted part of this light decreases and conversely, the radiation induced attenuation (RIA) increases. The objectives of the RIA control are to develop radiation tolerant systems capable of operating in the radioactive waste storage sites or, on the contrary, of improving the sensitivity of fibers when used for the detection of the radiation dose or dose rate present in the radiative environment. This work focuses on building of a physical model capable of predicting RIA in this severe/harsh environment through an experimental study based on thermoluminescence (TL) and absorption spectroscopy leading to the understanding of the point defects creation mechanisms induced by the irradiation. The resulting radiation induced attenuation is a complex process depending on several parameters like the wavelength, dose, dose rate, temperature and fiber composition. All these parameters that must be considered in the modeling reflect the several issues that limit the fiber integration in combined environments.

**Keywords: Thermoluminescence, Radiation induced attenuation, silica, optical fibers, radiative environment**

## Acknowledgements

This Thesis is the result of the work I carried as PhD fellow under research project *CERTYF* at the Institute de Physique de Nice.

The most important acknowledgment are addressed to my supervisors Mourad BENABDESSELAM and Franck MADY for their constant support and guidance for the entire duration of this PhD, without which all the results of this thesis would have never been obtained.

I thank the members of the jury Johan BERTRAND, Sylvain GIRARD and the Referees Marco CANNAS and Frédéric WROBEL who with their competence have constructively revised this manuscript.

I thank the director of the *INPHYNI*, all the *fibres optiques* group's members: Wilfried BLANC, Bernard DUSSARDIER, Stanislaw TRZESIEN and Michèle UDE whom we had fruitful discussions and they were always willing to help me. Finally i thank the administrative staff of the laboratory, in particular Nathalie KOULECHOUFF for her help and competence.

A big thanks goes to all the people of the *CERTYF* project from the *ANDRA*, the *IRSN* institute and from the Laboratory *Hubert-Curien* of the University Jean Monnet, namely Antonino ALESSI, Aziz BOUKENTER, Sylvain GIRARD, Youcef OUERDANE with whom I have always had the opportunity to exchange ideas and who have always welcomed me fondly during my visits in Saint Etienne. A particular thanks goes to Adriana MORANA, Cosimo CAMPANELLA and Vincenzo DE MICHELE with whom I shared very happy moments during these years and who were always present for me.

I thank all the people who made these years of PhD unforgettable: first of all the colleagues and friends that I met at INPHYINI during these years, especially Adam, Daniele, Dorian, Elie, Enzo, Francois, Guido, Martina, Nicola, Nino, Omar, Ying, Zhuorui and my dear desk partner for this three years Xin. Then i thank my first friends I had here in Nice: Carlos, Lorenzo, Sebastian and the PhD students of the OCA: Annelore, Emma, Gabriele, Marco, Max, Nacho, Nastia, Nicolas, Pablos, Sofia and Tobias. Having met so many people from different parts of the world has enriched me deeply.

♣♣♣

Voglio dedicare questo lavoro alla mia famiglia, che mi è sempre stata vicina e mi ha sempre sostenuto, e sono sicura lo avrebbe fatto qualsiasi scelta avessi preso nella mia vita. Senza l'appoggio dei miei genitori tutto il mio percorso di studi, che vedo completare in un certo senso adesso, con il dottorato, sarebbe stato ben più arduo, per cui li ringrazio profondamente. Un ringraziamento speciale va a mio fratello, che è sempre stato un modello da seguire sotto ogni aspetto e a sua moglie Assel.

Allargo i ringraziamenti ad altri membri della famiglia, i cugini e gli zii e alla famiglia Virruso, perchè il loro affetto mi rende ancora più piacevole il ritorno a casa e soprattutto perchè sono stati vicino ai miei genitori nel momento del bisogno mentre io ero via.

Ringrazio i miei più vecchi amici: Alessio Claudia Rosario e Valentina che sono ormai parte integrante della mia vita; le mie sorelle adottive MariaSilvia ed Elettra sono sempre vicine nonostante la distanza e con cui ho condiviso tutte le ansie e tutte le gioie di questi 3 anni ed insieme a loro i miei amici ed excolleghi Claudio ed Emanuele.

Infine, il più grande ringraziamento va ad Umberto, con cui ho trascorso questi 3 anni prima da amico e poi da compagno. Grazie a te ho tutti e problemi e le ansie che un percorso di dottorato può comportare sono state ridimensionate, perchè mi hai aiutato a dare il peso giusto alle cose. La tua presenza e la tua leggerezza ha reso tutto immensamente più bello.

# Contents

# Introduction

This thesis work takes part to the *CERTYF* project, whose name is an acronym for Combined Effects of Radiation, Temperature and hYdrogen in optical Fibers. The main objective of the *CERTYF* project is to improve the knowledge about the basic mechanisms leading to the degradation through the radiation-induced attenuation (RIA) of silica-based materials and optical fibers in harsh or severe mixed environments. The environments of interest combine temperature, radiations and hydrogen (R-H-T) constraints, as those encountered by ANDRA (Agence Nationale pour la gestion des Déchets Radioactifs).

Silica-based optical fibers have a broad range of use in harsh or severe environment applications with radiation constraints, for instance high-energy physics facilities, waste depositories, nuclear power plants and space too. The exposure of optical fibers to ionizing radiation involves damage to optical properties such as transparency and contributes to the degradation of the fiber performances in different ways depending on the fiber doping. This phenomenon is the direct effect of the Radiation Induced Attenuation (RIA): the attenuation of the transmitted intensity light due to the radiation exposure. The degradation of optical properties of the silica based materials can be explained by the structural adjustments in the silica lattice (generation of color centers, vacancies, interstitial defects...) and depends on the chemical composition of the glass. The knowledge of the nature and of the creation and annealing mechanisms after radiation of these defects is important in the RIA control.

In this context there is a strong interest in improving knowledge about the degradation processes through the RIA of silica-based optical fibers in severe or harsh environments.

By RIA control can be developed radiation tolerant systems able to operate in the radioactive waste storage facilities; or enhance the fiber radiation sensitivity in order to design radiation detectors and dosimeters able to detect the radiation dose or dose rate present in the radiative environment.

For the first intent are adopted radiation tolerant fibers, characterized by F doping or pure silica, while for the second one, are generally used Al- and P-doped fibers, having proven their sensitive response to radiation. In addition, Telecom grade fibers (Ge-doped) are also interesting because they are used for data transfer applications. All these fiber classes are tested in this thesis work. Despite the interest in this research area and the numerous studies devoted to this field, the response of a fiber-based system to combined constraints can still not be predicted by using the empirical laws or kinetics models discussed in the literature.

The aim is to build a physical model that predicts the RIA in this harsh envi-

ronment, valid for all the three main types of fibers mentioned above, valid for bulk and fibers (for this last one the propagation effects inside the fiber must be taken into account), for a huge range of dose and dose rate and that takes into account the presence of hydrogen and the temperature effects. The resulting RIA is a complex process depending on the several issues that limit the fiber integration in combined environments, such as the dose, dose rate, temperature and fiber composition. All these factors must be taken into account in RIA modeling.

Furthermore, the origins of the RIA in the near-infrared (NIR) part of the spectrum is of interest to the project, since in the NIR most of the applications investigated by ANDRA have their operating wavelengths. To understand RIA origins in this spectral domain, it appears mandatory to consider the convolution between the radiation response of bulk material and the guided modes propagating along the wave-guides.

The first step of the RIA modeling is to assign point defects to energy levels. This is made possible thanks to an initial exploration phase, where by means of several spectroscopic techniques, a characterization of the dedicated samples is studied. A set of experimental results that will be analyzed though a MultiVariate Analysis has the aim to validate a first version of physical models allowing to reproduce the dependence of the RIA versus the various R-H-T parameters and to extrapolate RIA in non-tested conditions. The radiation in the experimental test is made by X- or $\gamma$-rays. In this sense also the impact of these two different types of irradiation on the RIA is seen.

A second phase will be put in place to simultaneously consolidate the physical models and to exploit the knowledge acquired during exploration phase to investigate innovative structures of MCVD optical fibers with optimized properties for operation in ANDRA's R-H-T environments. Finally, the final deliverable of CERTYF project will be a guidelines report for radiation testing of silica-based fibers and fiber sensors in harsh mixed environments combining several constraints including radiations, temperature and hydrogen.

Exploit these knowledge and results to the benefit of radioactive waste management is the primary interest of the project. Concerning this aspect there is a wide range of silica-based optical fibers in ANDRA applications. Optical fibers can be used for several applications to transport signals over long distances, in this case we talk about *Data Transfer*. As a result of increasing interest in *dosimetry*, in literature are present a lot of studies on optical fibers used for dosimetry applications. In fact, optical fibers can be used in this field for monitoring of storage facilities. They are very sensitive in a large range of dose/dose rate, slowly intrusive and in some cases, spatially distributed. For all these systems, controlling the RIA dependence in varying R-H-T conditions also appears as crucial. Finally optical fibers can be exploited in *fiber sensing* applications. ANDRA is extremely active in the development of distributed or discrete sensors for the monitoring of environmental parameters for the CIGEO project: these studies covered the development of fiber-based sensors for radiation dose, hydrogen, strain, temperature measurements using a wide large range of sensing techniques, from discrete ones (FBGs, punctual measurements) to distributed (Raman, Rayleigh, Brillouin) technologies.

In accordance with one of the main objectives of the project, this thesis is focused on the modeling of RIA in the visible range combining radiation and tem-

perature constraints for silica based materials. It is divided in four chapters, the first two describe the context and the methodologies, and the last two concern the results, both experimental and modeling. We start with a chapter describing the theoretical context: the harsh environment and the optical fibers application related to it; a basic and small review about matter-radiation interaction and finally an overview about silica (its structure and the point defects related to pure and doped silica) and the optical fibers, how they work and how they are fabricated. In the last section more emphasis is given to the MCVD process, since the fiber preforms tested on this thesis are made by this technique at INPHYNI laboratory at University Côte d'Azur (UCA).

The second chapter concerns the methodologies and the materials. It aims to describe the phenomena and the technique encountered in this thesis: from the irradiation processes and the radiation effects on silica based materials, to the spectroscopic techniques. Concerning this last aspect, the chapter reports not only the theoretical aspect but also the experimental set up and conditions. The chapter about the experimental results is divided according to the fiber classes under study. The simulation results chapter is characterized by the same structure starting also with the modeling approach description in detail.

# Chapter 1

# Theoretical context



## 1.1 Optical fibers devices in harsh environment

The interest in optical fiber technologies applied in a harsh environment has been growing since the 70s. At the beginning this interest was limited to data transfer application, since the ionizing radiation damaged the optical fibers performances in signal transmissions. The first studies devoted to the characterizations of the decrease on transmitted intensity, identified the RIA as phenomenon at the origin of this degradation. It was thus figured out that the RIA is caused by the generation of optically active point defects in silica [1–5]. The typical harsh or severe environment with radiation constraints interested in optical fibers application can be natural, as space, or artificial, such as those associated with fusion

related facilities, nuclear power plants or high energy physics facilities [1]. There are several advantages of silica-based optical fibers use for telecommunications: such as low attenuation level, high bandwidth, high efficiency, small size... [6]. These characteristics are exploitable and valid also for data transfer application in an environment with radiation constraint. In addition, optical fibers feature other characteristics that make them a good choice for several kinds of application in harsh mixed environment. One of these characteristics is the resistance to high temperatures. In fact, with a proper acrylate coating they can operate up to 200°C but it is possible to use metal based coating extending their range to higher temperatures (up to 400°C) for aluminum or copper coated fibers and up to 800°C for gold-coated fibers [1]. Furthermore, fiber based devices are lightweight, reliable and profitable for integration into a spacecraft or in nuclear facilities and are almost immune to most electromagnetic perturbations since they are made by a dielectric material as silica. This property is important in diagnostics operating in Megajoule class lasers, where very high parasitic currents are generated in the coaxial cables [1, 7]. Concerning the space applications, fiber-based technologies are widely used in spacecraft and their potential incremental use is under investigation. The main issues in this kind of device are the RIA due to radiations in space. The RIA can affect the performance of these devices. In nuclear industries or high energies facilities, optical fibers can be used for transfer information (Data transfer) or as a sensor, especially for dose and temperature sensing. In the same way in waste storage repository, optical fibers (OFs) are largely used as distributed sensor to detect the dose in the surrounding environment [7–11]. Finally in the medical field, optical fibers offer considerable advantages over conventional techniques for radiotherapy dosimetry, the small dimensions of optical fiber-based dosimeters, together with being lightweight and flexible, mean that they are minimally invasive and thus particularly suited to in vivo dosimetry [12]. In table 1.1 are summarized the main applications for the optical fibers in the radiative environment just mentioned.

The following section is dedicated to the characteristics of the radiation environments.

| **Type of environment** | **Applications for fibers** |
|---|---|
| Space | Data transfer |
| | Fiber laser |
| | Gyroscopes |
| | Fiber sensing |
| Nuclear industries and waste storage | Sensing |
| | Data transfer |
| | Distributed sensing |
| High energies facilities | Data transfer |
| | Plasma diagnostics |
| | Sensing |
| | Distributed sensing |
| Medicine | Radiotherapy |
| | Proton-therapy |
| | Beam monitoring |
| | Dosimetry |

**Table 1.1:** Optical fibers applications in radiative environments [1].

## 1.2 The radiative environment

Several types of radiation environments exist. The principal ones interested in optical fibers uses are the medical, space, high energy facilities and nuclear plants. For this thesis we are mainly interested in the last two kinds of environment, thus in the final part of this section are reported some examples of typical installations relative to these radiative environments. The following concerns the main parameters used to define a harsh environment, such as the nature of particles, the dose, the dose rate, the temperature, hydrogen and other constraints. The presence of these factors in the same environment brings to a difficult evaluation and predictability of the RIA. Optical fibers may operate in an harsh mixed environment with radiation, temperature and hydrogen constraints, and it is the main interest of this thesis to characterize the response of silica to these constraints. In figure 1.1 is reported a 3D graph in dose, dose rate and temperature where are designed some installations and radiative environments where the optical fibers find a large use.

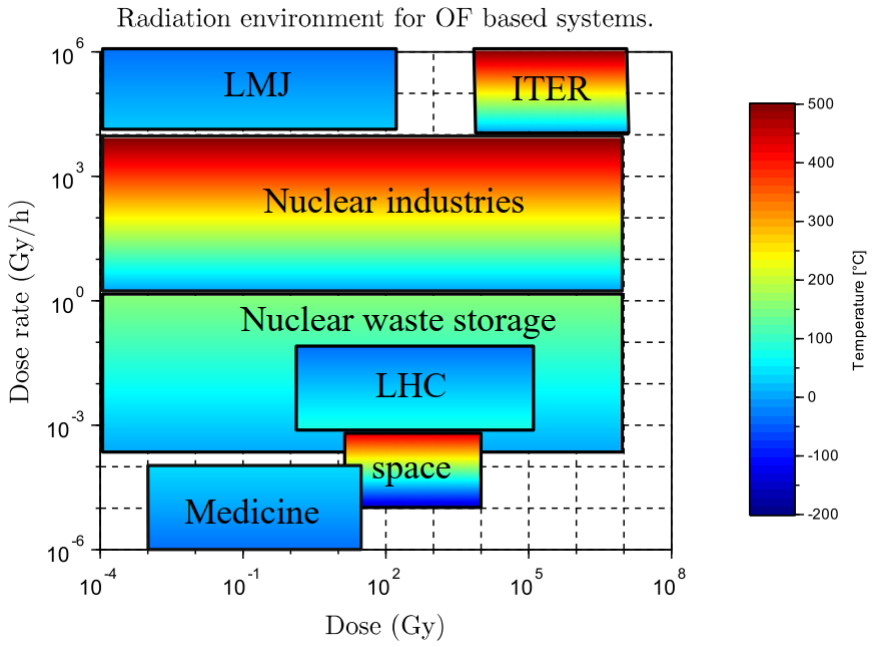


**Figure 1.1:** A representation of the range in dose, dose rate and temperature of the radiative environment where the silica based OFs operate. Adapted from [13].

The nature of particles is an important factor when defining a radiative environment. Depending on the impacting particles in fact, the relative contributions of ionization and displacement damage processes in silica differ as well as the radiation response of silica-based material and OFs [1, 4]. As it will be seen in section 2.1, the radiation response in an OF based device is principally governed by ionizing processes. Despite the displacement damage contribution is strongly present as structural signatures in silica in environments associated with very high neutron fluences or heavy ions [1, 14].

The dose defines the quantity of energy deposited in the material per mass unit.

It is generally expressed in Gy (1Gy=1J$kg^{-1}$), or rad (1Gy=100 rad). In this work we use to define the dose as dose deposited in silica: Gy($SiO_2$).

The dose rate is defined as the dose deposited in the material in unit of time. One can encounter a high dose spread in a very long time, such as in the space where the dose rate lies between $10^{-5}$ and $10^{-3}$ Gy/h [15], or in a very short time like in the Megajoule laser facility, where the dose rate reaches the MGy/s [7].

The temperature is a significant factor for a lot of applications. Temperature may damage the performance of silica based OFs as well as the radiation do, especially when these constraints are both present. The temperature for OFs application may range from $-200^oC$ to $800^oC$ for spacecraft and reactor monitoring respectively [1]. The hydrogen presence is an other constraint in harsh environment, especially in nuclear one such as radioactive waste storage sites, since here the waste releases hydrogen in the atmosphere [1, 11]. The hydrogen interacts with silica lattice, so it is necessary to take into account the presence of this gas in designing optical fiber based devices that operate in this kind of environment.

Some of the installations shown in fig.1.1 concern the industries, that is interested in the domain of high to very high energies, with all possible types of radiations. Some of the most important nuclear installations are:

- Particle accelerators, such as the one at CERN: LEP (Large collider Electron Proton) which was replaced by the LHC (Large Hadron Collider) in 2008. The LHC consists of a 27-kilometer ring of superconducting magnets with a number of accelerating structures to boost the energy of the particles along the way. The mixed field at the LHC is composed of charged and neutral hadrons (protons, pions, kaons and neutrons), photons, electrons and muons. This complex field is due to particles generated by proton-proton (or ion-ion) collisions in the LHC experimental areas, distributed beam losses (protons, ions) around the machine, and the beam interacting with the residual gas inside the beam pipe. Electronic components and systems exposed to a mixed radiation field will experience three different types of radiation damages, these are displacement damage (DD), Single Event Effects (SEEs) and damage from the Total Ionising Dose (TID) [8].

- High energy experiments. Represented by two projects: ITER (International Thermonuclear Experimental Reactor: fusion by magnetic confinement) and the LMJ (Laser Mega Joule: fusion by inertial confinement). These two installations intended for fusion aim to convert deuterium and tritium into energy. The fusion will also produce radiation such as $\gamma$ photons and neutrons. Clearly the diagnostic designs for these projects will require components to operate in harsh environments [7, 9] such as the optical fibers, that are employed in plasma diagnostic as well as data transfer and sensing of these installations.

- Nuclear Power Plants, which nuclear reactors, are able to generate radioactive fission products, photons, electrons, and neutrons. In this kind of installations the dose can reach the GGy and high temperatures up to $800^oC$. As seen at Fukushima-Daiichi, instrumentations have gone out of order during this nuclear accident as a consequence of power supply losses. Possible

improvements in strengthen instrumentations concern materials and structures, which may be remotely monitored thanks to Optical Fiber Sensors (OFS). OFS are widely involved in severe environment constraints detention in nominal conditions as well as in case of severe accident. They include distributed sensing (Rayleigh, Raman, Brillouin) for temperature sensing, H2 concentration and ionizing radiation monitoring [10].

- Radioactive waste storage sites, where products from nuclear reactors require appropriate storage. One of the most recent challenge is offered by the French project Cigéo of ANDRA, the underground repository for high-level and intermediate level long-lived radioactive wastes [11].

## 1.3 Matter-radiation interaction

As we will see deeply in the following sections of this chapter, the degradation of optical fibers is a consequence of the formation of Color Centers (CC), that are due to the "redistribution" of charges in the silica matrix after the exposure to ionizing radiation. Before explaining the characteristics of silica and of the related color centers, it is worth to report some fundamental notions about the radiation-matter interactions and how the energy released by radiation can interact with the matter which will undergo modifications.

With the term of ionization we refer to the process of extraction of an electron from an atom and the following formation of electron-hole pair. This process can be described by a bullet (charge particle or photon) interacting with the electrons of the atom target that remains ionized [16]. All the types of radiations that interact with the matter cause the ionization of the atoms or molecules that compound it. The radiations can be directly ionizing, such as charge particles, or indirectly ionizing like the electromagnetic radiations (X or $\gamma$ photons).

### 1.3.1 Particle radiation

Particle radiation can be made up of protons, electrons, $\beta$ particles and $\alpha$ particles; it interacts with electrons and nuclei by transferring of energy in the crossed medium. There are two types of interactions:

- with electrons: excitation and / or ionization;
- with the nucleus: elastic / inelastic diffusion, *Brehmsstralung*, pair creation.

The energy transfer from these interactions is called energy loss rate or stopping power and denoted as $dE/dx$. This loss of energy per unit of length is given by the equation [16]:

$$\left.\frac{dE}{dx}\right|_{total} = \left.\frac{dE}{dx}\right|_{electronic} + \left.\frac{dE}{dx}\right|_{nuclear} \tag{1.1}$$

For charged particles the average energy loss $dE/dx$ is given by the *Bethe-Bloch* formula:

$$-\frac{dE}{dx} = \frac{z^2\varepsilon^4 N_e}{4\pi\epsilon_0^2 m_e v^2}\left[\ln\left(\frac{2m_e v^2\gamma^2}{\bar{I}}\right) - \frac{v^2}{c^2}\right] \tag{1.2}$$

Where $N_e = NZ$ is the density of electrons target, obtained by $Z$, the atomic number of the medium through which the high energy particle passes, multiplied by the number density of atoms $N$; $ze$ is the charge of the incident particle, $v$ the velocity of incident particle, $m_e$ the mass of the electron, $\bar{I}$ is the medium excitation potential. According to the Bethe–Bloch formula, the energy loss rate depends only upon the velocity of the particle and its charge [16]. The dependence of the loss rate upon the kinetic energy of the particle is shown schematically in Fig.1.2.

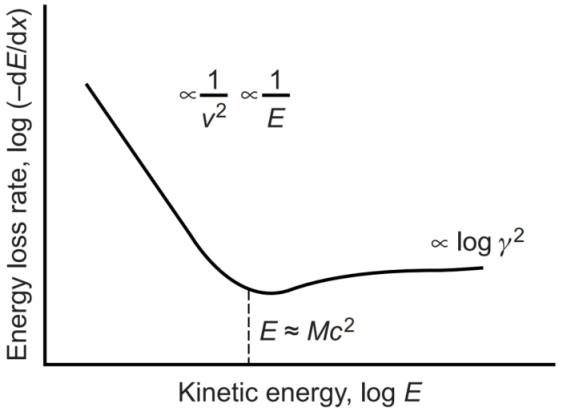


**Figure 1.2:** A schematic representation of the energy loss rate upon the kinetic energy of the charged particle. Adapted from [16].

Energy loss varies as the particle goes through the material, reaching a maximum at a certain depth. The curves representing the energy loss $dE/dx$ as function of the penetration depth of the particle into the material are called *Bragg curves*, and the Bragg peak is a pronounced peak occurring immediately before the particle comes to rest. Their knowledge becomes very useful in medical radiotherapy field, for example when you want to target cancer cells with a minimal damage to surrounding healthy tissues. Knowing the energy loss per unit path of a particle turns out important for the calculation of its range ($R = \int \frac{dE}{dE/dx}$), from which you can go back at the average ionization potential of the target and therefore to the type of atoms of the target. In good approximation, the minimum ionization loss rate for each species atomic and by any medium, is given by:

$$-\frac{dE}{dx} = 2Z^2 MeV(cm^2/g) \tag{1.3}$$

The stopping powers are standardized values for different materials and they can be found on the NIST (National Institute of Standards and Technology) which provides many references in the field of physics [17].

### 1.3.2 Electromagnetic radiations

Electromagnetic radiation is a form of indirect ionizing radiation and is composed of photons whether they are $\gamma$ or X-rays. Depending on their energy they will produce different kinds of effect that are summarized in table 1.2.

| Energy (E) | Effect | Physical phenomena |
|---|---|---|
| E<1eV | thermic | oscillation of atoms |
| 1eV<E<10eV | excitation | excitation of the valence electrons |
| E>10eV | ionizing | excitation of electrons in the inner orbitals, nuclear transition with atomic and nuclear ionization. |

**Table 1.2:** The effects and physical phenomena of the electromagnetic radiation based on the energy range.

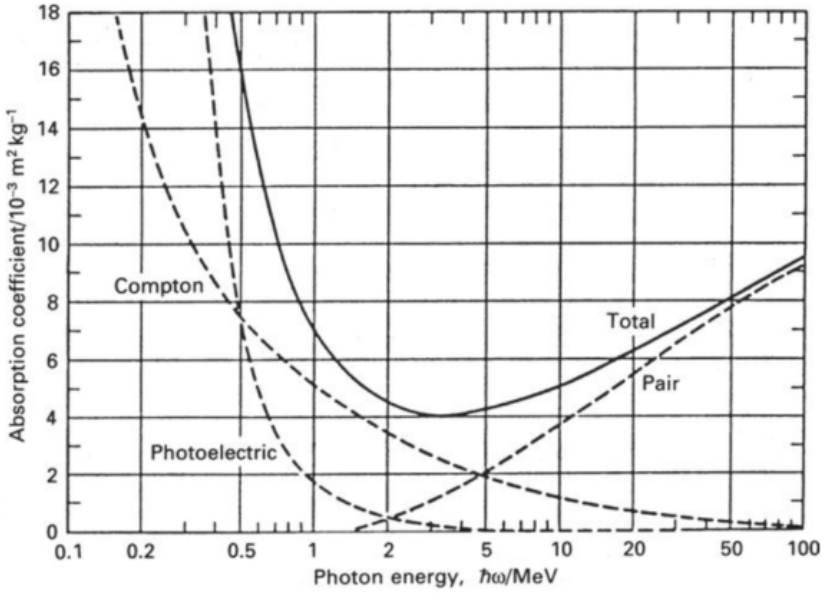


**Figure 1.3:** The total mass absorption coefficient for high energy photons in lead, indicating the contributions associated with the photoelectric absorption, Compton scattering and electron–positron pair production. Adapted from [16].

Pair production probability increases with the atomic number Z as $Z^2$. In Fig.1.3 is reported the total mass absorption coefficient for high energy photons in lead, in order to represent the contributions associated with the photoelectric absorption, Compton scattering and electron–positron pair production. These various radiations have a contribution in radiative environments to which our applications are dedicated such as space environment and nuclear environment, thence these are the possible ionization that will be responsible for the degradation of the material.

The interaction mechanisms between electromagnetic radiation and matter will be mainly of three types: photoelectric effect; Compton effect; pair production. Each of these processes will result in a transfer of energy from the photon to the

kinetic energy of the electrons. The energy transferred to the electrons from the photon can be complete or just a fraction, in the last case the energy can be lost also with the interaction with the lattice or with the nuclei. These processes will be very sensitive to the energy of the incident photon but also to the atomic number of the material absorbing the photons.

In the photoelectric absorption process, a photon undergoes an interaction with an atom target in which the photon completely disappears; in its place, an energetic photo-electron is ejected from one of the bound shells of the atom. For $\gamma$ rays of enough energy, the most probable origin of the photo-electron is the most tightly bound or K shell of the atom. The photo-electron appears with an energy equal to $E_{e^-} = h\nu - E_b$, where $E_b$ represents the binding energy of the photo-electron in its original shell and $h\nu = hc/\lambda$ is the quantized energy of the photons, where h is the Planck constant, c the speed of light and $\lambda$ the wavelength of the incident radiation. The photoelectric interaction is most likely to occur if the energy of the incident photon is just greater than the binding energy of the electron with which it interacts. The gap left will be filled by a free electron of the medium, thus the filling of an inner-shell vacancy is accompanied by the emission of an electron (Auger effect) or by a fluorescence radiation [16]. The photoelectric process is the predominant mode of photon interaction at relatively low photon energies (E<1 MeV) and high atomic number Z.

The Compton effect describes the scattering of photons on free electrons. The incident photon $\gamma_i$ will collide with an electron giving rise of a photon and an electron. The latter, called electron Compton, will acquire kinetic energy and the emitted photon $\gamma_e$ will be emitted with an angle $\theta$ relative to the direction of the incident photon [16]. The Compton electron is always projected forward therefore the $\gamma_e$ photon can be back scattered. The Compton effect probability is almost independent by the atomic number Z and it decreases as the photon energy increases.

The electron-positron pair production occurs for photons of high energy (E$\geq 2m_ec^2$ = 1.022 MeV). It takes place in the Coulomb field of the nucleus, the photon disappears completely producing an electron and a positron, both having the same mass and the same kinetic energy. The electron will be free and will be able to bind to an atom, whereas the positron meeting an electron will annihilate itself by transforming into two $\gamma$ photons with energies equal to 511 keV each and emitted in the opposite way [16].

## 1.4 Amorphous silica and point defects

In this section are presented and explained the characteristics of silica, its structure and the point defects, ranging from pure to doped silica. We start by explaining the structure and the features of the pure silica in crystalline and amorphous state. Later, having introduced the variety of defects present in silica, we then focus on the Aluminum, Phosphorous, Germanium and Fluorine related defects, which are the main doping elements used in this thesis work.

### 1.4.1 Silica structure

Silica ($SiO_2$) is an amorphous compound of silicon and oxygen. It's one of the most exploited insulators in solid state physics thanks to its physical characteristics and low manufacturing cost. It presents high transparency in a wide spectral range (from the UV-visible to the NIR) and low conductivity due to an energy gap of about 9 eV between valence band (VB) and conduction one (CB) [18–20]. The silica is present in a great portion of the Earth's surface so it is one of the most widespread materials [21]. For these reasons silica finds applications in a lot of fields, from electronics and chemical processing to technological applications like optoelectronic devices and optical fibers [18].

In general the $SiO_2$ crystallizes in at least seven known compact polymorphs, which, with the exception of one high-pressure form (stishovite), comprises networks of $SiO_4$ tetrahedra bonded to each other through an oxygen [19]. The atoms are held together by covalent bonds and this structure is the unitary cell. The structure and properties can be defined with few parameters and information can be obtained through diffraction data [18, 22]. The most studied form in the field of solid state physics is the $\alpha$-quartz [18]. In $\alpha$-quartz each tetrahedron is characterized by an $O - Si - O$ angle of $109.5^o$ and an angle between two tetrahedron $Si - O - Si$ of $144^o$ [18, 22]; in each tetrahedron the two long Si-O bonds are 1.6145 Å, and the two short bonds are 1.6101 in length [23].

The crystalline network is characterized by a perfect structure defined by the crystallographic unit cell plus translational symmetry [22]. So the structure can be defined by few parameters and from diffraction data over a region of reciprocal space it is not hard to determine uniquely the structure of a crystalline solid [22].

The $\alpha$-quartz can be transformed into the vitreous state by rapid cooling of the melt but the optical and electrical characteristics do not change a lot from the $\alpha$-quartz state [19], since the amorphous state has the same primitive cell than the crystalline one [18, 19]. Anyway in the amorphous form, on the entire macroscopic structure, the symmetry and periodicity properties are lost in large scale.

To describe the structure of the glass, different theories have been devised since 1835, the one that continues to be accepted is the Zachariasen's random network theory (RNT) [18, 21, 24]. According to this theory, the basic network is the same both in glass and in crystal. The main difference lies in the non periodic structure leading to a lack of order and symmetry in the amorphous form that is due to the atoms randomly bounded.

Zachariasen's ideas about a general oxide glass as the $SiO_2$, can be summarised by the following rules [21, 24]:

- an oxygen atom is linked to not more that two Si atoms;
- the number of oxygen atoms surrounding Si atom must be small;
- the oxygen polyhedra share corners with each other, not edges or faces;
- at least three corners in each oxygen polyhedron must be shared.

Generally the characterization of amorphous solid structures is based on three ranges of interest: short medium and long. But for silica, it is more convenient to examine four ranges [22].

The first range includes the structural unit: the AX4 tetrahedron, which in the case of silica A corresponds to Si and X to O, namely one silicon bonded to four oxygen creating a tetrahedral structure. In this range the elements of interest are the $A - X$ bond length and the $X - A - X$ bond angles ($\delta$). Silicon is bound to four oxygen with an angle of $109.5^0$ (see fig. 1.4a) [25].

The second range includes interconnection of adjacent structural units of the type described above. The structure adopted for silica is composed by two tetrahedrons of $SiO_4$ bonded to each other through an oxygen. The second range involves three variable parameters: $A - X - A$ bond angle ($\beta$) and two torsion angles ($\alpha_1$ , $\alpha_2$) [22, 25], (see fig. 1.4a). In the crystalline structure the two tetrahedrons are bound to form a precise angle ($Si - O - Si$ of $144^o$) but not in the case in the amorphous structure, where this angle may vary between $120^o$ and $180^o$ involving a random distribution in the tetrahedron orientation [22, 25]. Figure 1.4b shows this distribution normalized by the maximum bond angle.

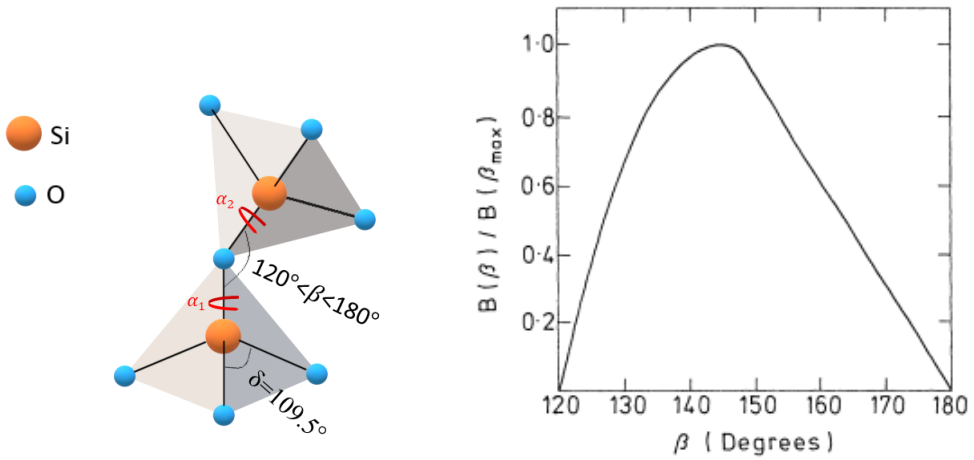


(a) (b)

**Figure 1.4:** a) Interconnection between two structural units in silica in view of describing the bond angles ($\delta$, $\beta$) and torsion angles ($\alpha_1$ , $\alpha_2$). b) Distribution of the $Si - O - Si$ ($\beta$ angle) adapted from [25].

The third range involves lattice topology, which, for an amorphous structure, may be completely specified in terms of "first neighbor" theory, by means of a first neighbor table with values for each of the topological units present [25]. However, because of the disordered nature of the matrix, this is clearly impossible for real glasses and hence their network topology is frequently discussed in terms of the shortest path ring statistics [25].

This structure is called ring and it is defined as the smallest loop that contains a pair of Si-O bonds relative to a same silicon atom. The ring number is given by the number of tetrahedrons participating in the ring formation[22]. The shortest path ring statistics for $\alpha - quartz$ gives a ring number of 6 and 8, whereas for silica is expected to exhibit a distribution of ring sizes [22]. Most of the rings have order

n=6, but there are rings of order 3 and 4 whose vibrations can be easily observed by Raman measurements [26, 27].

Finally, the fourth range is given by density fluctuations which give rise to microhetereogenity on longer scale of the order of 10s of Angstroms [22].

In figure 1.5 is shown the Zachariasen's random network diagram for a glass composition $A_2X_3$, here are also highlighted in black the first, the second and the third range order labeled respectively by I, II, III.

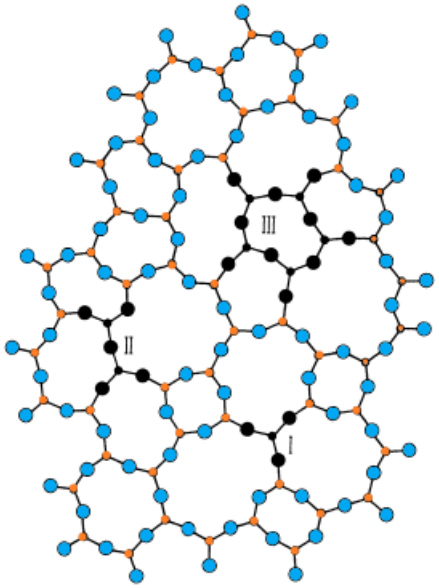


**Figure 1.5:** Zachariasen's original random network diagram (retraced) for a glass composition $A_2X_3$ adapted from [22], where A is designed by a small orange circle and X by a large cyan circle. The roman numbers I, II, III indicates the range order with the respective structural unit highlighted in black. $SiO_2$ may occur in the vitreous state represented by this random network diagram, where Si is represented by small orange circle and O by a large cyan circle.

### 1.4.2 Pure silica point defects

Ideal silica has a transparent region in the electromagnetic spectral range from NIR to UV due to its wide band gap [18]. However this property can be corrupted and the optical characteristics of silica may change as a result of manufacture processes or radiation exposure. In fact, during the same material preparation an over or under stoichiometry state could cause localized defectiveness due to the presence of more or less atoms with respect to the ideal lattice. In addition, the presence of impurity atoms (atoms different from Si, O) is the origin of modifications of the energy levels distribution with consequences on the optical and electric features of $SiO_2$ [22]. Finally, as said extensively at the beginning of this chapter, for many applications the material is exposed to ionizing radiation or particles; after this

exposure its transparency is damaged due to the creation of radiation-induced defects. Overall the defects (also named color centers) can be divided into intrinsic and extrinsic defects. Extrinsic defects result from impurities, that is atoms that should not be present in the glass matrix. The intrinsic defects involves erroneous arrangements of Si, O atoms, incomplete or broken bonds. Some of the basic vacancy interstitial type defects are reported in fig.1.6.

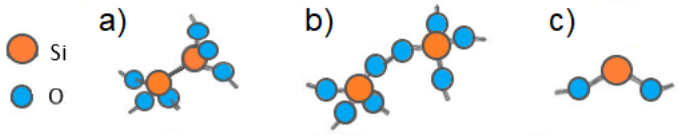


**Figure 1.6:** Vacancy interstitial type defects observed adapted from [28]. a):Oxygen vacancy ("Si-Si" bond); b) Peroxy bridge (interstitial O); c) Divalent Si ($Si_2^o$ center)

E' center and oxygen deficient centers (ODC(I) and ODC(II)) belong to the family of intrinsic colors centers in non doped silica, while POR (peroxide radical) and NBOHC (nonbridging oxygen hole center) are typical colors centers in oxygen excess silica [22]. These defects are characterized by the presence of an unpaired electron and therefore they are paramagnetic.

♢ *E' center*

The E' center is a paramagnetic defect characterized by an unpaired electron in the $sp_3$ orbital of Si ($\equiv Si\bullet$), as represented in fig.1.7. Electron Paramagnetic Resonance (EPR) measurements enabled to study several forms of E' centers, they are distinguished in $E'_\gamma$, $E'_\delta$,$E'_\beta$, $E'_\alpha$ [29, 30].

The $E'_\gamma$ center is the most important and can be induced by UV, X, gamma and neutron irradiation. It is characterized by an axially symmetric EPR line shape and has a hyperfine structure consisting of an EPR doublet of 42 mT. On the structural origin of this signal there were several issues, but two main currents can be distinguished: the first assumes that it is given by the interaction of an electron with the nucleus of $^{29}Si$, which makes $E'_\gamma$ the equivalent of $E'_1$ in Crystalline silica [22]. The second states that it is due to the hyperfine interaction of an electron with a proton, but this theory was finally eliminated by the studies made by D.Griscom [22, 31]. Several works find a correlation between the optical absorption (OA) band of silica at 5.8eV and $E'_\gamma$ EPR signal [22, 28, 30, 32].

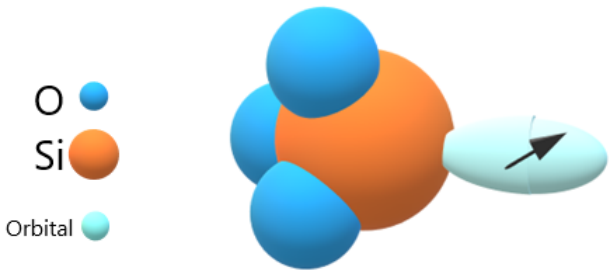


**Figure 1.7:** Microscopic structure of SiE' center

♢ *ODC*

ODC (I) (oxygen deficient center) is a diamagnetic defect which most accepted model is the single relaxed oxygen vacancy: O=Si-Si=O (see fig.1.8) consisting in bonding between two Si atoms. This defect is considered a precursor of many types of E' centers. To this defect is assigned the optical band induced by radiation at 7.6 eV, which was founded both in $\alpha$-quartz and silica [28].

The ODC(II) is a diamagnetic defect consisting in a twofold coordinated Si atom(II) with two electrons not involved in any bond (=Si:). The most accepted steric model is represented in fig.1.8. This defect is responsible for an optical absorption band localized at about 5 eV that it is typically 102-103 times lower that ODC(I) band at 7.6 eV [28]. The precise position of ODC(II) band depends on the intrinsic or extrinsic character of the defect. In fact, the ODC(II) could be observed in pure as well as in Ge or Sn doped silica [32]. Two photoluminescence (PL) bands in at 4.4 eV and 2.7 eV are due to this defect, the first emission band is due to the singlet-singlet transition with a lifetime of 4.2 ns, the second one is due to a triplet-singlet transition with a lifetime of 10.2 ms [32] (see fig.1.8), this last band is also observed by TL emission, as it will be reported in the results if this thesis.

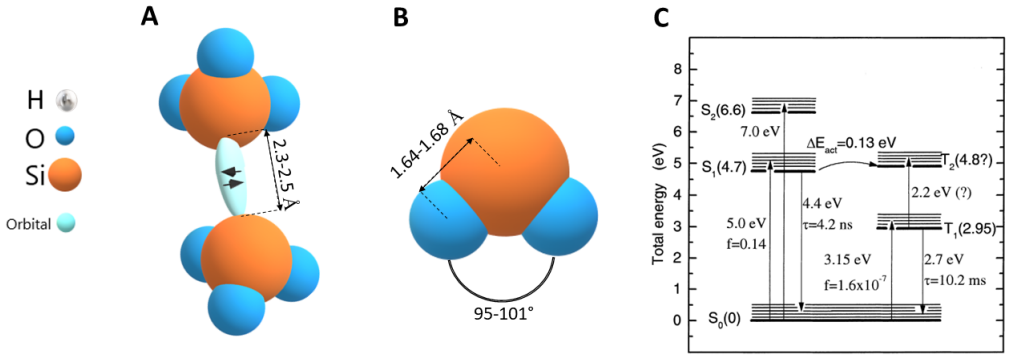


**Figure 1.8:** Models of oxygen deficient centers: (A) Relaxed oxygen vacancy or SiSi "wrong bond", denoted also as ODC (I). (B): Probable structure of the oxygen deficiency center ODC(II): twofold coordinated Si atom. (C) Energy scheme for silicon-related oxygen deficient centers SiODC(II) adapted from [32].

♢ *H(I) center*

In silica containing hydrogen, the ODC(II) are the precursor sites of the H(I) paramagnetic centers. It is originated from the capture of a hydrogen in an ODC(II). This reaction requires the presence of hydrogen that can be produced by the reaction between a H2 and an NBOHC [22, 23, 33]. H(I) is the analogous of SiE' center but with an H atom instead of one O bounded to Si, as represented in fig.1.9. This center present an optical absorption band at 4.9 eV [32].

♢ *NBOHC*

NBOHC, non-bridging oxygen hole centers, ($\equiv Si - O\bullet$) is a defect very common in silica, consisting in a dangling bond of one of the oxygen bonded to silicon, as represented in fig.1.10a. EPR work on irradiated bulk silica established that the unpaired spin resides in the 2p-like non-bonding orbital of the terminal oxygen

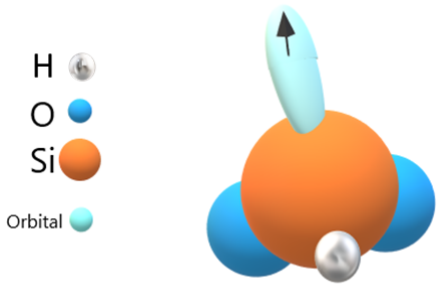


**Figure 1.9:** Models of twofold-coordinated silicon with a trapped hydrogen atom or H(I) center.

atom of NBOHC. This signal is often related to *wet OHC* signal, because it is found in wet (high-hydroxyl content) silica. There is a wide EPR and optical evidence that NBOHC can be created by radiolysis of hydroxyl groups [19]:

$\equiv Si - O - H\ H - O - Si \equiv \longmapsto \equiv Si - O\bullet\ H - O - Si \equiv + H\bullet$

However this reaction is not the only way to create NBOHC's. Oxygen dangling bonds may be created as well in "dry" silica, with have a negligible amounts of SiOH and a tendency to O deficiency, by rupture of Si-O bonds of the glass network (e.g. by fiber drawing or neutron irradiation [19]) which allow for creation of pairs of SiE' centers and NBOHCs by the intrinsic mechanisms [34]:

$\equiv Si - O - Si \equiv \longmapsto \equiv Si - O\bullet\ \bullet Si \equiv$

In glasses where this last process is favorable, E' centers often occur without the complementary NBOHCs; however, the opposite situation, NBOHCs without E'-centers, is highly unusual [34]. NBOHC present three optical bands at 1.9 eV, 4.8 eV and 6.8 eV [35]. The energetic scheme of absorption transition is reported in fig. 1.10b.

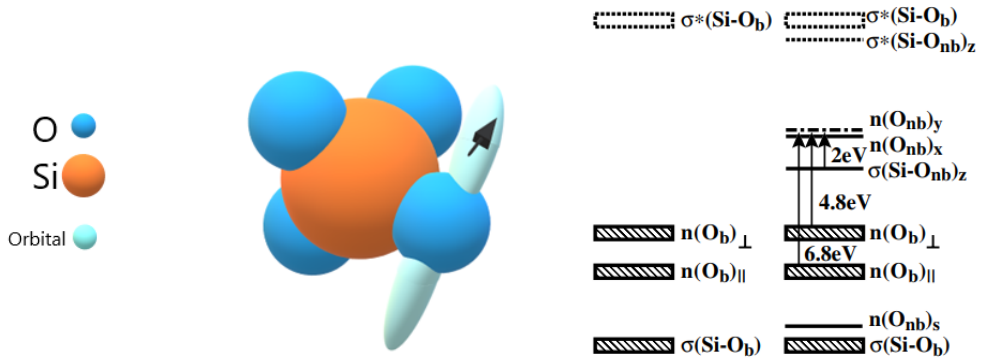


**Figure 1.10:** (a) Microscopic structure of NBOHC center. b) Energetic scheme of absorption transition adapted from [36].

In this work from "ab initio" calculation, the band at 2.0 eV is attributed to tran-

sition from the $\sigma$ bond between Si and dangling oxygen to nonbonding $\pi$ orbital on the dangling oxygen. Skuja highlighted that the absorption of this defect light in the UV spectral domain can be described by a semi-continuous band from 4 to 8 eV[34]. A luminescence band related to this defects was observed at 1.9 eV [37]. The OA and PL bands are reported in fig.1.14.

♢ *POR*

The POR (peroxy radical ($\equiv Si - O - O\bullet$)) consists of a silicon bound to a molecule of oxygen having a delocalized unpaired electron over antibonding $\pi$-type orbitals of the O-O bond [22, 28] (see fig.1.11). It can be originated by the reaction of interstitial O2 molecule with silicon dangling bond [28]. POR is best-characterized in irradiated silica by EPR spectroscopy [28] whereas its optical properties are not accurately known due to the close proximity of the POR and NBOHC absorption bands parameters. This complication, due to the fact that the bulk POR's and NBOHC's typically interconvert via adding or detaching O atom [38], often causes complex changes in absorption spectra, including pseudobands formed by difference spectrum of two close gaussians [28]. Anyway to silica surface POR is assigned a large absorption band peaked at 5.4 eV and and one at 5.3 eV assigned to the corresponding bulk defect[28, 32].

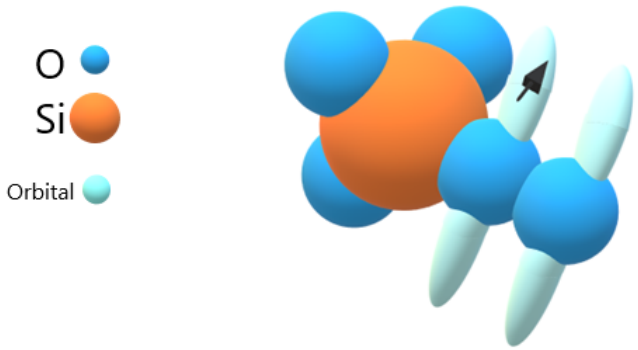


**Figure 1.11:** Microscopic structure of POR center.

♢ *POL*

The POL (peroxy linkage $\equiv Si - O - O - Si \equiv$ constituted by silicon atoms connected via two oxygen atoms, is formed when interstitial oxygen atom associates with the bridging oxygen both in $\alpha$-quartz and in silica [28]. It is a diamagnetic center usually associated with oxygen rich silica samples[28]. A weak absorption band at 7.1 eV is associated to this defect [28], as well as the one at 3.8 eV [39] even if the origin of this band is not clear and some works attribute it to the interstitial chlorine molecule [40, 41]. A rapresentation of this defect is reported in fig.1.12.


**Figure 1.12:** Microscopic structure of POL center.

♢ *STH*

Self Trapped Holes (STH) are metastable intrinsic defects in silica. They are responsible for most of the optical loss in the IR part of the spectrum in fibers containing few OH radicals [42]. Exist two variants of STH (STH1 and STH2), both are reported in fig.1.13.

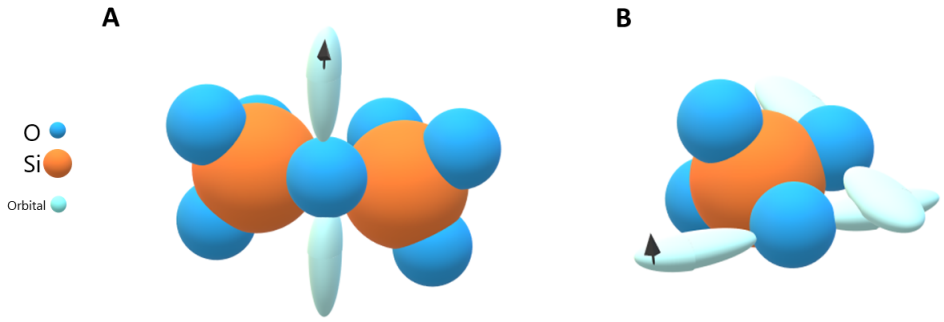


**Figure 1.13:** Microscopic structure of (a) STH1 and (b) STH2 centers.

STH1 can be found anywhere in the glass, due to the potential hole trapping of the glass itself. While STH2 are much rarer because the precursor sites able to trap holes to form these STH2, present a local structure of $\alpha$ quartz [42]. Both are paramagnetic defects observable in EPR [43].

The optical absorption bands assigned to them vary considerably depending on the nature of the glass, if this last is bulk or fiber. Sasajima *et al.* report bands centered at 2.60 and 2.16 eV for STH1 and STH2 respectively in bulk samples [44]. The values established by Griscom in an optical fiber are lower, around 1.63 and

1.88 eV respectively [43].

♢ *OH-group*
Finally the OH group which is an extrinsic H-related defect. It is characterized by some optical bands in the NIR peaking at 1380 nm, 1250 nm, 1140 nm, 945 nm and 880 nm, which are overtones and combination mode of the fundamental absorption band at 2.7$\mu$m [45].

A summary of the optical bands, luminescence excitation bands and emission bands of defects cited above is reported in fig.1.14.

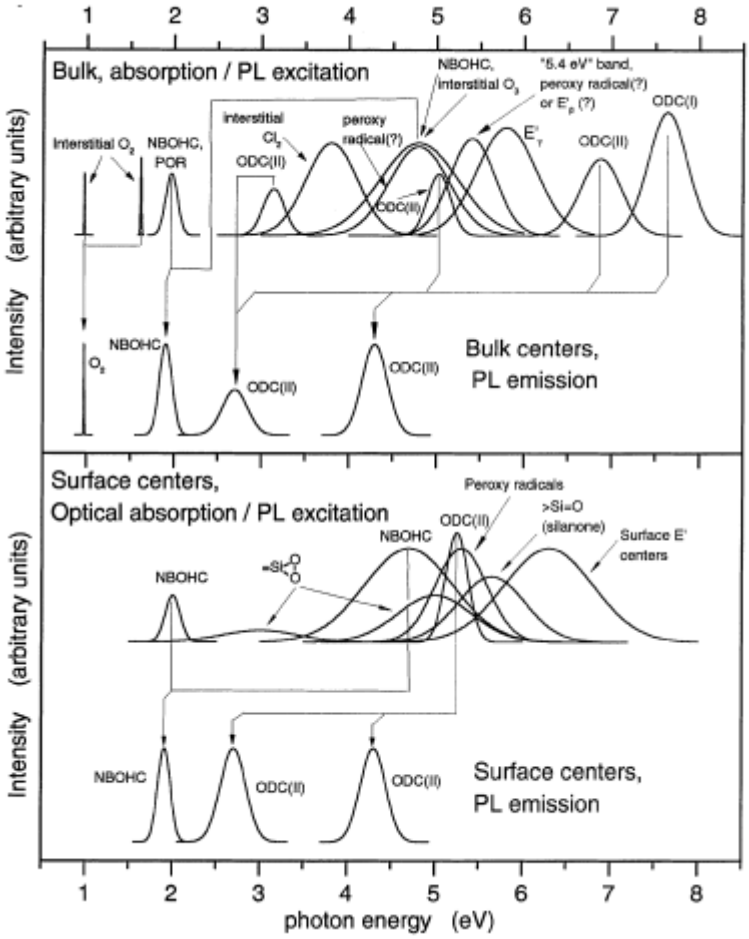


**Figure 1.14:** Resume of the most optical absorption, luminescence excitation bands and emission bands of defect centers in synthetic silica (top) and on the surfaces of $SiO_2$ (bottom); adapted from [32].

In addition, in Fig.1.15 is reported a representation of the optical absorption bands related to pure silica defects usually observed in pure silica bulk samples and OFs, which characteristic positions in energy and the FWHMs are the typical found in literature [32].

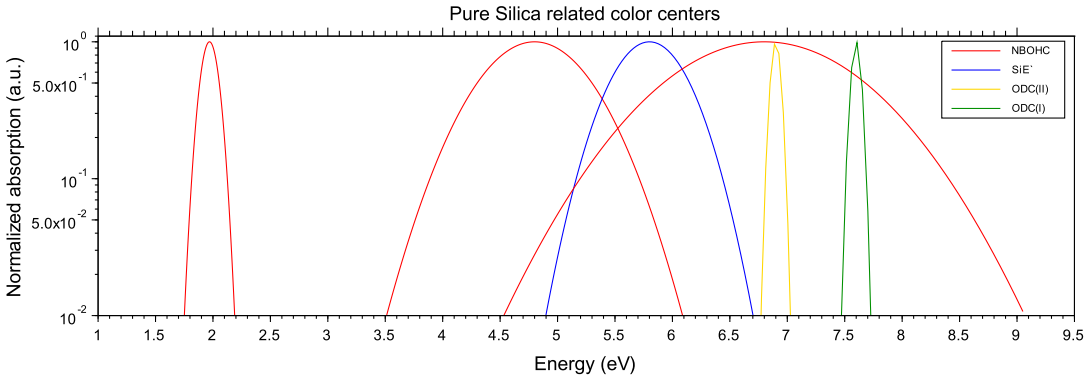


**Figure 1.15:** Normalized Absorption bands associated with different pure silica related point defect structures. Bands parameters adapted from [32].

A deep investigation on RIA in pure silica core fibers (PSC) was made by Girard *et al.*[46]. In this work a comparison between RIA after 1s of Xray pulse and during $\gamma$-rays (200 Gy dose and 3 mGy/s dose rate) shows that the contribution of self trapped holes (STH) in the visible domain is more important in the RIA obtained after Xray pulse, while is negligible the contribution of NBOHC at 1.9 eV. In both RIA spectra anyway, the RIA level reaches $10^{-1}$dB/m at around 3.5 eV. The main contribution of this RIA level is due to impurities of chlorine ($Cl_2$ and $Cl^o$ AO bands peaking at 3.7 eV and 3.2 eV respectively).

One choice to reduce the amount of chlorine and as consequence the loss in the visible part of the spectrum due to these impurities, is to increase the Si-OH group, and by particular preform deposition technique allowing the manufacturing optical fibers with low-OH and low-Cl contents [46]. In this case, at MGy dose levels, the main contribution to the RIA in due to the NBOHCs [46]. Furthermore, to improve the radiation resistance response of PSC fibers, it is possible to make a H2 loading treatment (technique explained in the following section). Some works investigate this effects for ITER project or for space applications [47, 48] Concerning the NIR domain, especially the two telecommunication windows at 1310 nm and 1550 nm that retrieve most interest for applications in this domain, it has been shown that O2-loaded fibers exhibit better radiation response that the standard ones. In fact, the contribution of STH defects to RIA seems to be less for O2-loaded fibers [49, 50].

In is worth to know that several works [51–53] report the presence of one long wavelength non-Gaussian OA band peaking at the wavelength greater than 1.7 $\mu$m at doses higher than 10 kGy in PSC fbers, but also in Ge- and N-doped fibers by several researchers [46, 52–54]. The behavior of this absorption is very similar to that of low-temperature infrared absorption (LTIRA) discovered by Chernov *et al.*[55] that is associated with inherent STHs, but even if both bands are peaking around 0.6-0.7 eV and are non-Gaussian composed of a continuum of states, the LTRIA component shows a very short lifetime [55], while the former band appears very stable even at increased temperatures. Finally, few studies [56–58] also report the possible presence of an OA band around 1 eV in PSC fibers which needs also further investigations to be definitively associated to a defect structure.

### 1.4.3 Al-related point defects

Aluminum, which is incorporated by substituting a Silicon site, is one of the most abundant impurities in $SiO_2$. It results in a hole trapped in an oxygen bridging an Al and a Si atom: Aluminum-Oxygen-HoleCenter (AlOHC). It is considered to be the major structural origin of a "smokey" coloration in quartz [19, 23, 59, 60] and the first study was interpreted in detail by o'Brien's in 1955 [61]. Despite it being such a dated study, over the years, not many studies are developed concerning the optical properties of the defects related to Aluminum. Moreover the majority of these studies focused on point defects created in sapphire (crystals) or crystalline [23, 60]; only few of them are related to aluminum effects in amorphous silica [62].

More recently several works demonstrate how the Aluminum may be used as main doping element in silica optical fibers for dosimeter applications, because it would lead to a high sensitivity ideal for some applications such as sensors [63–65]. A recent work made by Alessi *et al.* [66], demonstrates that Al-doped fiber can be good dosimeter in a certain usable range of dose and dose rate. In this work in fact, all the Al-doped fibers tested present in fact a linear RIA kinetics up to 2-3kGy(SiO2) for different dose rates and even irradiation temperatures (from RT to $50^oC$).

In this context, the choice of Al was born in principle after some observations of the RIA in erbium-doped amplifier (EDFA) used in space applications [18, 67–70]. The Al was used as co-doping in EDFA devices but its radiation induced defects resulted as the main causes of the high RIA level observed after the ionizing radiation exposure in space that affects the optical properties of the amplifiers [63–65].

To the aluminum are related two point defects: the AlOHC and the AlE'. In the following are reported their structures and their optical characteristics.

♢ *AlOHC*

The AlOHC is a paramagnetic center deeply characterized by the EPR technique[71–73], which corresponds to a hole trapped in a non-bridging oxygen atom, as represented in fig.1.16 [20, 60]. The absorption bands are centered around 2.3 and 3.2 eV [59]. A band at 2.5 eV, associated with this center has also been observed in quartz [74].

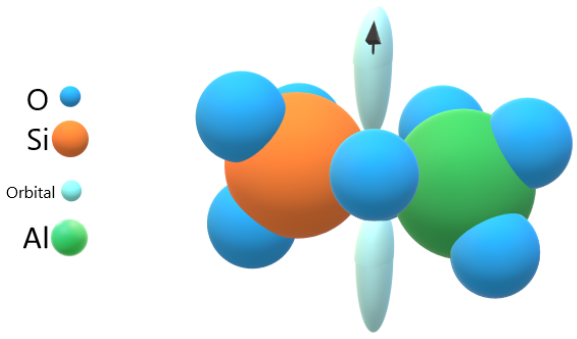


**Figure 1.16:** Microscopic structure of the AlOHC center.

♢ *AlE'*

AlE' is another paramagnetic defect [72], it is the analogous of the E' center but with an aluminum substituting the silicon (see fig.1.17). This defect presents an optical band at 4.1 eV [59, 75]. AlE' centers are formed by trapping electrons at neutral oxygen vacancies shared by two Al atoms [$\equiv Al\ Al \equiv$] [76, 77], or much more probably at positively charged oxygen 'pseudo vacancies' [$\equiv Al\ ^{+}Si \equiv$][78]. It is worth noting the capture of an electron at such unit does not only lead to AlE' centes [$\equiv Al^{\bullet}\ Si \equiv$], it can alternatively form a SiE' center [$\equiv Al\ ^{\bullet}Si \equiv$] [76–78].

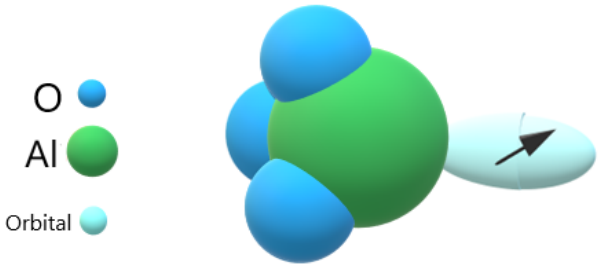


**Figure 1.17:** Microscopic structure of AlE' center.

In fig.1.18 is reported the work of Hosono, in which optical absorption bands induced by irradiation were examined in high purity synthetic $SiO_2$ [59]. Gamma-induced absorption signal was decomposed into 5-Gaussian bands peaking at 2.3, 3.2, 4.1, 4.9 and 5.8 eV (see fig.1.18b). The bands at 2.3 and 3.2 eV are assigned to AlOHC, whereas to the AlE' center is associated the band at 4.1. The allocation of the band at 4.9 eV to one of these two defects is uncertain [59, 73, 79].

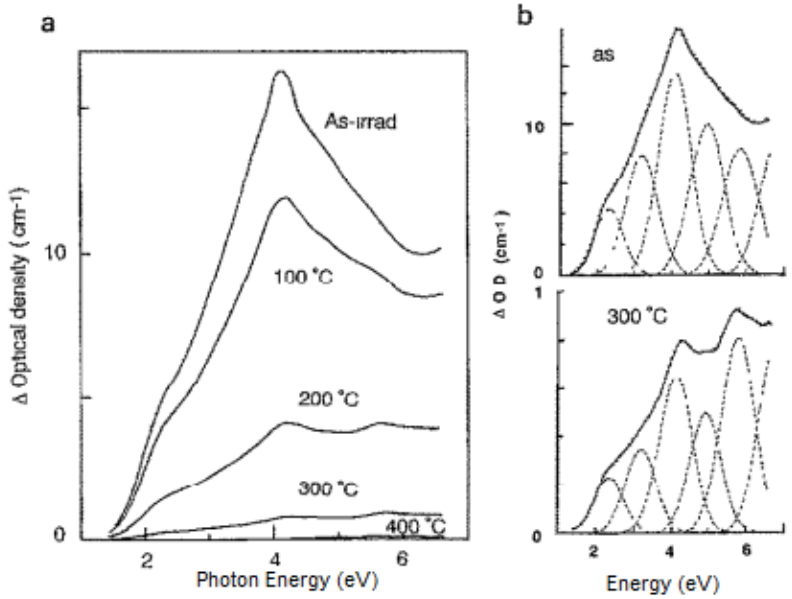


**Figure 1.18:** (a) Changes in $\gamma$-induced optical absorption spectra with isochronal annealing.(b) Examples of deconvolution of spectra, adapted from [59].

Some optical absorption bands attributed to aluminum have been characterized in a sample of silica containing Al by N. Trukhin [80], where is shown how the amount of Al may change the optical absorption spectra. In [73], are reported several optical absorption bands due to induced color centers appearing under ArF laser at 290 K which conversely are not present for irradiation at 80 K. In this work [73] a thermally stimulated luminescence induced by ArF laser in Al-doped silica is observed at 2.7 eV ("blue band") associated to the ODC defect. Trukhin *et al.* pointed out the formation of AlOHC as a result of a cascade of reactions. Irradiation with an ArF laser induces the trapping of holes on defects that were identified as STH in an aluminosilicate glass at 80 K. The thermal relaxation of STH releases holes that will diffuse into the matrix to trap on $Al^{3+}$ ions and ODC, leading to the formation of AlOHC and SiE' respectively [73].

Regarding the TL recombination mechanism Mady *et al.*[77], with an experimental approach combining the characterization of TL, RIA, and RIA annealing during TL readouts, showed that the main annealing process involves the recombination of thermally de-trapped holes with AlE' would thus reform Al-related vacancies (called Al-ODC) and subsequently the main TL band at around 3 eV which was assigned to these vacancies [77].

The main loss in Al-doped silica after exposure to radiation is in the UV-visible part of the spectrum, due to AlOHC and AlE' related optical bands. Girard *et al.* showed that in Al-doped optical fibers the RIA at around 600 nm can reach 200-500 dB/m after 200 Gy dose of X-rays radiation [46].

In fig.1.19 are reported the main optical absorption bands related to Al-doped silica defects.

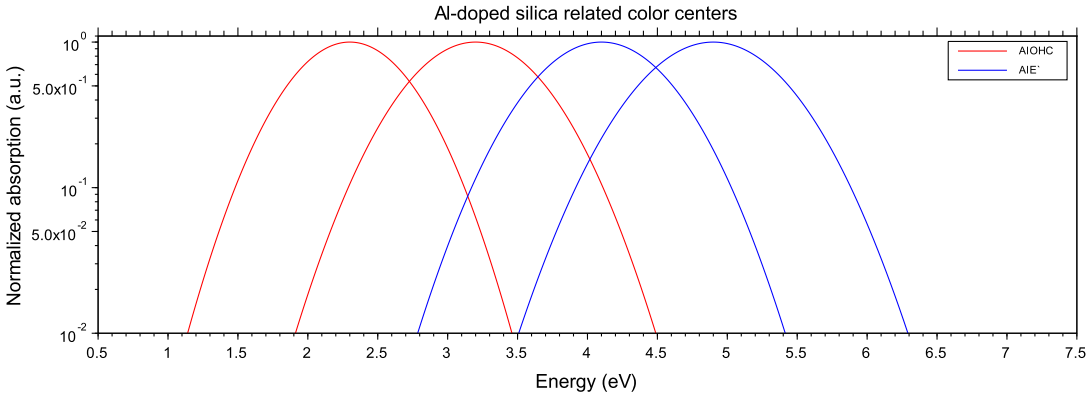


**Figure 1.19:** Normalized Absorption bands associated with Al-related point defect structures. Bands parameters adapted from [59].

### 1.4.4 P-related point defects

The choice of phosphorous as dopant in silica glass involves several advantages in optical fibers use: P doping increases the refractive index of silica, reduces its melting temperature [22] and changes its viscosity during the fiber drawing. Another important property of P- doped silica is the increase of the solubility of rare-earth ions with the consequent minor risk of cluster formation respect to the aluminosilicate glasses [81].

From an optical point of view, it is known that P-doped optical fibers are very sensitive to radiation and for this reason they are widely used in sensors or dosimetry applications [82, 83].

One of the first and most complete work on P-doped samples was made by Griscom in 1983 [84], on the basis of optical absorption and EPR studies; while a recent deep investigation of the radiation effects in P-doped silica has been done by di Francesca *et al.* [85].

The major defects related to P-doped silica glasses are presented in fig.1.20, where one can see the stochiometric structure of the defects, the precursors, the carrier trapping mechanisms and the structures of the defects arising from the different possible mechanisms. The last line report the nomenclature of the different defects. The structure and the main optical characteristics of these defects are reported below.

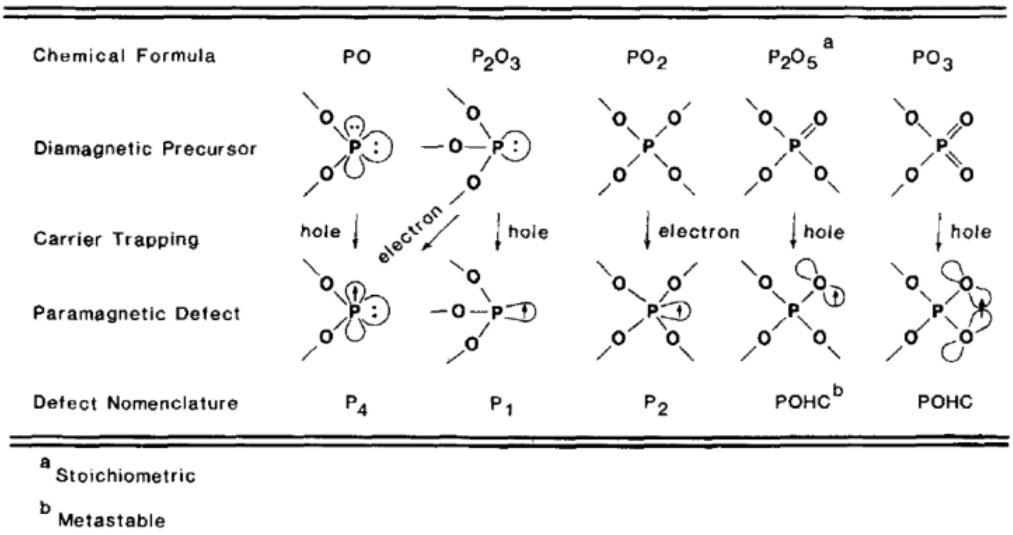


**Figure 1.20:** Phosphorus related radiation induced defects and the inferred precursor structures in a $P_2O_5 - SiO_2$ glass. Adapted from ref.[84].

♢ *P1*

P1 consists in a P atom with an unpaired electron and bonded with three oxygen atoms. This defect, characterized by an absorption band at 0.78 eV in the NIR [84, 85], is considered as the analogue of the SiE' center. This analogy comes from their similar structure, since the P1 formation, shown in in the upper branch of Figure 1.21, would be due to an hole trapping from the $P_2O_3$ molecule [84].

♢ *P2*

P2 is considered as the equivalent of the $[PO_4]^0$ center in phosphorus-doped $\alpha$ quartz [84]. In a $SiO_2 - P_2O_5$ glass, this same defect would be defined as silicon-substituted phosphorus. Since P has a higher valence (+5) than silicon (+4), such a precursor defect would provide a coulombic trapping potential for an electron. On this basis, P2 has been ascribed to a silicon-substituted phosphorus in silica tetrahedron, which has trapped an electron [84]. This defect is linked to an absorption band at 4.5 eV [84].

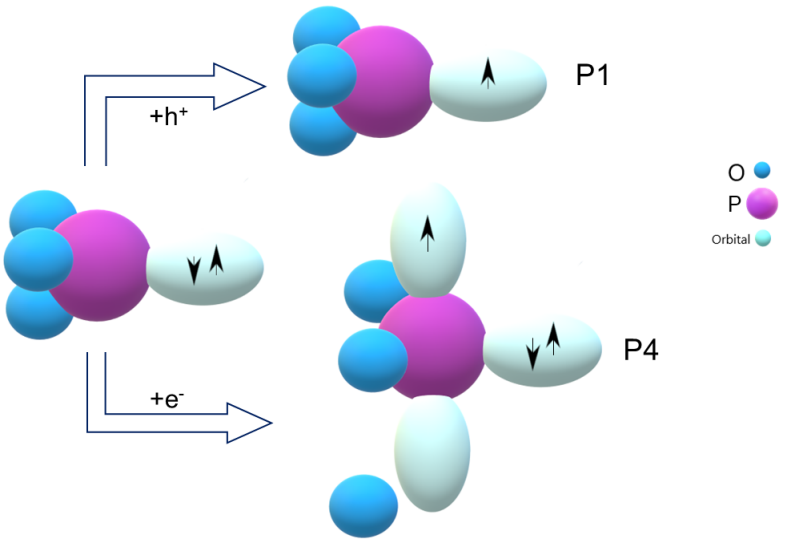


**Figure 1.21:** Model for the formation of the P1 and P4 centers by hole and electron trapping, respectively, at the site of a three-coordinated $P^{3+}$ precursor structure.

♢ *P4*

P4 is characterized by a P atom bonded with two oxygen ones and attached to a lone pair and an unpaired electron [84]. A potential precursor of P4 defect would be a trivalent phosphorus ion ($P^{3+}$) bonded to three bridging oxygen atoms. It is described by the figure 1.21 in which an electron is trapped by the precursor defect forming the P4 [84], but another possible precursor of the P4 is the twofold coordinated P, where a hole trapping gives rise to the conversion into P4 [84] (Figure 1.20). This defect is characterized by an absorption band located at 4.8 eV.

♢ *POHC* POHC is a P atom bonded to four atoms of oxygen with an unpaired electron. If the unpaired electron is located on a non-bridging oxygen the POHC defect is in the metastable configuration (${}^{b}POHC$), while, if the unpaired electron is shared by two non-bridging oxygen atoms, the defects is in a stable configuration (${}^{a}POHC$). A representation of both configurations is reported in fig.1.22.

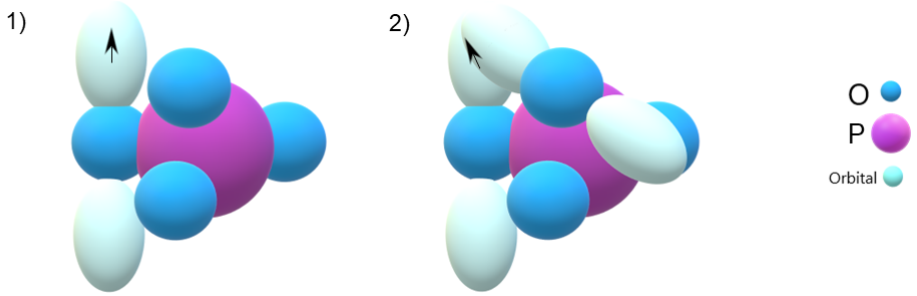


**Figure 1.22:** Microscopic structure of POHC metastable (1) and stable (2).

In the past, it was thought that the metastable form of POHC was unstable at room temperature, but successive studies have shown that this is not correct [86]. To this defect are associated several bands in the UV-visible range located at 2.2, 2.5, 3.2 and 5.3 eV [84]. A work made by Chan *et al.* attributed a photoluminescence band at around 2.1 eV to the POHC centers [87].

In Figure 1.23 are reported the main absorption bands associated to P-related defects in doped silica. It is worth to know that a strong optical absorption bands related to P defects appears only after irradiation.

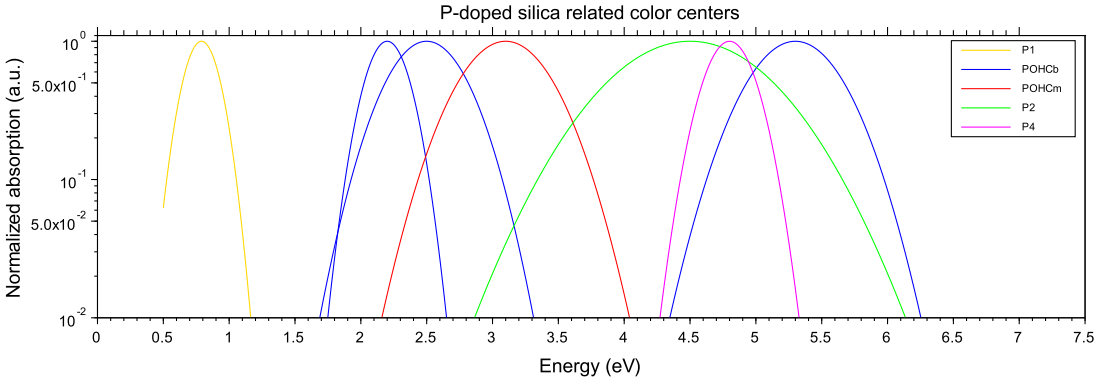


**Figure 1.23:** Normalized Absorption bands associated with different P-related point defect structures. Bands parameters adapted from [84].

As reported in Fig.1.23 the P1 band is located in the NIR around 0.78 eV without any overlap of other bands. This absorption property may compromise the fiber performances in radiation field applications; especially during the recovery process, when a decrease of POHC centers and the increase of P1 defects has been observed [88, 89].

Concerning the potential dosimetry application of P-doped optical fibers, a work made by di Francesca *et al.* [85] showed that the drawing conditions does not affect the radiation response of this kind of fibers in the UV-vis domain. In addition, studying the radiation response in the NIR together with EPR measurements, it has been shown that the creation of P1 defect is promoted by the increase of temperature up to $280^oC$. As said before, P1 defect is associated with an absorption band which is the main source of optical losses in the NIR domain in irradiated P-doped OFs, so this result is particularly relevant for the dosimetry applications [85]. The RIA in P-doped silica optical fiber is very high in the visible domain, reaching 100dB/m after an irradiation dose of 200 Gy [46]. The main contribution to this RIA comes from the POHCs defects in the UV-Visible and from P1 in the NIR [46].

### 1.4.5 Ge-related point defects

Germanium has been used as dopant in silica for decades and is widely used to realize different optical devices. Several reasons justify this choice. First of all, germanium increases the refractive index of silica glass that is an important property used to realize OFs for telecommunication; then Ge increases the photosensitivity which is an important property that offers the possibility to induce variations of

the refractive index of the material using radiation [22, 31]. In addition, the second harmonic generation (SHG) was observed in Ge doped silica [22, 31]. SHG was observed for the first time in 1985 by Osterberg and Margulis. In their experiment they injected pulsed light at 1064 nm from a Nd:YAG laser in a germanosilicate OF and they observed the generation of light at 532 nm with an intensity growing with the exposure time to the Nd:YAG laser. Concerning the dosimeter purposes in radiative field, it has been shown that germanium doped silica fibers have thermoluminescence properties that make them an excellent TL-mode detector in radiotherapy and in nuclear facilities too [90]. The main characteristic TL features of Ge-doped fiber to be a good TL dosimeter (TLD) is its high sensitivity to all types of radiations (X-rays, $\gamma$-rays, neutrons, ...), [91]. Ge belongs to the same chemical group of Si, therefore in nature germanium dioxide $GeO_2$ as crystalline structure, or "germania" as amorphous structure, exists as fundamental unit. it is characterized by a tetrahedron with a Ge atom at the center and four oxygen atoms at the vertexes. As for silica, it was shown that the continuous random network (CRN) method can be applied to describe the germania structure too [22]; but in the $GeO_2$ structure, the distribution of O-Ge-O angle is narrower than the O-Si-O one of silica (about $132^o$), and the length of Ge-O bonds is about 1.7 Å [22]. As a consequence of the above similarities, when a $SiO_2$ glass is doped with germanium, the atoms of the latter mainly replace those of silicon in the tetrahedral fundamental unit. The exposition of the Ge doped silica to ionizing radiation induces the generation of several optical absorption bands [31]. Given that Ge atoms are incorporated in silica mostly as substitution atom to Si, it is natural to expect that some of silica intrinsic defects would have their Ge-modified counterpart in which the Si atom has been substituted by a Ge one [22, 92]. In the following we report the main defects usually found in a Ge silica glass and their optical properties; a normalized representation of the Ge-related typical absorption bands is reported in Fig. 1.24.

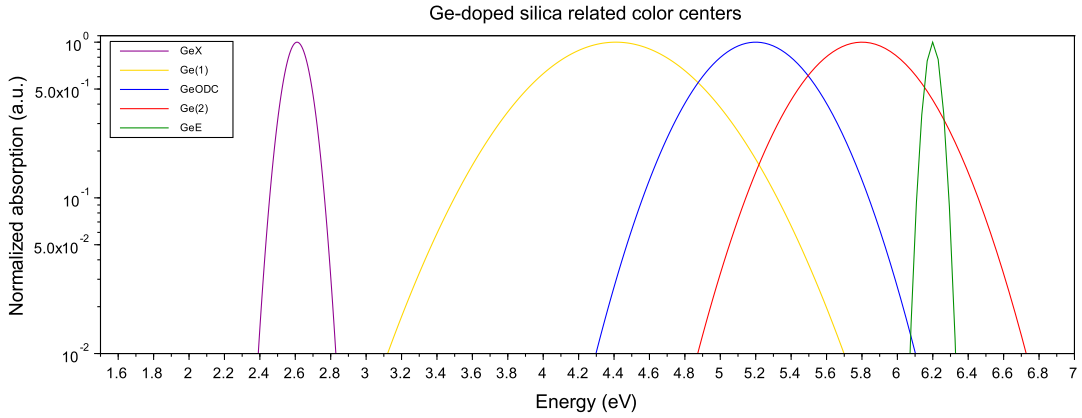


**Figure 1.24:** Normalized Absorption bands associated with different Ge-related point defect structures. Bands parameters adapted from [31].

♢ *Ge(1)*

Ge(1) is a paramagnetic defect consisting of an electron trapped on a tetra-coordinated Ge atom (see fig.1.25). The electron trapping is followed by a structural reorganization [31]. It is characterized by an absorption band at 4.5 eV [31]. The concentration

of Ge(1) is independent from Ge content for low doses of irradiation [31].

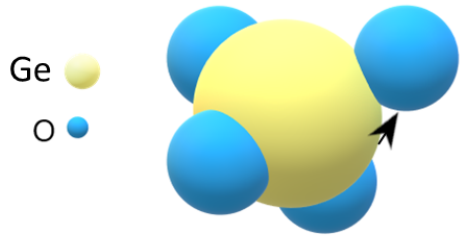


**Figure 1.25:** Microscopic structure of Ge(1) center.

♢ *E'(Ge)*

GeE' is a paramagnetic center where the Ge atom is three-coordinated, forming three covalent bonds with three different O atoms, and it has an unpaired electron in a $sp^3$ orbital (see fig.1.26). It shows the same structure than SiE' defect and presents an absorption band at 6.3 eV [22] .


**Figure 1.26:** Microscopic structure of GeE' center.

♢ *GLPC*

The germanium lone pair center (*GLPC*) is a diamagnetic defect that consists of a germanium atom linked to two oxygen atoms by single bonds and with a pair of electrons not involved in any bond (lone pair). This defect is associated with a band centered at 5.2 eV, the so called $B_{2\beta}$ band [93]. It was shown in several works [94–96] that under UV and Xray radiation, the concentration of GLPC decreases with the creation of other absorbing and species. Furthermore, this defect has the same structure of ODC (II) and has two photoluminescence bands peaked at about 4.3 and 3.2 eV [32, 93], this last band is observed also by thermoluminescence [90, 94]. A microscopic structure of GLPC and SiODC(II) center is reported in fig.1.27.

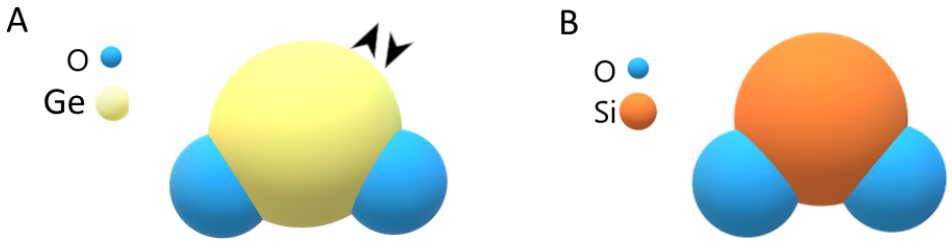


**Figure 1.27:** Comparison between the structures of A) GLPC center and B) ODC(II).

♢ *Ge(2)*

Ge(2), would be, according to some part of literature, a positively ionized GLPC ($GLPC^{+}$) but its stucture is still debated [97], as well as its attribution to an absorption band at about 5.5-5.8 eV [97].

In the literature there exist three different models describing the structure of the Ge(2) defect. In addition to the first one, namely the ionized GLPC [94], an other model considers the Ge(2) as a variant of the Ge(1) [78], and the last one and more recent based on simulation modeling, proposes that the Ge(2) is a variant of the E'(Ge) and that it can be generated after the ionization of a GLPC [98].

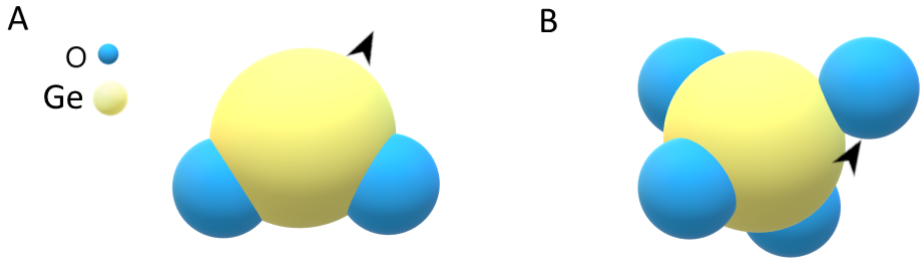


**Figure 1.28:** Comparison between two structures of Ge(2) A) the ionized GLPC type and B) the structure similar to the Ge(1).

In the perspective of exploiting the Ge-doped silica OFs applications, a large interest in exploring co-doping with other elements has been developed. Some studies related to F-co-doping in germanosilicate OFs have been that the use of Fluorine as co-dopant can reduce optical losses and their on the drawing parameters [99–101]. Moreover, concerning the response of Ge-F OFs to radiation exposure, it has been highlighted that F can reduce the radiation induced losses acting as terminator of some preexisting precursor defects (like GLPCs) [102, 103].

Unlike what happens in pure silica or in Al-, or P-doped silica materials, in Germano-silicate fibers or preforms the presence of point defects is observed before and after irradiation. OA and PL signatures of GLPC and Ge-NBOHCs were observed before exposure to radiation [94, 104]. From a known work by Fujimaki [94], is reported in fig.1.29a the optical absorption of a Ge-doped silica sample before (solid line) and after the KrF excimer laser irradiation (dashed line). One can

see that the band located around 5.1 eV and related to GLPC occurs before irradiation, while after exposure there is an increase of the optical absorption intensity at around 4.5 and 5.8 eV. These two features are well shown in fig.1.29b, where is reported the radiation induced absorption spectrum with its decomposition into gaussian bands. One can see the presence of Ge(1) at 4.5 eV, Ge(2) at 5.8 eV. The negative band at 5.1 eV corresponds to the decrease of GLPC centers after irradiation. This last particular feature can be explained by the fact that GLPCs are present in the native fibers as precursor sites for generation of Ge(1) and Ge(2) defects under irradiation [105]. Therefore the GLPC concentration decreases with irradiation, explaining their absence in the RIA spectra [106].

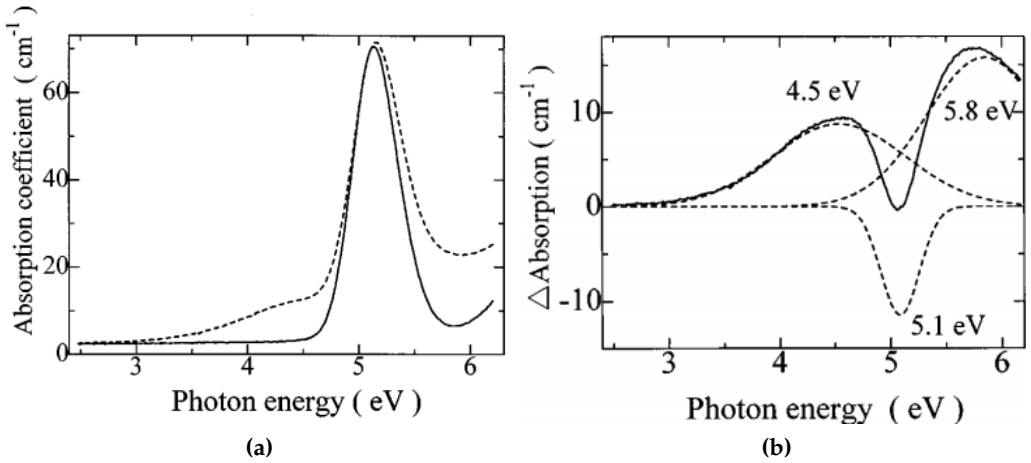


**Figure 1.29:** (a) Absorption spectra of a Ge-doped silica sample with Ge contents of 1.0% mol before (solid line) and after (dashed line) the KrF excimer laser photon irradiation. (b) Radiation induced absorption spectrum with its Gaussian decomposition. Adapted from [94].

The typical photoluminescence spectrum of Ge-doped silica fiber excited at 325 nm is reported in fig.1.30. The two bands located around 400 nm and 650 nm are assigned to GLPC and NBOHC defects respectively [104].

Defects such as GeE' and Ge(2) absorbing in the UV do not give a huge contribution to the RIA in the NIR-VIS spectral range, while the largest contribution is due to the Ge(1) defect. In addition to Ge(1), GeX and GeNBOHC centers were also observed in the RIA during steady state X-, $\gamma$-rays or neutron exposure [107, 108].

A work made by Girard *et al.* [46] pointed out by the RIA spectrum, the presence of metastable defects at 3.28 eV in Ge-doped multimode fiber after X-rays pulse, using a dose of 200Gy(SiO2) and a dose rate of 1MGy/s. He concluded that these defects strongly contribute to the RIA at high irradiation dose-rate or low temperature. In the infrared part of the spectrum the RIA in Germosilicate OFs are still unknown [46]. It was observed just a band at 1.38 eV, attributed to a Ge-related defect called GeY, whose structure still remains unknown and which require further investigations [46].

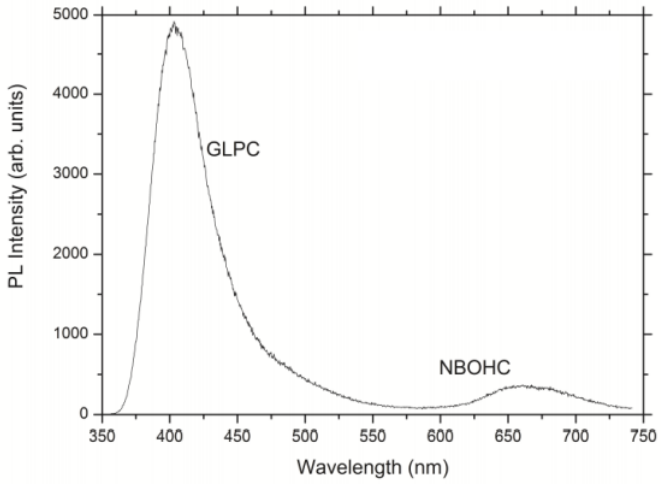


**Figure 1.30:** Photoluminescence spectrum of the core of an irradiated Germanosilicate fiber excited at 325 nm. Adapted from [104].

### 1.4.6 F-related point defects

Fluorine is a particular doping element in optical fiber use because it decreases the refractive index of silica [109]. In fact in optical fiber design F is generally inserted in the core of a pure silica fiber to guide the light. F-doped fiber has good resistance to radiation compared to that of other Ge, P or rare-earth doped fibers [110]. For this reason F is used as dopant in radiation hardened fibers and there is a strong interest in exploiting the design of this kind of fiber. In fig. 1.31 is reported the F2-lased-induced absorption spectra of F-doped silica samples with different amount of F [111]. Intensity of the absorption spectrum above 4 eV and then the mainly defects induced by irradiation (SiE' and NBOHC) is drastically reduced when increasing the F content in the samples [111].

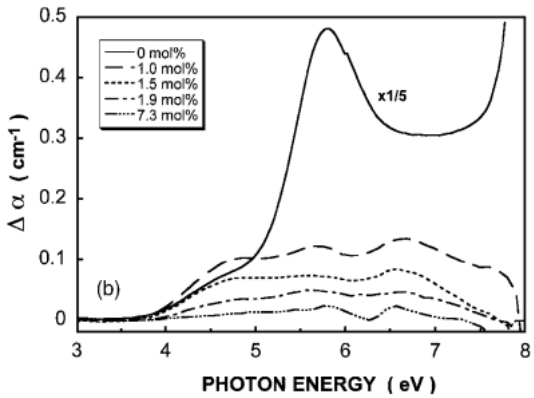


**Figure 1.31:** Optical absorption induced by F2-laser irradiation on F-doped silica changing the F content, adapted from [111].

In fact, the main effects of this dopant in the silica matrix is to reduce the defect precursors of the SiE' or NBOHC, such as Si–O strained bonds [86, 111, 112], as

represented in fig. 1.32.

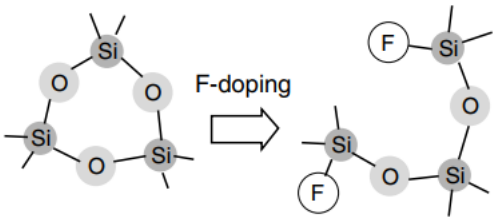


**Figure 1.32:** Schematic illustration of relaxation of glass structure by fluorine doping, adapted from[113].

The fluorine is incorporated in the silica matrix as Si-F group, instead of the usual Si-O for silica. The replacement of a single bringing oxygen atom with a terminal fluorine results in the formation of $SiO_{3/2}F$ tetrahedra, but for glasses containing more than $1wt\%$ of fluorine a small amount of fluorine is bonded to silicon atoms containing four bridging oxygen atoms, resulting in a five-fold coordinated silicon as $SiO_{4/2}F$ [112].

Some effects of F doping are: the quenching of distinct color centers absorbing in the edge region; the reduction of the structural disorder thanks to the breaking up of the strained bonds in the glass network; the increase of the band gap due to the $Si-F$ bond, since it has a higher energy respect to the $Si-O$ bond in silica; and reducing the viscosity of the glass making it easier to reach a lower fictive glass temperature [114].

In a work carried out by K.Arai *et al.*[115] it was quantitatively studied the generation of defect in F-doped low-OH silica glasses as a function of both the F concentration and the dose of $\gamma$rays. It was found that F doping effectively removed ≡Si-Cl bonds without introducing ODCs or ≡Si-H. Furthermore the concentration of E′ centers decreased steeply with the increase of F content, while the one of NBOHC still remains the same [115]. By removing the precursors of the E′ center it was revealed that the E′ center formed intrinsically is generated in a pair with the NBOHC ones [115].

In 1993, Kyoto *et al.* showed by spectroscopic techniques that the absorption band at 7.6 eV in high-purity silica glass is removed with the addition of fluorine [116]; giving the glass more excellent transparency in UV and V.U.V spectral regions. It was found that -Si:Si- defects in silica glass could be perfectly removed during fluorine incorporation and the best UV-V.U.V , transparency occurs in F-$SiO_2$ glass with 1 wt % fluorine content. Furthermore, this high transparency is maintained even under high-energy irradiation such as by an ArF excimer laser (6.4 eV) [116].

More recently Girard *et al.* [110] studies on both radiation and H2 loading effects on F-doped silica based OF, showed an increase of the RIA in the UV part of the spectrum (200-300 nm), this loss is due only to Si related defects, whereas in the visible part it is related to some absorption impurities such as Cl (2-4 eV) [110].

To resume all the optical properties of the samples studied in this thesis, in fig.1.33 and table 1.3 are reported the colors centers related optical absorption bands with their parameters and referencies.

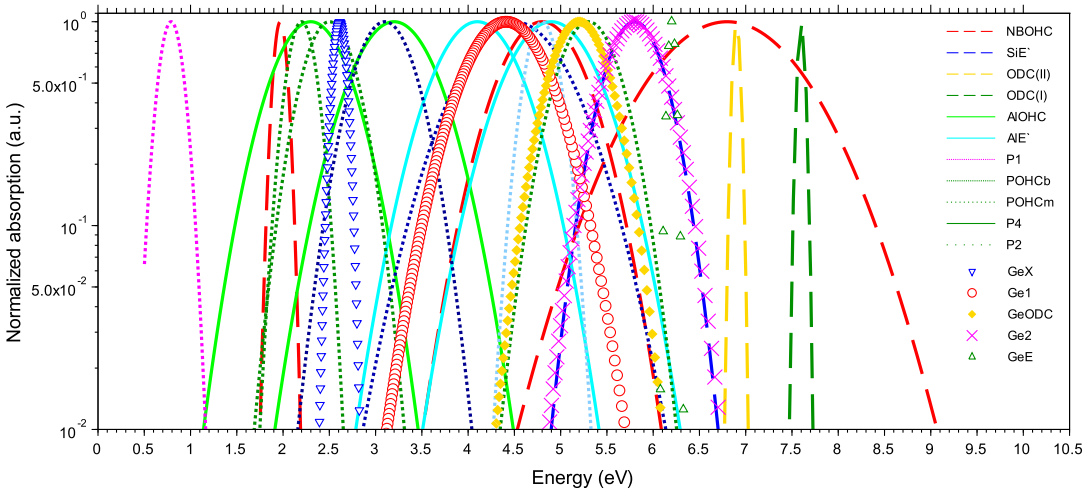


**Figure 1.33:** Main absorption bands in pure, Al-, P- ,Ge- doped silica.

| center name | $x_c$ (eV) | FWHM (eV) | $f$ | ref. |
|---|---|---|---|---|
| SiE′ | 5.8 | 0.7 | 0.4 | [32] |
| | 1.97-2 | 0.17-0.18 | 1.5e-4-4e-4 | [22]-[32] |
| NBOHC | 4.8 | 1.05 | 0.2 | [32] |
| | 6.8 | 1.76 | 0.05 | [35] |
| SiODC | 7.6 | 0.5 | - | [32] |
| SiODC(II) | 6.9 | 0.4 | 0.1-0.3 | [32] |
| AlOHC | 2.3 | 0.9 | 0.06 | [59] |
| | 3.2 | 1.0 | 0.124 | [59] |
| AlE′ | 4.1 | 1.02 | 0.214 | [59] |
| | 4.9 | 1.08 | 0.167 | [59] |
| POHC | 2.2 | 0.35 | 0.5 | [84] |
| | 2.5 | 0.63 | 0.5 | [84] |
| | 5.3 | 0.74 | 0.5 | [84] |
| POHCm | 3.1 | 0.73 | 0.5 | [84] |
| P2 | 4.5 | 1.27 | 0.035 | [84] |
| P4 | 4.8 | 0.41 | 0.014 | [84] |
| GeX | 2.61 | 0.97 | - | [46] |
| Ge1 | 4.4-4.4 | 1-1.4 | 0.15-0.42 | [97]-[117] |
| Ge2 | 5.8 | 0.9 | 0.6 | [97]-[117] |
| GeODC | 5.15 | 0.41-0.46 | 0.07-0.12 | [94] |
| GeE′ | 6.2 | 0.8 | 0.7 | [97] |

**Table 1.3:** Main absorption bands parameters in pure, Al-, P- ,Ge- doped silica.

## 1.5 Optical fibers (OF)

This chapter ends with a section on the optical fibers, explaining briefly their structure and the physical processes involved in their operation, such as the mechanisms of light propagation and the optical loss Finally we focus on OFs fabrication, in particular on the MCVD process, since it is the technique used to manufacture the samples for this thesis work.

### 1.5.1 Optical fibers structure

An optical fiber (OF) is typically a cylindrical dielectric waveguide that operates at optical frequencies, from Ultraviolet (UV) to Infrared (IR) range [6, 118, 119]. It confines the light in one of the specific parts, called the core and guides it in a direction parallel to its axis. The basic structure of an optical fiber is a solid dielectric cylinder called the core, with a refractive index (or simply index) $n_1$, surrounded by a solid dielectric cladding with a refractive index $n_2$. $n_2$, being smaller than $n_1$ so as the optical signal propagation occurs in the core through successive reflections on the separation surface between the core and the cladding [6, 18, 118]. Furthermore an external coating covers the fiber, it is an elastic, abrasion-resistant plastic material. This material adds strength to the fiber and buffers it from small irregularities and distortions [18, 21]. The core material is generally pure $SiO_2$, while cladding can be made by either a glass or plastic [18, 118]. In fig. 1.34 we can see the basic structure of an OF.

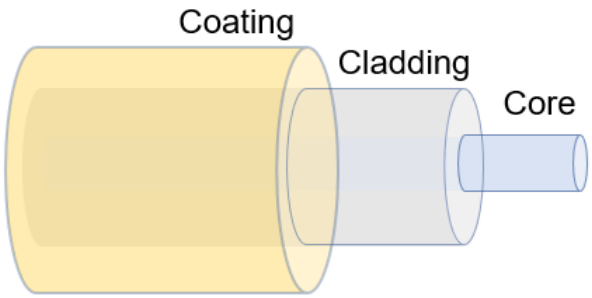


**Figure 1.34:** Basic design of an OF.

The refractive index is a fundamental parameter for the light propagation in an OF. In view of this the change of the index can be obtained by opportune chemical composition of the material [21]. As we can see in figure 1.35, doping silica with germanium or phosphorous, as well as with aluminum, increases the refractive index; unlike fluorine or boron doping, which induce a decreases in the refractive index [6, 18, 106, 118]. These doping elements are usually employed to opportunely change the refractive index in the core or in the cladding and guide the light.

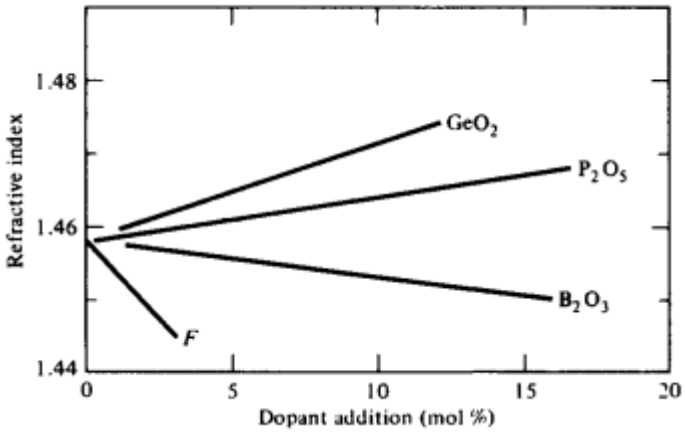


**Figure 1.35:** Variation in refractive index as a function of the dopant and its concentration in silica glass, adapted from [118].

### 1.5.2 Light propagation in OF

To describe the light propagation in an OF we can use two approaches: one consists in using the concepts of electromagnetic modes and the other is the geometric optics in the small wavelength limit [6].

Propagation properties of light inside an OF, in a rigorous way, are obtained by solving the wave equations for the electromagnetic field [6]. The solutions are expressed in terms of waveguide modes, which are the electromagnetic field spatial configurations that maintain their intensity profile during the propagation [6]. With the other method we can study the propagation of light in terms of rays obeying to the geometric optics [6].

Despite these two different methods and the great difference between the concept of light rays and that of a mode, we can find qualitatively the relationship between them. A guided mode can be decomposed into a family of superimposed plane waves forming a standing-wave pattern in the direction transverse to the fiber axis [118]. The family of plane waves in a particular mode forms a set of rays (rays congruence), in fact we can associate to each plane wave a light rays perpendicular to the phase front of the wave [118]. Since only a certain number $M$ of discrete guided modes exists in a fiber, the possible angles of the rays congruence corresponding to these modes are also limited to the same number $M$ [118], although a simple rays picture appears to allow rays at any angle less than a critical angle to propagate in a fiber [18, 118].

Some parameters of the fiber like the diameter of the core, the size of the cladding, the refractive index profile and also the signal wavelength, determine the characteristics of the mode propagating in the OF. If a fiber sustains only one mode (fundamental mode) of propagation, it is a single mode (SM) type. Generally typical SM OFs have core diameters of 8 $\mu$m and a small refractive index difference between the core and the cladding ($\sim$ 0.3%)[18, 118]. Whereas if the fiber drives many hundreds of modes it is a multi mode (MM) fiber. MM OFs have large core

diameters ($> 40\ \mu$m) and larger refractive index differences [118].

Multi mode fibers offer several advantages compared to single mode ones, the larger core radii make it easier to launch optical power into the fiber and facilitate the connecting together of similar fibers, but a disadvantage of MM OF is that they suffer from intermodal dispersion [118]. In fact, the optical power traveling in the OF is distributed over all of the modes of the fiber and each of them travels at a different speed. So the modes in a given optical pulse arrive at the end of the fiber at different time, this intermodal dispersion can be reduced by using a graded-index profile in the fiber core as is reported further on [120].

In the geometrical representation, the fiber can guide the light if the angle formed by the incident light and the fiber axis ($\phi$) is less than

$$\cos^{-1}(n_{core}^2 - n_{cladding}^2) \tag{1.4}$$

where $n_{core}$ is the refractive index of the core and $n_{cladding}$ is that of the cladding. This is the case of a total internal reflection. Eq (1.4) is directly obtained from the weel-known Snell Law [6].

In general many modes will be possible, and a parameter $V$ determines the number of modes propagating in the OF. $V$ is the normalized frequency or $V$-number, it is a dimensionless parameter that determines the number of modes that a fiber can support [118]. It is related to the numerical aperture (NA) characteristic of the fiber and to the wavelength $\lambda$, by the equation

$$V = 2\frac{\pi r}{\lambda}\sqrt{(n_{core}^2 - n_{cladding}^2)} \tag{1.5}$$

where NA = $\sqrt{(n_{core}^2 - n_{cladding}^2)}$ and $r$ is the core radius [118]. If V<2.4 a single mode will propagate, if V>2.4 N modes will propagate, where N=$\frac{V^2}{2}$ [18].

It is worth to note that the single mode behavior depends on the wavelength and the separation between the single mode from the multimode region is defined by the critical wavelength called cutoff wavelength.

From eq. (1.5) it is easy to see that the theoretical cutoff wavelength is given by

$$\lambda_{th,c} = \frac{2\pi r}{V} NA \tag{1.6}$$

with V=2.4 for step index fiber. At this wavelength only the fundamental mode should propagate in the fiber [118]. So also multimode fibers can have a single mode behavior if the wavelength is near the cutoff wavelength [18].

Changing material composition of the core it is possible to realize different fiber types. When in a fiber the refractive index of the core is uniform throughout the core and undergoes an abrupt change at the cladding boundary [118], it is a typical step-index fiber and it is schematically represented in fig.1.36. A graded-index fiber core is rather characterized by a refractive index made to vary as a function of the radial distance from the center of the fiber [18]. This last profile is necessary to obtain a good output pulse. In fact, a multi mode fiber is affected by multimodal dispersion and the shape of the signal is then distorted. This effect can be reduced by producing a graded index [18, 120]. An example of this consists typically of

a smooth parabolic increase of the refractive index in the core of the OF which reaches its maximum in the center of it as shown in fig.1.36 .

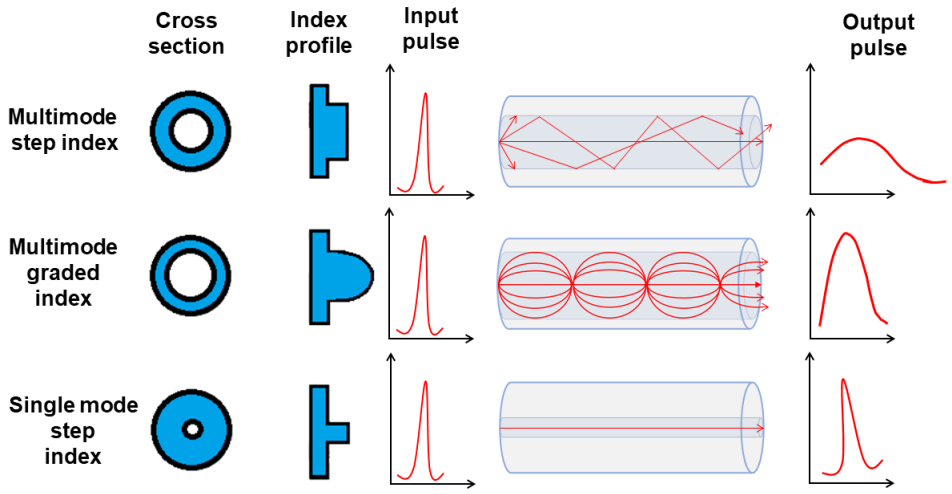


**Figure 1.36:** Structure of optical fiber showing light trajectories for different refractive index profiles and output signal degradation, adapted from [120].

As mentioned before, the propagation of light is described in a rigorous way by the waveguide representation. Thus, it the propagation of optical field in fiber is governed by *Maxwell's equation* for a linear isotropic material having no currents and free charges[118]. With a deep and long procedure it is possible to obtain the following equation of the electromagnetic field **E** for our system [6]

$$-\nabla\tilde{\mathbf{E}} + n^2(\omega)k_0^2\tilde{\mathbf{E}} = 0 \tag{1.7}$$

where n is the refractive index and $k_0$ is the free-space wave number defined as $2\pi/\lambda$. $\lambda$ is the vacuum wavelength of the optical field oscillating at the frequency $\omega$ [6].

### 1.5.3 Optical loss

When the light travels in an OF, launched by the emitter, it is important that the signal remains the same and arrives to the receiver without optical loss and distorsions. Typical distortions of pulses of light traveling through a fiber with a given refractive index profile of the core are already reported in Fig.1.36.

The signal attenuation or fiber loss is another important property that determines the maximum number of signal amplifiers needed between a transmitter and a receiver. The attenuation depends on the wavelength of the transmitted light [6] and is due to several mechanisms which are reported in fig. 1.37 where is shown a typical attenuation spectrum of silica-based OF.

The most important losses are [21]:

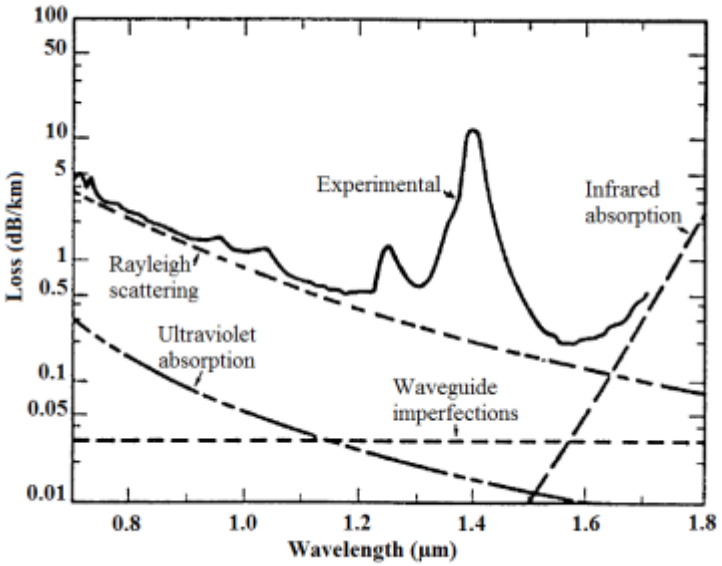


**Figure 1.37:** Typical attenuation spectrum of silica-based OF. Wavelength dependence of several fundamental loss mechanisms is also shown by dotted curves, adapted from [121].

- The fundamental absorption bands of the pure glass occurring in IR and UV regions and their tails. The UV-tail first one arises from absorption of light associated with the electronic transition in the UV spectral domain between valence and conduction band electronic states, the IR tail arises from the absorption of light due to the vibrations of atoms as well as some impurities like hydrogen [18];

- the absorption resulting from the presence of impurities such as transition metal atoms occurs in the wavelength range between 0.6 and 1.6 $\mu$m;

- absorption due to the presence of water vapor, presents as -OH group in the glass [21]. A vibrational resonance of the OH ion occurs near 2.73 $\mu$m. Its harmonic and combination tones with silica produce absorption at the 1.39, 1.24 and 0.95$\mu$m wavelengths, respectively the first, second and third overtone [6, 21];

- absorption due to atomic defects induced by irradiation or by manufacturing process damages;

- Rayleigh Scattering.

The first four loss mechanisms reported above are related to the material absorption, while the Rayleigh scattering, arises from local fluctuations density that lead to a random ones of the refractive index. This contribution in optical loss in silica takes a form varying as $C/\lambda^4$ where C is a constant depending on the composition of the fiber core [6].

Finally in an OF, as shown in fig.1.37, the structural imperfections at the interface between the core and the cladding, causes a net attenuation in all the wavelengths [6]. Other processes cause signal loss: radiative losses that depend on the perturbation in the fiber geometry; bending loss caused by curvature of the fiber, and core/cladding losses that affect the modal coupling between the core and the cladding [18, 122]. A quantitative expression that is widely used to calculate the optical loss $\alpha$(dB/km) in an OF [6] is described by the equation (1.8):

$$\alpha(dB/km) = -\frac{10}{L} log\left(\frac{P_{out}}{P_{in}}\right) \tag{1.8}$$

where $P_{in}$ is the power launched at the input end of a fiber of length L and $P_{out}$ is the output power.

### 1.5.4 Absorption

Light propagating inside a medium can undergo some processes that give rise to an attenuation of its initial intensity. So when we measure the transmitted light in an OF, the number of photons initially impinging on the sample could be reduced due to the energy absorption process. In the case of a silica matrix, this process is due to the presence of defects that introduce new electronic levels in the energy bandgap of the material [6, 118, 123]. The absorption coefficient $\alpha$ can be derived from *Lambert-Beer's law* [124], which states that, if a beam of light passes through a sample of size d, the relationship between the incident ($I_0$) and the transmitted ($I_T$) intensity of the light is [124]

$$I_T = I_0 \exp^{-\alpha d} = I_0 \exp^{-\sigma N d} \tag{1.9}$$

where $\sigma$ is the cross section of the absorbing centers and $N$ is their concentration. If both the absorption coefficient $\alpha$ and $N$ of the absorbing species are known, $\sigma$ can be obtained as:

$$\sigma = \alpha / N \tag{1.10}$$

According to equation (1.9) it is simple to obtain an expression for the absorption coefficient that in OF applications is expressed in $dB/m$:

$$\alpha = -\frac{10}{d} log \frac{I_T}{I_0} \tag{1.11}$$

Since $\alpha$ depends on $\lambda$ and on the absorbing centers concentration, the absorption effect could be induced by the introduction of defects generated by irradiation. The radiation induced absorption (RIA) measurements is based on this principle and by this technique we can measure the attenuation during irradiation processes and evaluate the concentration of induced defects. A useful quantity related to absorption data is the *oscillator strength* $f$ of the electronic transition from an initial state to a final one [22]. This is a dimensionless quantity defined as the ratio between the integrated absorption over an experimental band at $\omega$ and the theoretical absorption calculated approximating the atomic system as a charged harmonic oscillator with frequency $\omega$ and is related to the electronic dipole moment between initial

and final state [22, 124, 125].

The oscillator strength can be expressed by different expressions, one of which is the Smakula's formula, that gives a quantitative relation between $f$ and the experimental quantity $\alpha_{max}$ (the absorption band amplitude at its maximum expressed in $cm^{-1}$)[22]:

$$Nf = n\left(\frac{E_0}{E_{eff}}\right)^2 \alpha_{max}\Gamma\Delta\left(\frac{m_e c}{2\pi^2 e^2 \hbar}\right) \tag{1.12}$$

where n is the refractive index of the medium, $E_0$ is the electric field in free space, $E_{eff}$ is the effective electric field acting on the defect (their ratio in Smakula's formula is the effective field correction due to the polarization of the medium surrounding the defect caused by the incident light), $\Gamma$ is a numeric coefficient, which depends on the bandshape, $\Delta$ is the halfwidth (FWHM) of the absorption band , $m_e$ is the electron mass, $e$ the electron charge, $c$ the velocity of light in vacuum and $\hbar$ the Planck constant[22].

For a Gaussian lineshape this formula can be related directly to the experimental parameters $\Delta$ and $\alpha_{max}$ [125]

$$Nf = 0.87 \times 10^{17} n\alpha_{max}\Delta/(n^2+2)^2(eVcm^{-2}) \tag{1.13}$$

Using this formula it is possible to determine the oscillator strength associated to given point defects. On the other side by optical measurements, knowing the oscillator strength, it is possible to derive the defects concentration and to study their optical properties, as well as their mechanisms of generation by irradiation.

### 1.5.5 Glass and fiber fabrication

Glass is typically made by fusing mixtures of metal oxides, sulfides, silicates or selenides [21]. Concerning silicate glasses, on the basis of the manufacturing features and on the concentration the most diffused impurity, the OH group, we can define four type of silica [125, 126]: natural and synthetic, each of them can be dry and wet.

The Type I is natural dry, it is made by fusion of quartz powder by electric arc in a crucible in vacuum or inert gas atmosphere at low pressure. The amount of OH content is less than 30 percent by weight ($[OH] < 30$ ppm), other impurities are usually less than 10 ppm.

The natural wet is Type II silica, it is a flame fusion of quartz powder in water vapor atmosphere. The [OH] content is $150 \div 400$ ppm; other impurities are less than the starting material since some of them are volatilized in the flame.

To the synthetic type of silica belong the Type III (wet) and Type IV (dry). Type III is obtained by hydrolysis of pure silicon compounds, usually $SiCl_4$, injected in gas-phase into a hydrogen/oxygen flame, the compound is then transformed by the flame into fused drops of $SiO_2$. In this type of silica we found $[OH] \geq 100$ ppm while other impurities content are negligible since the starting material contains much less impurities than the natural quartz.

Finally the Type IV is the result of a reaction of $O_2$ with $SiCl_4$ in water-free-plasma. [OH] content is very low, less than 1 ppm but it is possible to find another

relevant impurity: $[Cl] \sim 100$ ppm [125, 126].

The manufacturing processes in glass for optical wave-guides can be distinguished in two basic techniques: the vapor phase oxidation process and the direct-melt method. The direct method follows traditional glass making procedures where optical fibers are made directly from the molten state of purified components of silicate glasses [21, 120, 127]. In the vapor phase oxidation process, highly pure vapors of metal halides (like $SiCl_4$, $SiF_4$) react with oxygen to form a white powder of $SiO_2$ particles. The particles are then collected on the surface of a bulk glass by one of different commonly used processes and are sintered (transformed to a homogeneous glass mass by heating without melting) by one of various techniques to form a clear glass rod or tube [18, 21, 127]. This tube is called preform. It is typically around 10 to 25 mm in diameter and 60 to 120 cm long and has the radial refractive index profile which reproduces, on much larger scale, the refractive index profile of the final OF [118].

The preform can be produced by several techniques: Outside Vapor Deposition (OVD), Modified Chemical Vapor Deposition (MCVD), Vapor Axial Deposition (VAD), Plasma Chemical Vapor Deposition (PCVD) and Surface Plasma Chemical Vapor Deposition (SPCVD) [106, 120, 127]. In MCVD process, as represented in Fig.1.38, high-purity gas mixtures are injected into a rotating tube which is mounted in a glass− working lathe and heated by a traversing torch. A homogeneous gas−phase reaction occurs in the hot zone created by the torch to produce amorphous particles which deposit downstream of the hot zone. The heat from the moving torch sinters this deposit to form a pure glass layer. The torch is traversed repeatedly to build up the core or the cladding coat by coat [120]. One can see some pictures of this process used at INPHYINI in fig.1.39.

Composition of the gas and process conditions can change in order to produce different kinds of glass layers, according to the type of fibre to be manufactured [128]. In the laboratory installation only germanium, silicon, phosphorus and fluorine can be brought in gas form, the other dopants will be brought in by solution. The porous will be immersed in an aqueous or alcoholic solution containing the dopants like Rare Earth or transient metals. Following this soaking the preform will be dried before being annealed to vitrify the deposit.

At the end of the glass deposition, a collapse phase is started: the tube's internal hole is progressively reduced by successive slower burner passes at higher temperature ($1800 - 2000^oC$), due to the action of surface tension when the high temperature lowers the viscosity of the glass, until a solid cylindrical rod is produced, with a refractive index profile correspondent to the final optical fiber profile [128]. With the MCVD process the amount of [OH] content is about 0.03 ppm [128], this makes the fiber produced with this method a synthetic dry type of silica.

The preform thus produced is a glass preform of about 30 cm of approximately 1 cm in diameter. It will be used to produce bulk samples, (slices of preforms which preparation is reported in section 2.6.1) or, by drawing process, it will be an optical fiber.

The drawing process creates the optical fiber from the preform. As shown in Fig.1.40, in this process the preform is put vertically at the top of the building called drawing tower, where the temperature reaches $2000^oC$ and heating the preform a molten drop preform starts to fall dawn.

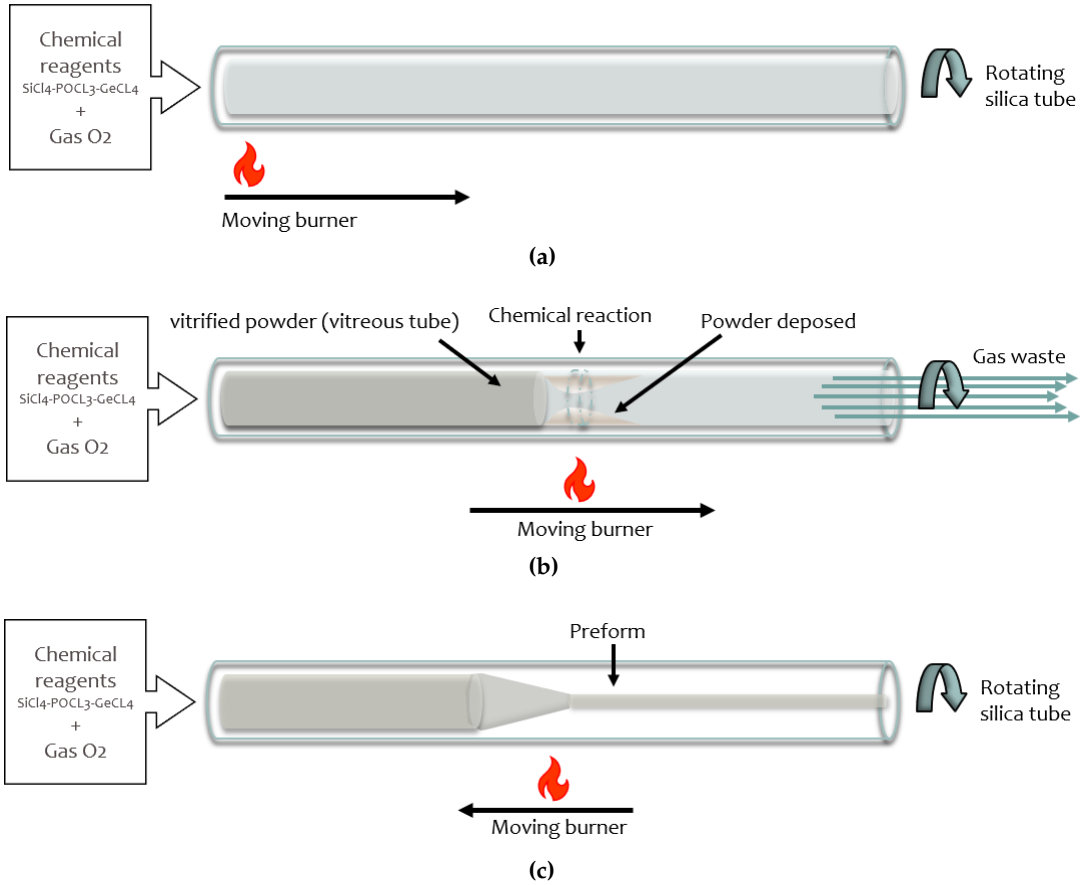


**Figure 1.38:** MCVD process consists of deposition of glass layers inside silica tube, collapse of tube to solid rod, and drawing of preform into fiber.

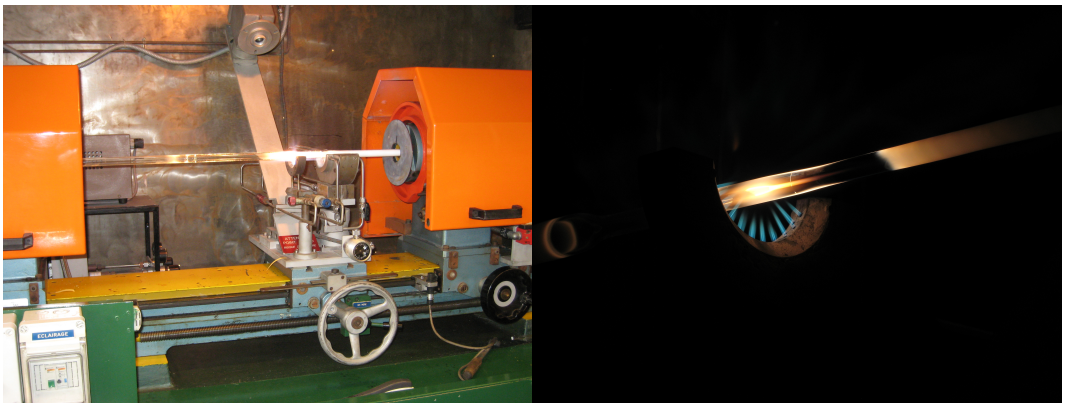


**Figure 1.39:** (a) MCVD machine used at INPHYNI. (b) Detail of preform silica tube during the manufacturing process.

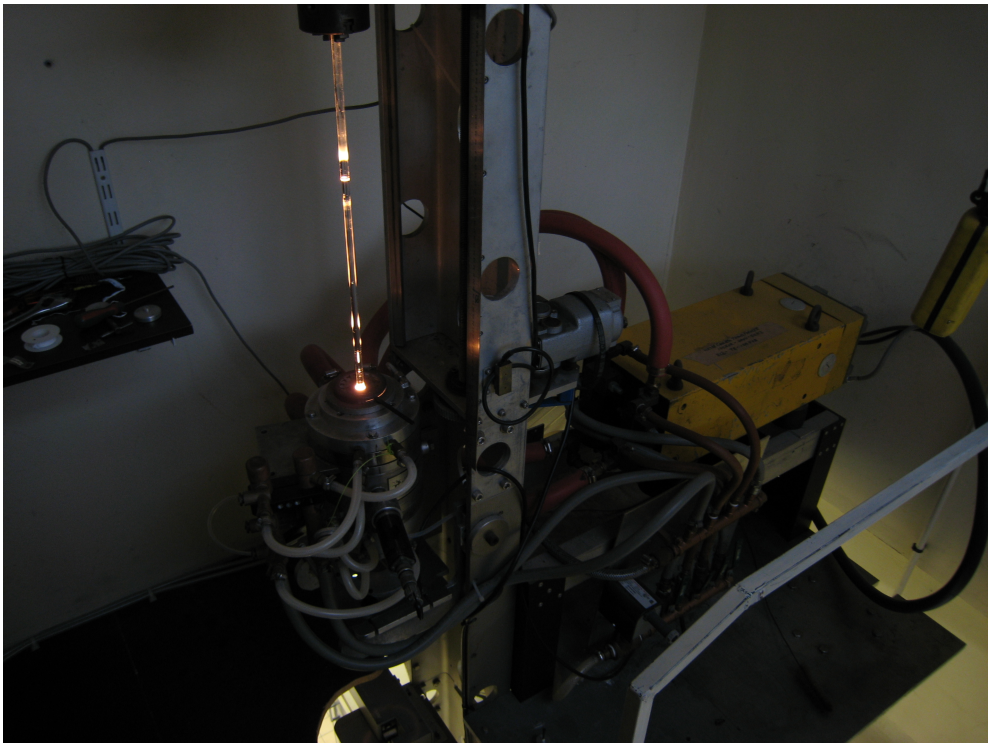

**Figure 1.40:** Picture of a preform installed in the drawing tower during the drawing process.

This forms a neck-down region which provides transition to a small-diameter filament. Uniform traction on this filament results in a continuous length of fiber. Before this fiber contacts a solid surface, a polymer coating is applied to protect the fiber [118, 120]. All the drawing parameters are controlled during the process to make the OF with the desired parameters such as the size of the outer diameter of the cladding. The optical fibers obtained have an external diameter of about 125 $\mu$m. A schematic representation of the drawing tower with all its components and picture of the installation used at INPHYNI are shown in fig. 1.41a and 1.41b respectively.

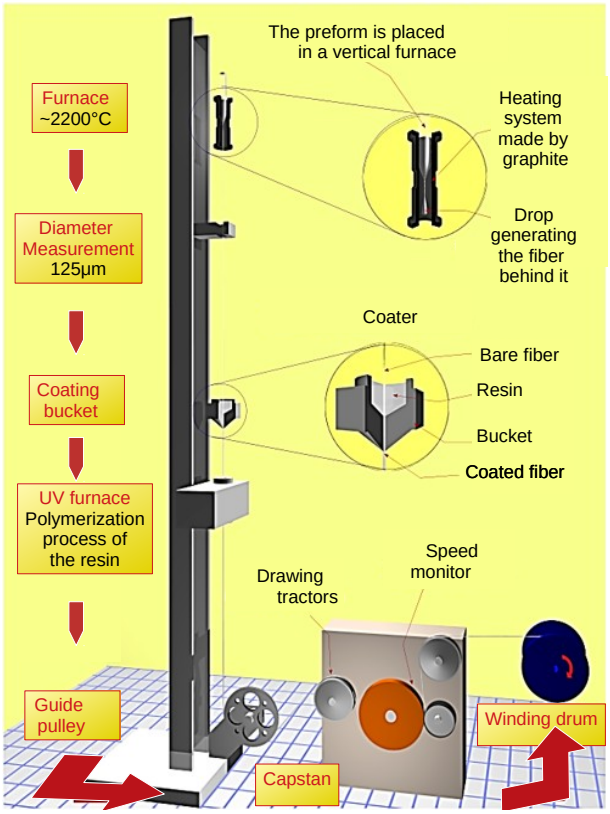


**(a)**

**(b)**

**Figure 1.41:** (a)The essential components of a drawing tower, are a preform feed mechanism, a furnace, a diameter monitor, a resin-coating applicator, a UV furnace, a guide pulley, an attraction capstan, and a take-up unit. (b) Picture of the drawing tower used at INPHYNI.

# Chapter 2

# Methodologies and materials



This chapter basically deals with the methodologies characterizing this thesis, discussing their theoretical background until to get closer into more detail in the experimental techniques, as well as the materials used. The chapter starts with a section dedicated to the irradiation processes and the radiation-induced effects, such as the RIA. Then, the basics of luminescence are presented, followed by a more detailed discussion on the thermoluminescence phenomena. Finally, is explained the way in which the samples were prepared and the experimental setups.

## 2.1 Irradiation processes

In this thesis, we explore the response to radiation exposure of silica based preforms by spectroscopic techniques. The type of radiations used in this work are

X-rays and $\gamma$-rays. As explained deeply in section 1.4, the exposure of silica-based material to ionizing radiation brings to the creation of radiation-induced point defects. Their study requires to review the damage creation processes taking place in the silica lattice during irradiation (sec.1.3). Two main mechanisms dominate these processes [18, 22]:

- knock-on, where the atom displacement is caused by direct transfer of the projectile kinetic energy;
- Radiolysis, in which the atomic motion is caused by ionization and electron excitation.

In the knock-on process the particles from the incident beam act as bullet particles interacting directly with the lattice atoms and giving rise to a displacement. The kinetic energy of the bullet is then transferred to the target atom and, if this energy is greater than the atom-lattice bond energy, this bond is broken. Furthermore the energy transfer must be high enough to avoid the hit ("knocked-on") atom being caught by nearby atoms. This energy is called displacement ($T_d$ ) energy and considering a bond energy between two Si and and O atoms of 5 eV, for the $SiO_2$ it is estimated that to displace an Si atom occurs a $T_d$(Si) of 20 eV and to displace the oxygen a $T_d$(O) of 10 eV. The knock-on process could be elastic or inelastic, the last occurs when the bullet energy is lost in electronic transitions or nuclear reactions [18]. A knock-on process could be followed by a collision cascade, it happens especially for radiation involving neutrons. In fact, energetic neutrons interact essentially only with nuclei in direct ballistic collisions in which the kinetic energy transferred to the "knock-on" atom is distributed among hundreds of neighboring atoms which are subsequently displaced in energetic collision cascades [18].

In radiolysis process the irradiation acting on the electrons of the material induces a change of the state of an electron. The energy absorbed is invested in the creation of electron-hole pairs in the conduction and the valence band respectively. These charges may recombine immediately or can be trapped at impurities or other defective network sites. Generally, the radiolysis process occurs when the atom is unstable in the coulombic field and it moves to nearby configurations with less potential energy [22]. In the case of X-rays and $\gamma$-rays irradiation, the principal driving mechanisms in defects production is the radiolysis [18, 22].

A fundamental parameter to describe and characterize radiation processes is the dose, or rather the deposited energy in the material [18, 125].

### 2.1.1 X-rays irradiation

X-rays correspond to photons coming from the de-excitaction of electrons orbiting around the nuclei. But one can call X-rays also the radiations emitted by electric charges accelerated or decelerated. They are produced when a substance is bombed from high velocity electrons and the radiation mechanism is based on the phenomenon of *Bremsstrahlung* [129] : an electromagnetic radiation produced by the deceleration of a charged particle caused by the deflection by another charged particle; the moving particle loses its kinetic energy, which is converted into photons [129].

X-rays generators are built around a vacuum tube in which electrons are emitted by an heated metalic filament (cathode), accelerated by high voltage and focused on a metal target (anode) [129]. Electron bombardement of solid targets is the most usual method to generate x-rays. In our laboratory, we use an X-ray generator with a Copper anticathode tube.

The electron-anode interaction could give rise to ionization collisions and radiation ones. In the first type an incident electron ejects a K shell electron from a Cu atom, giving rise to a characteristic radiation. The second one is characterized by a collision between an electron of energy E and a nucleus, leading to a *Bremsstrahlung* of Energy h$\nu$. The electron recedes from the collision with energy E-h$\nu$. The resulting spectrum consists in a continuous bell shape spectrum forming a produced by *Bremsstrahlung*, and a spectrum of emission lines consisting of narrow peaks superimposed on the continuous spectrum. These peaks are caused by the characteristic radiation and their positions depend on the atomic number of the substance forming the anode. For Cu anode these characteristic emissions are $K_\alpha$ at 8.04 keV (0.154 nm) and $K_\beta$ at 8.9 keV (0.139 nm), in Fig.2.1 are reported $K_\alpha$ emissions from the work by H. Berger [130]. Concerning the intensity of the $K_\beta$, for a copper anode, it is approximately 5 times less intense of $K_\alpha$ intensity.

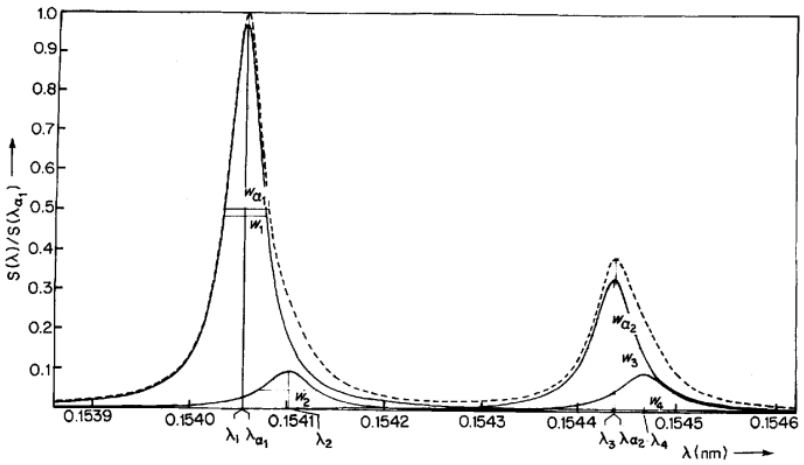


**Figure 2.1:** *kα* emission spectrum of Copper (dashed line) with the spectral line decomposition (continuous lines), adapted from [130]. The two peaks named $K_{\alpha 1}$ and $K_{\alpha 2}$ are located at 0.154056 nm and 0.154439 nm respectively.

A typical *Bremsstrahlung* spectrum for a voltage of 30 kV in Cu target material is reported in figure 2.2.

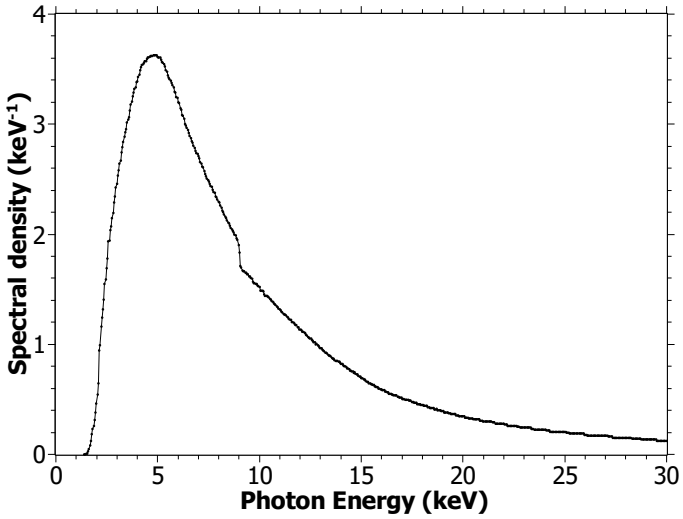


**Figure 2.2:** Simulated *Bremsstrahlung* spectrum for a voltage of 30 kV in Cu target material. Data for the figure taken from [129].

The irradiation beam hitting the material to be irradiated has a very low penetration efficiency in the case of X-rays. In figure 2.3 the transmitted intensity is normalized to that of the incident one of the beam as a function of thickness of the material for 8 keV. The choice of 8 keV is related to the fact that for a typical Cu anode X-rays tube running with a typical operating voltage of 30 kV, more than 60% of the emitted intensity correspond to the characteristic emission at 8-8.9 keV.

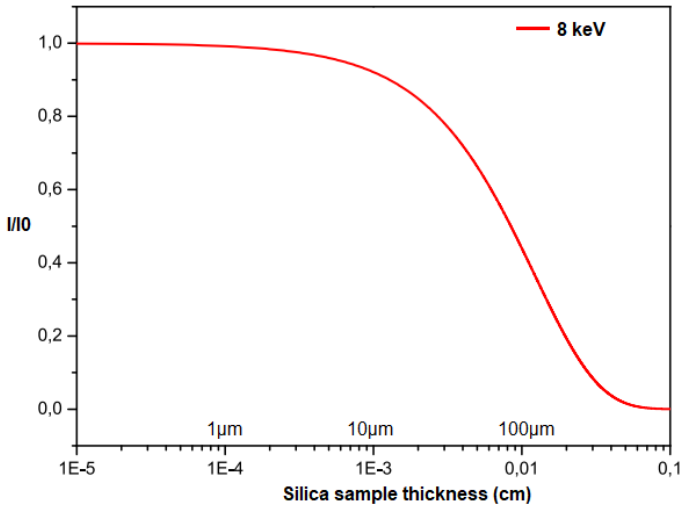


**Figure 2.3:** Simulated X-rays penetration efficiency described by the intensity of the beam operating at 8 kV as a function of the thickness of the material.

The trend is described by an exponential attenuation law of the form [131]:

$$\frac{I}{I_0} = \exp\left[(-\mu/\rho)x\right] \tag{2.1}$$

It describes a narrow beam of monoenergetic photons with an incident intensity $I_0$,

penetrating a layer of material with mass thickness $x$ and density $\rho$, emerging with intensity $I$ [131]. The ratio $\mu/\rho$ is the mass attenuation. For composite substance as silica, it is possible to obtain the value of the mass attenuation coefficient from a simple additivity [131]:

$$\left(\frac{\mu}{\rho}\right)_{SiO_2} = wi_{si}\left(\frac{\mu}{\rho}\right)_{Si} + wi_{O_2}\left(\frac{\mu}{\rho}\right)_{O_2} \tag{2.2}$$

where $w_i$ is the fraction by weight of the atomic constituent. The typical values of mass attenuation coefficients for X-rays are reported in fig.2.4 for some representative atoms and molecules of interest for this work[1].

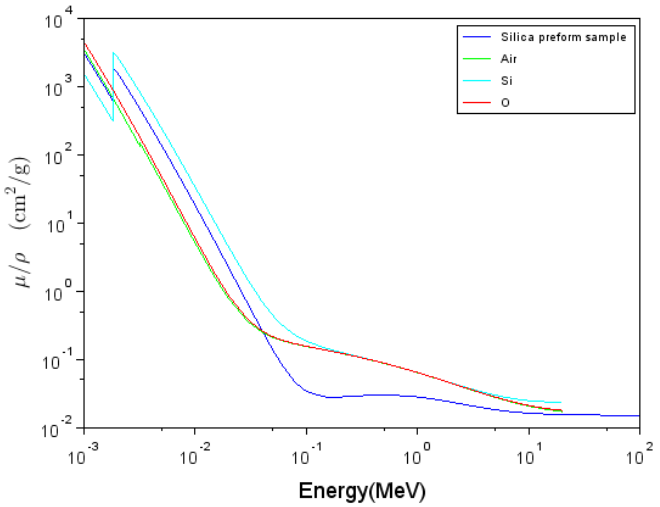


**Figure 2.4:** Mass attenuation coefficient as a function of the energy for silica preform sample, oxigen, silicon and air.

Sometimes, it is useful to use the difference in the dose deposition in two different materials that can be seen as the ratio between the mass attenuation coefficients between these materials [131]; this quantity is of course strongly wavelength dependent and differs from X-rays irradiation machines [131].

$$CF(SiO_2/Air) = \frac{\left(\frac{\mu}{\rho}\right)_{SiO_2}}{\left(\frac{\mu}{\rho}\right)_{Air}} = 0.28 \tag{2.3}$$

This quantity gives the dose discontinuity of the interface of the two materials in electronic equilibrium condition. The probe used to measure the dose rate gives a mass attenuation in air, this value is then multiplied for 0.28 to obtain the value in silica. In our measurements and results, dose and dose-rate values are all converted in silica. Figure 2.5 shows the dose depth distribution in pure silica estimated for mass proportions of 46.7155% silicon and 53.2845% oxygen. In abscissa, this profile expressed as deposited dose is the equivalent of silica dose ($Gy(SiO_2)$) for 1 Gy measured in the air through an ionization chamber (Gy(air)).

[1]This simulation is built from data sheet obtained by website NIST [131]

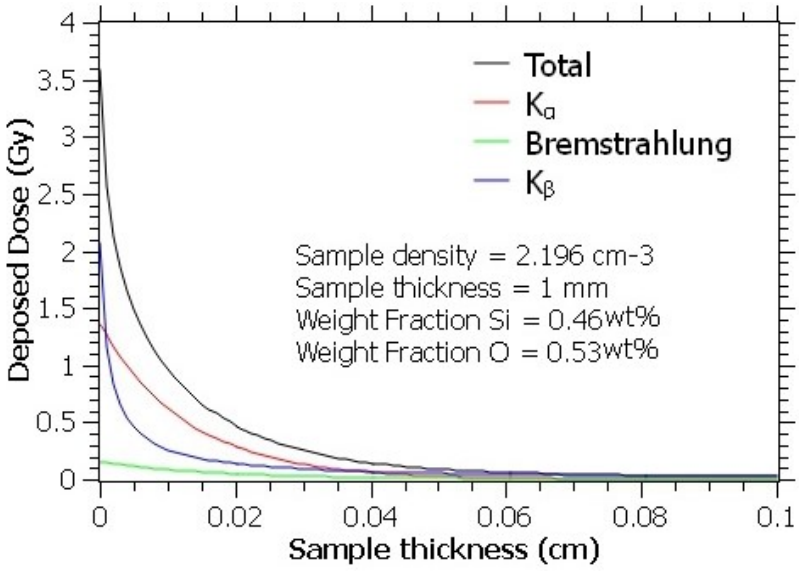


**Figure 2.5:** Deposed dose profile in pure silica sample for 1Gy measured in the air as a function of sample thickness, d.

Using these results, we plotted on Fig.2.6 the curve of the ratio of the average dose deposited in a silica of thickness $d$ and the dose deposited in air, as a function of $d$. For thicknesses less than 0.23 mm (red dashed line), the average dose in silica is higher than the one in air. The energy deposited in the material at a $d$ greater than the radiation penetration depth in silica, then considering a sample thickness greater than this value, no longer depends on $d$. Conversely, the average dose decreases as $1/d$ law.

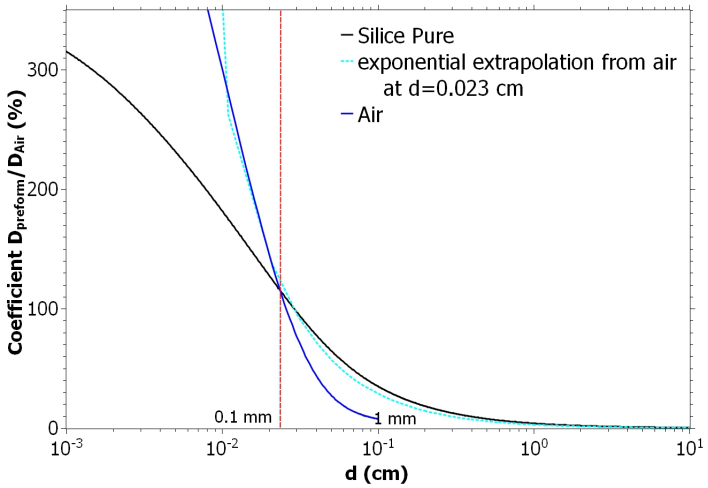


**Figure 2.6:** Ratio between coefficient of deposited dose in silica preform and air as a function of thickness sample, $d$.

### 2.1.2 $\gamma$-rays irradiation

A $\gamma$ ray is a photon emitted by excited nuclei of radioactive atoms with energies from some keV to several MeV. The sources of $\gamma$ radiation are the radionuclides,

that can be distinguished in:

- naturals: primordial radionuclides, secondary radionuclides, and cosmogenic radionuclides;
- made by human activities.

Primordial radionuclides are produced in stellar nucleosynthesis and supernova explosions along with stable nuclides, they are going back to the creation of the solar system. Generally they have a half-lives of about some hundred of million years, in fact they have not yet completely decayed. Uranium-235, Uranium-238, Thorium-232 and Potassium-40 are some primordial nuclides.

Secondary radionuclides derives from the decay of primordial radionuclides. They have shorter half-lives respect to the primordial ones. Cosmogenic isotopes are made by interactions of cosmic rays, an example is the carbon-14. Radionuclides can be produced as a result of nuclear fission such as Cs-137. Further radionuclides can be created by the activation process such as the $^{60}Co$ .

The activation process is a process of secondary induction of radioactivity in materials subjected to a neutron flux. It happens when the atomic nuclei capture free neutrons, thus becoming heavier and passing to another excited state. The excited nucleus decays immediately for the emission of particles such as protons, neutrons or $\alpha$ particles. In the case of the $^{60}Co$ it decays for the emission of a $\beta$ particle along with two very intense $\gamma$ rays (1.1732 MeV and 1.3325 MeV) becoming a $^{60}Ni$ (Fig.2.7).

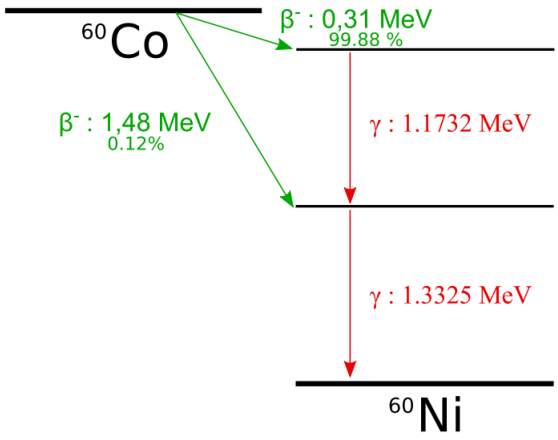


**Figure 2.7:** Disintegration diagram of the $^{60}Co$.

The $\gamma$ irradiation of this thesis were carried out in the IRSN facility at Saclay with cobalt sources ($^{60}Co$).

## 2.2 Radiation-induced effects

There are three main processes originating by irradiation exposure involving the guided light in optical fibers: Radiation-Induced Emission (RIE), Radiation-

Induced Refractive Index Change (RIRIC) and Radiation-Induced Attenuation (RIA).

### 2.2.1 The radiation induced emission: RIE

The RIE can be generated from different mechanisms. One of them is due to the Cerenkov effect, that may lead to the observation of the typical Cerenkov light during the irradiation exposure [46].

Furthermore, always during irradiation, some luminescence bands associated to precursors or radiation induced defects can be observed. The cathodoluminescence (CDL), and radioluminescence (RL) are based on these mechanisms. A deep characterization by CL of point defects induced by irradiation in optical fibers can be found in [132]. The main difference between RL and CL is that the first one consist in the detection of emission of photons during X- or $\gamma$-rays irradiation, and the second one by electron beam. Whereas, if the emission is observed after the end of the irradiation exposure, the techniques involved are the thermoluminescence (TL) and optically stimulated luminescence (OSL), which consist on the detection of the emission stimulated by heating and by light, respectively.

The TL is the main spectroscopic technique used in this thesis and its special description is presented in section 2.5.

### 2.2.2 Radiation induced refractive index change: RIRIC

The RIRIC is the change in refractive index (RI) due to radiation exposure. The refractive index change is explained by Kramers-Kronig relations [46] and is directly related to the absorption bands of point defects. According to the Kramers-Kronig relations, the RIRIC increases with the amplitude of the induced absorption and it is inversely proportional to $(\lambda^2 - \zeta^2)$, where $\lambda$ is the wavelength at which the RIRIC has to be evaluated and $\zeta$ is the wavelength of the absorption [133]. The contribution of point defects in the near IR to RIRIC is negligible at high doses, since the concentration of most of the point defects saturate at values lower than $10^{19}\ cm^{-3}$ for doses of 10kGy [18, 85, 105]. Exceptions being the SiE' and NBOHC defects whose larger concentrations do not exceed $10^{20}\ cm^{-3}$. For high doses the main contribution to the RIRIC is due to glass densification. From Lorentz-Lorentz equations [18] it is possible to describe the densification with a power law $A \cdot \dot{D}^k$ where A is a constant, $\dot{D}$ the dose rate and k is a parameter equal to 1 for fast neutrons and swift ions and around 0.67 for $\gamma$-rays, electrons, or UV light [134, 135].

### 2.2.3 Radiation induced attenuation (RIA)

The Radiation induced attenuation corresponds to the attenuation of the transmitted light passing through a fiber or a preform when exposed to radiation. This attenuation is due to the creation of radiation-induced color centers (CC). RIA spectra can be decomposed into Gaussian bands assigned to well-identified intrinsic or dopant related color centers.

The RIA levels and kinetics strongly depend on the wavelength ($\lambda$) and the time elapsed (t) since the beginning of the exposure. They are higher in the UV-visible part of the spectrum than in the NIR, where it is more difficult to identify

the optical absorption pattern of widely-admitted color centers as they are defined in the visible part of the spectrum.

In Fig.2.8 is reported an example of RIA for a Ge-doped fiber spreading from the UV-visible to the NIR. One can see that in the visible range it is possible to recognize some absorption bands and a broad band tail in the NIR range.

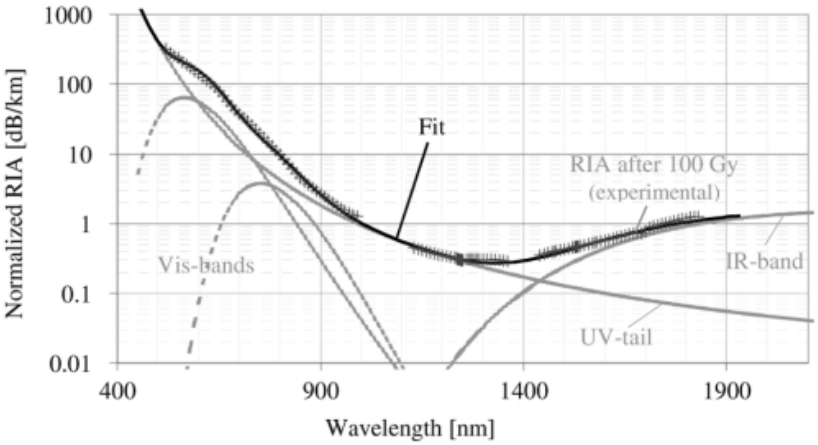


**Figure 2.8:** Normalized RIA (after 100 Gy) decomposition for the Ge-doped fiber. Adapted from [83].

During the exposure of a fiber to irradiation, the RIA grows with the dose and decreases when the irradiation stops. Generally its intensity is also strongly depending on the temperature. This behavior can be explained by competitive mechanisms of defect generation and bleaching, dominating in the irradiation and post irradiation processes respectively. RIA levels and kinetics depend on many others parameters: dose D, dose rate $\dot{D}$, temperature T, and hydrogen H (eq. (2.4)), in other words all the parameters that reflect the constraints encountered in harsh environments, but also by some fiber intrinsic characteristics such as the composition of its core and cladding ($\chi$) and its light guiding properties [46].

$$RIA = f(\lambda, t, D, \dot{D}, t, H, \chi) \tag{2.4}$$

Several approaches have already been proposed to model dose and dose rate effects [136–141] on the RIA and very few of them take into account the effect of temperature during the irradiation [136, 140, 142].

The RIA is usually fitted by power [136], stretched exponential [143], or saturating exponential [67] models relaying from first to higher order kinetics formulation [144–146]. All these models have the common assumption that two antagonist mechanisms control the RIA growth, one related to the generation of color centers and one to their annihilation such as the recombination processes.

Some empirical models [138, 141] use the "stretched exponential" Kohlraush function [147] to fit the experimental data of the thermal decay of the colors centers in glasses. This function is defined as [138]:

$$N(t) = N(0) exp - (t/\tau)^{\beta} \tag{2.5}$$

where N(t) is the number density of color centers, $\tau$ is the characteristic decay time and $\beta$ is a number between 0 and 1. Derivations of the equation 2.5 can be re-conducted from the more generalized classical first order rate equation

$$dN(t)/dt = -RN$$

where R=1/$\tau$ is the decay rate constant.

The first derivation of the Kohlrausch-type solutions for color-center creation was obtained by Mashkov *et al.* [137]. Its solution reproduces the observed power-law growth curve in the low dose regime before saturation sets in. The authors assume in this derivation that the process involved in the formation and destruction of color centers are : a creation of colors centers from damageable sites due to irradiation, a creation of colors centers from precursor sites (activation process) and a deactivation of precursors that decrease the formation of colors centers. The solution of Mashkov *et al.* for the number of activated color centers is:

$$N(D) = N_c(kD)^{\beta} + N_a\left[1 - exp(-k\dot{D}t^{\beta})\right] \tag{2.6}$$

Where the first term on the right-hand side represents the creation of new defects from the glass network and their activation, while the second term represents the activation of a fixed number of preexisting precursors limited by radiation-stimulated deactivation. Mashkov *et al.* applied Eq.(2.6) to the case of E' centers successfully fitting the growth curves for the number densities of these color centers over more than four decades of dose. Anyway this analysis is based on a first-order kinetics and it assumes the radiation-stimulated back reactions mentioned before as the only mechanisms of color-center destruction, without taking into account higher order kinetics and other color-centers destruction processes such as the thermally activated recombination of holes and electrons [138].

The main problem of these empirical (or semi empirical) models is that, as empirical (so basically a phenomenological description of the measurements), they do not fit the project aim needs. The aim is to develop a physical model of the RIA based on the mathematical translation of well-understood mechanisms. in fact, although empirical models may work in some cases, validity domain is not guaranteed; for example under different conditions than those of the experimental measurements on which they were built.

Some models are built to explain one particular feature or empirical law. It is a kind of kinetics model, very common in literature describing the growth or the decay of the RIA [136, 142, 148–150].

Griscom *et al.* proposed a kinetics model to fit the power law dependence on dose for the concentrations of radiation-induced defect centers, predicting the recovery post irradiation behavior in Ge-doped optical fibers. This treatment considers the empirical growth curve of the form: $\alpha_{RIA} = CD^f$ where D is the radiation dose and C and f are constants, as the envelope of a series of discrete classical curves given by the solutions of Eq. (2.7) [136]:

$$\frac{d\alpha_{RIA}}{dt} = K\dot{D} - R{\alpha^n}_{RIA} \tag{2.7}$$

where the first term on the right is considered as a contribution of creation of the defects, and the second term as an annihilation according to the $n^{th}$ order kinetics formulation.

Gilard *et al.* [142] proposed a model that can explain the enhanced low-dose-rate sensitivity (ELDRS) observed in certain type of erbium-doped optical fibers. It is a first-order dispersive kinetic model able to simulate the growth of the density of color centers during an irradiation. The assumption of dispersive kinetic means that the reaction rate coefficient for the color center recombination depends on time assuming that the recombination mechanisms are related to diffusion limited processes [142]. This model is based on the assumption that the density of the color centers responsible for the RIA evolves according to the following differential equation:

$$\frac{dn}{dt} = N_p(g\dot{D})^{\gamma} - \frac{\alpha}{\tau^{\alpha}}t^{\alpha-1}n \tag{2.8}$$

where $n$ is the color-center density, $N_p$ is the preexisting-defect density, $\dot{D}$ is the dose rate, $\alpha$ and $\gamma$ are numbers between 0 (excluded) and 1, $\tau$ is the trapped carriers decay time, t is the irradiation duration, and g is a constant. The same model generalized at $n^{th}$-order dispersive kinetic was applied to simulate the growth of the density of color centers in irradiated Ge-doped glasses [149].

Concerning the Er-doped fibers, another model was proposed to predict the gain of an EDFA in an ionizing environment obtaining good extrapolations at other doses and dose rates than those used for testing [150].

Although these types of models are very common, do not exist a unified framework that allows to understand which kinetics to apply. Moreover they cannot explain the possible cross effects due to more parameters, such as the presence of more than one population of color centers and other constraints. Finally, it is worth to highlight that all these models are based on recombination mechanism to explain the decay; but they only consider a single population, whereas it is in our interest to find a solution for two population to recombine.

To conclude, it is reminded that in literature exist some *ab initio* models used in prediction of structure and spectroscopic properties of point defects. They addresse atomic scale and are able to predict the formation energies and optical properties of the defects. Kimmel *at al.* applied a theoretical prediction of self trapped holes in silica [151] and in a work by Sukuzi *et al.* [36] were calculated the electronic structure and the nature of optical transitions in NBOHC.

This approach is too complex to be used in RIA prediction since it is based on a very high theoretical level at the expense of experimental parameters and should be implemented in a scale different from the microscopic one. Moreover, we are interested in temperature and radiation effects that could make the approach even more complex. In this thesis a RIA modeling approach is proposed and reported in chapter 4.

## 2.3 H2 loading effect

H2 loading of the silica glass is often used to modify the materials properties [22, 28, 48, 152], such as the more rapid index change when writing FBGs

in fibers [22]. The most widely applied method of low-temperature hydrogen photo-sensitization is called *hydrogen loading* and it was developed in the 90's [153]. This method consists on storing the fiber in high pressure hydrogen atmosphere at a temperature below $100^oC$ for several days [22]. When the glass is stored in a hydrogen-rich environment, the H2 molecules, penetrating into the glass, can form bonds with the silica lattice. As a consequence of the interstitial hydrogen and related defects within the lattice optical absorption bands ranging from the UV to the IR could appear. A typical high-pressure reactor is showed by a schematic representation in Fig.2.9.

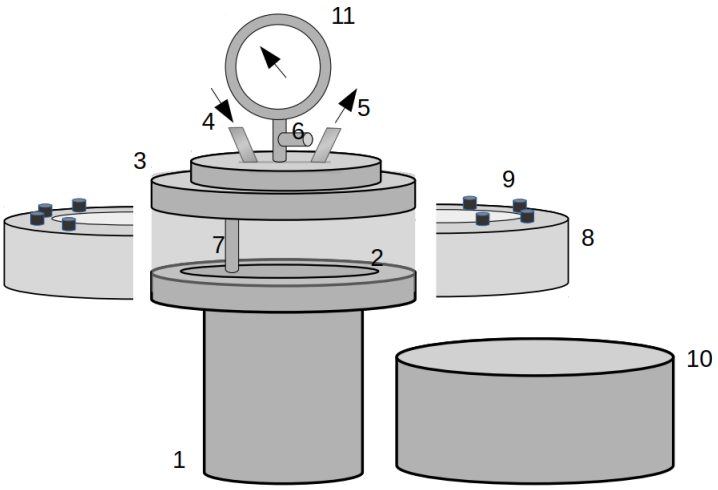


**Figure 2.9:** Schematic representation of a typical reactor employed for the H2 loading treatments. **1** is the vessel, **2** is a gasket, **3** is the cover of the vessel, **4** and **5** are the input and output valves for the gases, **6** is a pressure transducer, **7** is the well in which a thermocouple is placed, **8** and **9** are two steel half-rings for closing, **10** is a safety steel ring, **11** is an analogical pressure gauge.

Compared with the non-hydrogen-loaded fibers, the fibers treated in this way exhibit excellent photosensitivity in UV irradiation. Consequently, this approach is adopted to enhance the photosensitivity of optical fibers prior to UV light exposure in the fabrication of fiber gratings [154].

A diffusion model is employed to describe the characteristic of the hydrogen diffusion into and out of optical fibers. The concentration of hydrogen diffusing into the fiber is a function of its radius $r$ and time $t$, and can be obtained by solving the diffusion equation [155]:

$$\frac{\delta C}{\delta t} = \frac{1}{r}\frac{\delta}{\delta r}\left(rD\frac{\delta C}{\delta r}\right) \tag{2.9}$$

where $C$ is the hydrogen concentration and $D$ is the diffusion coefficient.

The presence of hydrogen in glass brings to the formation of hydroxyl(OH) [22, 156].

This formation can have clearly different magnitude depending on the type of silica, on its manufacture process and on the H2 treatment too. Some important

results related to H2 loading effects regard the passivation of some defects created in the fiber after exposure to radiation [48, 157], as well as the reduction of the generation rate of some silica-related radiation-induced defects like non-bridging oxygen hole centers (NBOHCs) [48]. In addition, it has been highlighted that the hydrogen loading in fibers with different types of doping, involves the reduction or disappearance of some defects due to radiation and the appearance of the peaks due to hydrogen [157]. H2 loading treatment was especially used in P-doped silica [158–162]. Then, the OH content depends on P concentration and two optical features related to OH formation are observed: one band peaking at 1.6 $\mu$m, characteristic of a P(OH) overtone and a monotonic increase of absorption tail starting at about 1.3$\mu$m [158]. Recently, the effects of hydrogen loading of a multi-mode OF after exposing to radiation was also studied [81]. The H2 loading is able to eliminate the RIA related to P1 centers (absorption band around 1600 nm) as well as the long tail of the RIA induced below 600 nm by POHC. The remaining 1240 nm absorption peak related to H2 molecules should disappear after few days due to out-diffusion processes. More recently, the effect of a hydrogen-treatment in low-OH and high-OH P-doped fibres under $\gamma$-rays irradiation was studied by Girard *et al.* [110]. They showed that the use of hydrogen allows to reduce significantly the RIA in the visible region [163]. In F-doped silica fibers, the same authors showed that a pre-treatment with H2 seems of poor interest as it does not decrease the contribution species responsible for the induced losses in the UV-visible part of the spectrum [110].

## 2.4 Luminescence

Luminescence is the emission of photons by a wide bandgap material previously exposed to ionizing radiation. Under exposition, being the radiation incident on the material, some of its energy may be absorbed and re-emitted as light of longer wavelength [164].

In Figure 2.10, a summary of the basic electronic excitation and relaxation mechanisms concerning a molecule or a point defect are reported. In the absorption process (highlighted by the red arrow) the electrons complete a transition from the ground state ($S_0$) to the excited one ($S_1$), then the nuclei instantly relax toward the minimum energy configurations in a time scale of the order of $10^{-12}$ s. Successively, it relaxes back towards the ground state so the electronic system will be in the minimum energy level. If the relaxation from the excited state to the ground state is radiative, a photon is re-emitted and finally the nuclei undergo a last relaxation toward the initial vibrational ground state. Since the excitation of phonons reduces the energy available for the emitted photon, the photoluminescence is shifted towards lower energies compared to the excitation light. The altering energy is known as Stokes shift [124]. It may happen a transition from the singlet electronic state $S_1$ to the triplet one $T_1$ by intersystem crossing process (ISC). This is a forbidden transition leading to a spin state change.

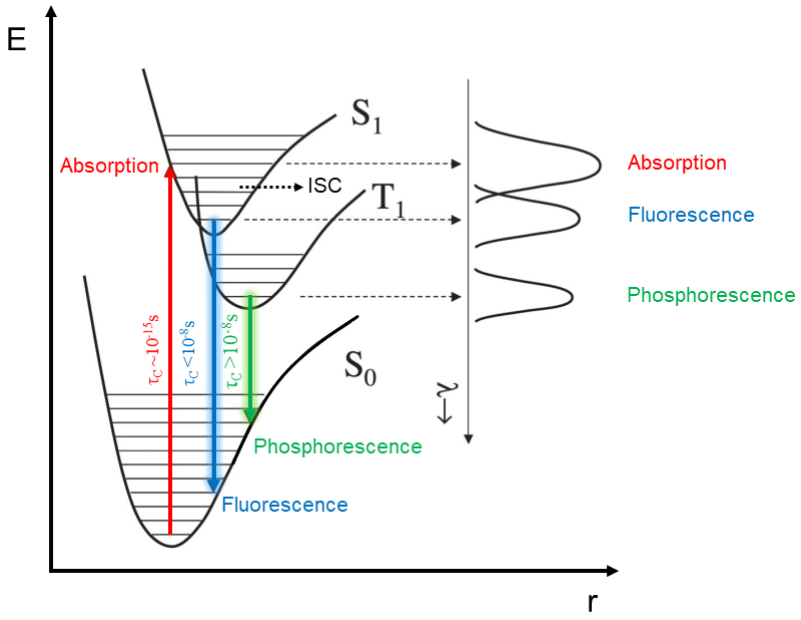


**Figure 2.10:** Jablonski diagram of the excitation and relaxation pathways involving the ground (S0) and the first excited (S1,T1) electronic levels of a molecule. S0, S1 represent spin singlet states, and T1 a spin triplet state. Red arrow highlights absorption transition, green and blue the emission ones, with respectively the characteristic time $\tau_C$ of each transition.

The time decay $\tau_C$ defines the type of radiative transition, which can be:

- allowed, in this case $\tau_C < 10^{-8}$ s and the process involved is the fluorescence;
- forbidden, with $\tau_C > 10^{-8}$ s, case called the phosphorescence.

In fluorescence the luminescence is almost simultaneous to irradiation: the electron in the excited state after the absorption transition, returns directly to its ground state by emitting a photon. In phosphorescence, the luminescence is delayed compared to irradiation. The electron transferred to an excited state will not de-energize radiatively directly to the fundamental level but being trapped on a metastable level in the energy band gap. If the difference energy between this metastable level and the closest band is greater than some $k_BT$ units, then the electron remains trapped on this level. To get this electron out of the trap, it must be supplied with sufficient energy to bring it back to the excited state from which it can then de-excite to its ground state. Phosphorescence itself may be conveniently subdivided into two main types: namely short period ($\tau_C < 10^{-4}$ s) and long period ($\tau_C > 10^{-4}$ s) [164]. It is in this second category that the thermoluminescence (TL) phenomenon can be done.

## 2.5 Thermoluminescence

Under the name of Thermally stimulated processes belong several physical phenomena in which a certain property of the sample is measured as a function

of the temperature. One of these phenomena is the thermoluminescence (TL). It is the property of some previously irradiated wide band gap materials to emit light when heated.

Figure 2.11 shows a standard model of TL based on the generation of electron-hole pairs by ionization processes between the valence and conduction band. Excited carriers get trapped on energy trap levels located in the band gap and related to defects, impurities or luminescent ions. After irradiation, the equilibrium state of trap filling is probed by the TL measurement consisting on collecting the emitted luminescence during heating of the material at a constant heating rate.

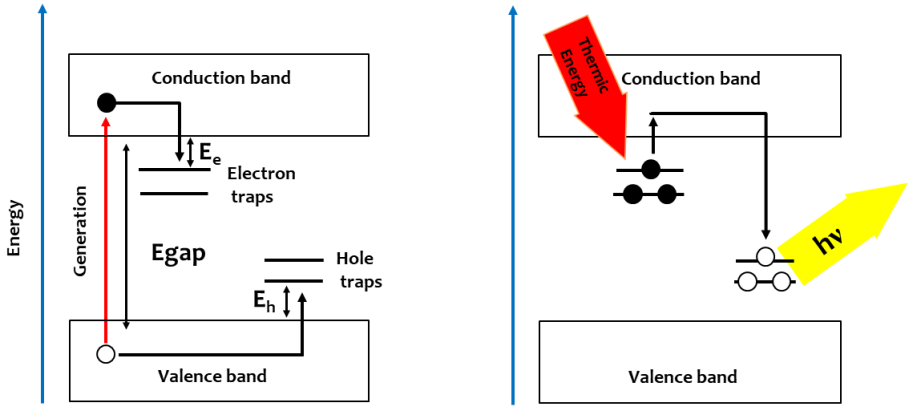


**Figure 2.11:** Schematic standard TL model: on the left the generation of electron-hole pairs and trapping by the traps; on the right the recombination between electrons and holes giving rise to photons.

The supply of thermal energy frees carriers from deeper and deeper traps as the temperature rises. Released carriers can recombine on the trapped-carrier centers of opposite polarity called Recombination Centers (RC). When this recombination is radiative the TL signal is collected by a PM tube and the plot of the intensity of the signal as a function of temperature gives rise to a "glow curve". A typical TL glow curve on Al-doped silica (1.97 $at.\%$ Al) is reported in fig. 2.12.

The TL curve is a superimposition of several TL peaks each of which originates from a single trapping level characterized by its depth E, the energy which separates this level from the nearest band edge. The distribution of the peak temperatures reflects the distribution of the trap depths, since deeper is the trap, higher is the temperature required to empty it. The TL standard scheme distinguishes 'traps' from RC. Traps are not too deep level states between the valence band and conduction band that are thermally released during TL readout, and RC consists of deeply trapped states that remain thermally stable throughout the readout. RCs are often formed upon electron or hole capture on defect- or dopant-related luminescent centers. When carriers are thermally released by the supply of thermal energy during the TL readout, they can recombine with RC of opposite polarity [165].

During the recombination process, the RC passes from an excited state to a ground state and a photon is emitted. The rising front of the peak is due to the steep increase of the thermal release probability and is thus governed by the Boltz-

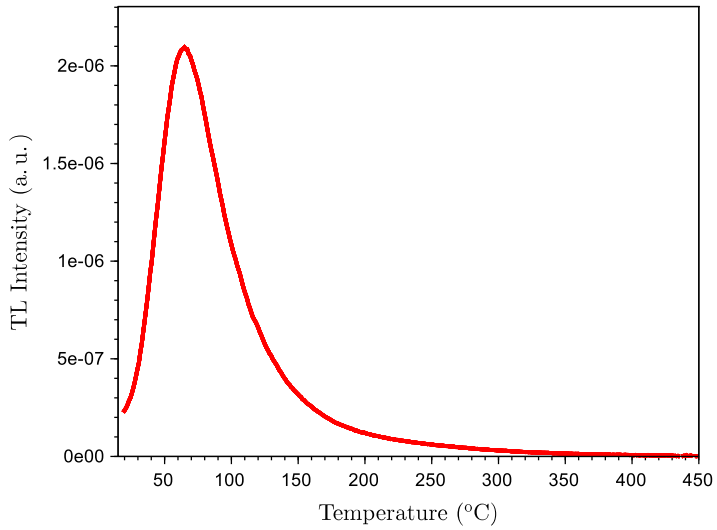


**Figure 2.12:** A typical TL glow curve on Al-doped silica (1.97 *at*.% Al).

mann term in $exp(-E/k_BT)$ as long as the level depletion remains small. The exhaustion of the carrier reservoir at $E$ finally dominates and explains the falling peak flank. Resulting from the transition between the two regimes, a peak maximum is reached. TL also be spectrally-resolved when acquired with an optical spectrum analyzer. Through the assignment of characteristic emissions, TL spectra allows the identification of the recombination centers that are reformed during the thermal relaxation process and, as a result, reveal the polarity of carriers in traps.

It is therefore a very complete characterization technique that can be reinforced thanks to its coupling to absorption measurements, through so-called protocols of "thermal annealing". This procedure, which will be explained deeply in appendix 4.3.4, may reveal the link between the trap centers (characterized by TL with in particular their activation energy) and color centers revealed by RIA.

### 2.5.1 First order kinetics

The simplest model of TL is obtained by assuming it obeys a first-order kinetics process. The latter is obtained when the re-trapping of carriers released from shallow levels is neglected. Then, the population of electrons trapped at a depth $E$, noted $n$ (the electrons density in $cm^3$) decays according to 2.10 [165].

$$dn/dt = -w \cdot n = -w_0 exp(-E/k_b T)n \tag{2.10}$$

where $w$ ($s^{-1}$) is the thermally-activated release frequency. The pre-exponential factor $w_0$ actually depends on temperature but at this stage it can be considered as a constant [165].

The thermoluminescence intensity associated with the single level $E$, can be

described by the following rule:

$$I_{TL} = -\eta(T)\frac{dn}{dt} \tag{2.11}$$

where $\eta$ is the luminescence yield (equal to 1 if every recombination is radiative) which can be written as:

$$\eta(T) = \frac{1}{k_r + k_{nr}} = \frac{1}{1 + Cexp(-W/k_B T)} \tag{2.12}$$

where $C = \tau_0 \nu$ is a dimensionless constant[2]. The function $\eta(T)$ is an inverted sigmoid between 1 and 0 when the temperature increases. Its inflection point at $\eta = 1/2$ is achieved at the temperature $T_{inf} = W/(k_B In(C))$. For values of T such as $T > T_{inf}$ the non-radiative recombinations become most probable and the TL is fully extinguished. To write the TL intensity as a function of the temperature, one has just to consider a linear heating law $T = T_0 + qt$, where q is the heating rate set experimentally:

$$I_{TL} = -\eta(T)\frac{1}{q}\frac{dn}{dt} = \eta(T)\frac{1}{q}w_0 * exp(-E/k_B T)n \tag{2.13}$$

The following steps are reported to solve equation 2.10 giving an expression of *n(T)* which can be inserted in 2.11 and calculate the TL intensity produced by a single level $E$ [165]:

$$dn/dt = -w_0 exp(-E/k_b T)n$$

$$dn/n = -w_0 * exp(-E/k_b T)dt = -\frac{w_0}{q} * exp(-E/k_b T)dT$$

$$d(\ln n) = -\frac{w_0}{q} exp(-E/k_b T)dT$$

$$\int_{T_0}^{T} d(\ln n) = -\frac{w_0}{q}\int_{T_0}^{T} exp(-E/k_b T)dT$$

$$\ln(n(T)) - \ln(n(T_0)) = -\frac{w_0}{q}\int_{T_0}^{T} exp(-E/k_b T)dT$$

$$n(T) = n(T_0)exp\left[-\frac{w_0}{q}\int_{T_0}^{T} exp(-E/k_b T)dT\right]$$

$$I_{TL}(T) = \eta(T)\frac{w_0}{q} exp(-E/k_b T)n(T_0)exp\left[-\frac{w_0}{q}\int_{T_0}^{T} exp(-E/k_b T)\right] \tag{2.14}$$

where $T_0$ is the initial temperature of the TL readout. The two main contributions of this function, are the first exponential, from which we can estimate the activation energy (see in 2.5.2), that grows with the temperature (peak rise), and

[2] C takes generally a value between $10^6 - 10^{10}$, considering $\nu \sim 10^{12}\ s^{-1}$, and $\tau \sim 10^{-4} - 10^{-8}$ s. W is typically some 0.1 eV

a second exponential term, that decreases with the temperature (responsible for the peak fall); at the intersection of these two contributions, these is a pick of TL intensity that represents the total emptying of the traps. The shape of the curve is not symmetric, the falling front being steeper.

A more generalized model, with respect to the first order process, is based on the possibility of thermally-released carriers to re-trap instead of recombine at recombination centers. This general kinetics will be explained in chapter 4, since it is the theoretical model based on the TL simulations.

### 2.5.2 Initial rise method

The initial rise method is the simplest and most generally applicable method for evaluating the activation energy $E_t$ of a single peak [165–169].

This method is used on the assumption that at the low temperature end of the peak all the relevant occupancy of the states can be considered as constant. Under this assumption, the early rise of the measured intensity as a function of the temperature is close to the first exponential term explicated in eq.(2.14), the second remaining very close to 1:

$$I_{TL}(T) = Cexp(-E_t/k_BT) \tag{2.15}$$

where the constant C includes all the dependencies on the other parameters and occupancy. From 2.15 one can obtain:

$$\ln(I_{TL}) = \ln C - E_t/k_BT \tag{2.16}$$

This leads to estimate the activation energy $E_t$ just plotting $I$ as a function of $1/T$ obtaining a line of slope $-E_t/k_B$. The equation (2.15) is in fact true for every equation describing the TL curve, whatever the actual kinetics order of the TL process, at the very beginning of the TL peak rise.

Considering eq. (2.14), if the last integral is zero $T \simeq T_0$ , and one well finds:

$$I_{TL} = \eta(T)\frac{w_0}{q}exp(-E/k_bT)n(T_0) = Cexp(-E/k_bT) \tag{2.17}$$

Experimentally, this approximation is considered roughly valid as long as the intensity remains below $1/10$ of that of the TL peak. As will be shown later in chapter 3, the procedure requires to measure a TL curve, then the measure is performed again. It is repeated as long as the measurements are possible, giving a series of successive TL peak at higher and higher temperatures. From the Arrhenius plots, the distributions of the trap depth as a function of the temperature is obtained. In fig.2.13 is reported an example adapted from [170].

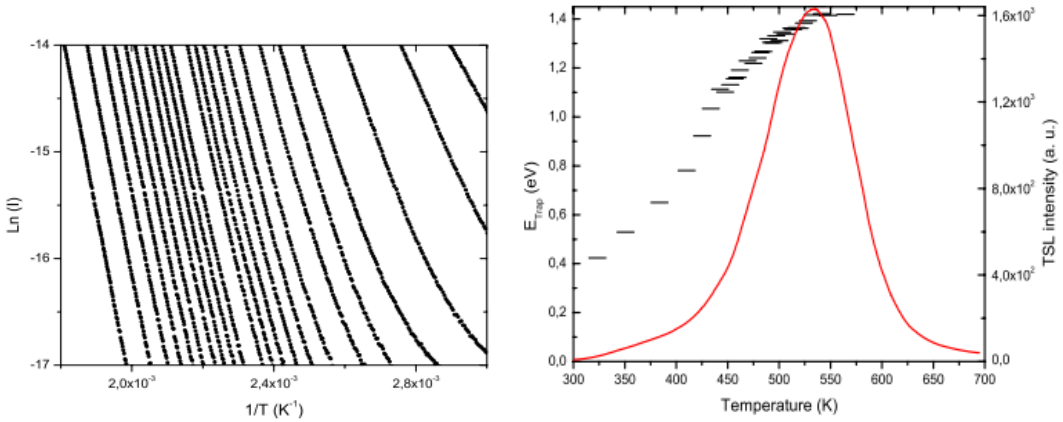


**Figure 2.13:** a) Arrhenius plots of the TL of Ge-doped core fiber after partial cleaning at different temperatures. b) Typical TL glow curve of Ge-doped core fiber after X-ray irradiation at RT and the trap depth distribution evaluated by IR method. Adapted from [170].

## 2.6 Materials and experimental setups

In this section we present the materials and the experimental techniques used in this thesis. First of all, is reported a description of the tested samples focusing on their preparation. Then, are described the radiation conditions and the experimental set-up of the spectroscopic techniques involved in the experiments.

### 2.6.1 Samples

**Sample preparation** The preparation of the samples is characterized by two steps: cutting and polishing.

In the first step the preform is cut into slices using a diamond wire saw to obtain discs at most 2 mm thick.

Once the slices obtained, it is necessary to polish them on both sides. This step is needed for the characterization measurements (optical absorption and TL), which require the performance of an optical quality polishing of both sides, in order to make them optically clean. Moreover, once the slice is polished, it is possible to make chemical analyzes, allowing to check the doping concentrations designed during the manufacturing process.

For the polishing procedure the samples were glued in a rotating support (see fig.2.14a) that is inserted into a cleaning machine, where is thrown on it an alumina powder and water compound during the process (see fig.2.14b). This step is repeated few times for several alumina powders of decreasing particle size (alumina 40$\mu$m, 12$\mu$m and 3$\mu$m) in order to abrade more and more finely the surface of the samples, with different times of polishing. In a second time, with the same support and a similar machine, is used a silica solution deposited on a synthetic tray to obtain an optical polishing (see fig.2.14c).

(a) (b) (c)

**Figure 2.14:** The polishing procedure used to prepare the samples: a) the rotating support where are glued the sample slices, b) the cleaning machine during the polishing procedure with alumina powder and water compound, c) cleaning machine during the polishing procedure with silica solution deposited on a synthetic tray.

**EDX** The Energy-Dispersive X-ray spectroscopy (EDX), is a microscopy technique which allows to carry out a quantitative chemical analysis of the elements in a target. An electron beam is collimated on a metal-coated target which will emit a set of characteristic X-rays of the target's constituent elements [171]. These X-rays appear in the form of the well-defined lines for given energies, characteristics of the chemical elements present. The electron beam pull off electrons in internal orbitals of the various elements, the vacancies created will lead to a de-excitation cascading electrons from outer orbital to fill them. The energy of these radiative de-excitations is carried away by X photons whose energy is characteristic of the element, which are collected and analyzed by the EDX spectrometer [171]. Fig.2.15 gives a schematic representation of this process.

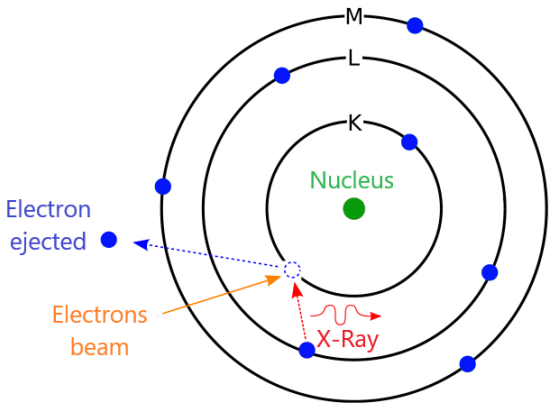


**Figure 2.15:** Atomic diagram of the X-rays generation by electronic bombardment.

EDX technique is a powerful method of localized chemical analysis that makes it possible to observe the elements of atomic numbers Z ranging from 4 (beryllium) to 90 (uranium) and it has a detection limit of around a thousand ppm, basically around 0.1% molar [171]. Since our samples are a not conductive materials, it has therefore previously been covered with a conductive carbon coating on one of its faces [171]. The instrument EMB-EDX (Microscopie Electronique à Balayage) used to measure the dopants concentration in our samples is reported in fig.2.16.

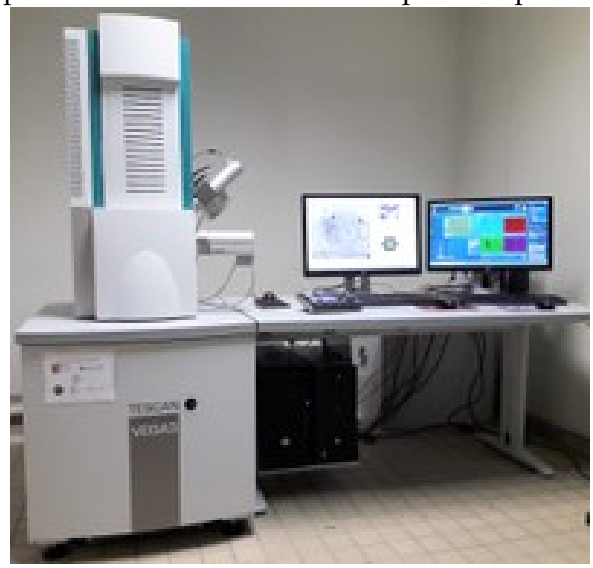

**Figure 2.16:** Instrument EMB-EDX (Microscopie Electronique à Balayage) used for EDX measurements.

Example of EDX results on one P-doped silica sample used in this thesis, is shown in fig.2.17. In figure is reported the distribution of the P content as % of weight (up) and % atoms (bottom) over all the diameter of the preform.

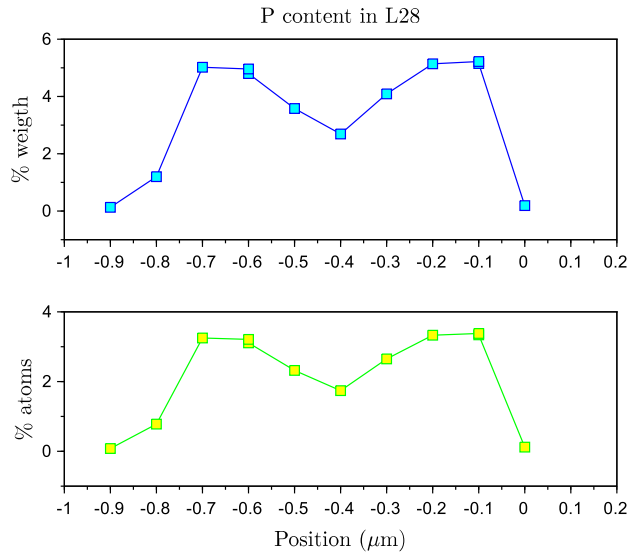


**Figure 2.17:** EDX results on a P-doped silica sample with 4 *at*.% P used in this thesis.

**Refractive Index Profile (RIP) Measurements** The index profile of the preforms was measured with the preform analyzer PK2600 (by Photon Kinetics). The precision on refractive index measurement is less than 0.005%.

Measurements are performed on several points along the preform length. Moreover at each distance the measurement of the refractive index $\Delta n$ is made rotating the preform in order to have a $\Delta n$ profile at four different rotation angles.

The profiles of $\Delta n$ in fig.2.18 are reported as function of the preform radius (mm) at four different distances. Then, the $\Delta n$ of the core is calculated from both the left and right part from the center (0 mm). The average values at different distances are reported in fig.2.19

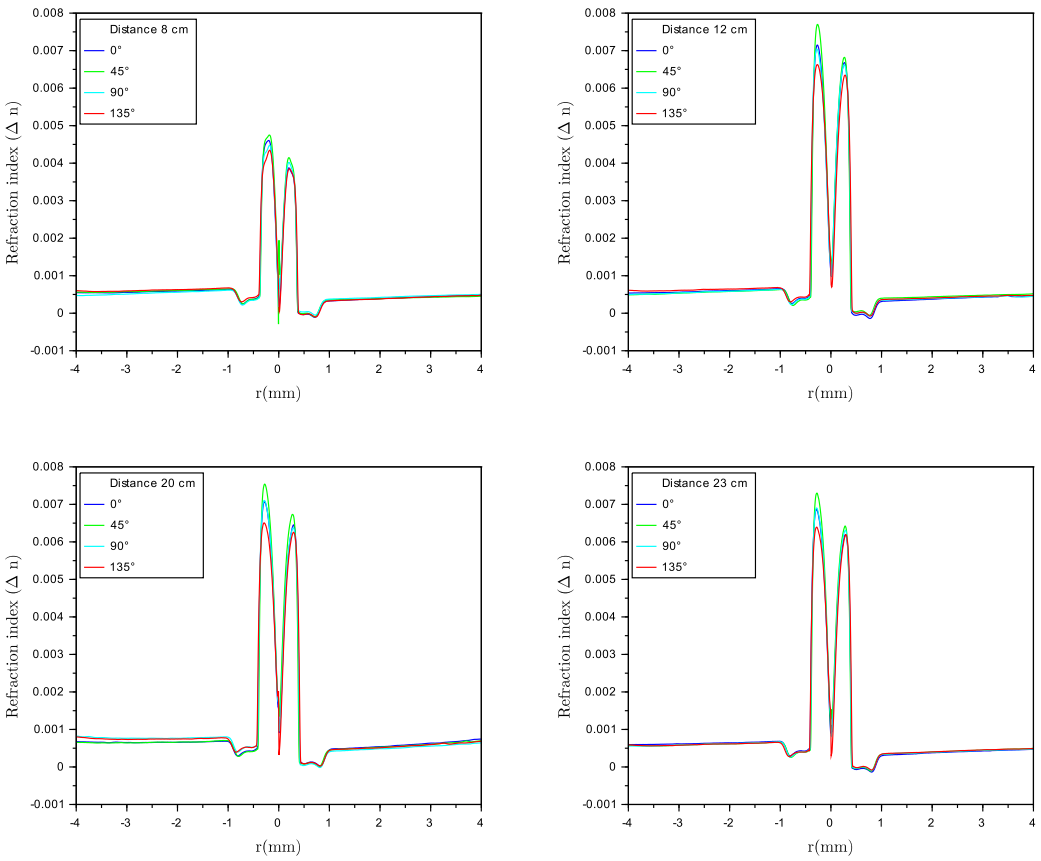


**Figure 2.18:** Refraction index on P-doped silica preform (4*at*.% P) at different distances from the end of the preform. For each distance is measured the $\Delta n$ at four angles.

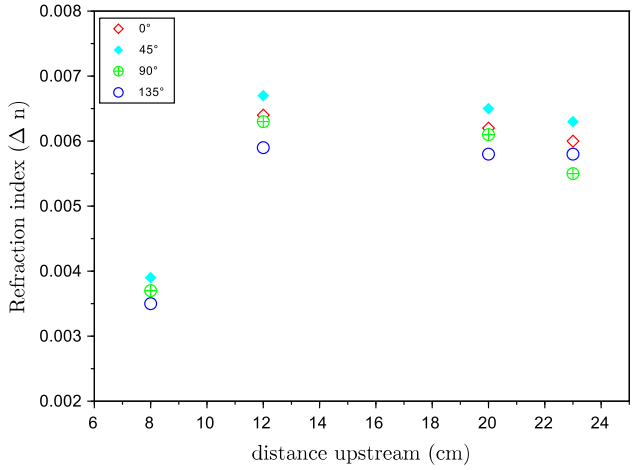


**Figure 2.19:** Example of refraction index measured in a P-doped silica preform (4 *at*.% P). The values correspond to the $\Delta n$ in the core of the preform for each curve in fig.2.18.

The RIP measurements are performed also on fibers, by means of a S14 profiler. The measurements are made at several positions respect to its total length. We report in Fig.2.20 just one to show a profile of $\Delta n$ in the same P-doped fiber.

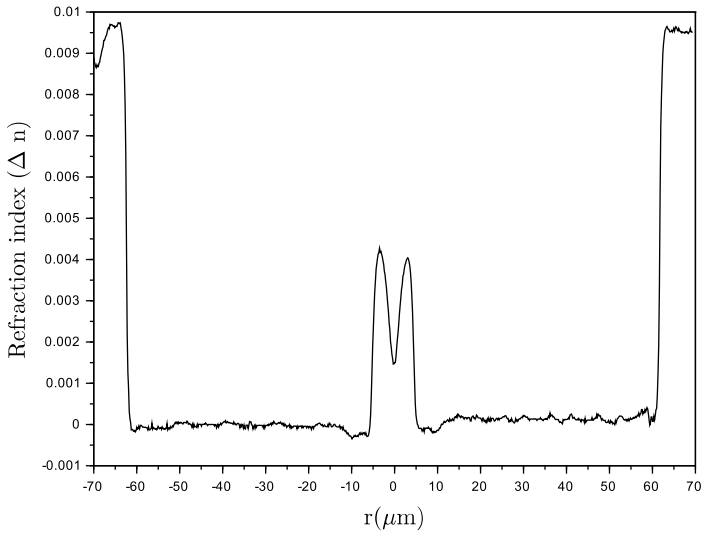


**Figure 2.20:** Example of refraction index profile measured on a P-doped silica fiber (4 *at*.% P).

**Cut-off wavelength** The wavelength at which a mode ceases to propagate is called the cut-off wavelength for that mode. However, an optical fiber is always able to propagate at least one mode, the fundamental one, which can never be cut-off (see subsection 1.5.2). Determining the cutoff wavelength of a single mode fiber involves finding the wavelength above which the power transmitted through the fiber decreased abruptly, for this reason it is important to estimate this value.

The cut-off wavelength of a fiber may be measured from the *bend-reference* technique [172, 173]. The estimated value is considered to be the effective wavelength, that is generally always smaller than the theoretical one. The *bend-reference* technique which experimental setup is shown in fig.2.21, is based on the attenuation obtained from two different configurations of the tested fiber.

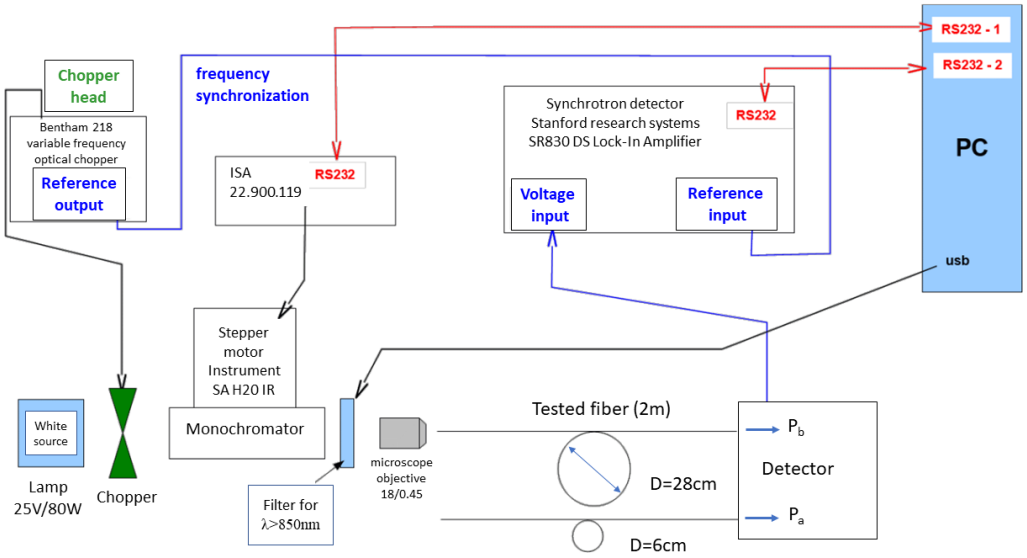


**Figure 2.21:** Experimental setup of the cut-off wavelength.

The power $P_b$ transmitted through a 2 meter long fiber arranged in a single loop of diameter D (shown as a circle in Fig.2.21), is determined as a function of the wavelength. Then the reference power $P_a$ is obtained after introducing an additional small diameter loop as shown by the small circle in fig.2.21. The attenuation of the first higher mode is then calculated as:

$$R(\lambda) = 10log_{10}\frac{P_b}{P_a} \tag{2.18}$$

In Fig.2.22 is reported the plot of measured attenuation as a function of the wavelength for a P-doped silica fiber ($4w\%$ P). The effective cutoff wavelength $\lambda_c$ is defined as the wavelength where the long-wavelength-edge of the attenuation increases by 0.1 dB over the long wavelength baseline [173] as highlighted by the red dashed lines in Fig.2.22.

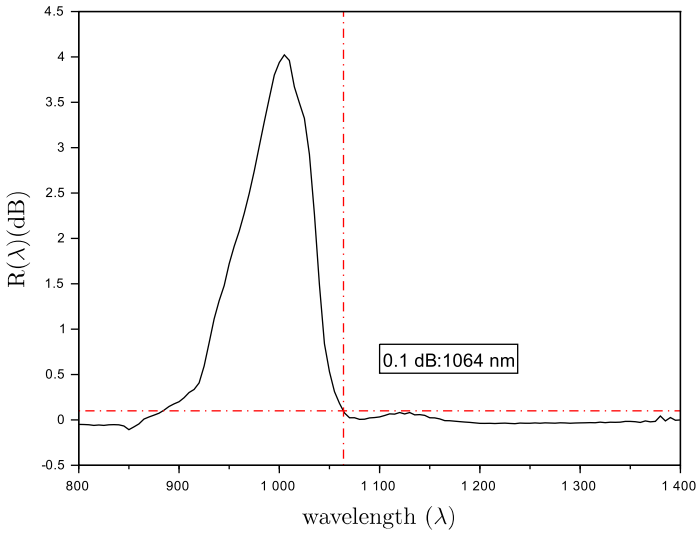


**Figure 2.22:** Measured attenuation as a function of the wavelength by *bend-reference* technique on a P-doped silica fiber (4$w$% P). The red dashed line corresponds to the value of 0.1 dB, which crosses the spectrum at a wavelength value of 1064 nm defining the $\lambda_c$

**Sample details** As reported in the introduction, some one of the main goals of the CERTYF project are to:

- develop radiation tolerant fibers able to operate in the radioactive waste storage facilities;
- enhance the fiber radiation sensitivity in order to design detectors very sensitive to radiation dose and dose rate;
- to characterize Telecom grade fibers being used for data transfer applications.

In accordance to these objectives, the samples tested in this thesis are grouped into three classes depending on their optical radiation responses: radiation tolerant, radiation sensitive and Telecom-grade fibers.

The physical-chemical characteristics of the samples are summarized in table 2.1.

The radiation sensitive preforms are characterized by two different dopants: Al and P. We tested for each dopant two kinds of samples differing in dopant content: K04 and K05 for Al-doped samples, and L28 and L27 for P-doped samples; for the radiation tolerant preforms: pure silica and F-doped fibers (Q11 and Q25). It is worth to note that the preform containing only deposited silica (L02) was made to serve as a reference and point of comparison for preforms of more complex compositions . Finally, as Telecom grade fibers, we tested three types of Ge-doped core preforms: one containing only silica in the cladding (called Q01), the second one and the third one are silica cladding doped with P (Q07) and F (Q09), respectively.

The samples are slices of preform made by MCVD process, prepared according to section 2.6.1.

| fiber class | name | doping | | characterization | |
|---|---|---|---|---|---|
| | | Cladding | Core | *at.*% | $\Delta n$ |
| Radiation Sensitive | K04 | Si | Al | 1.9 Al | $4.7 \cdot 10^{-3}$ |
| | K05 | Si | Al | 0.5 Al | $1.9 \cdot 10^{-3}$ |
| | L27 | Si | P | 0.6 P | $2 \cdot 10^{-3}$ |
| | L28 | Si | P | 4 P | $4.5 \cdot 10^{-3}$ |
| Telecom grade | Q01 | Si | Ge | 2.88 Ge | $3.5 \cdot 10^{-3}$ |
| | Q07 | P | Ge | 4.46 Ge, 0.89 P | $3 \cdot 10^{-3}$ |
| | Q09 | F | Ge | 1.01 Ge | $7 \cdot 10^{-3}$ |
| Radiation Tolerant | Q11 | F | Si | 0.85 F | $-4.01 \cdot 10^{-3}$ |
| | L02 | Si | Si | | $4 \cdot 10^{-4}$ |
| | Q25 | F | F | 1.19 F, 0.36 F | $-2.3 \cdot 10^{-3}$ |

**Table 2.1:** Certyf preforms and fibers under investigation.

### 2.6.2 X-rays

The X-rays irradiations were performed at room temperature (RT) by means of an INEL XRG3D generator using a Copper anode tube operated at an accelerating voltage of 30 kV.

The estimated X-rays spectrum (*Bremsstrahlung* spectrum for a voltage of 30 kV in Cu target material) is shown in fig.2.23. The characteristic lines Cu K$\alpha$ and Cu K$\beta$ leaving the X-ray tubes at an accelerating voltage of 30 kV (after all corrections required by the energy-dispersive method [129]) are estimated respectivly 46.38% and 6.35% respect to the total spectrum (Bremsstrahlung plus characteristic lines) [129].

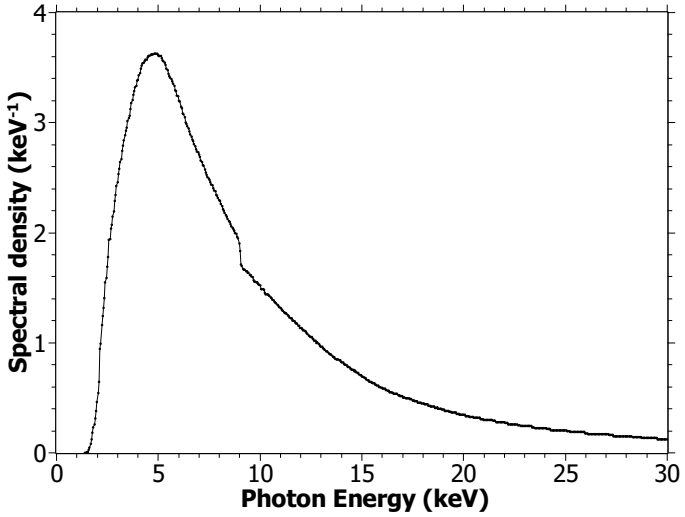


**Figure 2.23:** Simulated *Bremsstrahlung* spectrum for a voltage of 30 kV in Cu target material. Data for the figure taken from [129].

The dose rate used for most of measurements is 200 Gy($SiO_2$)/min on silica

preform. The X-rays chamber and a schematic representation of the irradiation setup are reported in fig.2.24 and 2.25 respectively.

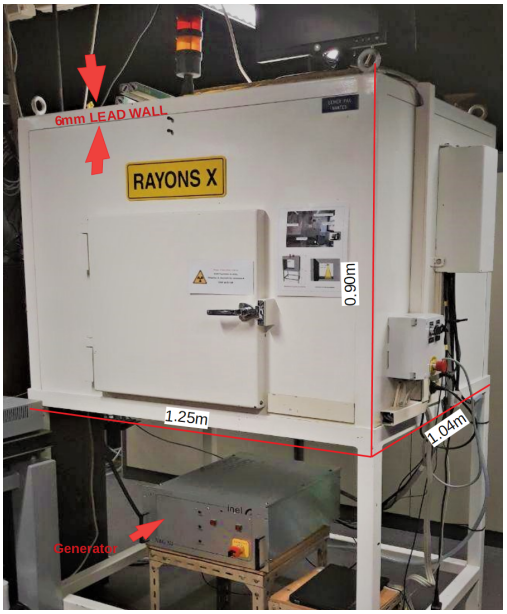


**Figure 2.24:** X-rays chamber used in this thesis and dimension details.

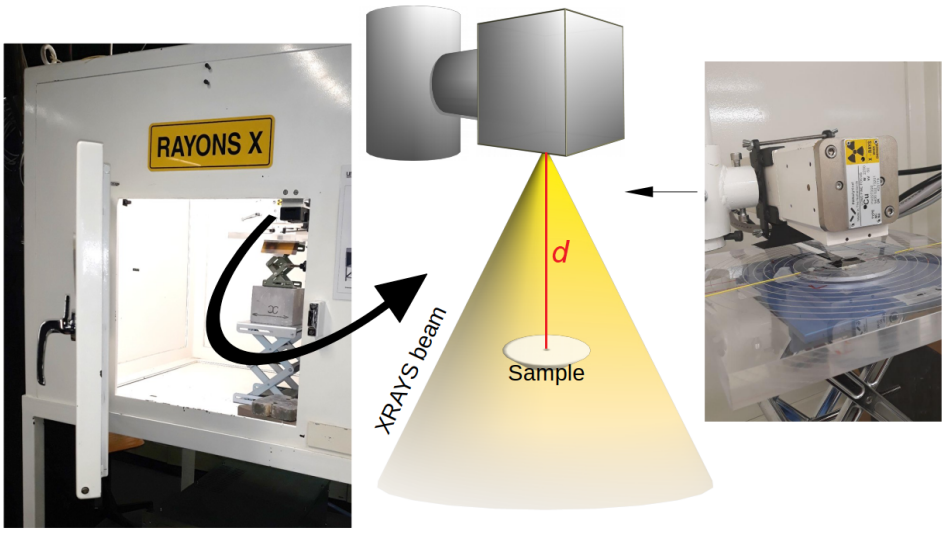


**Figure 2.25:** Detail of X-rays tube and a schematic representation of the irradiation setup.

Before measurements, a calibration of the dose rate is made my means of an ionization chamber. The dose rate in air is measured at several distances from the X-rays tube using a fixed voltage and current: 30 kV and 30 mA in the representation reported in Fig.2.26a. Moreover, the dose rate in air (Gy/min) is measured at different intensities of the current (mA) at a fixed voltage and a fixed distance ($d$) from the window of the tube. The calibration represented in fig.2.26b, was made

at 30 kV and at a fixed distance of 2.58 cm, a distance mostly used in our measurements.

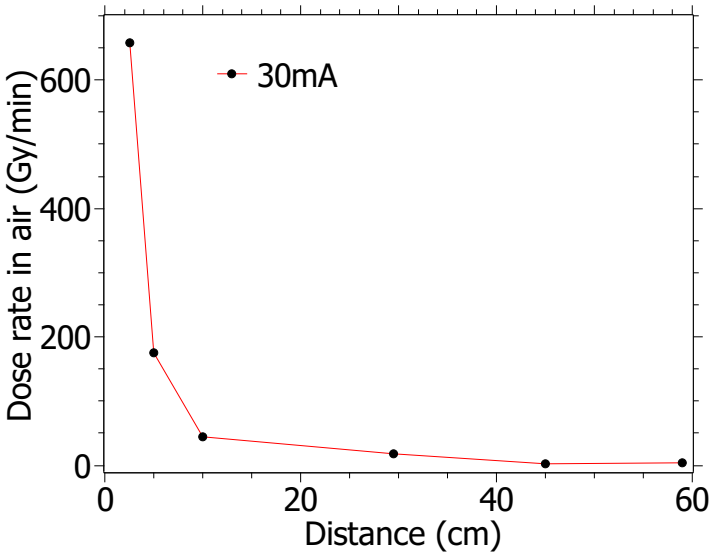


**(a)**

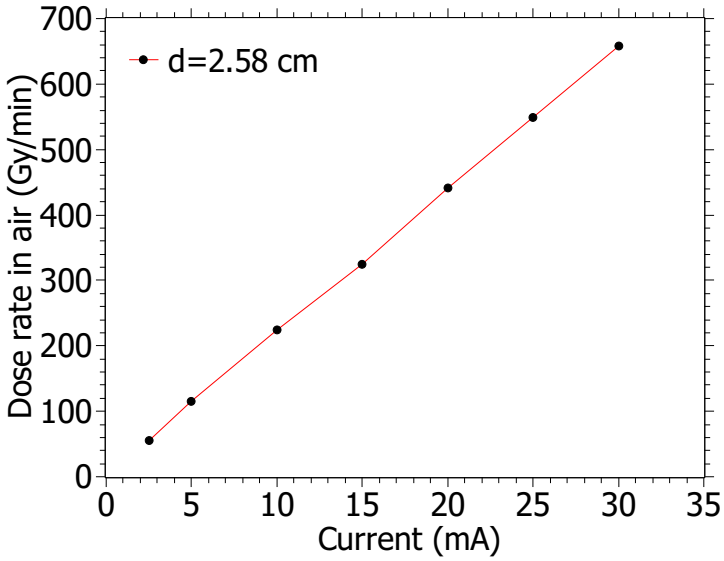


**(b)**

**Figure 2.26:** X-rays calibration procedure. The dose rate in air is reported a) as a function of the distance from the X-ray tube at a intensity current of 30 mA and b) as a function of the current at a fixed distance of 2.58 cm from the window of the X-rays tube.

### 2.6.3 $\gamma$-rays

The $\gamma$-radiation was performed at IRSN (Institut de Radioprotection et de Sûreté Nucléaire) by IRMA facility (IRradiation de MATériaux). This irradiation cell is composed by four sources of $^{60}Co$. The dose rate ranges from 5 $\mu$Gy/h to 16.4 kGy/h. The irradiation temperatures can reach 600 °C, thanks to the temperature-regulated heating plates specifically developed for the CERTYF project. For the present work, irradiations were performed at a dose rate of 50.3 Gy/min and a dose of 1MGy. In addition, some other samples were irradiated at 1MGy at three different temperatures (50, 90 and 250 °C).

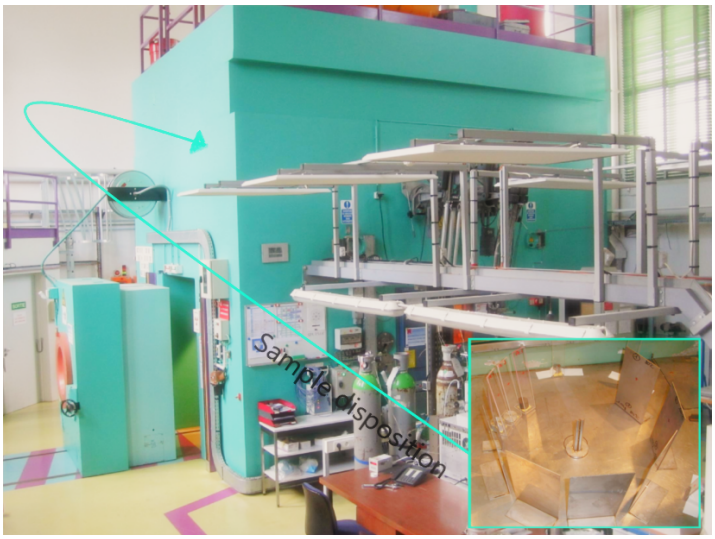


**Figure 2.27:** Picture of IRMA facilities at IRSN.

### 2.6.4 Optical Absorption measurements

The optical absorption measurements were performed using the Perkin Elmer Lambda 1050 spectrophotometer. This instrument and its main components are schematically shown in fig.2.28.

In this figure, at each number correspond the following components: 1 source system: Deuterium and Tungsten Halogen light sources; 2 double holographic grating monochromators for ultra-low stray light performance; 3 common beam mask that allows to adjust the beam; 4 common beam depolarizer; 5 chopper; 6 sample and reference beam attenuators that can assumes the value of 0%, 1% 10% and 100%; 7 Largest sample compartment; 8 detectors system: PMT and Pbs to cover the UV/Visible/NIR range; 9 second sampling Area; 10 high sensitivity PMT and 3 stage Peltier Cooled InGaAs to cover the full range (175-3300nm).

The main components of the spectrophotometer are the source, the optic system made by a double monochromator with a complex grating system, a sample compartment and a detector system. In fig.2.29 are reported the pictures of the instrument (a), the sample compartment (b) the sample holder (c) and an example of an irradiated preform (c). One can note the dark core size thanks to the darkening induced by the radiation exposure.

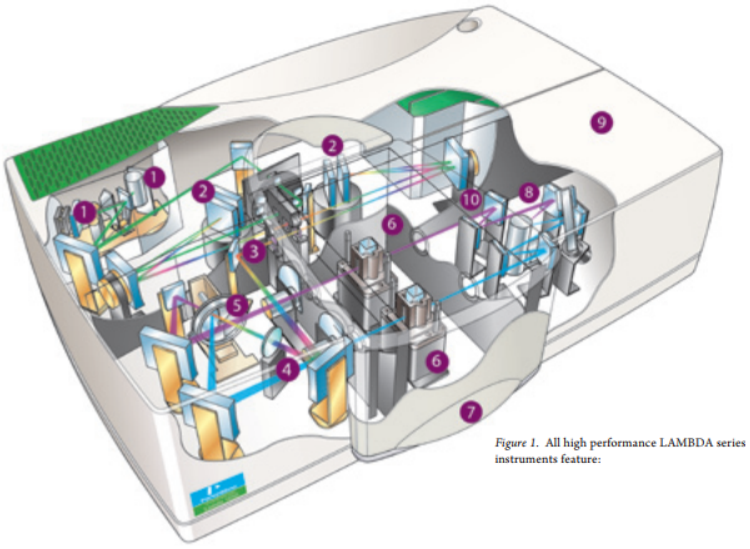


**Figure 2.28:** Design of the spectrometer Perkin Elmer Lambda 1050. At each number correspond the components described in the text (adapted from Perkin manual).

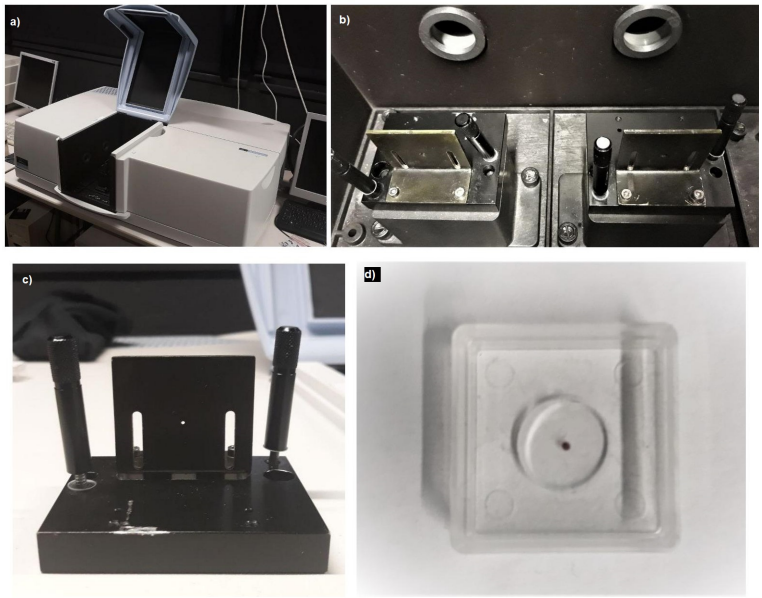


**Figure 2.29:** Pictures of the optical absorption setup: a) Perkin Elmer spectrophotometer, b) sample compartment; c) sample holder generally used to focus the light only in the core part of the sample and d) a typical preform slice with a dark core due to the irradiation.

The source is made by two lamps, deuterium and halogen, while the detector system made of a PMT detector in the UV/Vis range, a PbS and an InGaAs detector in the NIR. These detectors set allows covering a spectral range from 175 to 3300 nm. Change between detectors is automatic along the measurement at user-set.

The light from the lamp hits a complex optical system of mirrors and choppers that filters the light before it reaches the monochromators (this is helpful to cut off the higher orders of the wavelength). From some mirrors the light reaches the monochromators having passed a slid with modified dimensions. Then it reaches a grating system that makes the radiation more monochromatic and characterized by an high spectral quality.

Then, the incident bream arrives on an optical system that divides into one passing to the reference arm and another through the sample placed on its holder (see fig. 2.29 for the sample compartment). For our measurements we generally used a sample holder with a hole which dimensions are similar to the core of the studied preforms (1mm) (see fig.2.29).

The instrument is characterized by an accuracy of $\pm$ 0.08 nm in the UV/Vis range and $\pm$ 0.30 nm in the NIR. The spectral resolution is 0.05 nm, step 0.01 nm in the UV/Vis and 0.20 nm, step 0.04 nm in the NIR.

### 2.6.5 Thermoluminescence setup

Thermoluminescence (TL) readout is carried out from RT ($19^oC$) up to $500^oC$ with a constant heating rate by using a laboratory-made TL setup. It consists of a resistivly-heated Inconel alloy on which can be placed a preform sample, of a thermocouple placed very close to the sample and a PID regulation to achieve linear temperature ramps at different heating rates $q$ ranging from $0.1^oC$ to $5^oC\ s^{-1}$. The emitted TL signal is recorded by means of a UV-Visible photomultiplier tube (PMT) Philips XP-262B cooled by water circulation that maintains the operation temperature close to RT. A schematic set up representation is reported in fig.2.30a, then in fig.2.30b is shown a picture of the instrument.

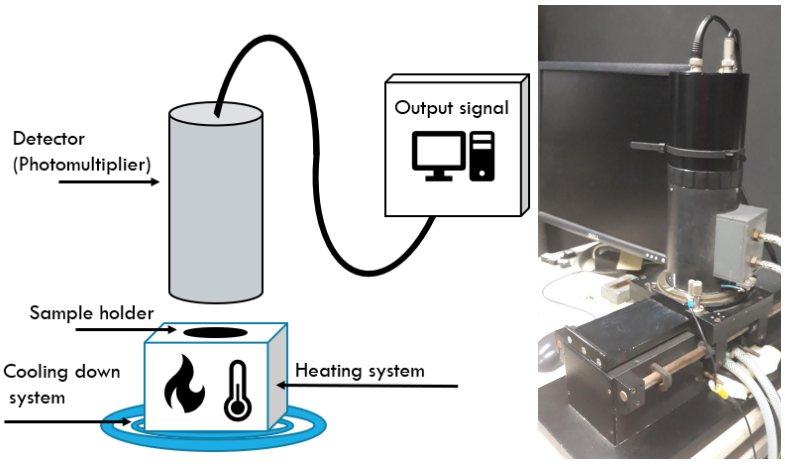


(a) (b)

**Figure 2.30:** Block diagram of the TL setup. The sample holder is a circle of ∼1cm of diameter.

The spectral distribution of TL peaks can also be recorded from RT to $500^oC$ with a CCD detector (Fergie). The Fergie instrument is an integrated 80.8 mm

focal length imaging spectrograph with a built in 256 x 1024 (row x column) TEC cooled back-illuminated CCD detector and a motorized single turret grating drive. The usable wavelength range is 200 nm-1100 nm, with a resolution of 0.16 nm. A picture of the instrument is shown in fig.2.31a, whereas in fig.2.31b is shown the coupling between the home made TL setup used as heater and the fiber bundle connected to the spectrograph for the TL spectrally distributed measurements.


(a) (b)

**Figure 2.31:** Pictures of TL setups: a) Fergie spectrometer instrument, b) the coupling between the home made TL setup used as heater and the fiber connected to the Fergie for the TL spectrally distributed measurements

# Chapter 3

# Experimental Results



The chapter reports on the experimental results obtained by using the Thermoluminescence (TL) and optical absorption (AO) technique after exposure to X-rays or $\gamma$-rays irradiation. The aim is to characterize the samples and investigate the mechanisms of creation and annealing of point defects by means of these two spectroscopic techniques.

This chapter is organized into four sections, each of which related to:

1 the radiation tolerant fiber preforms results;

2 the radiation sensitive fiber preforms results;

3 the impact of the irradiation temperature in radiation sensitive fibers;

4 the Telecom-grade fiber preforms results.

We proceed reporting for each sample the TL measurements, in which we investigate the TL response at different heating rates and at different doses, and the initial rise method results. Then, are presented the optical absorption measurements, that consist in the Radiation induced attenuation spectra (RIA) and the thermal annealing experiment (see appendix 4.3.4). In a slightly different way it

is instead articulated the third section 3.3, where particular attention is paid on the impact of the irradiation temperature in radiation sensitive fibers. This study is more focused on the thermal annealing measurements after exposure to $\gamma$ irradiation.

## 3.1 Radiation tolerant fiber preforms

It is well admitted that the most radiation-resistant fibers are pure silica and F-doped fibers. The corresponding TL emission is then so low that it is impossible to estimate the energy depth of the traps by initial rise method. For the same reason, since this kind of fibers show a high tolerance to radiation, the absorption measurements during the thermal annealing protocol reveal a too low and noisy RIA level. For the last issue we managed to perform $\gamma$-irradiation, which allows reaching very high doses (up to 1MGy) in order to obtain much higher RIA levels. Whereas the trap depth levels are determined by another method based on changing the heating rate of the TL readout. Below we report the TL and the optical absorption results on pure silica and F-doped preform cores (L02 and Q25 respectively). We finally, discuss on the creation and recombination processes of radiation induced point defects in this kind of fiber preforms.

### 3.1.1 Thermoluminescence

TL glow curves measured from the pure silica core sample (L02) at four heating rates is shown in fig.3.1. They are characterized by a main peak located at around 70-90°C, depending on the heating rate used in the readout. The TL intensity decreases with the increasing heating rate, as well as the TL area under the glow curve (red scatters in fig.3.1).

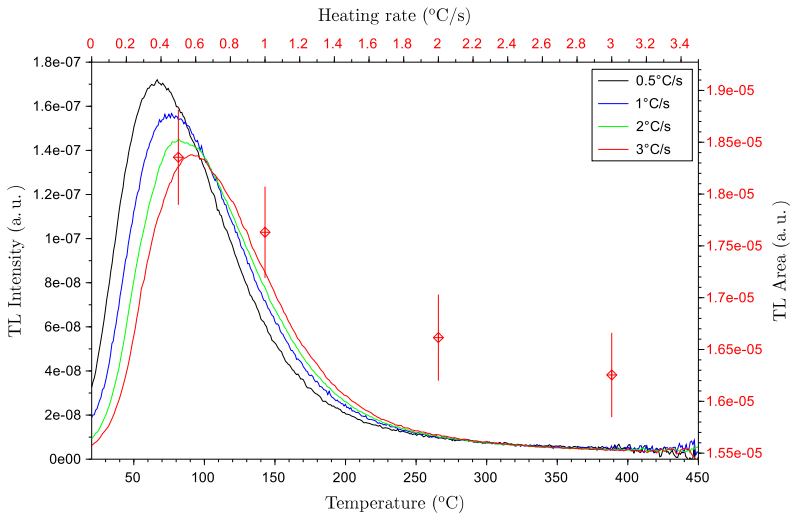


**Figure 3.1:** TL on pure silica sample (L02) at four heating rates after irradiation at a dose of 3 kGy. The red scattered points show the TL areas at three different heating rates with an error bar representing a relative error of 5%.

The same shapes and peak positions are found for the TL curves of the Q25 sample (fig.3.2). This kind of sample shows a higher resistance to radiation because of the presence of fluorine in the core. Q25 is more tolerant compared to L02. Its radiation resistance is evident also from the TL results, which glow curves recorded by the PMT tube are very noisy and of low intensity.

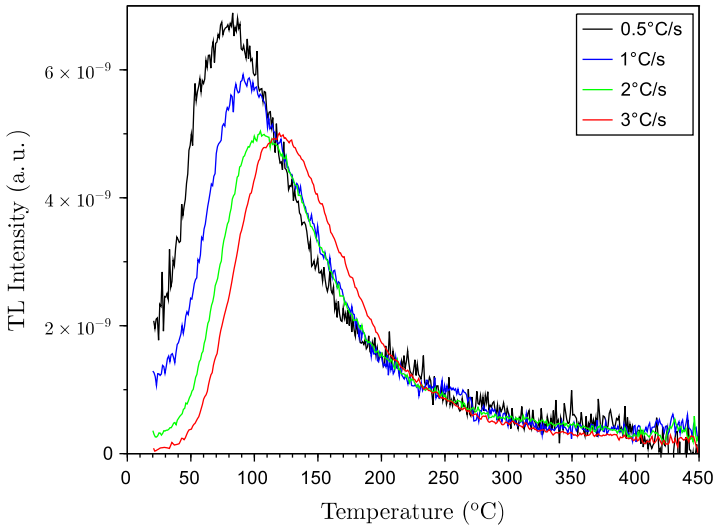


**Figure 3.2:** TL curves of the Q25 sample at four heating rates after irradiation at 3 kGy.

The TL curves of fig.3.1 and 3.2 consist of broad peaks, which reach the maximum emission between 60 and 100°C depending on the heating rate. The broadening of TL glow peaks results from the spread of trap levels reflecting the amorphous structure of the sample. The TL peak at 80°C (at 1°C/s) is usually observed in silica and corresponds to a common intrinsic defect in this material [164].

Together with the decreasing of the TL intensity we observe a decrease of the TL areas as shown in fig.3.1. The decreasing of the area as well as the intensity is an usual behavior due to the thermal quenching of the luminescence following the shift of the peak to higher temperature. This shift is a common feature due to the different heating rate used in the TL recording. The use of a higher heating rate means that any given temperature is reached in a shorter time along the TL readout; but since the thermal release frequency $w$ of a level $E_k$ remain the same ($w = w_0 exp(-E_k/k_B T)$), it takes more time and therefore a higher temperature to release the same amount of carriers [174]. The lowering of the TL intensity and therefore of the peak area, is a direct consequence of this shift of the TL processes towards high temperature. The radiative de-excitation of the luminescent species, responsible for the TL emission, indeed competes with a non-radiative de-excitation route which relative probability increases at high temperature [174].

The shift of the TL peak with increasing heating rate is an effect that can be used to estimate the energy depth of the peak [164]: within the first-order approximation of the TL process, any single trapping level $E$ gives rise to a single peak whose maximum is reached at a temperature $T_m$ which depends on the heating rate $q$ and

$E$; $q$ and $T_m$ are linked by eq.(3.1):

$$qE/k_BT_m^2 = w_0 exp(-E/k_BT_m) \tag{3.1}$$

In fig.3.3 is reported the trap depth with the variation of the temperature for several values of $w_0/q$ from a computation of the first order TL glow curve made by Christodoulides and Ettinger in 1971 [164].

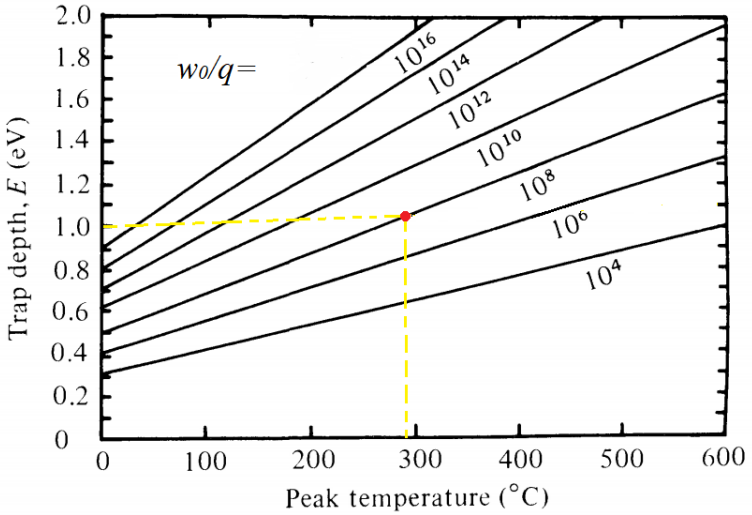


**Figure 3.3:** Variation in $T_m$ with E for different values of $w_0/q$ for a first order kinetics. Adapted from [164].

This picture shows very directly the influence of the heating rate. If one imagines an horizontal line at a certain value of $E$ and a given frequency factor, the heating rate $q$ is associated with a shift of $T_m$ to higher temperatures.

From the relationship 3.1, different methods in calculating E can be obtained. We do not go deeply because in our analysis we used the initial rise method to estimate the energy depth, since it is the most accurate experimental method. Anyway from 3.1 and from the TL curves at four heating rate shown in fig.3.1, it is possible to estimate the corresponding trap depth of the peak. This can be useful when we cannot perform the initial rise method as in the case of pure silica samples. It is worth noting that from the initial rise method we obtain an estimation of the energy depth of the distribution of traps for all the glow curve, from which we can determine the energy of the trapping levels associated with the stopping temperature $T_{stop}$. From eq.(3.1) we have just an estimation of the energy at the peak, so we obtain only one value. As one can easily understand from 3.1, plotting $\ln T_m^2/q$ against $1/T_m$ we obtain a line of slope $E/k$ from which $E$ can be calculated. This line with the linear fit is reported in fig.3.4. From the slope we estimate a trap depth of 0.76 eV corresponding to the main TL peak .

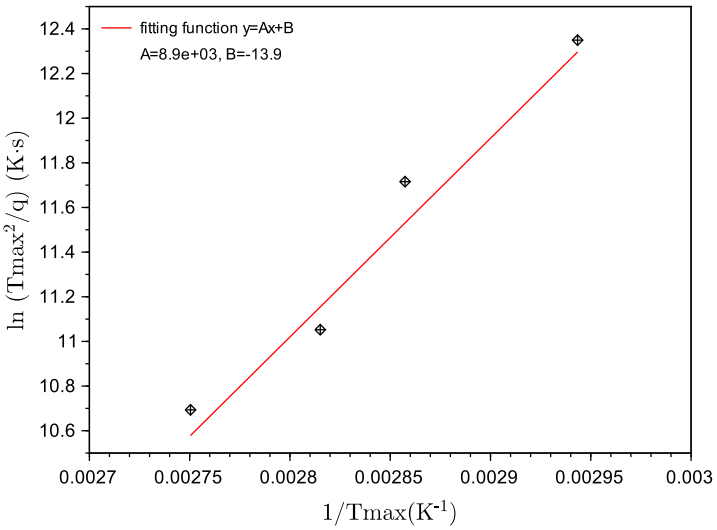


**Figure 3.4:** $\ln T_{max}^2/q$ as a function of $1/T_{max}$ in order to estimate the trap depth. Each $T_{max}$ and the relative q value correspond to the TL curve reported in fig.3.1 for L02 sample.

Fig.3.5a shows the TL glow curve recorded from the L02 sample at 1°C/s. It presents a main peak at 80°C. The fact that it starts from a non-zero intensity level reveals that a phosphorescence does exist at RT. It corresponds to the recombination of the carriers thermally released at RT from shallow traps.

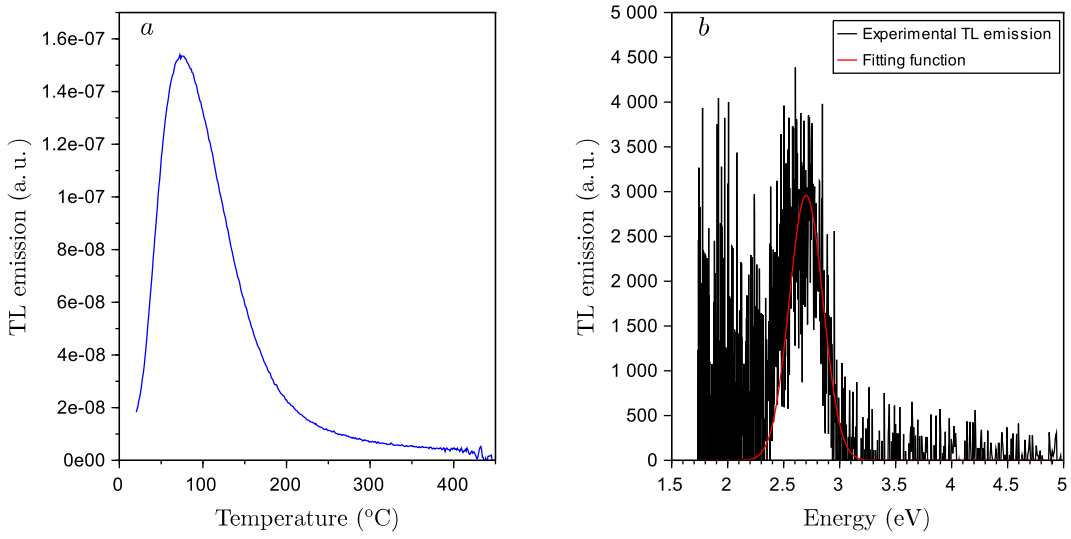


**Figure 3.5:** a) TL curve recorded at 1°C/s on a pure silica sample (L02). b) Spectral TL emission (black curve) and Gauss fit (red curve) of L02 at the maximum of the peak.

The spectral TL emission of this peak is shown in fig.3.5b. The Gauss fit superimposed on the experimental spectrum reveals the presence of only one band peaking at 2.7 eV and with a full width half maximum (FWHM) of 0.35 eV, indicating that the TL emission mainly takes place around 2.7 eV. This well-known emission is characteristic of oxygen deficient centers (ODC) [32, 73, 175], which is the only luminescence center responsible for the TL signal on L02 sample. This indicates that the ODC are reformed in excited state, by recombination, during the TL process.

The spectral TL emission of Q25 sample, tentatively measured by the spectrophotometer, was impossible to record due to the low emission level.

### 3.1.2 Optical absorption

A typical RIA spectrum of pure silica sample is shown in fig.3.6. It was recorded on L02 sample after an irradiation dose of about 10 kGy. The RIA intensity reaches a maximum value of about 110 dB/m in the UV region. The low intensity in the visible part of the spectrum is a characteristic of the radiation tolerant fibers such as the undoped silica types studied here. A Gaussian decomposition attempt, superimposed on the experimental data in figure 3.6, shows the presence of three Gaussian bands, centered at 5.8 [1.0], 4.7 [1.1] and 6.8 [3.0] eV (the values in brackets expressed in eV correspond to the FWHM.) These bands have been assigned to the intrinsic defects SiE' (at 5.8 eV) and NBOHC (at 4.7 and 6.8 eV) in silica [32, 42].

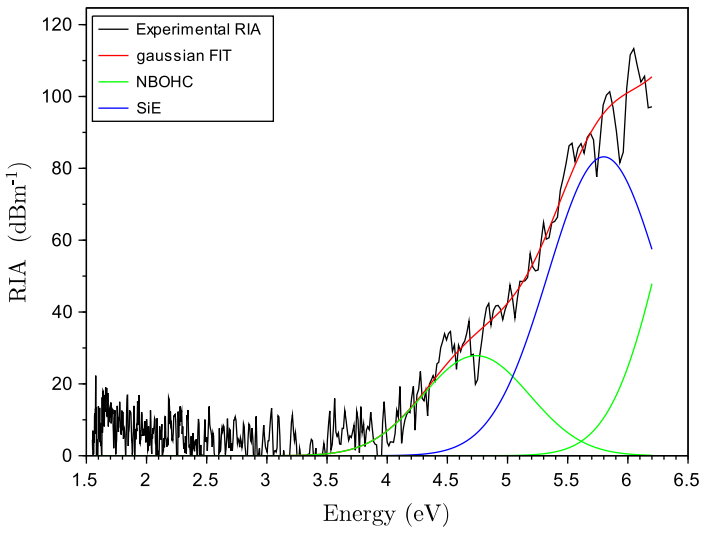


**Figure 3.6:** RIA on pure silica sample (L02) after an irradiation dose of 10 kGy.

The RIA spectrum for the Q25 sample is shown in fig.3.7. The absorbance recorded after irradiation with a dose of 6 kGy (red line) has still an intensity close to the one recorded in the pristine sample (black line). In the inset is shown the RIA deduced from these absorption spectra. As one can see, it is difficult to highlight any clear Gaussian bands related to defects due to the very low and noisy RIA level. This highly radiation tolerant behavior is probably due to the presence of

fluorine in the core of the preform. The presence of fluorine decreases the presence of precursor defects [86, 111, 112], so the radiation induced ones are also decreased respect to a pure silica sample such as L02. This kind of sample can be very useful for radiation tolerant application where the RIA level must remain low at any radiation dose.

Due to the low RIA level, the thermal annealing results are not exploitable at the dose generally used in our laboratory. For this reason we performed the thermal annealing experiment after an irradiation of 1MGy by $\gamma$-rays at IRMA facility (see section 2.6.3). The TL and optical absorption measurements were made long time after the end of irradiation (about 26 days). This delay, together to the very long irradiation time characterizing IRMA expositions ($\sim$ 14 days here), induce strong changes in the energy distribution of trapped carriers by comparison with routine laboratory irradiation, leading to a depletion of shallow levels and carrier condensation in deep levels.

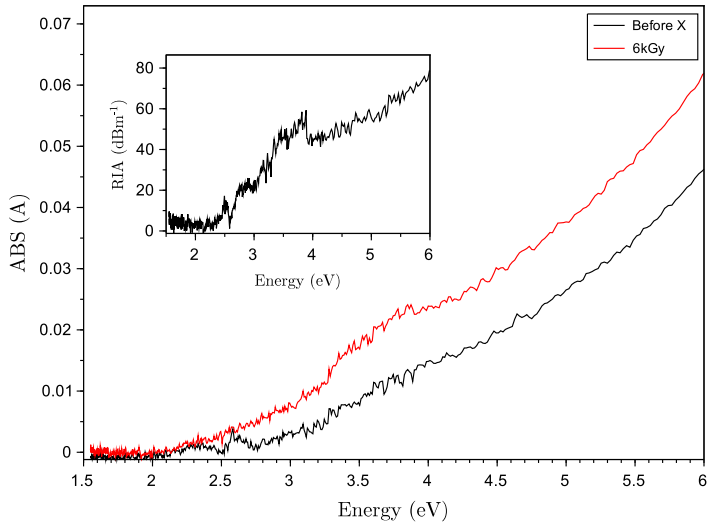


**Figure 3.7:** Optical absorption in terms of absorbance before and after irradiation (6kGy) on Q25 sample and the relative RIA in the inset.

As a result, the TL on a sample after an irradiation of 1MGy by $\gamma$-rays at IRMA facility, presents a TL peak shifted at higher temperature with respect to the TL at $1^oC/s$ reported in fig.3.1 (blue curve). The TL at 1MGy reported in Fig.3.8a shows a TL peak at about 170°C(instead of 80°C in fig.3.5) and an evident shoulder at around $350^oC$. In this figure are also reported the TL curves obtained during the thermal annealing treatment on another sample slice cut from the same preform and irradiated at 1MGy but intended for the optical absorption measurements. As one can see the heating process empties the traps bringing to a lower and lower TL intensity.

The thermal annealing measurement protocol is explained in appendix 4.3.4. The RIA spectra recorded during this process and the bleaching map built from them are reported in Fig. 3.8b and 3.9 respectively. In the bleaching map is reported also the TL glow curve shown in fig. 3.8a in a semilog representation; with the aim

to show clearly the correlation between temperature of the TL features and the one of the bleached color centers in RIA by the thermal treatment.

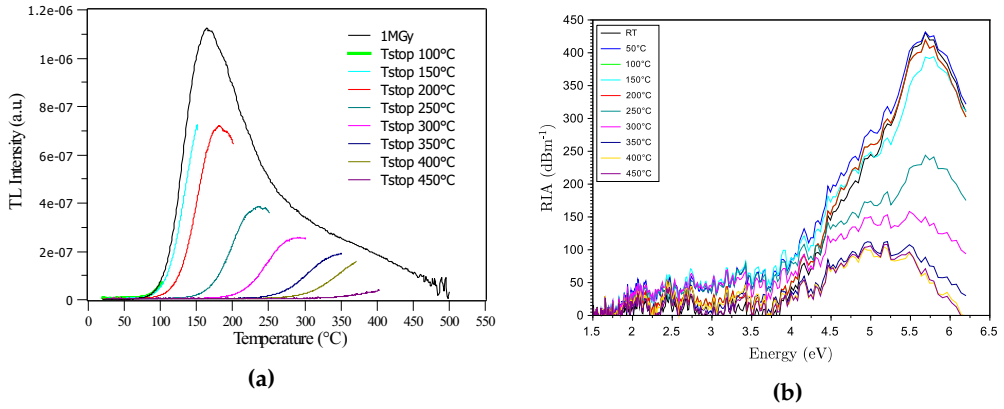


**Figure 3.8:** a) TL on L02 sample after an irradiation of 1MGy (black curve). The colored curves correspond to the thermal annaling treatment at different $T_{stop}$. b) RIA of L02 sample at each stopping temperature of the fig.3.8a during the thermal annealing treatment after an irradiation dose of 1MGy by $\gamma$-rays.

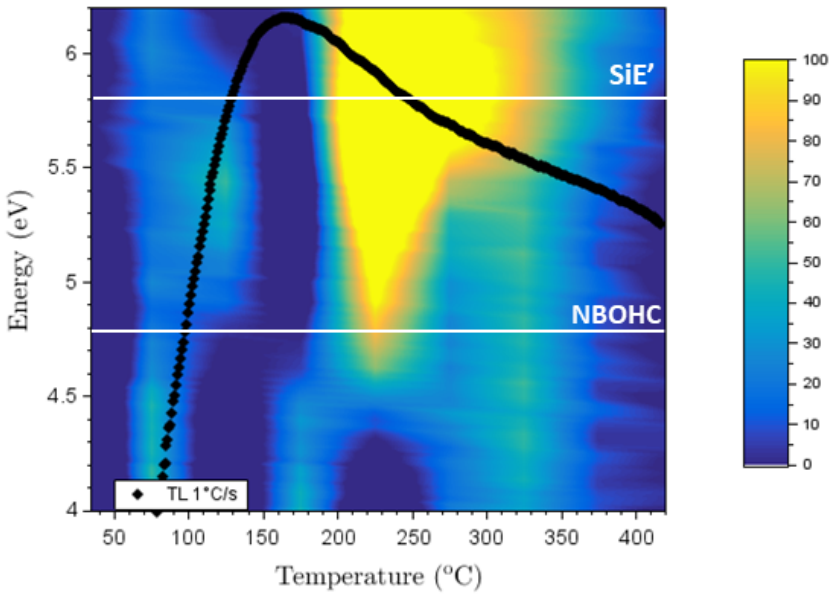


**Figure 3.9:** Thermal annealing bleaching map obtained from the RIA curves in fig.3.8b. In a semi-log representation is superimposed the TL glow curve (black line) recorded at a dose of 1MGy by $\gamma$-rays.

As one can see from figure.3.9, the main bleaching takes place between 5 and 6 eV between 70 and 150$^oC$ and again from 200$^oC$ to 400$^oC$, but the most important bleaching occurs around 225$^oC$. This is clearly due to the bleaching of SiE' centers which destruction mechanism probably involves the release of their captured

holes. In fig.3.10 and 3.11 are reported the RIA curves at RT and at each heating step of the thermal annealing treatment with the gaussian fit in order to show the annealing of the radiation-induced color centers previously identified in fig.3.6: the NBOHC and the SiE' centers. The fits were done fixing the center of the single Gauss band and the FWHM and let running only the amplitude. The amplitude obtained from each fit is reported in fig.3.12a as a function of the temperature. One can see that the behavior of the NBOHC and SiE' annealing is quite similar. Moreover to highlight their correlation during the annealing, in fig.3.12b is reported the amplitude of the NBOHC peaking at 4.8 eV against the amplitude of the SiE' at 5.8 eV. As one can see from the logarithmic representation, the behavior is linear with a slope close to 1, which means that both defects anneal within the same way.

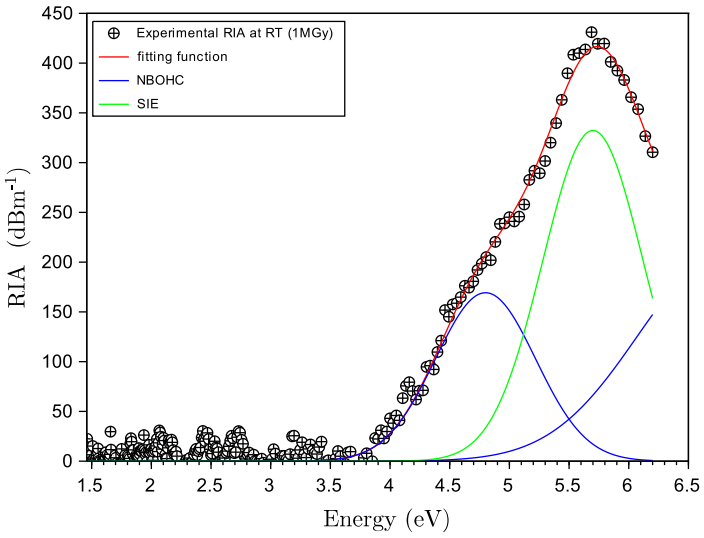


**Figure 3.10:** a) Experimental RIA (black points) recorded at RT 26 days after the irradiation at 1MGy. The fit (red) is composed by three gaussian bands centered at 4.8, 6.8 eV and 5.8 eV, related respectively to NBOHC (blue) and SiE' (green) centers, as in fig.3.6.

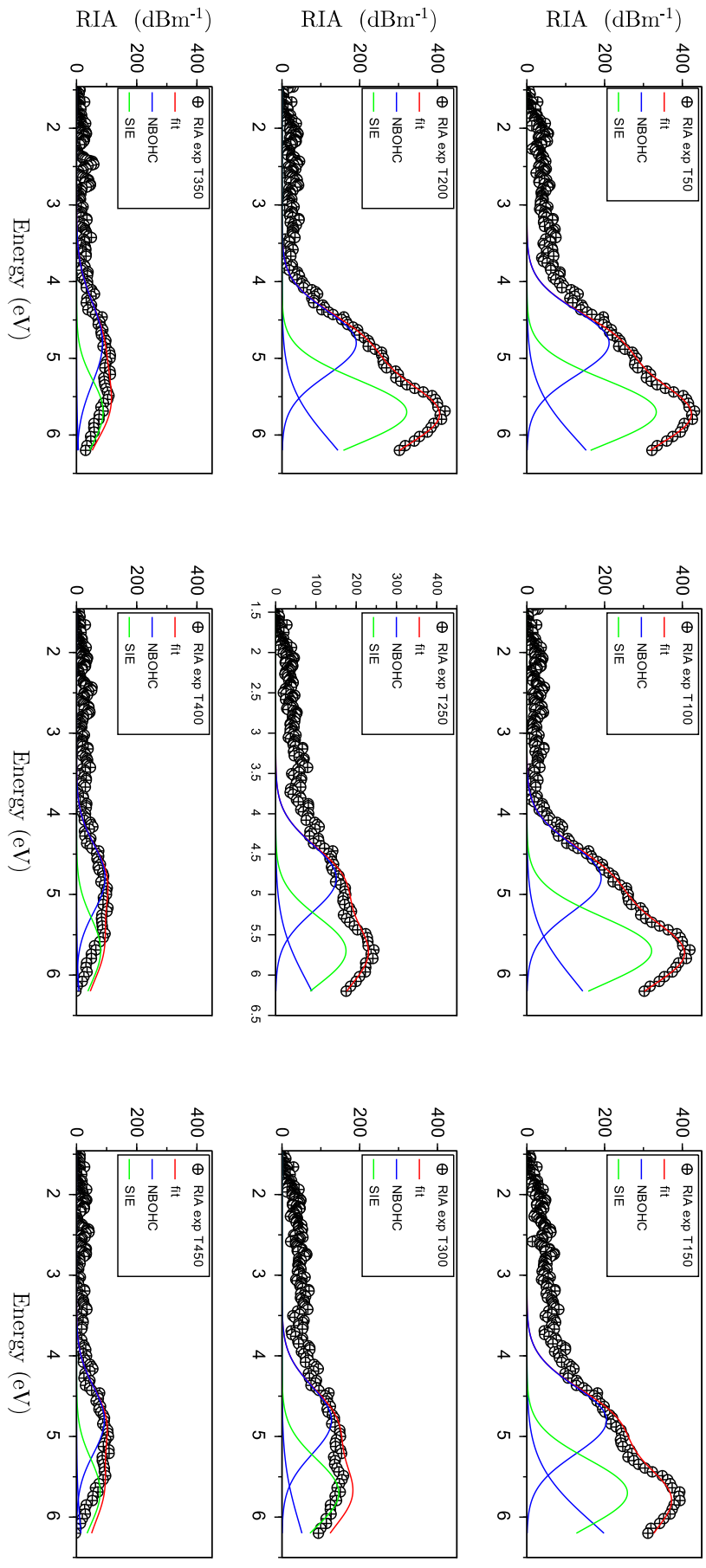


**Figure 3.11:** Experimental RIA recorded during the thermal annealing protocol with the gaussian fit at each heating step (various $T_{stop}$ values).

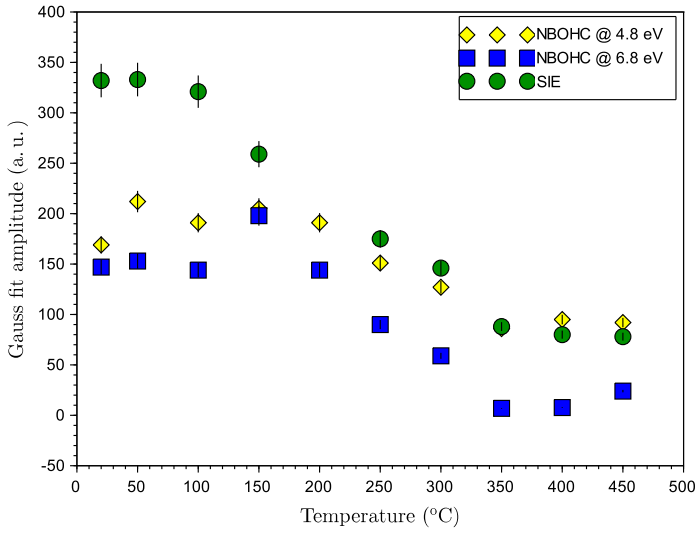


**(a)**

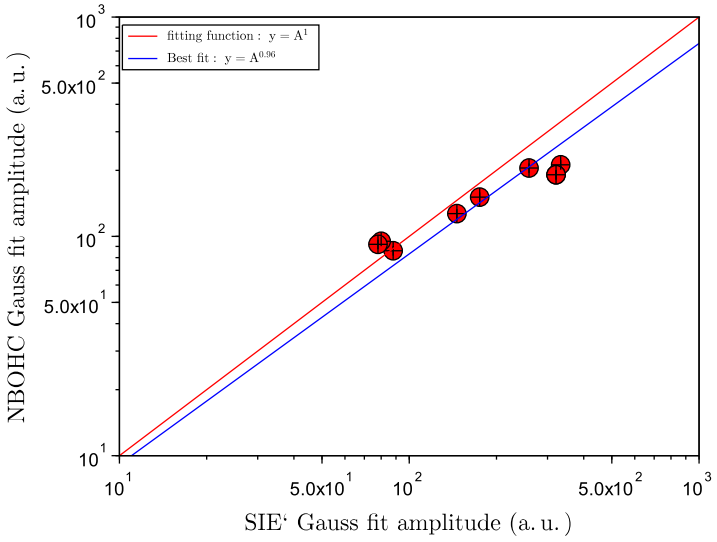


**(b)**

**Figure 3.12:** a) Amplitude of the NBOHC and SiE′ Gauss bands fit reported in fig.3.10 and 3.11 as a function of the temperature. b) Amplitude of the NBOHC centers (at 4.8 eV) against the amplitude of the SiE′ center (at 5.8 eV).

The TL spectrum of the pure silica sample (fig.3.5) indicates that the TL emission mainly takes place around 2.7 eV. This well-known emission is characteristic of oxygen deficient centers (ODC) [32, 73, 175]. This TL emission confirms that such SiODCs are clearly reformed in excited state by recombination during the thermal annealing process that accompanies the TL readout. Both two structural models of SiODC centers can trap a hole to give a SiE′ center [32]:

$$h^+ + SiODC \mapsto SiE' \tag{3.2}$$

SiE′ are clearly formed during the irradiation as proved by the RIA spectra (fig.3.6 and fig.3.10).

We argued, based on strong evidence [77, 175], that such $SiODC : e^-$ centers act as the recombination centers in the TL process. During this process, the reformation of SiODC occurs as a result of de-trapping of holes that subsequently recombine at $SiODC : e^-$ centres.

From the bleaching map, we can say that the reservoir of holes released during the TL readout is given by the intrinsic levels and the SiE′ centers. The TL curve superimposed to the bleaching map in fig.3.9, shows that the rising front of the TL correlate with bleaching between $50^oC$ and $100^oC$. The TL feature in this temperature range is probably due to the release of holes from some intrinsic trapping levels.

Between $50^oC$ and $100^oC$ is observed a small bleaching of the SiE′ centers which annealing involves the release of holes may contribute to the TL process right before the peak. Once the intrinsic levels are emptied, the TL curve reaches a maximum, which in our case is located at around $160^oC$, which means the most massive re-formation of SiODC centers.

Right after the peak, at temperature greater than 200°C, starts the strongest annealing of SiE′ centers, which continues with a slow decay up to 400°C. This regime corresponds to the release of holes from SiE′ [77]. This annealing roughly parallels the TL shoulder, showing that SiE′ are the main hole providers in this region.

To summarize the process at play, a schematic diagram is proposed in fig.3.13.

Under irradiation SiE′ and NBOHC are formed in pairs by radiolysis:

$$\equiv Si - O - Si \equiv \mapsto NBOHC + SiE' \tag{3.3}$$

SiE′ centers are also produced by the capture of holes at SiODC:

$$h^+ + SiODC \mapsto SiE' \tag{3.4}$$

$SiODC : e^-$ are formed by the capture of electrons at the same neutral center:

$$SiODC + e^- \mapsto SiODC : e^- \tag{3.5}$$

Holes generated in the valence band (VB) can be captured to form hole trapped centers (with the hole traps concentration $H_k$, the density of trapped holes $h_k$ and the hole trapping coefficient $\beta_k$) such as SiE′ and NBOHC centers. They can also recombined at RC consisting of electrons trapped into the form of SiODC:e-, which

electron traps concentration and the density of trapped electrons are referred respectively as $N_{RC}$ and $n_{RC}$. This recombination process can be written as:

$$SiODC : e^- + h^+ \mapsto SiODC + hv_{2.7eV} \tag{3.6}$$

Electrons generated in the conduction band (CB) can be trapped by a set of intrinsic trapping levels (not shown in the figure to streamline the description) or be captured at SiODCs. Holes can be released from some intrinsic unstable levels (bandtails) and from deeper SiE′ centers.

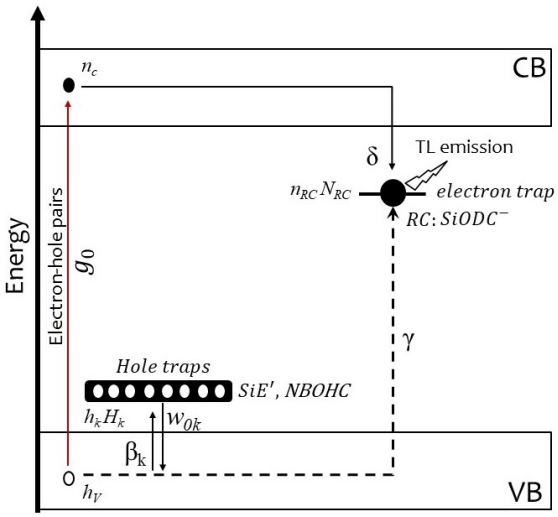


**Figure 3.13:** Diagram of recombination processes in silica samples.

## 3.2 Radiation sensitive fiber preforms

The doping of optical fibers with aluminum or phosphorous enhances their sensitivity to radiation. For this reason, Al- and P- doped OFs are widely used as sensors or dosimeter materials [82, 83]. In this section we report the experimental results of P-doped (L27, L28) and Al-doped (K04, K05) samples.

### 3.2.1 P-doped samples (L27, L28)

**Thermoluminescence** The TL curve on P-doped samples with more (L28) or less (L27) content of phosphorous are reported in fig.3.14. The shape is the same except (especially in intensity) for the shoulder at higher temperature, that is more evident in L28, apparently as a results of its higher P content. The curves are characterized by a main peak at around 80°C, similar to the one previously observed in a pure silica sample.

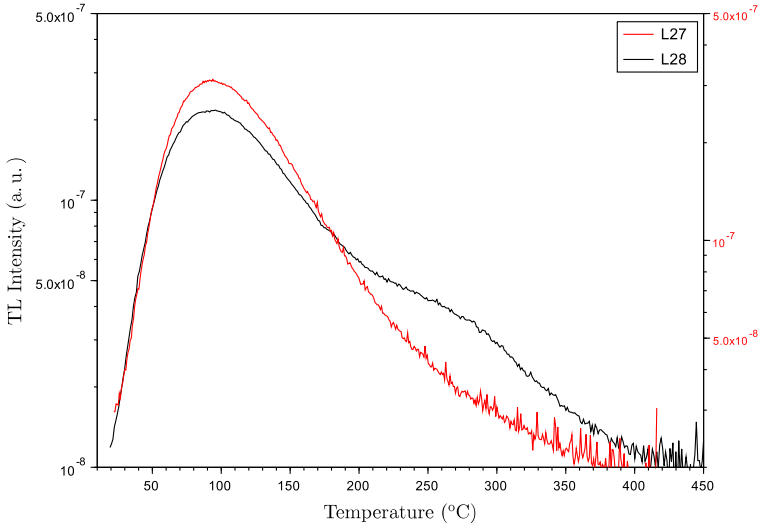


**Figure 3.14:** TL at 1°C/s on L27 (0.6 *at*.%P) and L28 (4 *at*.%P) P-doped silica samples.

The typical TL spectrum is shown in fig. 3.15. The TL intensity is here plotted at the maximum intensity frame ($\sim$ 100°C), but it keeps the same components through the temperature range covered by the TL readout. A gaussian fitting reported as a red line in fig.3.15 reveals a single band located at 2.7 eV with a FWHM of 0.5 eV. This energy, as already seen for pure silica, is associated to the SiODC center [32].This similarity indicates that radiation-induced P-related defects do not act as recombination centers in the TL scheme but rather as "traps", i.e. as trapped carriers states that are primarily annealed by detrapping between RT and 450 °C.

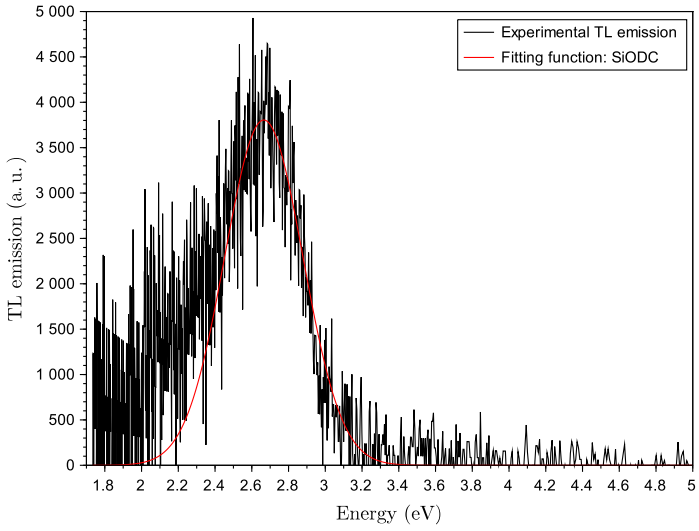


**Figure 3.15:** TL emission of P-doped silica sample (L28) and its fitting with a Gaussian band.

The dependence of the TL glow curves on the heating rate shows the same features as those encountered in pure silica. As fig.3.16 shows, whatever the P content is, the TL intensity decreases with the increasing of the heating rate and the peak is shifted towards higher temperatures.

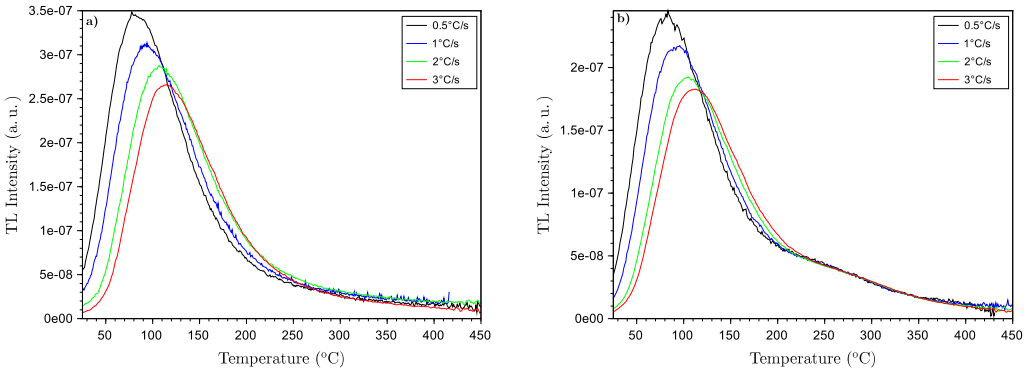


**Figure 3.16:** TL curves obtained at four heating rates after irradiation at a dose of 3kGy on the P-doped silica samples L27 (0.6 $at.\%P$) (a) and L28 (4 $at.\%P$) (b).

The dependence of the TL on the absorbed dose for L27 and L28 samples is shown in fig.3.17 (a)L27, b)L28) and 3.18, where one can observe the increase of the TL intensity with the dose and the corresponding areas, respectively. The TL response is found to increase according to a power-law ($kD^{\alpha}$) with an exponent of 0.55 for L27 and 0.65 for L28. The small difference of their slopes does not deal to the presence of the shoulder in the TL of L28, since we obtain the same slopes plotting the maximum TL intensity as a function of the dose, instead of the TL area.

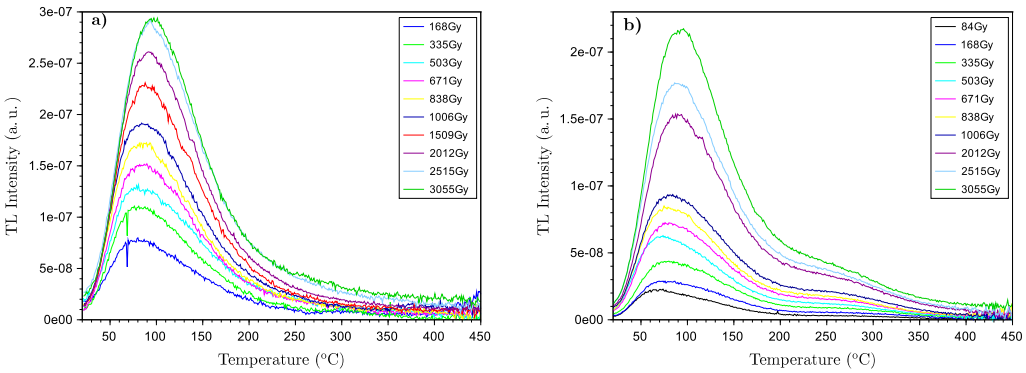


**Figure 3.17:** TL curves recorded at 1°C/s at different doses on P-doped silica samples L27 (a) and L28 (b).

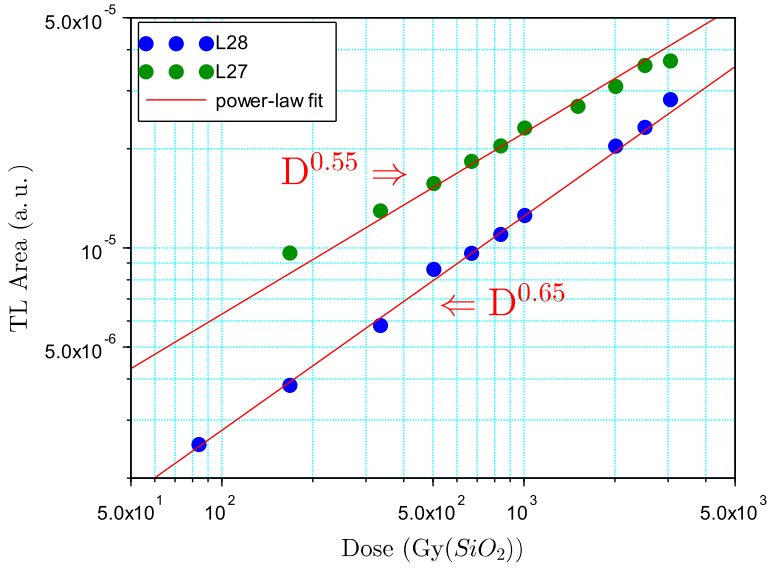


**Figure 3.18:** TL areas as a function of the dose, on P-doped silica samples L27 and L28.

The initial rise method was impossible to perform because of a too low TL intensity. As made for pure silica we give an estimation of the mean activation energy by the TL glow curves obtained changing the heating rate shown in fig.3.16 for L28 sample. From a linear fit made on data in fig.3.19, we estimate a mean activation energy of 0.66 eV.

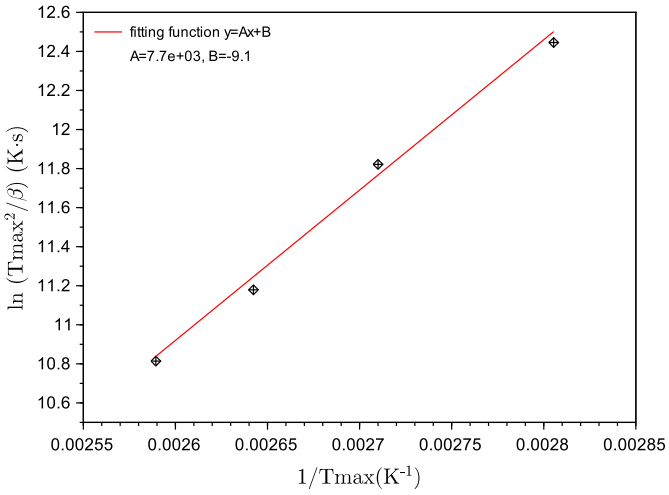


**Figure 3.19:** $\ln T_{max}^2/\beta$ as a function of $1/T_{max}$ in order to estimate the energy depth of the peak and its linear fit, which slope is $7.7 \cdot 10^3$ $E/k$.

**Optical absorption** Fig.3.20a presents the optical absorption recorded on L28 before and after irradiation, at a dose of ∼1 kGy. The spectra, ranging from the UV-Visible to NIR, give the RIA according to eq.(63), which is shown in the inset. The near-infrared part of the spectrum does not show any induced band, but all the P related defect bands are recognizable in the UV-visible part [84]. The RIA was recorded at 6 kGy on the sample (L28) in the UV-visible range to obtain a higher RIA. The RIA spectrum with Gaussian fit is shown in fig.3.20b.

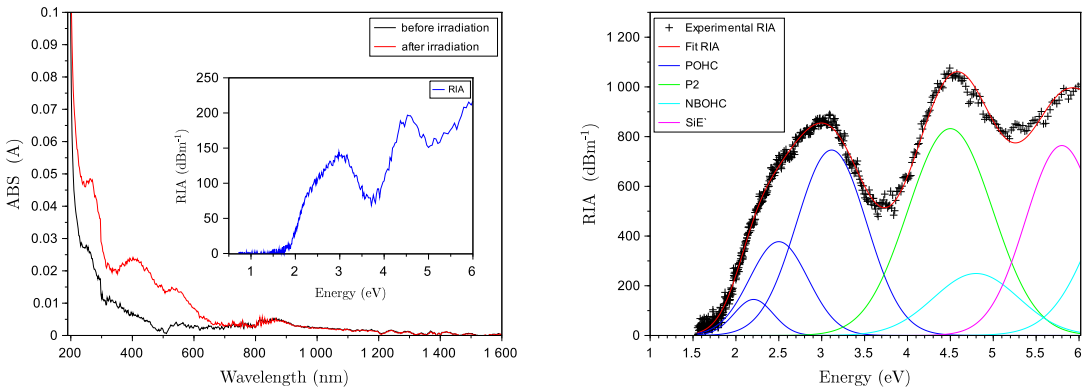


**(a)** **(b)**

**Figure 3.20:** a) Absorption and RIA (inset) at 1 kGy from NIR to UV-visible on P-doped silica sample L28 (4 $at.\%P$). b) RIA on L28 after irradiation at a dose of 6 kGy with Gaussian fit.

The obtained bands are summarized in table 3.1. One can see that in addition to

SiE' and NBOHC centers already obtained on pure silica, we obtain some P-related defects like POHC, POHCm and P2 [84].
The RIA obtained on L27 sample is much less important compared to the one obtained for L28 sample in the same conditions (approximately 10 times smaller). Because of both the noise and low RIA level, it turns out to be very hard to decompose it in gaussian bands.

| Defect | $x_c$(eV) | FWHM (eV) |
|---|---|---|
| POHC | 2.2; 2.5 | 0.5; 0.8 |
| POHCm | 3.1 | 1.0 |
| P2 | 4.5 | 1.1 |
| NBOHC | 4.8; 6.8 | 1.2; 1.3 |
| SiE' | 5.8 | 1.0 |

**Table 3.1:** Gauss fit parameters

The RIA on L28 sample was also recorded changing the irradiation dose at a fixed dose rate of 200 Gy($SiO_2$)/min, in the NIR and in the UV-visible. As seen in fig. 3.20a, the RIA recorded the NIR part of the spectrum is flat compared with the visible one and can be considered as a tail of the RIA bands from the visible. Furthermore, the RIA intensity recorded at several doses do not increase and it remains more or less in the same noisy level. For this reason we do not think it is interesting to show the dose dependence results recorded in this part of the spectrum.
Fig.3.21 shows the RIA variation in the UV-visible part of the spectrum with the irradiation dose. RIA measurements at the same dose and changing the dose rate were also performed. But no dose rate effects were observed.

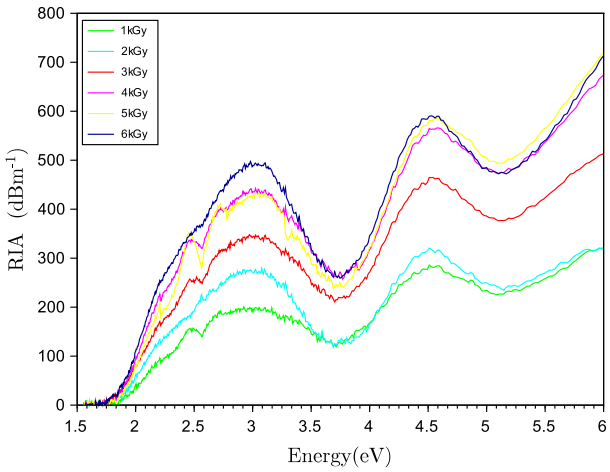


**Figure 3.21:** RIA at several doses on L28 sample.

Fig.3.22 shows the thermal annealing (protocol described in appendix 4.3.4) on L28 from RT to 500°C after an irradiation at about 5 kGy. In figure are reported the RIA spectra recorded after irradiation at RT (black line) and after every $T_{stop}$ annealing up to 500 °C.

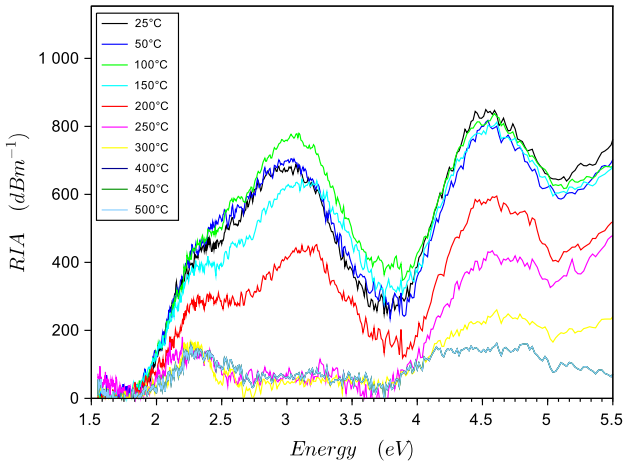


**Figure 3.22:** Thermal annealing on P-doped silica sample (L28) after irradiation of a dose of 5 kGy reported as RIA spectra.

The corresponding bleaching map is shown in fig.3.23. To guide the eye, we also presented in the figure the TL curve recorded at the same heating rate (black line) and the energy positions of the color centers found (red lines). The main bleaching occurs between 150 °C and 300 °C. 40% of the RIA induced at 3.5-4 eV is bleached between 200 and 250 °C. This spot is probably due to the linking point between the POHC and P2 bands. This shape, when is calculated the intensity plotted in the map, brings to a high value of the bleach intensity. One can observe that at 2.2 eV and 2.5 eV, about 20-25% are bleached between 200 and 250 °C. The SiE' (5.8 eV) and P2 (4.5 eV) centers are mainly bleached between 200 and 300 °C.

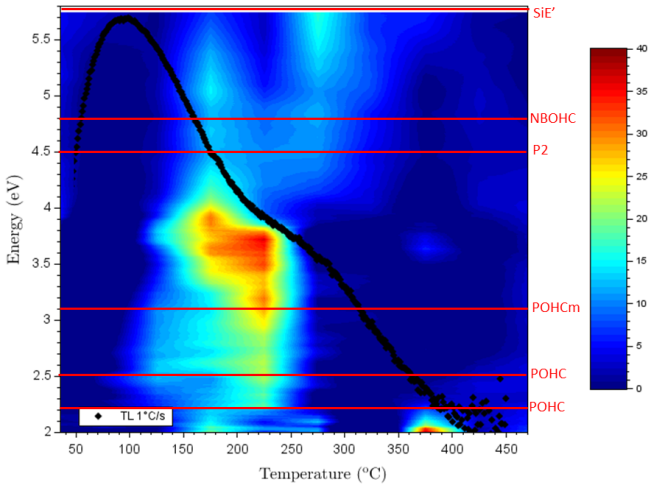


**Figure 3.23:** Thermal annealing on P-doped silica sample (L28) after irradiation of a dose of 5 kGy reported as bleaching map. The black line superimposed on the bleaching map represents the TL glow curve recorded at the same heating rate (1 °C/s).

The TL spectrum of P-doped silica sample (fig.3.15) indicates that the TL emission

mainly takes place around 2.7 eV, so as said for pure silica, the TL emission confirms that such ODCs are clearly reformed in excited state by recombination during the thermal annealing process that accompanies the TL readout. Following this parallelism with pure silica, one can conclude again that the reformation of ODC during TL could be the result of the recombination of thermally-released holes at such trapped-hole centers. The main TL emission mechanisms are the same of the one reported for pure silica, summarizing again here we have free holes ($h^+$) that recombine at $SiODC : e^-$ centers (see fig.3.24):

$$SiODC : e^- + h^+ \mapsto SiODC + h\nu_{2.7eV} \tag{3.7}$$

Watching the bleaching map in fig.3.23, one can see that at the temperature corresponding to the main TL peak there is no bleach of defects. As said for pure silica, it is probable that the holes released that recombine with $SiODC : e^-$ come from intrinsic levels. When this reserve is exhausted we observe the descending part of the TL peak. Then between $200^oC$ and $250^oC$ we observe the bleaching of POHC and SiE', this last center keeps annealing up to $300^oC$. The annealing of SiE' in this temperature range, means a release of holes that could be one of the main source of holes responsible of the shoulder of the TL curve between 200 and 300°C.
Also, we argued above, from the TL spectrum (fig.3.15), that all radiation-induced trapped-hole P-related centers should act as TL traps and not as recombination centers. The annealing of POHC centers, found to take place between ∼200 and 250°C in fig.3.23, is therefore most probably due to release of their holes that subsequently recombine at $SiODC : e^-$ centers to contribute to the TL curve between ∼200 and 250°C. This region is precisely the one where a shoulder appears in TL curves at the higher P concentration (L28).

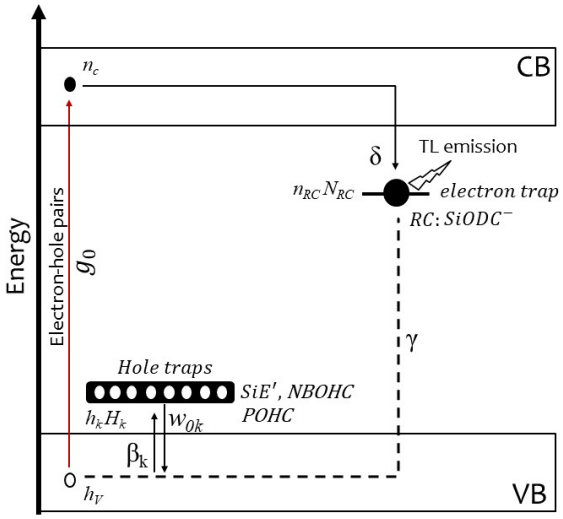


**Figure 3.24:** Schematic diagram on the recombination processes in P doped silica sample.

### 3.2.2 Al-doped samples (K04, K05)

**Thermoluminescence** TL glow curve of Al-doped silica sample (K04) is presented in Fig3.25. The glow curve recorded at $1^oC/s$, measured with the PMT, is characterized by a main peak at around $70^oC$ with a shoulder between 200 and $350^oC$, highlighted by the semi-logarithmic representation in the inset.

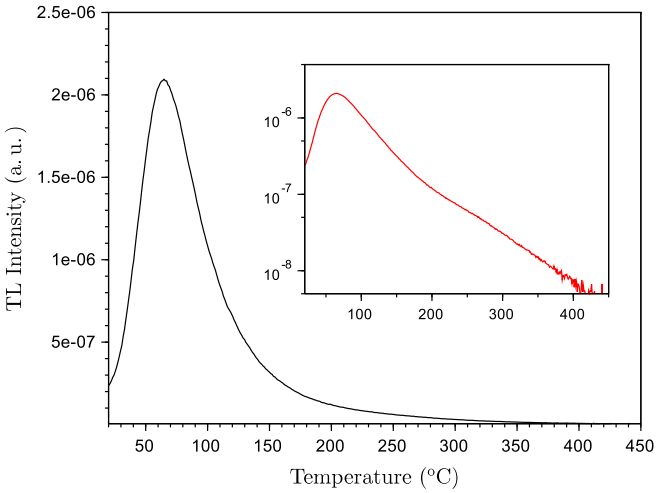


**Figure 3.25:** TL glow curve on Al-doped silica sample (K04, 1.97 *at*.%Al) measured at $1^oC/s$.

Fig.3.26 represents the spectral analysis of the TL in the same measurement conditions. The emission map in fig.3.26a is a 3D plot of the TL intensity as a function of the optical energy and the temperature. The main emission is located around 50-100°C between 300-500 nm (4.1-2.5 eV). The TL emission reported in fig.3.26b is the spectrum corresponding to the peak emission at 70 $^oC$.
A tentative fit reveals two emission bands: one is around 2.7 eV, already seen in pure silica and in all doped silica preform, related to SiODC (revealing the reformation of this center during thermal annealing) and a more intense one peaking around 3 eV related to the presence of aluminum. Since these various emission bands parallel each other along the TL process, they all result from the recombination of the same type of carriers. Mady *et al.* [77] showing the same TL features, proposed a recombination mechanism where the reformation of this Al-related center, assigned as a Aluminum oxygen deficiency (Al-ODC), is due to the recombination of holes with AlE' ($e^-$ trapped at Al-related oxygen deficient centers, Al-ODC) [77]. In fact, if one supposes that the recombination involves holes, so that Al-induced recombination centers should be trapped-electron centers, the only trapped electron defect related to aluminum is the AlE'. Thus, the recombination of holes with AlE' would reform Al-ODC and the main TL band peaking at 2.9-3 eV can be assigned to these centers [77].

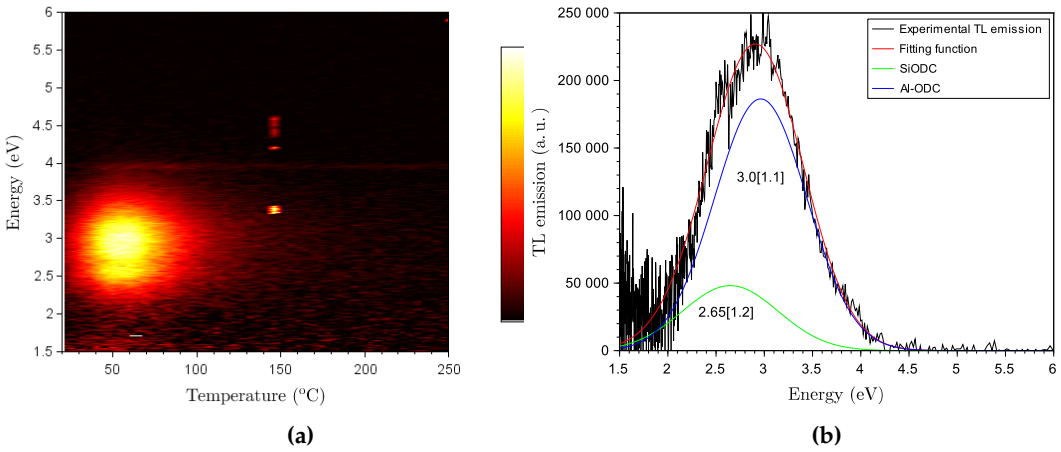


**Figure 3.26:** Spectral analysis of the TL emission from the K04 sample at a dose of 1 kGy. (a) TL map; (b) TL spectrum at 70°C with Gaussian band decomposition. The Gaussian bands are located at 2.65 (SiODC) and 3.0 eV (Al-ODC) with a FWHM of 1.2 and 1.1 eV respectively.

The TL glow curves at different heating rates reported in fig.3.27 show the same characteristic already seen in pure silica and P-doped one. The decrease of the TL intensity with the increasing heating rates is naturally followed by the decreasing of the TL areas, highlighted by the red points.

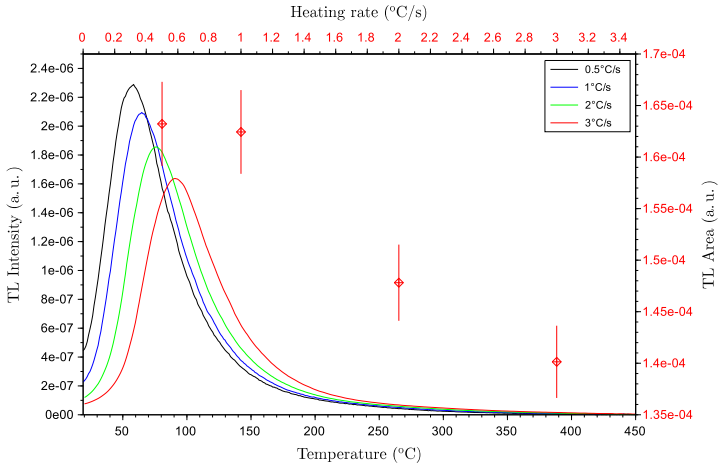


**Figure 3.27:** TL glow curves on K04 sample at four heating rates after irradiation of a dose of 3 kGy. The integrated area of each TL is plotted as a function of the heating rate (red scattered line).

The dependence of the TL on the dose is illustrated in fig.3.28. In fig.3.28a one can observe the increase of the TL glow peak with the dose. The area of these curves are then plotted against the dose in fig.3.28b in a log/log representation, revealing a power-law in $D^{0.7}$ behavior.
The initial rise measurements reported in fig.3.29 shows an energy depth distribution between 0.6 and 0.8 eV.

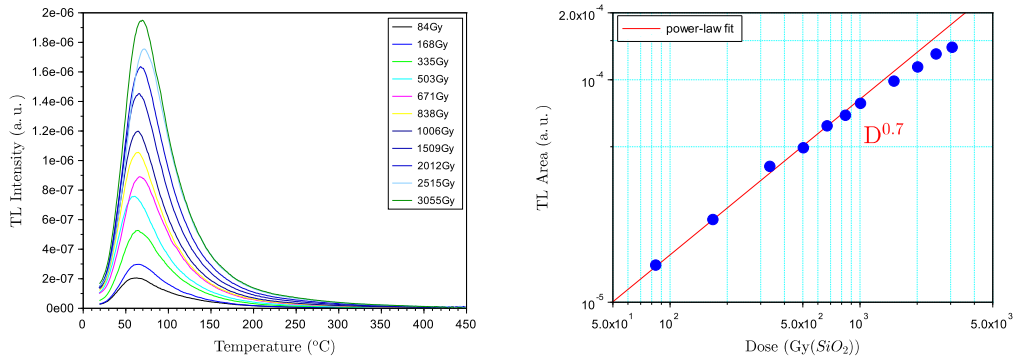


**Figure 3.28:** a) TL on K04 sample at different doses. b) Area TL on K04 sample as a function of the dose.

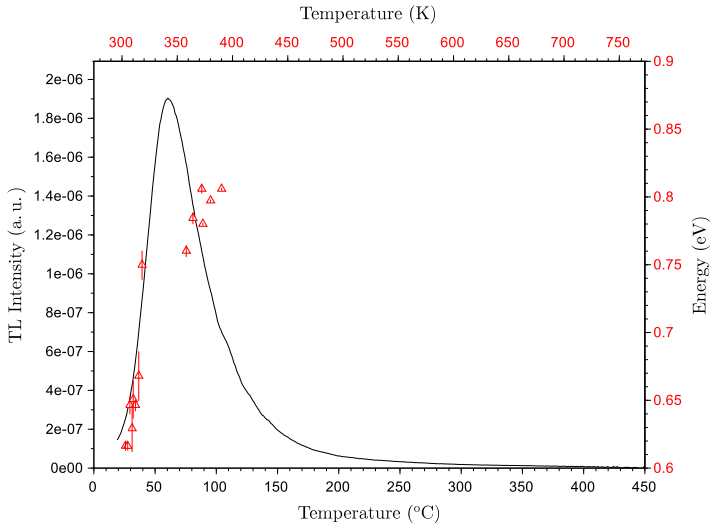


**Figure 3.29:** Estimation by initial rise method of the distribution of the trapping depths in Al-doped silica sample (K05, 0.53 *at*.%Al).

**Optical absorption** The RIA of the Al-doped sample (K04) is presented in Fig. 3.30. A gaussian fit attempt is proposed, which parameters are reported in table 3.2. This decomposition includes silica related centers such as SiE' and NBOHC [32], and Al-related defects like the Al-Oxygen Hole Center (AlOHC) and the AlE' center [59]. AlOHC is characterized by OA bands at 2.3 and 3.2 eV whereas an OA band at 4.1 eV is assigned to AlE' centers [59]. The fitting procedure was initiated in accordance with values found in [59] for the AlOHC and AlE' centers, and to [34] for NBOHC, where Skuja found a semi-continuous spectrum of NBOHC from 4 to 7.8 eV that cannot be represented by a pair of distinct Gaussian bands but can be described by several gauss bands. An additional band is required around 2.7 eV, between the 2.3 and 3.2 eV ones [77]. As one can see from the RIA intensity,

the presence of Al enhances the RIA and the main contribution in the UV-visible is due to the Al related absorption bands (we found a maximum of ∼100 dB/m for pure silica sample L02 irradiated at 10 kGy in fig.3.6 and ∼750 dB/m at 3 kGy here for K04 sample).

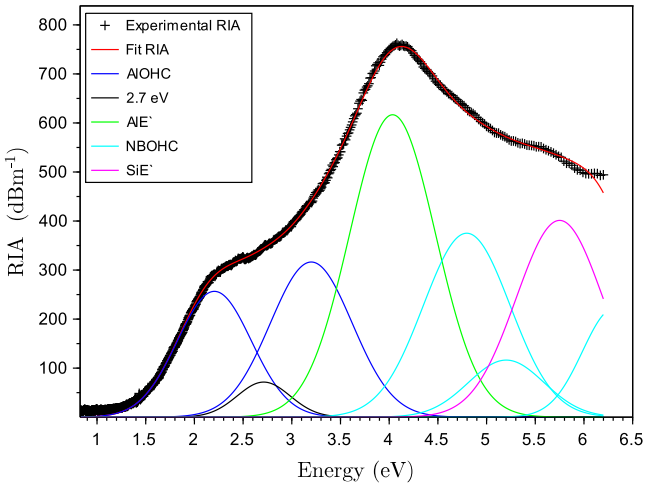


**Figure 3.30:** RIA of Al-doped silica sample K04 after irradiation at a dose of 3 kGy. The optical band properties related to NBOHC defects are based on [34].

| Defect | $x_c$(eV) | FWHM (eV) |
|---|---|---|
| AlOHC | 2.2 | 0.9 |
| | 3.2 | 1.0 |
| 2.7 band | 2.7 | 0.65 |
| AlE′ | 4.1 | 1.0 |
| NBOHC | 4.8 | 1.01 |
| | 5.47 | 0.9 |
| | 6.09 | 0.8 |
| SiE′ | 5.76 | 1.0 |

**Table 3.2:** Parameters of Gassian fit reported in fig.3.30.

Fig.3.31 illustrates the increase of the induced absorption with the dose, between 1 and 10 kGy. The absorption spectra shows an increasing of the absorption with the increasing of the dose, at least taking into account the repeatability error. We also performed measurements between 800 and 1600 nm, but the spectra in this region are just a tail of the absorption of the visible range. It is worth to note that to investigate the low RIA levels characterizing the NIR range using thin preform samples is hard and we cannot have accurate measurements in this region. To investigate this part of the spectrum it is preferable to integrate on long distances, i.e. to use fibers instead of preform slices [66, 176].

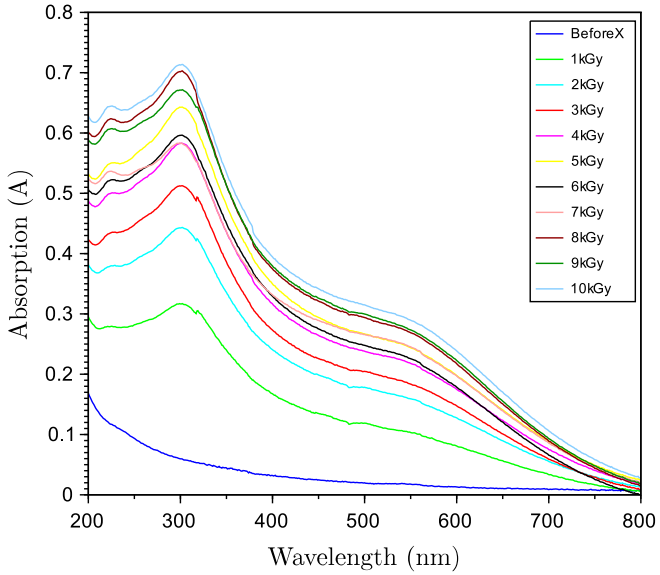


**Figure 3.31:** Absorption spectra in at several doses from 1 to 10 kGy.

To study the RIA kinetics we shown in fig.3.32 the RIA intensity at the energies of interest as a function of the irradiation dose in a logarithmic representation. Again, one can observe a power-law behavior up to the maximum dose used. In the explored range, all the bands increase as $D^{0.57}$.

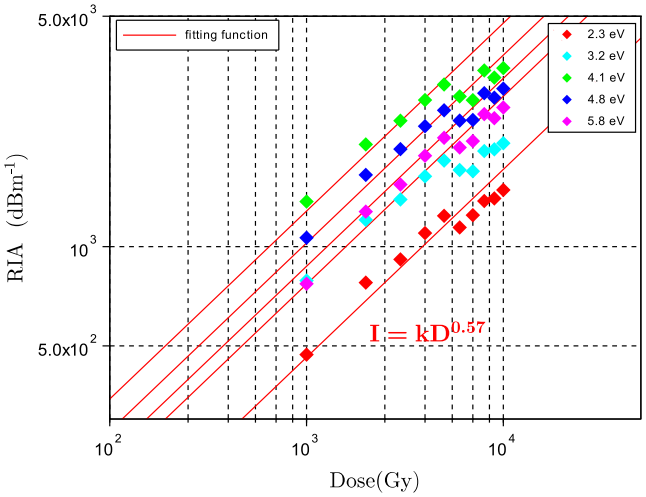


**Figure 3.32:** RIA Intensity at several doses from 1 to 10 kGy.

The results of the thermal annealing protocol conducted on the Al-doped silica sample are reported on the Fig. 3.33 and 3.34, according to the procedure exposed at the beginning of this chapter. The RIA spectra in fig.3.33 decrease progressively as the $T_{stop}$ temperature is increased reaching an almost total annealing at $T_{stop}$ = 450 °C.

Fig.3.34 represents the bleaching map built according to these RIA spectra, where

the RIA bleaching can be directly correlated with the superimposed TL curve (black line), the red lines mark the centers of the OA bands used in the Gaussian decomposition of Fig.3.30 and table 3.2.

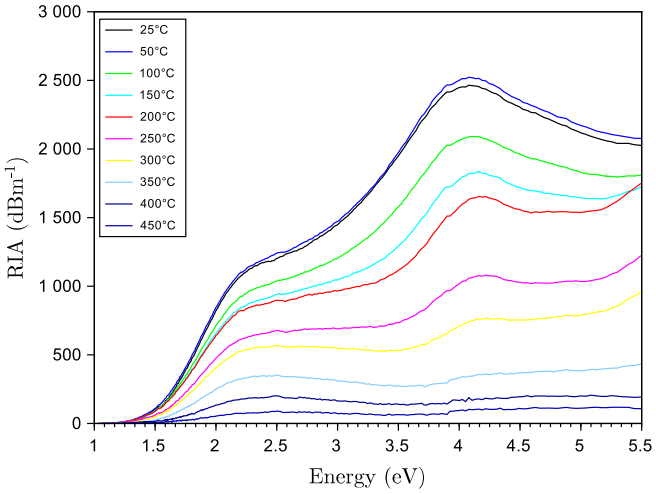


**Figure 3.33:** Thermal annealing on Al-doped silica sample (K04) after irradiation of a dose of 10 kGy at different $T_{stop}$.

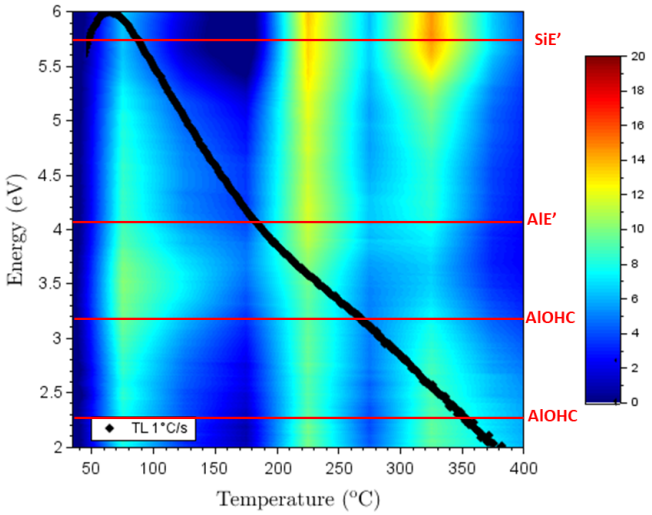


**Figure 3.34:** Thermal annealing on Al-doped silica sample (K04) after irradiation of a dose of 10 kGy reported as bleaching map. The black line superimposed on the bleaching map represents the TL glow curve measured after identical irradiation at the same heating rate.

A detailed description of the mechanisms at play along the temperature range concerning the alumino-silicate fibers is given in [77]. In this work similar results were obtained and thus the mechanisms proposed by Mady *et al.* are confirmed.
The TL curve, resulting from the recombination of AlODC, parallels the annealing of AlE' centers. From fig.3.34, one can see that the AlE' annealing is observed:

**I** within the main TL peak (50-100°C);

where it is accompanied by the partial annealing of AlOHC ($\sim$ 10% of the RIA);

**II** concurrently the TL shoulder (200-250 °C);

temperature range at which it is observed a strong annealing of SiE' ($\sim$ 20% of the RIA);

**III** concurrently the TL tail (300-350 °C);

where it is accompanied by the annealing of SiE' and AlOHC.

First of all, the annealing of AlE' concurrently with the TL, well supports the hypothesis that the TL process involves the recombination at AlE' centers that disappear while producing TL. As proposed by Mady *et al.* [77], the AlE' centers are destroyed as a result of the recombination of holes released during the annealing at AlE' sites (=$AlODC : e^-$).
Regarding the temperature range in the point **I** (main peak 50-100 °C), the TL is probably a results of the recombination with holes released from shallow intrinsic levels. In this temperature range, holes could be also released from AlOHC, which are partially bleached. But since these centers correspond to deeper trapped states and they are still stable up to 300°C, when occurs their annealing; it is more likely that holes are released from shallow intrinsic levels in the shoulder to the top of the main TL peak. This hypothesis is supported by the same results obtained for pure and P-doped silica samples. The rising front of the TL, located in the same temperature range in such kind of silica, is probably due to the same mechanisms, involving the releasing of holes from intrinsic levels.
Regarding the point **II**, it is probably that in this range of temperature (200-250°C) the TL shoulder (which is more important in Al-doped sample respect to pure silica thanks to the larger amount of traps) is given by holes de-trapped from SiE'.
Finally (point **III**), with the annealing of AlOHC and SiE', the holes released from such centers probably contribute to the noise-level tail of TL, since the reservoir of AlE' has been exhausted below 350 °C(see fig.3.34).
From the RIA measurements is observed a creation of Al-related point defects such as AlE' and AlOHC and clearly also SiE' and NBOHC. The TL measurements involving the emission of at the energies 2.7 and 3 eV, bringing to the conclusion that oxygen deficiency centers were reformed during the TL readout. Thanks to the thermal annealing protocol one can conclude, supporting the thesis reported in [77] that the TL is due to the recombination of holes at AlE' centers giving rise to the formation of Al-related oxygen vacancy (the so-called AlODC) and more marginally at $SiODC : e^-$ centers and that the releasing of holes come from intrinsic levels (at the TL peak, near 50-100$^oC$) and from SiE' center. The TL recombination process can be summarized by (3.9)-(3.8) and by fig.3.35.

$$AlE' + h^+ \mapsto AlODC + h\nu_{2.9-3eV} \tag{3.8}$$

$$SiODC : e^- + h^+ \mapsto SiODC + h\nu_{2.7eV} \tag{3.9}$$

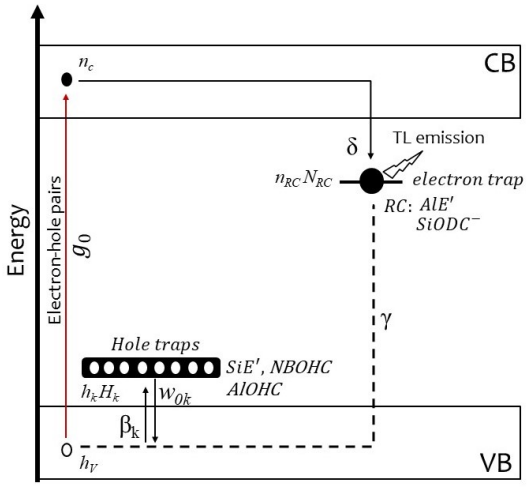


**Figure 3.35:** Energy level scheme proposed for Al-doped silica.

## 3.3 Effect of the radiation temperature on the RIA of sensitive Al and P- doped silica

This section reports on the annealing process of irradiated preforms by $\gamma$ radiation at several irradiation temperatures. This study aims to show:

1 the impact on the RIA intensity and on the annealing using a different type of radiation that allows to reach a very high irradiation dose (1 MGy).

2 how the thermal annealing response changes with an irradiation performed at temperatures differing from RT.

Using both the TL and RIA results we tried to design some bleaching behaviors on the defects created under irradiation in Al- and P- doped silica preforms.
As we shown above, the RIA obtained in Al-doped silica sample shows the presence of two OA bands located at $\sim$ 2.2 eV and 3.2 eV (Fig.3.30 and table 3.2). We assigned both bands to the AlOHC center, since the relation between the AlOHC and the 2.3 eV OA band is well supported by various investigations [59, 73]. The second one (3.2 eV) still remains to be confirmed. In opposition to the works that finds a correlation between these two bands assigning them to the same defect [59], some investigations [73] found the presence of the 2.3 eV OA band in the RIA spectrum whereas the 3.2 eV seems absent [46]. This work also investigates if this band correlates to the one at 3.2 eV, trying to affirm whether it is related to AlOHC or not.
Concerning P-doped samples, we saw that in the visible-NIR range, the induced losses are mainly caused by the OA bands of the POHC and P2 (Fig.3.20b and table 3.1)[84]. The POHC defect well described in [84], present both a stable and a metastable form at RT. It will be shown that they anneal in different way changing the irradiation temperature.
The samples are in the form of slices of about 1.5 mm thickness and 1 cm in total diameter. They were irradiated with $\gamma$-rays at IRMA facility (Saclay) (see sec. 2.6.3).

The dose used is 1 MGy with a dose rate of 50.3 Gy/min, at several temperatures: room temperature (RT $\sim$ 25$^oC$), 50$^oC$, 90$^oC$ and 250$^oC$. In table 3.3 are reported the nicknames and the irradiation temperatures of the samples. We performed a thermal annealing experiment for each sample from RT to 500$^oC$ in the same day for each type of preform. The measurements were made 26 days after the end of the irradiation.

| Al-doped | P-doped | irradiation Temperature |
|---|---|---|
| *Al*_25 | *P*_25 | 25°C |
| *Al*_50 | *P*_50 | 50°C |
| *Al*_90 | *P*_90 | 90°C |
| *Al*_250 | *P*_250 | 250°C |

**Table 3.3:** Names of the samples used in the present study.

**Al-doped sample** The RIA of *Al*_25 after exposure to $\gamma$ radiation at 1MGy and the fit obtained by gaussian decomposition are shown in fig.3.36. This decomposition shows again the presence of AlOHC (band peaked at 2.3 eV [1.6] and 3.2 eV [1.1]), AlE' (4.1 eV [1.0]), NBOHC (4.8 eV [1.05], 6.7 eV [2.0]) and SiE' (5.75 eV [0.8]), where the values in bracket are the FWHM expressed in eV. The peak assignment to color centers is proposed according to [32, 46, 59, 73, 177]. The RIA intensity in the UV-visible reaches 6000 dB/m.

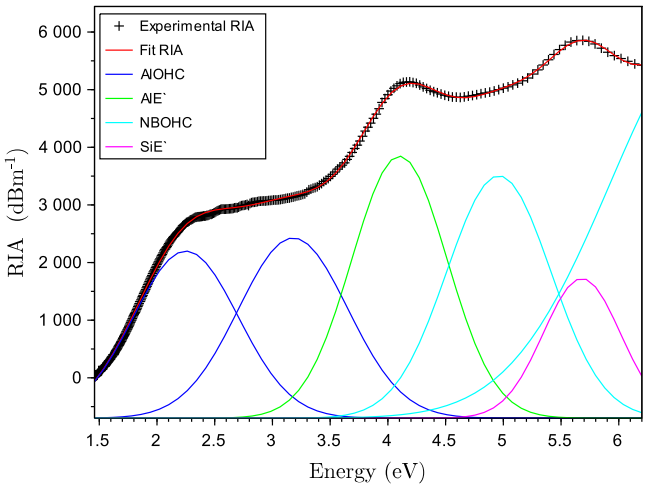


**Figure 3.36:** RIA on *Al*_25 sample after an irradiation dose of 1MGy at 25°C (RT) recorded after 14 days from the irradiation, and its decomposition by gaussian bands.

We report in fig.3.37 the RIA spectra for each sample at the different temperatures $T_{stop}$ of the thermal annealing protocol (see appendix 4.3.4) conducted after irradiation. The RIA intensity reaches the greatest value of 6000 dB/m for the *Al*_25 sample, whereas it does not exceed 2000 dB/m in Al_250. This is significant because the temperature at which the sample is irradiated affects the RIA response a

higher irradiation temperature leading to a lower RIA. As one can see for all the conditions reported this figure, the annealing is complete at $400^oC$. The main gap in RIA intensity is between $150^oC$ and $200^oC$, while up to $100^oC$ the RIA curves are within the experimental error.

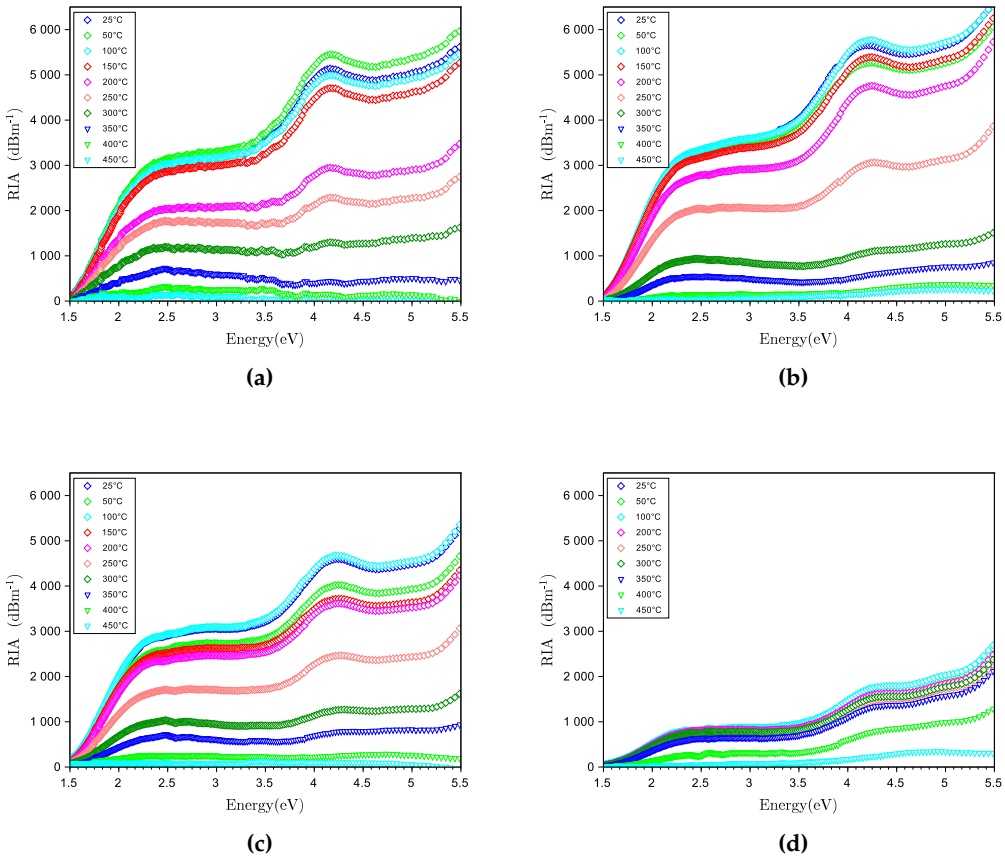


**Figure 3.37:** Thermal annealing of the RIA on (a)*Al*_25, (b)*Al*_50, (c)*Al*_90, (d)*Al*_250.

We carried out the fit of all these RIA spectra by means of the different characteristic bands by keeping fixed the energy ($x_c$) of these bands and their FWHM (values reported above for the fit at RT of fig.3.36). Only the amplitude was allowed to vary.
In figure 3.38 are reported the ratio of the areas of the gaussian bands at 2.3 eV and 3.2 eV as function of $T_{stop}$ at which the heating was stopped during the annealing). The error bars reported represent the 10% of the area ratio (appendix 4.3.4). As one can see the ratio of the areas oscillates during the thermal treatment between 0.9 and 1.4, result that makes them quite constant. The results at higher temperatures (400-450°C ) are not reported due to the degree of difficulty of a fit on such annealed RIA.

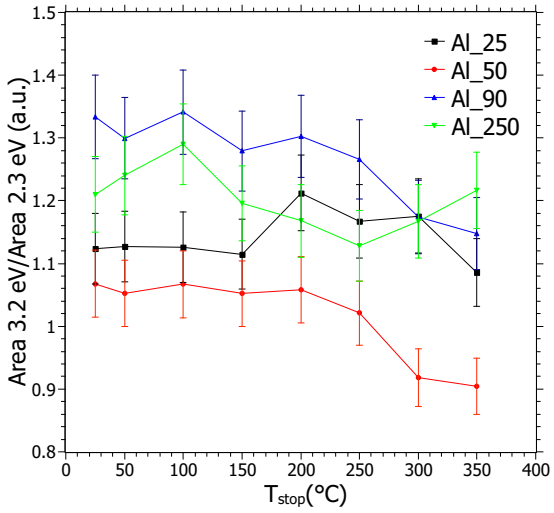


**Figure 3.38:** Ratio of the gaussian peak fit areas of 2.3 eV and 3.2 eV bands as a function of temperature stop during thermal annealing.

From the same fitting parameters is obtained another representation in fig3.39, reporting the area of the gaussian band at 3.2 eV as function of that at 2.3 eV in logarithmic representation. In the figure the experimental points follow quite well a power-law function with an exponent of 1.1 (cyan line).

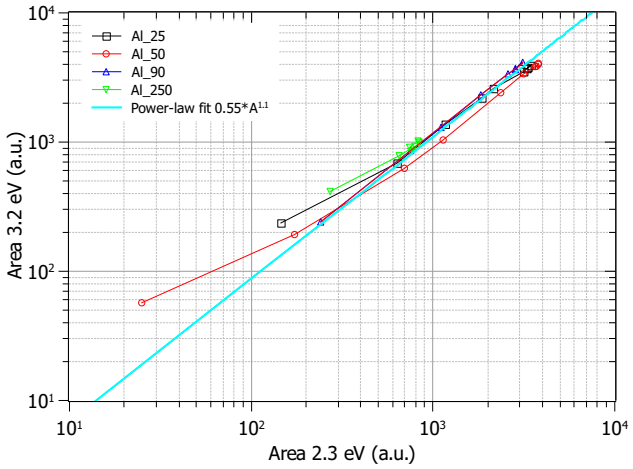


**Figure 3.39:** Correlation of gaussian fit area of band at 2.3 eV with the one at 3.2 eV in *Al*_25, *Al*_50, *Al*_90, *Al*_250.

These last results focus on the behavior of the AlOHC bands at 2.3 eV and 3.2 eV. If both OA bands belong to the same center they should correlate during all the thermal treatment. So the ratio of the areas in fig.3.38 should be constant during the treatment, and, in the same way, in fig.3.39, we should expect a straight line with a slope of about 1 for a good correlation. Both figures appear to show a correlation between these two bands.

**P-doped sample** In fig.3.40 is reported the RIA during the thermal annealing treatment after exposing to $\gamma$ radiation. The irradiation dose is 1MGy at room temperature and the fit obtained by gaussian decomposition. As radiation sensitive fiber type, the RIA is quite high reaching 2500dB/m at around 6 eV, even if less intense respect to the Al-doped specimen.
The RIA fit shows the presence of some P-related defects: POHC (band at 2.2 eV [0.4], 2.5 eV [0.7] for POHCb and 3.1 eV [0.8] for POHCm), P2 (4.5 eV [1.4]), and some others related to silica: NBOHC (4.8 eV [1.08], 6.8 eV [1.3]) and SiE' (5.75 eV [1.0]).

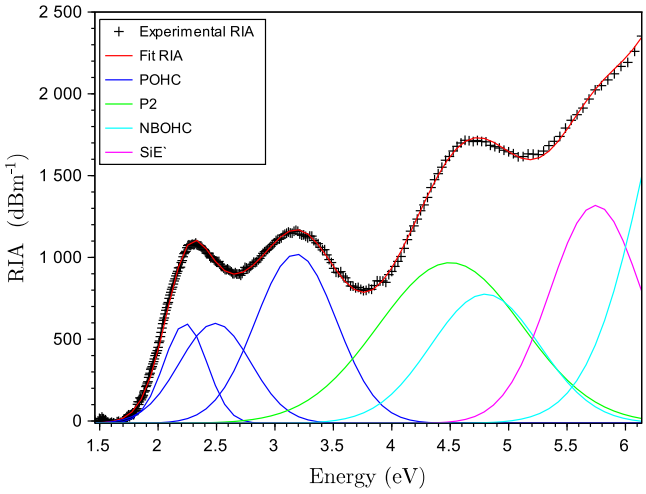


**Figure 3.40:** RIA of the $P$_25 sample after a dose of 1MGy (given in 14 days) and a possible Gaussian decomposition.

The left side of fig.3.41-3.44 are reported the thermal annealing RIA for all the samples irradiated at different temperatures: $P$_25, $P$_50, $P$_90 and $P$_250. The RIA spectra are reported for all the $T_{stop}$ of the thermal annealing protocol, from 25°Cto 500°C . As seen for aluminum, the irradiation temperature affects the RIA intensity: in fig.3.44 the RIA obtained after an irradiation temperature of 250$^oC$ is less intense than the one reported in fig.3.41, 3.42 and 3.43 at 25, 50 and 90$^oC$ respectively. It is worth to note that contrary to the Al-doped samples, whose RIA is completely annealed at 400$^oC$, the annealing is here not complete at 500$^oC$ and we can see some residual RIA at this temperature, in particular the POHC related ones.
To have a more quantitative view about the POHCs annealing, we made the fit of all the RIA spectra of the thermal annealing and for all irradiation temperatures. The areas of the POHC bands obtained by the fit are plotted as a function of the thermal annealing temperature stop (right side of fig.3.41-3.44). Before annealing and for annealing temperature $T_{stop} \leqslant$ 200°C the area of the band peaking at 3.1 eV is always greater than the others for the irradiation temperature of 25$^oC$ (fig.3.41), 50$^oC$ (fig.3.42) and 90$^oC$ (fig.3.43). The area of the band at 2.2 eV is always the smallest. Correspondingly, it is affected by a weaker annealing. At annealing temperatures greater than 300$^oC$, this band become more intense for all the samples. It then appears to be more resistant to thermal annealing than the other POHC's

bands.

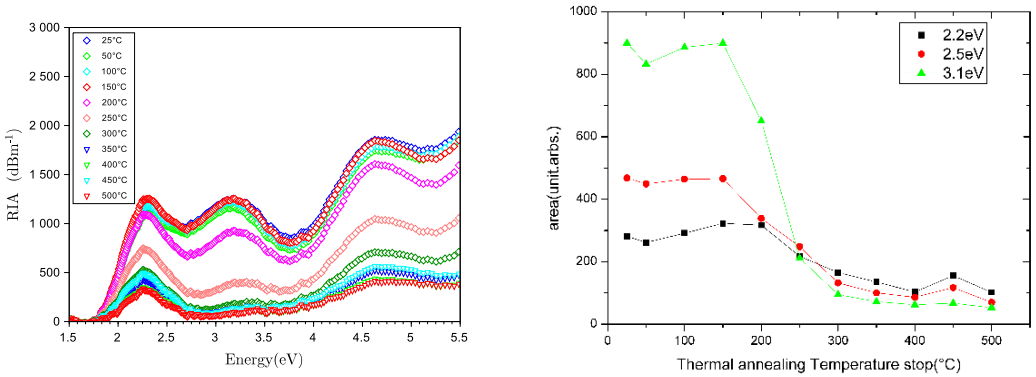


**Figure 3.41:** Thermal annealing RIA and the area gaussian bands as function of thermal annealing $T_{stop}$ for $P$_25 sample.

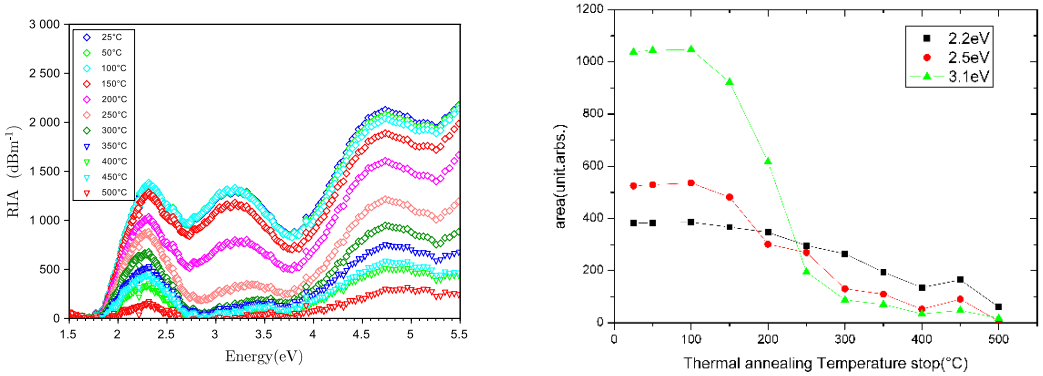


**Figure 3.42:** Thermal annealing RIA and the area gaussian bands as function of thermal annealing $T_{stop}$ for $P$_50 sample.

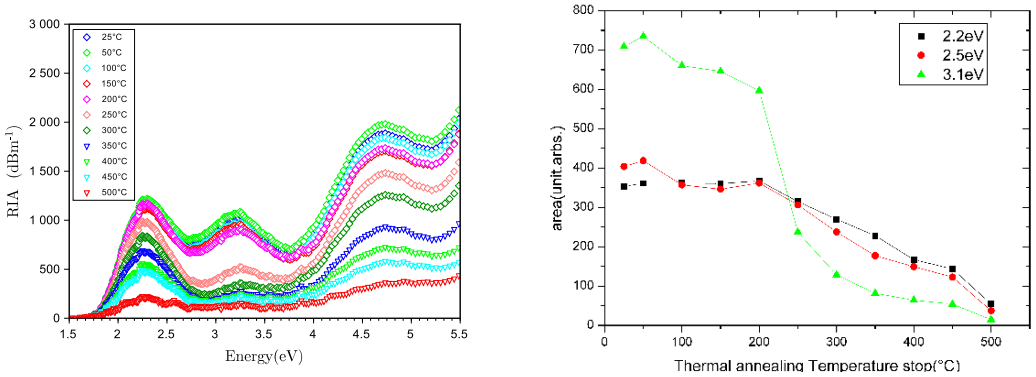


**Figure 3.43:** Thermal annealing RIA and the area gaussian bands as function of thermal annealing $T_{stop}$ for $P$_90 sample.

In fig.3.44, where the irradiation temperature is 250°C the bands at 2.2 eV appears less annealed during all the treatment. At this irradiation temperature, the band shows a higher RIA level during all the annealing process, proving again its higher tolerance to heating respect to the others POHCs centers.

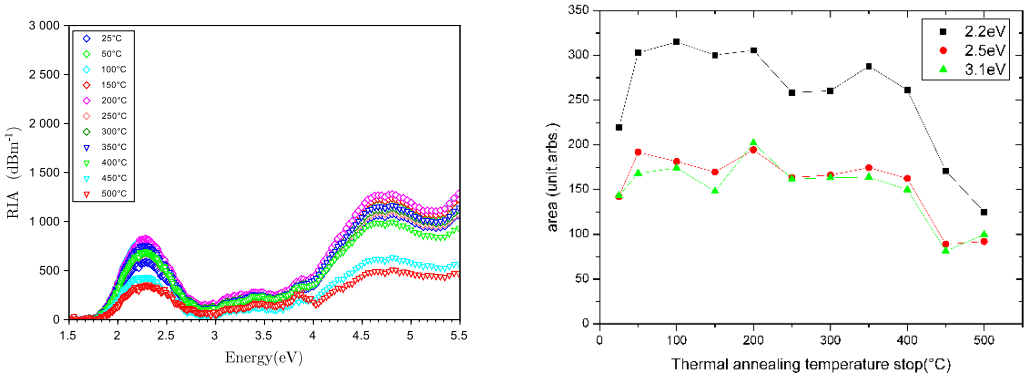


**Figure 3.44:** Thermal annealing RIA and the area gaussian bands as function of thermal annealing $T_{stop}$ for $P$_250 sample.

## 3.4 Telecom grade fiber preforms

### 3.4.1 Ge-doped sample (Q01)

Germanium doped silica-based optical fibers are widely used as telecom-grade fibers [178] and have been deeply evaluated for radiation-tolerant and telecommunication applications [90, 178, 179]. In this context, there is a strong interest in improving the knowledge about their degradation processes through the RIA developing and thus the creation/annealing mechanisms of radiation-induced point defects.
A procedure proposed by Mady *et al.* [174] for Al-, P- and rare-earth-doped silica allows extracting the energy distribution of the Density of Trapped States (DOTS) induced by ionizing radiations from TL experiments. As it will be reported in chapter 4, this knowledge is of first importance to understand and predict the temporal and thermal stability of the optical degradation, since the DOTS notably contains the energy levels of color centers that mainly contribute to the RIA. Unfortunately, the formalism introduced in[174] does not work in the case of Ge-doped glasses due to their "anomalous" TL features. It is precisely the goal of this work to extend the model and capability of the DOTS extraction technique to Ge-doped glasses. This model will be deeply presented in chapter 4. In the following, we present the experimental results obtained for Ge-doped and co-doped silica samples and the creation/annealing mechanisms we could demonstrate from these results for the radiation induced point defects and color centers in this kind of materials.

**Thermoluminescence** Fig.3.45 shows four TL curves obtained on the Ge-doped preform sample Q01, after identical irradiations at RT but recorded at four heating rates (0.5, 1, 2 and 3°C). In this figure, are superimposed in red symbols the areas (in arbitrary units) under the TL curve calculated at each heating rate. The TL peak at about 250 °C is typical of Ge doping [90, 170].

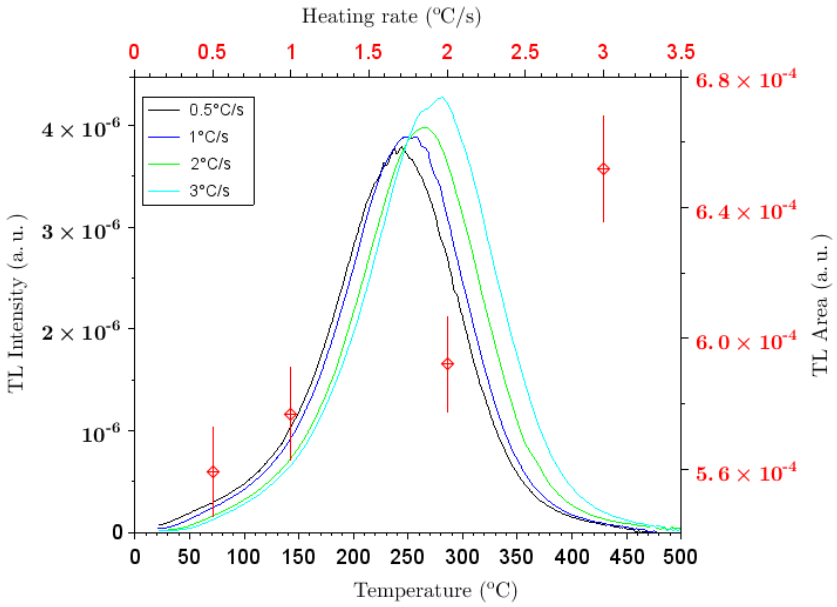


**Figure 3.45:** TL glow curves of Ge-doped sample (Q01) recorded at 0.5, 1, 2 and 3°C after the same X-ray irradiation at RT. The red points correspond to the TL area at each heating rate, the error bars represent the 5% of the measured area.

One observes the usual effect of the peak moving towards high temperatures with the increase of the heating rate, as in the case of silica whether pure (see section 3.1) or doped (Al-, P- see section 3.2). But contrary to the latter where the TL area decreases with the heating rate (see fig.3.27), here for Ge-doped silica we observe an abnormal effect since the area under the TL peak (in arbitrary units) increases with the heating rate.
The TL spectral analysis of Fig. 3.46 shows a wide emission band located at 3 eV. This spectrum has been recorded at $250^oC$, at the maximum of the glow curve, but it remains unchanged across the full temperature range of the TL readout.
The Gaussian decomposition of this emission clearly leads to two bands: a main one at 3.1 eV and a weaker one at 2.7 eV. These two luminescence bands have already been observed by photoluminescence (PL) and they have been clearly assigned to the luminescence of GeODC and SiODC centers, respectively [32]. This spectrum clearly demonstrates that GeODCs and SiODCs are reformed (in excited state) throughout the annealing accompanying the TL readout following the irradiation [4]. This result is consistent with the fact that some Si- and Ge-ODC are destroyed by irradiation (both centers absorb at 5.1 eV [32, 40, 94] and restored during the annealing process of the TL readout.

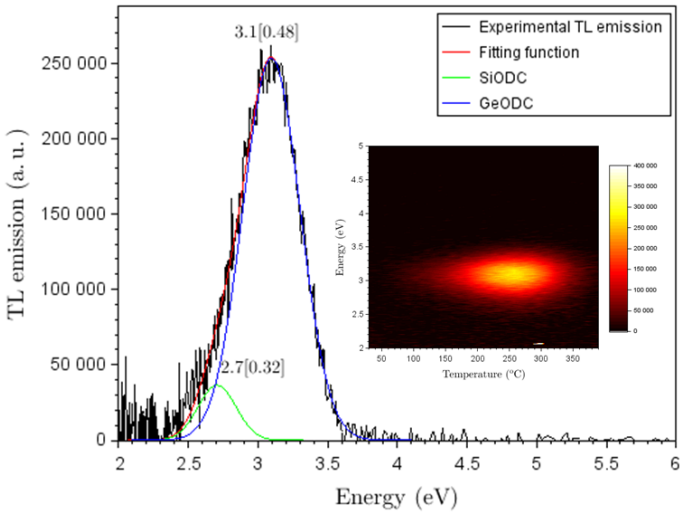


**Figure 3.46:** TL emission on a Ge-doped sample (Q01) at 250$^o$C and its Gaussian decomposition. The band characteristics are written in the graph as peak location and FWHM within brackets. In the inset is reported the 3D map of their emission.

In Fig. 3.47 is shown the energy trap depth levels (red symbols) evaluated according to the initial rise (IR) method. One can see that to the TL peak at 250$^oC$ corresponds an activation energy level lying between 1.2 eV and 1.4 eV.

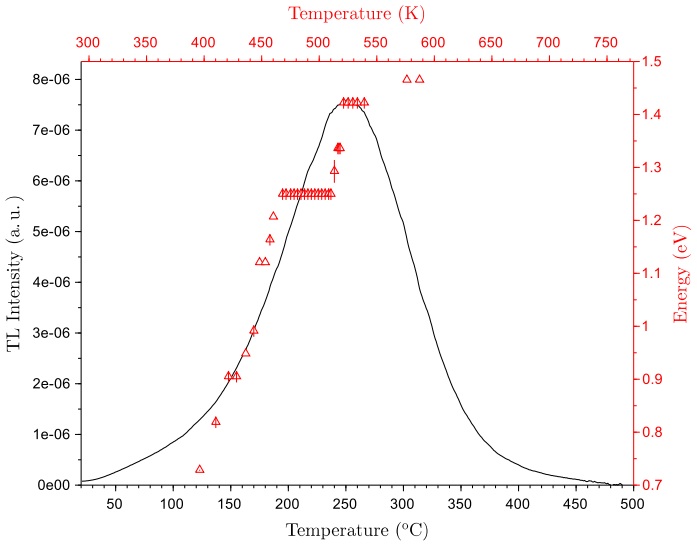


**Figure 3.47:** TL glow curve (black line) of Q01 acquired at 1°C/s and energy levels depth (red symbols) obtained according to the IR method.

The TL dependence on the irradiation dose is presented in fig.3.48, where is reported in a logarithmic representation the TL areas as a function of the dose. The behavior is more linear compared to the samples investigated until now, a linear fit in fig.3.48 reveals in fact a slope close to 1 (0.85). This value confirms that Ge-doped

silica is a good candidate for TL dosimetry, since a linear relationship between TL intensity and the absorbed dose is a desirable property for a TL dosimetry [91, 165].

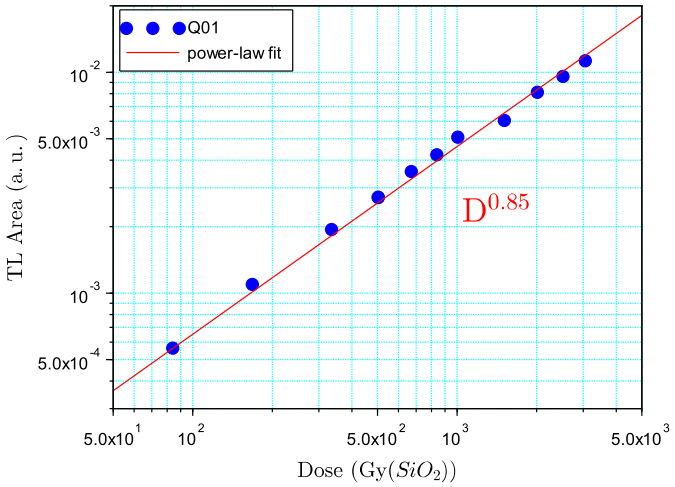


**Figure 3.48:** TL areas as a function of the irradiation dose.

**Optical absorption** Fig.3.49 shows the RIA obtained at RT on the Ge-doped sample (Q01) at a dose of 6 kGy(SiO2). The RIA intensity reaches a maximum value of about 1000 dB/m around 4.5 eV. Decomposition attempt of this RIA into Gaussian bands have been done to comply with usual bands attributed to well identified Ge-related centers: Ge(1) at 4.25 eV [1.2], GeX at 2.61 eV [0.9], and silica related centers such as NBOHC (1.97 eV [0.3], 4.8 eV [0.9]) [46, 94].

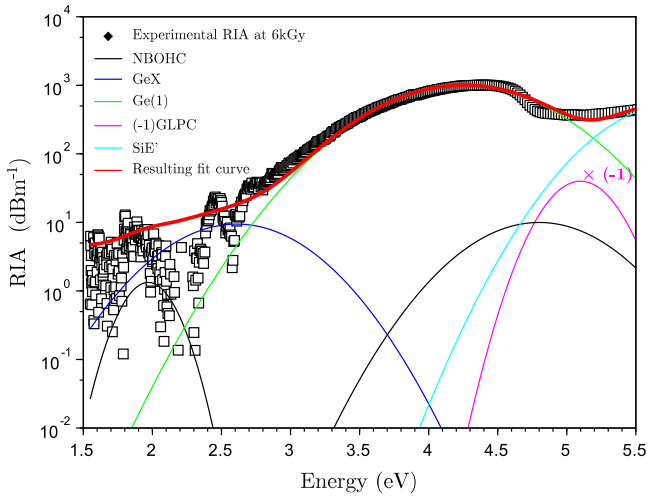


**Figure 3.49:** RIA of a Ge-doped sample (Q01) after 6kGy X-ray irradiation at RT

The band at 5.8 eV, corresponds to the intrinsic SiE' centers and to Ge(2) centers, both centers being probably present [78, 94, 97, 98]. The optical absorption by the

so-called Germanium lone-pair centers (GLPC), a variety of Ge-related oxygen deficient centers (GeODC), clearly appears as a band centered around 5.1 eV in the absorption spectrum of the pristine sample. In agreement with previous observations [94], we found that this band is reduced by irradiation. The decomposition attempt of the RIA in Fig. 3.49 well includes a band at 5.1 eV but with a negative amplitude, therefore it was multiplied by (-1) to be visible in the semilogarithmic representation used here. At lower energies, the RIA intensity is very low and noisy, we tried to assign the gaussian band at 2.61 eV and 1.97 eV to the defects mentioned above in order to follow the behavior of the tail [46]. One can note that the main contribution to this observed RIA is mainly due to Ge(1) centers around 4.25 eV.
The thermal annealing results are presented in the bleaching map of the RIA in Fig. 3.50. Here, bleaching is just represented just as the contour plot of the RIA intensities at each temperature.

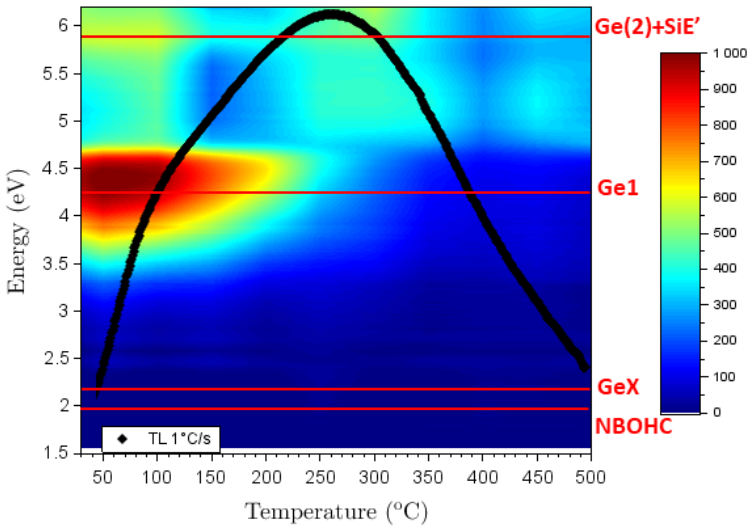


**Figure 3.50:** Bleaching map of Ge-doped sample after 6kGy of irradiation and thermal annealing treatment at $1^oC/s$ from RT to $450^oC/s$. The black line superimposed on the bleaching map represents the TL glow curve measured after 3kGy of irradiation at the same heating rate.

The bleaching is clearly observed for the predominant color center Ge(1) (at 4.25 eV) and to a lesser degree to the 5.8 eV band of SiE' centers. The greatest destruction of Ge(1) centers occurs between 75 and $125^oC$. Since Ge(1) centers are admitted to be trapped electron states [94], their annealing could originate from the thermal release of the previously trapped electrons. This point of view is confirmed by the parallel annealing of SiE' centers (around 5.8 eV) below $125^oC$. Indeed, SiE' centers are undoubtedly trapped-hole states (holes trapped at oxygen vacancies [32]) and it was clearly demonstrated in [77] that they release the previously trapped-holes between $225^oC$ and $300^oC$ in the TL process. Therefore, the annealing of SiE' centers below $125^oC$ can only be the result of their recombination by those electrons released from Ge(1) centers. According to Fig. 3.50, and as expected from the

previous results in this work, SiE' centers complete their annealing between 250 and $300^oC$, a region where they release the "de-trapped-holes" which is strongly correlated to the main TL peak.
As shown in Fig. 3.46 relative to the spectral analysis of TL emission, the SiODCs and GeODCs are reformed during the thermal annealing process that goes together with the TL readout. In silica, oxygen deficient centers (ODCs) were shown to have the common capacity to trap free electrons under irradiation, whether they are intrinsic (SiODCs) or associated with aluminum in Al-doped silica (AlODCs) [77]. Then the reformation of ODCs centers during TL heating can be readily interpreted as the result of the recombination of thermally-released holes $h^+$ at such trapped-electron states (i.e. at $ODC : e^-$ species) [77, 174]. This statement can be extended to the reformation of GeODCs, since this reformation parallels that of SiODCs as highlighted in Fig. 3.46 . It therefore appears to be the result of the radiative recombination of thermally released holes at $GeODC : e^-$ centers. To sum up the main mechanisms, we can retain that the trapping of electrons under irradiation leads to the formation of at least Ge(1), $GeODC : e^-$ and $SiODC : e^-$ centers. The Ge(1) centers apparently correspond to shallow trapped-electron states since they anneal by releasing their trapped electron from the beginning of the TL readout at RT. Si- and $GeODC : e^-$ states are obviously deeper: before any detrapping, they anneal thanks to their recombination by free holes (as those released from trapped-hole states along the TL readout). ODCs are then reformed in excited state according to the following processes explaining the TL emission:

$$GeODC : e^- + h^+ \mapsto GeODC + hv_{3.1eV} \tag{3.10}$$

$$SiODC : e^- + h^+ \mapsto SiODC(II) + hv_{2.7eV} \tag{3.11}$$

According to the bleaching map, free holes involved in these processes are mainly released from SiE' centers between 250 and $300^oC$ (according to the heating rate).
As shown in Fig. 3.45, the TL intensity tends to increase when the heating rate increases from 0.5 to $3^oC/s$. This behavior is unusual with respect to that of pure silica, P- or Al-doped silica specimens, for which the TL intensity decreases when increasing heating rate due to the well-known effect of thermal quenching of the radiative recombination luminescence yield [32, 170, 174]. The "anomalous" behavior reported here has been already observed in Ge-doped samples [170, 180] and it was tentatively argued to originate from the fact that the recombination cross-section, governing the rate at which the released carriers are transferred to the luminescence centers, increases with temperature [170, 180]. This proposal seems reasonable, since TL processes shift towards high temperature at high heating rate. In fact, it is not enough by itself to explain what is observed, namely an increase of both the TL peak intensity and the area at growing heating rates (see Fig. 3.45). If a temperature-enhanced recombination cross-section was the unique specificity, the total amount of holes recombined during the TL process should finally remain the same at the end of the readout, regardless of the heating rate (provided the TL traps are completely emptied and the TL peak fully extinguished, as observed here). This would undoubtedly affect the shape of the TL peak but not its total area that should be independent of the heating rate (the peak being integrated

over its whole temperature range). By contrast, the rise of the TL area indicates that the total number of recombined holes increases. The most straightforward explanation for this is that, in addition to the temperature-enhanced hole recombination, a hole trapping process on a very stable level must compete with recombination at $ODC : e^-$ states responsible for the TL emission. Competing traps must be too deep to be relaxed during the TL readout since they do not give rise to a TL peak in the glow curve. They can be referred to as 'thermally disconnected traps' or TDT. The permanent capture of holes released by shallow TL traps in the TDT eliminates many candidates for recombination and thus limits the area of the TL peak. If the recombination cross-section grows faster than that of capture on TDT with temperature, the competition progressively turns in favor of recombination when the heating rate is raised: the total number of recombined holes and the TL area increase. In fact, very stable Ge-related trapped-hole centers, namely the GeE' centers, were demonstrated to form in Ge-doped silica under irradiation[4]. These centers, which absorb in the UV part of the optical spectrum, have precisely been found to anneal only above 500 $^oC$ in isochronal annealing experiments (and thus certainly at an even higher temperature with the linear temperature profile used in TL) [4]. Therefore, it seems very likely that holes trapped in TDT can be assigned to GeE' centers. This proposal makes the TDT the precursors of GeE' centers and, as expected, a specific feature of Ge-doped silica. In what follows, we simply consider that the cross-section characterizing the recombination of holes at $GeODC : e^-$ centers obeys a thermally-activated Arrhenius-like law, as referred to 3.12:

$$\sigma_r = \sigma_{r0} e^{-E_b/k_B T} \tag{3.12}$$

Where $\sigma_{r0}$ is the recombination cross section in the absence of recombination barrier (at $E_b$ =0 eV), $E_b$ is the recombination activation energy, $k_b$ the Boltzmann constant and T the temperature.
The original model we propose to explain specific mechanisms in Ge-doped silica is sketched in Fig.3.51.

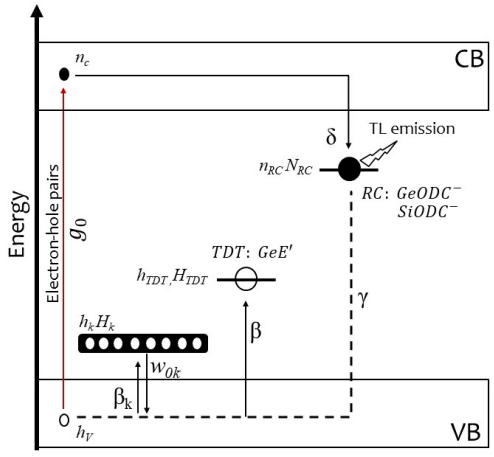


**Figure 3.51:** Energy level scheme proposed to explain the radiation-induced degradation in Ge-doped silica and its annealing Ge-doped silica.

Pair generation takes place at a constant rate $g_0$ per unit volume and time that is fixed with respect to the dose rate absorbed by the material during the irradiation process. Holes generated in the valence band (VB) can be captured to form hole trapped centers such as SiE' centers, and GeE' centers, the latter playing the role of the "thermally disconnected traps", with the hole trap concentration $H_{TDT}$, the density of trapped holes $h_{TDT}$ and a hole trapping coefficient $\beta_{TDT}$. They can also recombine at RC consisting of electrons trapped into the form of SiODC:e- ($SiODC^-$) and GeODC:e- ($GeODC^-$) states, which electron traps concentration and the density of trapped electrons are referred respectively as $N_{RC}$ and $n_{RC}$. Electrons generated in the conduction band (CB) can be trapped by a set of intrinsic trapping levels (which is not shown in the figure to streamline the description) or be captured at SiODCs and GeODCs by an electron trapping coefficient $\delta$. Holes can be released from some intrinsic unstable levels (bandtails) and from deeper SiE' centers. In Fig.3.51 the arrow pointing up represents the trapping, characterized by a trapping coefficient $\beta_k = \sigma_k v_{th}$ for the $k_{th}$ trap, where $\sigma_k$ is the capture cross-section and $v_{th}$ the thermal velocity in the VB; instead the arrow pointing down represents the de-trapping, described by the frequency factor $w_{0_k} = \sigma_k v_{th} N_v$, where $N_v$ is the equivalent density of states in the VB. The release frequencies are then of the form $w_{0_k} exp(-E_k/k_b T)$, where $E_k$ is the trapped-state level measured with respect to the closest band edge. The recombination coefficient is $\gamma = \sigma_r v_{th}$ where $\sigma_r$ is the recombination cross-section, which expression is given by 3.12. The stability of the traps induced by irradiation is determined by their thermally activation energy $E_k$ measured from the nearest band edge.

### 3.4.2 GeP and GeF samples (Q07, Q09)

In addition to the Ge-doped silica sample (Q01) as Telecom grade fibers, we also studied germano-silicate preforms co-doped with phosphorous (Q07) and fluorine (Q09) in the cladding.
The presence of P in the cladding does not affect too much the TL response previously observed on the Ge-doped sample, they in fact present similar TL curves.
In terms of RIA, that of sample Q07 has some characteristics associated with phosphorous, while that of sample Q09 is quite similar to that of the Ge-doped sample, as could be expected since there are no induced fluorine-related defects.

**Thermoluminescence** The TL of GeP (Q07) and GeF (Q09) co-doped silica performs present the same TL features to those presented for the Ge sample: a main peak ranging from 200 to 270 °C, depending on the heating rate, due to the luminescence of GeODC centers and a large shoulder at lower temperatures related to silica, as shown in fig.3.52. Moreover one can observe an increasing of the TL intensity with the increasing of the heating rate, due to the presence of Ge. Thus, all the considerations previously made in the case of the Ge-doped sample to explain the abnormal behavior of the TL are also valid for these two co-doped samples.

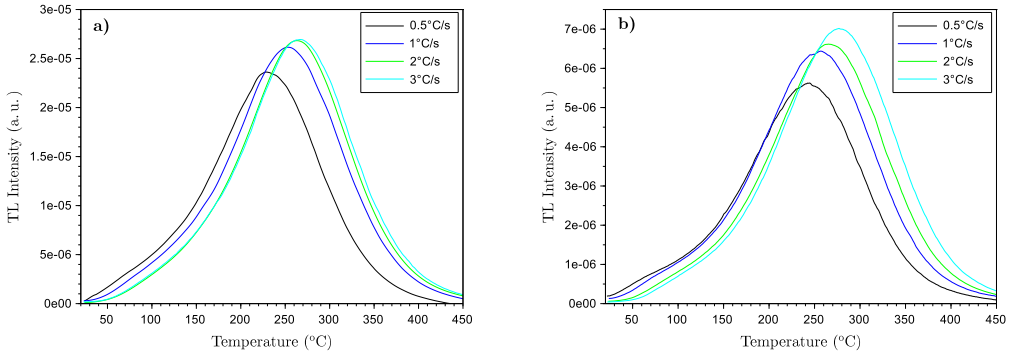


**Figure 3.52:** TL curves at different heating rates obtained on a) Ge-P (Q07) and b) GeF (Q09) co-doped sample after irradiation of 100 Gy($SiO_2$).

Fig.3.53 shows the TL area variations of the co-doped samples as a function of the dose in log/log scale representation. Both areas present a power-law dependence on the dose, with the same slope of $D^{0.85}$.

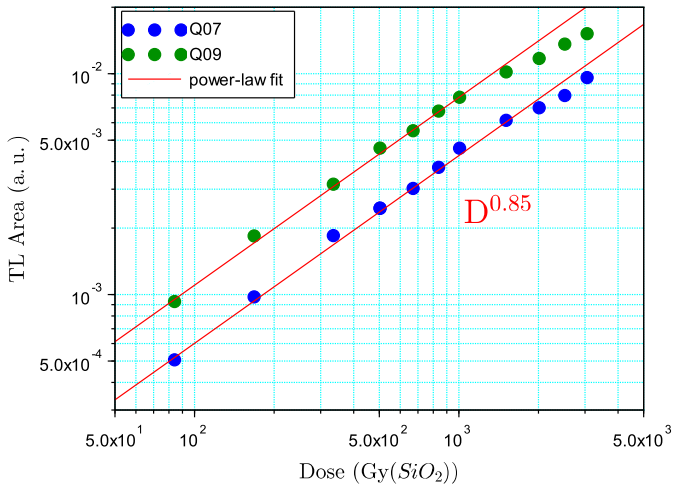


**Figure 3.53:** Area TL on Ge-P (Q07) and GeF (Q09) doped silica sample as a function of the dose and the fitting functions $A = kD^{0.85}$.

The TL spectra reported in fig.3.54 present the same features as those of Q01: a main band at 3 eV, resulting from 2 components: one band peaking at 2.7 eV related to SiODC, and a second one at 3.1 eV related to GeODC. What we observe in 3.54b) is a clear signal due to the high TL intensity which characterizes the Q09 sample.

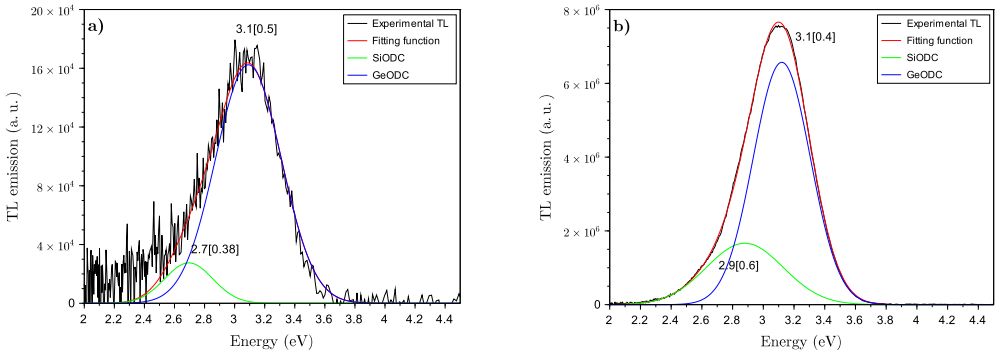


**Figure 3.54:** TL emission observed on a) Q07 and b) Q09 samples after irradiation at 1kGy.

From the initial rise experiment, which energy distribution is reported in fig.3.55 for Q07 (a) and Q09 (b), one can estimate the energy depth of the traps corresponding to the main peak between 1.2 and 1.4 eV as well were obtained for Q01 sample.

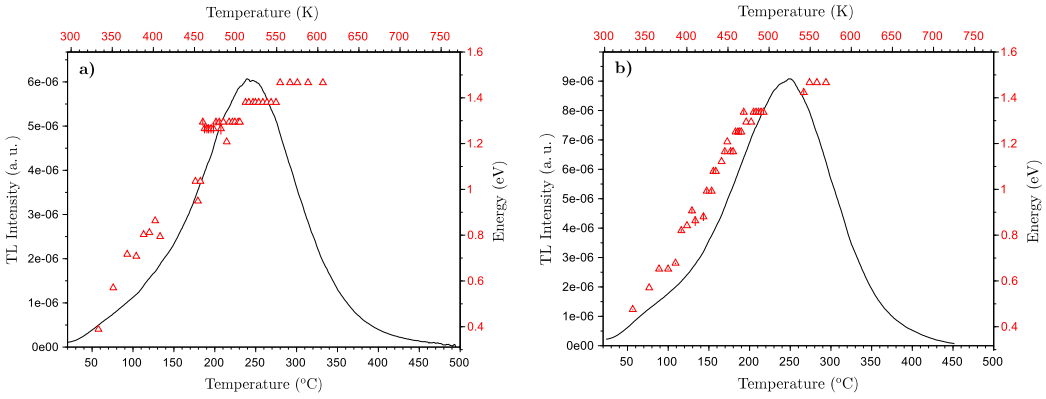


**Figure 3.55:** TL glow curve (black line) and energy levels depth (red symbols) obtained according to the IR method in Q07 (a) and Q09 (b) samples.

**Optical absorption** Fig.3.56(a) represents the RIA obtained on the GeP co-doped sample (Q07). A gaussian decomposition in reveals the same optical bands related to germanium and phosphorous.
Optical absorption measurements are, as always, focused in the core of the perform. The presence of phosphorous associated bands on the RIA spectrum means that this dopant present in the cladding probably diffused into the core of the preform during MCVD synthesis.
From the fit, which parameters are reported in table 3.4, one can see that the main contribution to the RIA is due to Ge(1) and P2 centers above 3.5 eV. The POHCs dominate the Visible part of the spectrum where are located three bands related to this center [84]. In the absorption spectrum before irradiation we observed the band attributed to the GLPC as seen also in Q01, thus this involves the presence of the negative amplitude band in the RIA at around 5 eV which is not visible in the logarithmic scale of the figure 3.56.

In fig.3.56b) is reported the RIA of the Ge-F sample and a gaussian fit which parameters are reported in table 3.4. As seen for the Ge doped sample Q01, the main contribution to the RIA is due to Ge(1) and we observe again a reduction of the GLPC band under irradiation which leads to a negative amplitude band in the RIA at around 5 eV.

| Defect name | Q07 | | Q09 | |
|---|---|---|---|---|
| | $x_c$(eV) | FWHM (eV) | $x_c$(eV) | FWHM (eV) |
| POHC | 2.2; 2.5; 3.1 | 0.2; 0.6; 0.7 | - | - |
| Ge(1) | 4.4 | 1.1 | 4.4 | 1.3 |
| P2 | 4.5 | 1.2 | - | - |
| GLPC | 4.9 | 0.47 | 5.0 | 0.6 |

**Table 3.4:** Parameters of the gaussian bands used in fig.3.56.

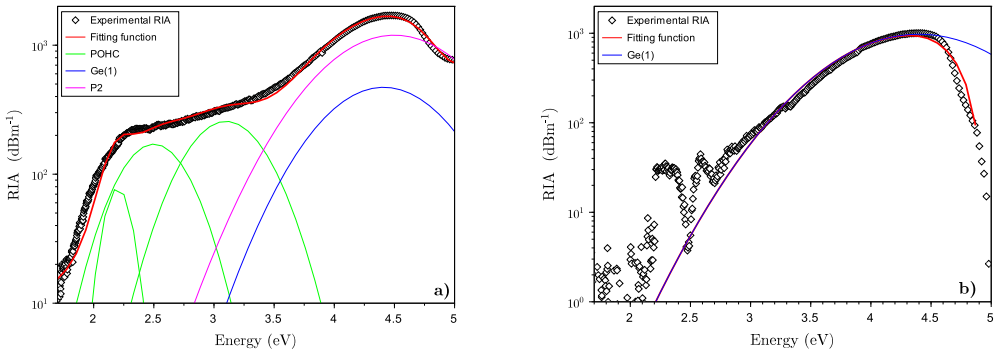


**Figure 3.56:** RIA spectra obtained on a) Q07 and b) Q09 samples after irradiation at 3kGy and related Gaussian decomposition.

### 3.4.3 The case of the F-doped sample Q11

The emission and absorption features shown by Q11 sample, is different from the other tolerant fibers. As one can see from tab.2.1 in chapter 2.6, Q11 is characterized by Fluorine doping in the cladding and silica in the core, but as it will be shown in this section, some features present in its RIA and TL spectra, brings to think that are present some other doping elements as impurities.

**Thermoluminescence** The TL in Q11 sample present a peak around 170°C with a shoulder between 250°C and 300°C (see fig.3.57). The TL shape is quite different from the other tolerant fibers, which suggests a significantly different defect composition. The intensity is much higher respect to the other tolerant fiber preforms (L02 or Q25). For this sample we were in fact able to perform the initial rise measurements.

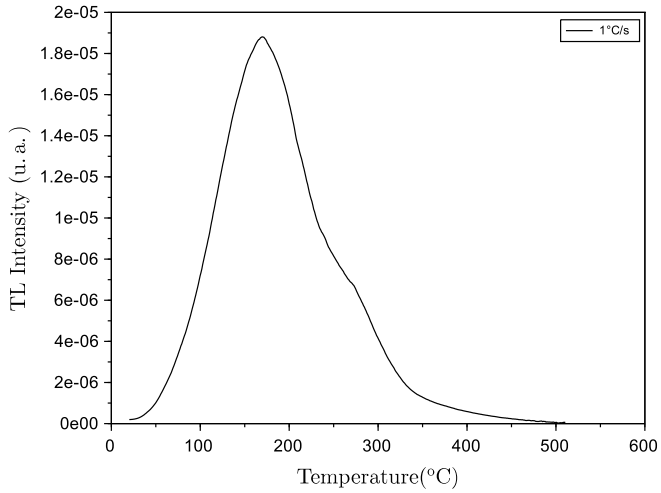


**Figure 3.57:** TL on F-doped silica sample at $1^oC/s$ after irradiation at a dose of 100 Gy($SiO_2$).

Fig.3.58 shows the energy level depth distribution estimated from the initial rise method. This procedure was made for the main peak at $170^oC$ and for the shoulder at around $250^oC$ (see fig.3.57). This was necessary to estimate the energy depth of the deeper traps which gives a clear and visible contribution to the TL at at higher temperature around $250^oC$. In fig.3.58 the red scatter graph shows a distribution in energies between 0.8 and 1.3 eV, with an energy level around 1 eV corresponding to the main peak. The energy trap depths concerning the second peak at 200-300°C are located around 1.2 eV. To perform these measurements the first peak was first depleted by pre-heating the sample up to 200 °C. The TL readout conducted after this treatment then provided us with the blue curve (here in Fig.3.58 re-normalized with respect to the original one).
The TL spectral analysis in Fig.3.59 shows a wide emission band peaking at around 3 eV. This spectrum has been recorded at $170^oC$, at the greatest TL intensity, but it remains with the same band features across the full temperature range of the TL readout. In the inset, the TL map reports the TL emission spectrally resolved during all the TL readout. As one can see the emission is located at the energies around 3 eV for all the temperature ramp. The Gaussian decomposition of the band clearly leads to two components: the main one at 3.1 eV and another one but with a less contribution at 2.7 eV. This last band have already been assigned to SiODC centers [32]. The band at 3.1 eV is generally attributed to GeODC, even if in Q11 should not be germanium-doped, it is possible that a very small quantity of Ge impurities entered in this preform during the MCVD process. The TL emission reaches the maximum intensity at around $170^oC$, in accordance with what is obtained with the PMT (fig.3.57).

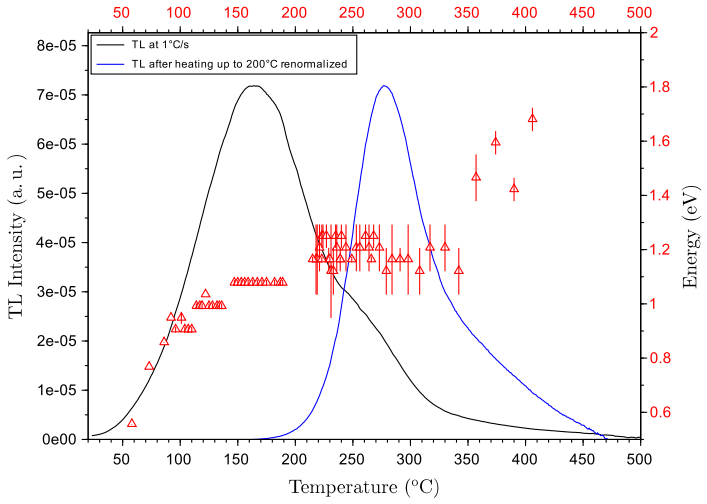


**Figure 3.58:** TL glow curve (black line) and energy levels depth (red scattered lines) obtained according to the IR method. The TL recorded after heating up to $200^oC$ is reported in blue and normalized respect to the maximum of the glow curve

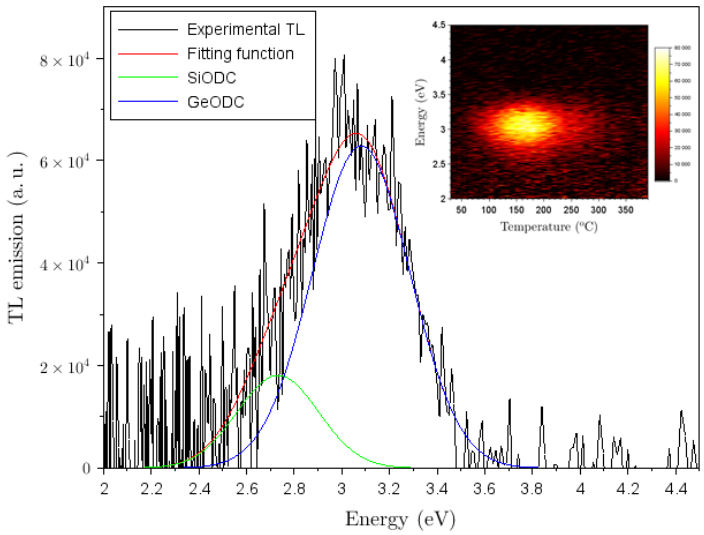


**Figure 3.59:** TL on F-doped silica sample after irradiation of a dose of 1kGy recorded at $160^oC$. In the inset, representation as contour plot of the TL recorded during all the TL readout as a function of the temperature and the energy.

In fig.3.60 are reported the areas of the TL glow curves as a function of the dose, obtained according to annex 4.3.4. From the log/log plot is observed a sublinear behavior, as suggested by the slope of 0.43, with a trend that seems to saturate.

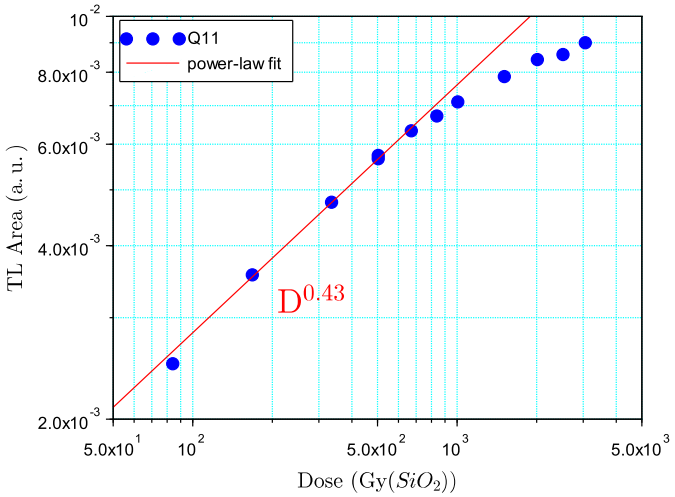


**Figure 3.60:** Area TL on F-doped silica sample as a function of the dose. c) TL on F-doped silica sample after irradiation of a dose of 1kGy recorded at 160°C.

Fig.3.61 shows a comparison between several TL curves recorder at four heating rates.

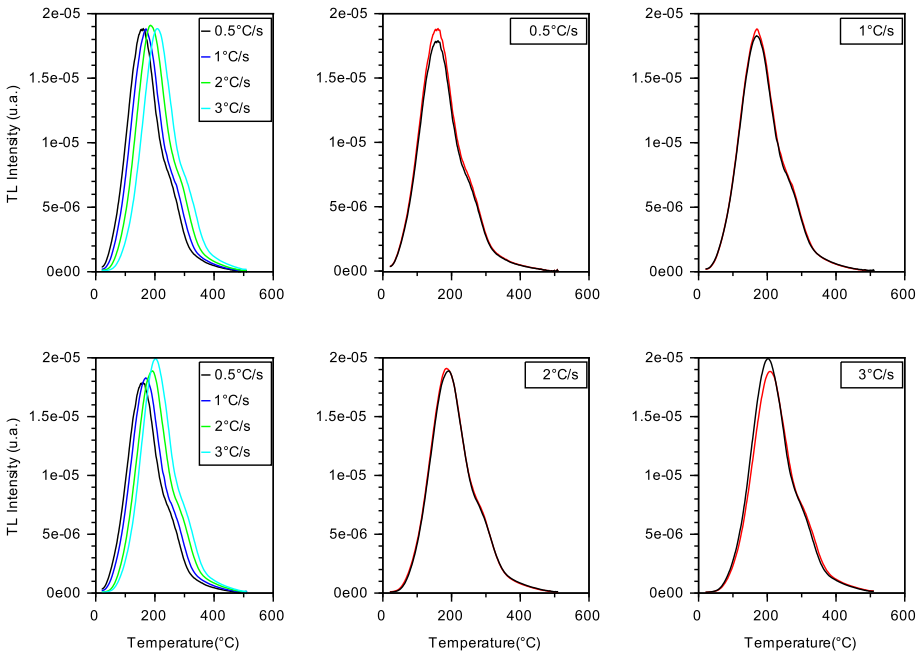


**Figure 3.61:** TL curves measured on F-doped silica sample at four heating rates after irradiation at a dose of 100 Gy($SiO_2$). It is also reported a comparison between two measurements made at the same heating rates.

Generally what we expect for this kind of samples is a decrease of the TL when increasing the heating rate, as for pure silica. Generally what one obtains performing the TL measurements, is a clear behavior of the TL when increasing the heating

rate (increasing or decreasing of the TL intensity), even considering the repeatibility error. For the case of Q11 sample one cannot conclude clearly whether the TL increases when increasing the heating rate. As one can see from the figure, if an increase is observed for one set of measurements (red lines, superimposed in the top-left corner plot), is not the case for the other set (black lines, superimposed in the bottom-left corner plot). For sure we do not observe any decrease if the TL with the heating rate.

**Optical absorption** The RIA intensity of the Q11 sample is low. Its spectrum, shown in fig.3.62, contains the typical intrinsic bands of silica found in the pure silica sample (L02, see fig.3.6): the well-known bands of the SiE' peaking at 5.8 eV [1.0], and two other bands related to the NBOHC center, at 4.8 [1.0] and 6.5 [1.0] eV. In addition to the well known silica related defects [32], there is another band centered at 3.8 eV [0.9].
In the literature, this band with a FWHM of about 0.7 eV is attributed to the interstitial clorine ($Cl_2$) or to peroxy linkage (POL) defect [32]. The attribution of this band to Cl impurities or to the POL is still questioned [41, 181], but the energy position and the FWHM of the band could be linked to chlorine impurity introduced during the MCVD process.

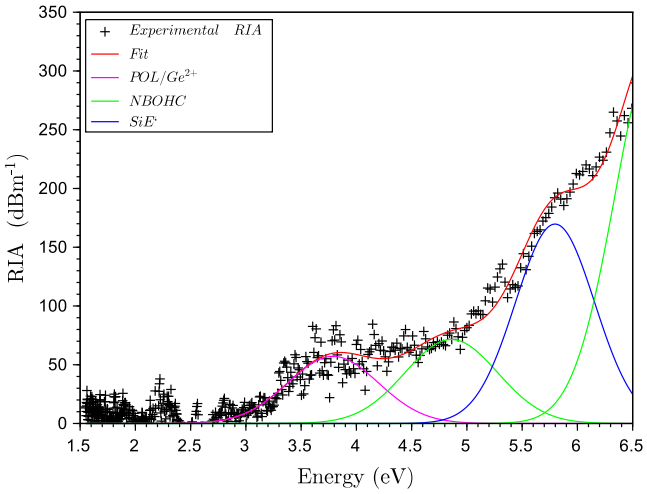


**Figure 3.62:** TL on F-doped silica sample after irradiation of a dose of 6 kGy.

Anyway, it is worth to know that to the absorption band at 3.8 eV is not related any PL emission band. Conversely, the dis-coordinated Ge impurity ($Ge^{2+}$) is related to an absorption band at 3.7 eV (with a FWHM of 0.4 eV) and a PL band at 3.1 eV [32]. Considering also the TL emission in Q11 at 3.1 eV (fig.3.59) related to germanium, it is probable that germanium impurities are present in this sample bringing to some features related to this dopant, such as the OA band at 3.7 eV and the TL emission and at 3.1 eV. The presence of germanium is justified by the fact that some impurities still remains present during the MCVD manufacturing process.
To conclude, several features related to germanium are all present in Q11:

- The high response of the TL (even at a small dose of irradiation, as in fig.3.57)
- TL emission at 3.1 eV (fig.3.59)
- the increase of the TL intensity with increasing heating rate; more precisely a small increase or a constant trend of the TL intensity peak (fig.3.61);
- a TL peak at 250°C which energy depth was estimated around 1.2 eV (fig.3.58)

Supported by these results, we are quite sure that a small amount of Ge is present in the preform, even if unfortunately it is a quantity small enough that it cannot be detected by EDX to confirm this assumption.

## 3.5 Summary

The experimental results reported in this chapter, aim to characterize the samples of this thesis. This characterization is based on the studies of :

1 the radiation induced color centers created during the irradiation, which are detected by the optical absorption thanks to the gaussian band decomposition of the RIA;

2 their annealing by means of thermal annealing protocol (annealed RIA);

3 the recombination processes during the annealing by means of the TL technique.

This strategy, based on a cross-check investigation, intended to provide an analysis of the mechanisms of the RIA development and annealing in silica-based fiber preforms taking into account different core compositions, thus exploring the main dopants characterizing our samples: Al, P and Ge. The combination of the three studies summarized above makes original this method, since it is based on the full investigation of the TL measurements (both along the annealing temperature and spectrally-resolved), with the characterization of the RIA and its annealing in the same TL conditions.
TL measurements induce thermal bleaching of the RIA and provides information on the luminescent centers that are reformed along the annealing process (i.e. *SiODC*, which emission at 2.7 eV is well detectable in all our samples). In addition, one can extract information on those centers non detectable with the TL (non luminescent) serving as radiation-induced trapped-carrier states.
On the other side, the RIA characterization allows the identification of the color centers (CCs) through the gaussian decomposition of the RIA spectra.
Since it is widely admitted that CCs correspond to radiation-induced trapped carriers, it was important to correlate these complementary techniques (TL and optical absorption) to make a connection between CC revealed in RIA spectra and the trapped-carrier states probed by TL.
Moreover, the annealed RIA detected according to the thermal annealing protocol, may reveal (i) a possible correlation of the recovery in CC; (ii) the temperature

range of the main bleaching of the centers. This last point is crucial in our analysis, since it gives access to the correlation between CC bleaching and energy depth of the trapping level. The correlation was established by measuring the progressive RIA annealing along the TL process. This protocol gives "bleaching maps" that reveal the annealing rate at any temperature of the TL readout and any wavelength of the RIA spectrum. Then we can relate the bleaching of a center at a certain temperature, to the energy depth of a trapping level through the DOTS revealed by the TL.
In table 3.5 are resumed the radiation induced defects and the restored ones during the TL for the Si-. Al-, P- and Ge-core doped samples. In the last column, the main TL emission mechanisms are reported. A schematic representation of these processes are illustrated in the energy level scheme of figure 3.63.

| Core doping | Radiation induced CCs hole traps | Radiation induced CCs electron traps | Restored centers (during TL readout) | Prevalent TL emission mechanism |
|---|---|---|---|---|
| Si | SiE' - NBOHC | $SiODC^-$ | SiODC | $h^+ + SiODC^- \mapsto SiODC + h\nu_{2.7eV}$ |
| Al | AlOHC | AlE' | AlODC | $h^+ + AlE' \mapsto AlODC + h\nu_{3eV}$ |
| | SiE' - NBOHC | $SiODC^-$ | SiODC | $h^+ + SiODC^- \mapsto SiODC + h\nu_{2.7eV}$ |
| P | POHC | P2 | | |
| | SiE' - NBOHC | $SiODC^-$ | SiODC | $h^+ + SiODC^- \mapsto SiODC + h\nu_{2.7eV}$ |
| Ge | Ge2, GeE' | Ge1 - $GeODC^-$ | GeODC | $h^+ + GeODC^- \mapsto GeODC + h\nu_{3.1eV}$ |
| | SiE' - NBOHC | $SiODC^-$ | SiODC | $h^+ + SiODC^- \mapsto SiODC + h\nu_{2.7eV}$ |

**Table 3.5:** Summary of the CC created during the irradiation and the main TL emission mechanisms determined in the results previously reported for the main dopants. The CC visible in the RIA are written in red.

In radiation tolerant fibers such as pure silica one (L02 sample), irradiation-excited holes trap to form of SiE' centers, NBOHC and a continuous distribution of shallow trapped-holes states. Only the SiE' centers and NBOHC are found to contribute to the RIA. Counterpart electrons most probably trap at oxygen vacancies, such as at SiODC. The annealing process consists in the recombination of thermally-released holes with trapped electrons and is accompanied by the characteristic emission of SiODC.
The doping with Phosphorous (L28 sample) induces an important increase on the RIA. This sensitivity to radiation is a characteristic of P-doped fibers. The decomposition of the RIA reveals the presence of intrisic defects (SiE' and NBOHC), shallow trapped-holes states and P-related radiation induced CCs, such as the hole trap POHC and the electron trap P2. As in pure silica, electrons most probably trap at oxygen vacancies, such as at SiODC.
In addition to the centers present in pure silica, as well as the distribution of shallow trapped-holes states, Al-doped sample (K04 sample) is characterized by the formation of Al-related radiation-induced CC: AlE' and AlOHC. AlE' centers correspond to electrons trapped at Al-related vacancies [77], whereas AlOHC are holes trapped at fourfold coordinated Al atoms. The main annealing process involves the detrapping of holes and their recombination at AlE' centers and with electron trapped at Si related vacancies. This process reforms both SiODC and Al-related vacancies, a kind of AlODC [77]. Holes are emitted from intrinsic trapped states, from SiE' centers and finally from AlOHC.

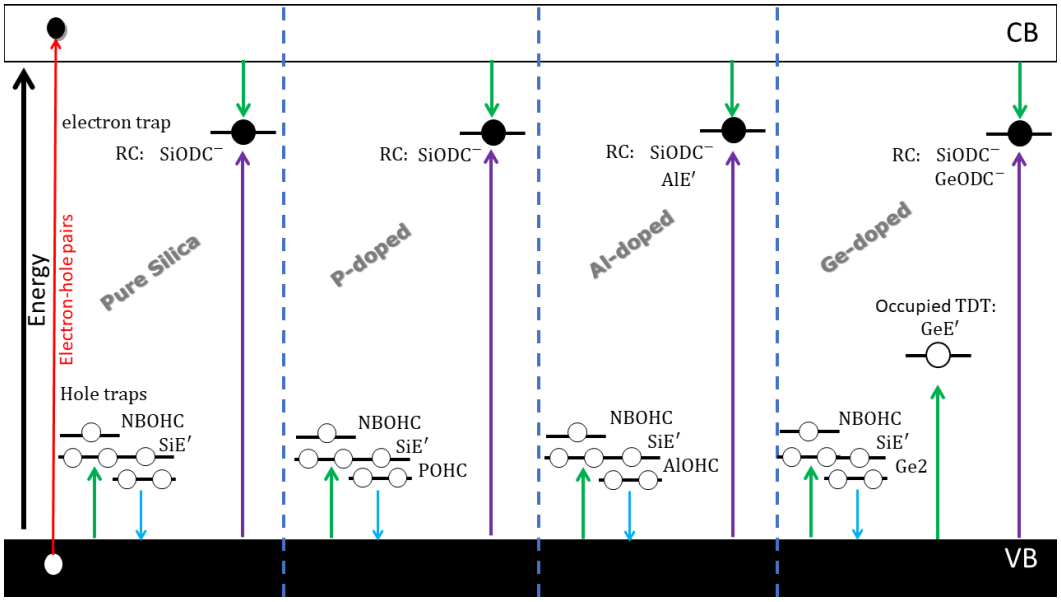


**Figure 3.63:** Energy level scheme for pure, P-, Al- and Ge-doped silica samples. The trapped hole centers created during the irradiation and the RC are reported in white and black respectively. The recombination is highlighted by the purple arrow, whereas the trapping and the thermal release process by green and blue arrow.

In Ge-doped sample irradiation leads to the formation of SiE′ centers, NBOHC a continuous distribution of shallow trapped-holes states and the Ge-related induced CCs Ge2 and GeE′. The latter is not visible in the RIA spectra recorded in our experimental condition but it might be formed at the irradiation dose used in our measurements. Moreover, as deeply explained in the section dedicated to Telecom-grade samples, the precursor of the GeE′ is a deep trap which trap holes and compete with the RC. The GeE′ is the occupied TDT. The main contribution to the RIA is due to the trapped electron center Ge1. During the irradiation, electrons most probably trapped at oxygen vacancies, such as SiODC and GeODC. Again, the annealing process consists in the recombination of thermally-released holes with trapped electrons and is accompanied by the characteristic emission of SiODC, which in Ge-doped sample is less intense compared to that of GeODC.
To conclude this chapter, we can point out that from the experimental results we get information of the extracted DOTS, which always correspond to distributions of trapped holes.
From the summary reported here and summarized in table 3.5, the main TL emissions for all the samples is characterized by free holes ($h^+$) recombined at electrons trapped at oxygen vacancies. Common to all samples is the fact that the TL emission is due to the release of trapped holes that subsequently recombine on RC formed by trapped electron states. As a consequence of this feature, the extracted DOTS always correspond to distributions of trapped holes in the gap, near by the valence band. These DOTS are necessary to predict and simulate the temporal and thermal stability of the RIA. To get this knowledge and probe the DOTS, we use a powerful means: the TL. To simulate the RIA and its behavior as a function of

time and temperature, we need the TL. From the simulation of the TL we can extract the DOTS and then, simulate the DOTS in several experimental conditions as well as the one encountered in the RIA. The prediction of the RIA is now possible knowing that the energy levels present within the DOTS are associated to certain CC. This association is possible thanks to the thermal annealing protocol.

# Chapter 4

# Modeling and simulations results



The main objective of this thesis is to propose a model able to simulate the RIA in the visible part of the spectrum. The ability of prediction of this model takes into account the experimental condition that induce the degradation inside silica based optical fibers, such as the time, the temperature, the dose and the dose rate.
As anticipated in section 3.5, we propose a model based on the connection between the color center and the DOTS, through the thermal annealing protocol. The DOTS is correlated to the thermal annealing of the RIA (protocol described in appendix 4.3.4) and this allow us to assign the main color center to energy levels present in the DOTS.
The temporal and thermal stability of the trapped radiation-induced states are mainly determined by their thermal activation energy. The latter corresponds to the "depth" E of the traps, which is the energy of each trapped state, located in the

forbidden band with respect to the edge of the closest band. In amorphous materials like silica, which are characterized by a structural disorder, it is reasonable to consider these energy levels closely distributed instead as discrete levels. We thus refer to the density of trapped states $n(E)$ or DOTS, as a collection of energies $E_k$ where $n_k$ carriers are trapped.
The knowledge of the DOTS is the first step to get a model capable of reproduce and predict the evolution of the radiation-induced states over different external conditions, such as the irradiation dose, irradiation time, the "relaxation time" spent between the irradiation and the TL readout, or the temperature.
The obtain DOTS we need a complex procedure based on simulations and experiments which will be presented in detail in the next section. Fig.4.1 summarizes through a block diagram this procedure.

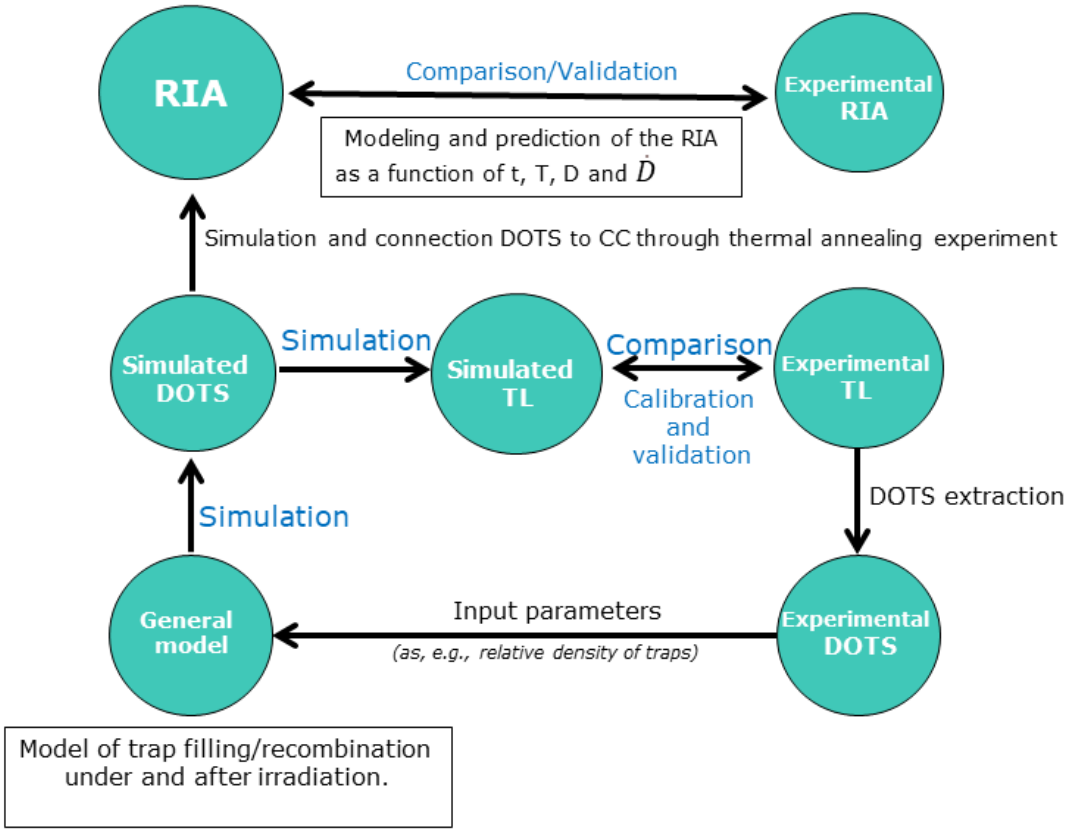


**Figure 4.1:** Block diagram of the simulation strategy adopted to built the RIA model.

To predict correctly the RIA, one should be able to simulate the DOTS in several conditions as those encountered in the RIA experiences. The DOTS are obtained through a modeling of trap filling and recombination, under and after irradiation. To get a correct prediction of the DOTS, the simulation model must be validated by strong evidences. In this respect, it is needed a strategy to calibrate the DOTS simulation in a certain condition (standard laboratory condition) and to assure their validity.

The calibration and validation procedure is built on the TL. Basically, from experimental TL curves we extract the experimental DOTS. This DOTS extraction procedure provides crucial inputs for the general model (as, e.g., the relative density of traps and kinetic parameters) which must be able to simulate the DOTS build-up. To validate simulated DOTS we use again the TL. We simulate the TL given by such theoretical DOTS, in order to prove that it well re-produces the measured TL. Of course the simulated TL is compared to the experimental one until a satisfactory result is obtained. At the same time, the simulated DOTS are compared to the experimental ones. This phase of calibration and validation against experimental results, allow us to built the DOTS for all the samples of this thesis in "standard conditions". The validated model can then be used for extrapolation purposes, i.e. to predict the DOTS and the RIA that should be expected in markedly different conditions (as those that are not readily achievable in a laboratory).
We proceed in the explanation of our modeling procedure illustrating the results for radiation tolerant fibers: L02 and Q25 fiber samples (see table 4.1 below to remind the details). The L02 fiber is not doped and it is reasonable to cite as an example the simplest and most general case of pure silica. Once the modeling approach is explained by reporting step by step the results for radiation tolerant samples, in the chapter will be reported the simulation results obtained for all the preforms studied in this thesis.

| sample name | doping | | characterization | |
|---|---|---|---|---|
| | Cladding | Core | *at.*% | $\Delta$n |
| L02 | Si | Si | - | $4 \cdot 10^{-3}$ |
| Q25 | F | F | 1.19-0.36 F | $-2.3 \cdot 10^{-3}$ |

**Table 4.1:** Radiation-tolerant fiber preforms under investigation.

## 4.1 Modeling approach. Case of Radiation tolerant fibers

### 4.1.1 General model for the degradation build up.

The approach adopted to simulate the build-up (under irradiation) and relaxation (after irradiation) of the DOTS, is based on the model used to simulate trap filling and emptying in standard description of TL. In chapter 2 is reported the description of the Thermoluminescence phenomenon. A more generalized TL model, with respect to the first order process reported in section 2.5, includes the possibility for thermally-released carriers to re-trap instead of recombine at recombination centers (RC). To understand this kind of process, one can start from a standard example of trapping-recombination model illustrated by the energy level scheme of fig. 4.2.
Following irradiation, pair generation takes place at a constant rate $g_0$ per unit volume and time, that is fixed by the dose rate absorbed by the material. Holes generated in the valence band (VB) only undergo capture on recombination centers (RCs). Electrons generated in the conduction band (CB) can be trapped by a set of discrete trapping levels or recombine with holes on RCs. $N_k$ is the concentration and $n_k$ is the electron density of trap $k$, $n_c$ and $h_v$ are the concentrations of electrons in the CB and of holes in the VB, respectively.

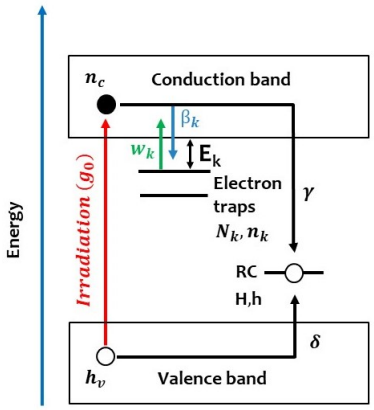


**Figure 4.2:** Standard scheme to simulated the DOTS build-up and related TL shown for discrete trapped electron states and a single trapped hole RC. The mechanism is generally reversed for silica, where the recombination takes place at trapped-electron RCs, following the release of holes from trapped-hole states.

The trapping coefficient is $\beta_k = \sigma_k v_{th}$ for the $k^{th}$ trap, where $\sigma_k$ is the capture cross-section and $v_{th}$ the thermal velocity in the CB. $w_{0_k} = \sigma_k v_{th} N_c$ is the frequency factor that is the coefficient of the thermal de-trapping process (see appendix 4.3.4). The recombination coefficient is $\gamma = \sigma_r v_{th}$ where $\sigma_r$ is the recombination cross-section. H is the concentration of hole traps, occupied by a density $h$ of holes ($h$ is thus the RC density), and $\delta = \sigma_h v_{th}$ is the hole trapping coefficient (here $v_{th}$ is the thermal velocity in VB). The stability of the radiation-induced trapped states is determined by their thermal activation energy, which energy $E_k$ (for the $k^{th}$ level) corresponds to the energy difference between the energy level of the trap and the CB.
The evolution over time of the electron density $n_c$ in the CB is given by equation (4.1) where the second member represents the generation, the trapping on $M$ levels, the thermally release from the same $M$ levels and finally recombination [182]:

$$\frac{dn_c}{dt} = g_0 - n_c \sum_{k=1}^{M} \beta_k (N_k - n_k) + \sum_{k=1}^{M} w0_k exp\left(-\frac{E_k}{k_B T}\right) n_k - \gamma n_c h \tag{4.1}$$

The evolution of the density of trapped electrons is assumed to result from trapping and release (4.2)

$$\frac{dn_k}{dt} = \beta_k n_c (N_k - n_k) - w0_k exp\left(-\frac{E_k}{k_B T}\right) n_k, \quad k = 1...M \tag{4.2}$$

The hole population in the VB varies according to the generation and trapping, and hence obeys to equation (4.3)

$$\frac{dh_v}{dt} = g_0 - \delta h_v (H - h) \tag{4.3}$$

At last, the population of trapped holes (RCs) evolves due to hole trapping and

recombination according to (4.4)

$$\frac{dh}{dt} = \delta h_v(H - h) - \gamma n_c h \tag{4.4}$$

The hypothesis of a single RC is made for simplicity, but it is rather justified for optical fibers where experimental TL spectra show that one RC most often prevails. Then, color centers are essentially related to the trapping of carriers whose polarity is opposite to the charge of RCs. Since RCs has been identified as trapped electrons, regardless of the dopant we consider in our silica samples, the thermal annealing and TL processes are in fact triggered by the detrapping of holes. This corresponds to the reverse situation compared with fig.4.2 which corresponds to the most convenient representation. This arbitrary choice does not limit generality since the role of carriers can be freely reversed.
After a certain time after the end of the irradiation, the material characterized by the equations (4.1)-(4.4) reaches a thermodynamic equilibrium where the filling of the different levels must obeys to the Fermi-Dirac statistics. This assumption is valid only if the frequency factor is expressed as a function of $\beta_k\ N_c$, which implies a temperature dependency of $T^2$ as reported in appendix 4.3.4 [165].
The coupled-non linear-differential equations (4.1)-(4.4) can be solved numerically to describe all the experimental phases:

1 the isothermal irradiation phase, which lasts as the irradiation time $t_{irr}$;

2 the isothermal relaxation phase, when we take into account the time $t_{relax}$ elapsed between the end of the irradiation and the start of the TL reading (in our case this time is maintained to 90 s);

3 the TL readout phase, during which the time $t$ is linked to the temperature by the heating rate $q(dt = dT/q)$.

The irradiation phase is solved at a constant temperature $T_0$ (generally RT) and with a zero initial charges concentration ($n_c = n_k = h = h_v = 0$), since the material is pristine. The $g_0$ value is set based on the dose rate absorbed by the material. When multiplied by the irradiation time $t_{irr}$, $g_0$ gives the total number $N_{EHP}$ of electron-hole pairs (EHP) created by irradiation per unit volume, a density representative of the total dose. We pass from the physical dose rate unit in Gy $s^{-1}$ to the generation rate in $cm^{-3}s^{-1}$ by using the generation efficiency G which was taken as $5.18 \times 10^{14}\ cm^{-3}Gy^{-1}(SiO_2)$ if a bandgap of 9 eV is considered for silica [182].
The relaxation phase starts with an initial populations different from zero which values are given by the solutions of the equations obtained at the and of the irradiation phase. Even if during this phase the irradiation is stopped ($g_0 = 0$), we can have a change on population due to the thermal instability of the traps. Notably the probability of release from filled states increases with the increasing time $t_{relax}$. Finally, the calculation of the TL readout phase starts with the populations obtained at the end of the relaxation phase and always for $g_0 = 0$. Furthermore, in this phase the temperature is not constant but increases linearly with the time from $T_0$ to $T_f$ at a constant heating rate $q$. As said before, the RCs have the characteristic to be stable during the TL readout (at least up to the the experimental temperature

of $550^oC$, that is the maximum temperature in our measurements). This means that RCs do not undergo de-trapping: they can only be depleted by recombination processes. This also implies that the trapping of holes rifle quickly the VB during the relaxation phase and this band stay empty during the TL readout in the scheme of fig.4.2. Thus the TL readout is described by the equations (4.1)-(4.3) with the condition $h_v = 0$, the TL intensity being calculated, as given by the equation (2.11), in term of number of recombined holes:

$$I_{TL} = -\frac{1}{1 + Cexp(-W/k_BT)} \frac{1}{q} \frac{dh}{dt} \tag{4.5}$$

Equations (4.1)-(4.4) are used for simulations. Among the parameters present in these equations, most of them are unknowns, namely: $g_0$, $\beta_k$, $N_k$, $w0_k$, $E_k$,$\delta$, $\gamma$, $H$. During the TL readout phase, we must add the the Mott-Seitz coefficient $C$ and $W$ to this list. Considering the k index which reflects the number of traps (k=1...M). This gives 4M+5 unknown parameters. In our simulation we used an arbitrary value M=60. This value sets the energy resolution of the DOTS, without impacting on general conclusions. We therefore have to deal with 243 unknown parameters, which became 245 when simulating TL. Obviously, this amount must be reduced, otherwise it would be impractical to solve these equations. The steps we follow to reach this goal are listed below and they will be described in detail in the next sections:

- The first step is the assumption of a *single cross section* $\sigma$ for all traps. This hypothesis brings to a reduction of the unknown parameters from $4 \times M + 5$ to $2 \times M + 7$, which means 127 for M=60. Under this assumption we have $\sigma_k = \sigma$, which implies $\beta_k = \beta$ and $w0_k = w0$. Summarizing, the unknown parameters are now: $N_k$ and $E_k$ (2M values), $\delta$, $\gamma$, $H$, $\beta$, $w0$, C, W (7 values).

- *First order analysis of DOTS extraction.* Assuming that TL processes can be modeled through first order kinetics, we propose an original protocol for the extraction of the DOTS from TL glow curves. This will further give access to most of the unknown parameters: $w_0$, C and W; but also to the collection of the pairs ($E_k$, $n_k(T_0)$) for $k = 1 \dots M$, i.e the DOTS at the onset of the TL readout (relative estimate, not absolute).

- *Dimensionless procedure.* From the first order analysis we obtain the relative DOTS and we drastically reduced the number of unknown parameters of eq. (4.1)-(4.4) from 125 to only 5: N, H, $\gamma$, $\delta$ and $\beta$. At this point of the procedure, it is in principle possible to solve the system of differential equations. But the modeling of radiation-induced processes can be further refined thanks to a new formulation which is based on the dimensionless treatment of equations (4.1)-(4.4). At this stage, the only remaining adjustable parameters are the total density of the traps N and the trapping coefficient $\beta$. The first one determines how the TL response depends on the total dose (the total density of generated electron hole pairs being fixed by the dose), since N sets the saturation degree of TL traps. Whereas the latter, $\beta$, set the trapping kinetics.

### 4.1.2 Single cross section for every energy level

The hypothesis of a single capture cross section $\sigma$ for all traps brings to a reduction of the unknown parameters from $4 \times M + 5$ to $2 \times M + 7$, which means 127 for M=60. Under this assumption we have $\sigma_k$ =$\sigma$, which implies $\beta_k = \beta$ and $w0_k = w0$. Summarizing, the unknown parameters are now: $N_k$ and $E_k$ (2M values), $\delta$, $\gamma$, $H$, $\beta$, $w0$, C, W (7 values). The consequences of this choice are analyzed in what follows. With the assumption that all the traps are characterized by the same coefficient $\beta$, their frequency factors $w0_k$ differ only by the concentrations $N_k$:

$$w0_k = \sigma_k v_{th} N_k = \sigma v_{th} N_k \tag{4.6}$$

The density $n_k$ of the carriers trapped on each level $E_k$ is then directly proportional to $N_k$ when the thermal release can be neglected, i.e. when the traps are deep and thermally stable. A reformulation of equation (4.2) considering $\beta_k = \beta$ and neglecting the detrapping term, indeed gives:

$$\frac{dn_k}{dt} = \beta n_c (N_k - n_k) \tag{4.7}$$

Then with a change of variable, we can rewrite the equation above as:

$$\frac{d\varphi_k}{dt} = \beta n_c (1 - \varphi_k) \tag{4.8}$$

where $\varphi_k = n_k / N_k$ is the evolution of the filling rate of the level $E_k$. From this last, it is easy to obtain:

$$\frac{d \ln(1 - \varphi_k)}{dt} = -\beta n_c \tag{4.9}$$

Thus, all the $\varphi_k$ follow the same evolution equation. As soon as their initial value is identical, which is the case if all the trapping sites are initially empty ($\varphi_k$ (0) = 0, k = 1... M), the rates of filling $\varphi_k = n_k / N_k$ always remain equal and therefore independent from $k$. We can then write $\varphi_k = \varphi$ , let $n_k = \varphi N_k$, which shows that $n_k$ and $N_k$ remain independent from k. In other words, the density of trapped charges is always proportional to the density of traps for thermally stable levels, sharing the same trapping coefficient. Obviously, this significantly simplifies the problem.

Now we introduce the notion of *demarcation energy* to set the limit between thermally unstable and stable levels. This notion is also very useful to interpret and understand the simulation results. The demarcation energy $E_D(T, t)$, at a given temperature T and time t after the beginning of the irradiation, is that energy which roughly separates the energy levels $E_k$ into two groups:

- shallower levels for which $E_k < E_D(T, t)$; which are subjected to thermal release, so they are empty at time $t$ after the beginning of the irradiation (at temperature T) because their dwell time $t_D < t$. The direct consequence is that $n_k = 0$ for these levels.

- deeper levels for which $E_k > E_D(T, t)$; which remain thermally stable at tem-

perature T during the time t. For these levels $t_D > t$ and one can assign to $n_k$ the value $\varphi N_k$.

We can define the demarcation energy as as a function of the critical time $t = t_D = \frac{1}{w_0} e^{E_D/k_B T}$ by [174]:

$$E_D(T,t) = k_B T \times \ln\left[w_0(300) \times (T/300)^2 \times t\right] \tag{4.10}$$

The values of the frequency $w_0$ estimated by simulations are around $10^{10}\ s^{-1}$ for all the samples studied in this thesis. From this order of magnitude, the demarcation energy reached at the beginning of the TL readout in standard conditions (RT, $t_{irr}$=15 min, $t_{relax}$=90 s) lies between 0.6 and 0.7 eV above the VB. This means that trapping levels shallower than 0.6 eV are no longer populated at the beginning of the TL readout and they cannot be characterized by TL, at least in our experimental conditions. One should keep in mind that, even by exploiting rather quick irradiation and measurements, the tests conducted at RT are unable to resolve the density of shallow trapped states. The proper characterization of shallow levels and their related effects would require irradiating at cryogenic temperatures [174].

### 4.1.3 First order analysis of TL curves: the extraction of the DOTS.

**Presentation of the procedure** With the assumption of a single cross section, the populations $n_k$ of trapped state are proportional to the densities $N_k$ for stable levels ($E_k > E_D$). However, even under the single cross section assumption, the general model introduced by equations (4.1)-(4.4) is still determined by too many unknown parameters. An useful strategy to run the simulations starting with some known parameters is to assume that the TL mechanisms follow kinetics of the first order.
Assuming that TL process can be modeled through first order kinetics, we propose an original protocol for the extraction of the DOTS from TL glow curves. This will further give access to most of the unknown parameters: $w_0$, C and W; but also to the collection of the pairs ($E_k$, $n_k(T_0)$) for $k = 1 \dots M$, i.e the DOTS at the onset of the TL readout. As far as $n_k(T_0)$ is proportional to the densities of the traps $N_k$ for $E_k > E_D$ (which is the case for all of the $E_k$ probed by TL), this provides us with the relative distribution of traps ($E_k$, $\xi_k = N_k/N$), where $N = \sum_{k=1}^{M} N_k$ is the total density of traps.
Thanks to this first order approach, the 2M unknowns introduced by the ($E_k$, $N_k$) pairs are thus replaced by only one adjustable parameter, namely the total density of the traps N, which order of magnitude will be later estimated from the comparison between the simulated and experimental dependencies of the TL response on the dose.
From first order analysis we reduce drastically the number of unknown parameters to 5, which are the total density of traps N, the transition coefficients $\gamma$, $\delta$, $\beta$ and the density of holes $H$.
Now, the DOTS extraction procedure is first explained starting from the first order approximation theory and then exemplified in the case of the pure silica sample L02.
The first order approximation is made when the capture cross section is assumed to be very small compared to the recombination cross-section, i.e. $\beta/\gamma \ll 1$. On

formal level, it is introduced by simply setting $\beta/\gamma = 0$ in the equations during the TL reading phase. This implies that the carriers released thermally from traps can only recombine with the RCs and they cannot be re-trapped. Due to the very large recombination cross-section $\gamma$, we also consider the lifetime of released carriers in the CB to be negligible. The consequence is that the density of the free charges passing through the CB remains negligible and that the rates of trapping and recombination are equal during TL readout. Under these conditions, equation 4.2 takes the characteristic form of a first order kinetic process (see section 2.5.1).

$$\frac{dn_k}{dt} = -w_0 exp(-E/k_B T) n_k, \tag{4.11}$$

where $w_0 = w_0(300)(T/300)^2$, see appendix 4.3.4 for details. The equivalence between total densities of electrons and holes is written as:

$$h = \sum_{k=1}^{M} n_k. \tag{4.12}$$

The individual TL response $I_k(T)$ produced by the carriers released from the energy level $E_k$ is then simply $I_k = -\eta(T) \times dn_k/dT$. So one obtains from equation (4.11):

$$I_k(T) = \eta(T)\frac{w_0}{q} e^{-\frac{E_k}{k_B T}} n_k(T_0) \cdot exp\left[-\frac{w_0}{q}\int_{T_0}^{T} e^{-\frac{E_k}{k_B T'}} dT'\right]. \tag{4.13}$$

In this expression, $T_0$ is always the temperature at which TL reading starts and $n_k(T_0)$ is the density of carriers trapped on the $E_k$ level at the start of the readout. Extending the process to more than one single trap (as M traps), and in absence of "retrapping", the total TL intensity is just the superimposition of individual responses:

$$I_{TL}(T) = \sum_{k=1}^{M} I_{TL_k}.$$

In practice, the temperature measurements are made at discrete points $T_l$, whereas for the traps we consider M traps labeled by the index k. We can write:

$$I_{TL}(T_l) = \sum_{k=1}^{M} n_k(T_0) M_{kl} \tag{4.14}$$

where $M_{kl}$ is:

$$M_{k,l} = -\eta(T_l)\frac{w_0}{q} \sum_{k=1}^{M} e^{-\frac{E_k}{k_B T_l}} \cdot exp\left[-\frac{w_0}{q}\int_{T_0}^{T_l} e^{-\frac{E_k}{k_B T'}} dT'\right] \tag{4.15}$$

In matrix notation we can rewrite eq. (4.14) as:

$$I_{TL} = \mathbf{M} n(T_0), \tag{4.16}$$

where $\mathbf{M}$ is the matrix whose elements are given in eq.(4.15), $I_{TL}$ is the vector of experimental TL points, and $n(T_0)$, the vector of the trap populations $n_k$ at the start of the TL readout. Introducing $\mathbf{M}^T$ as the transpose matrix of $\mathbf{M}$, $n(T_0)$ can be

calculated by matricial inversion:

$$\mathbf{M}^T I_{TL} = \mathbf{M}^T \mathbf{M} n(T_0), \tag{4.17}$$

$$n(T_0) = (\mathbf{M}^T \mathbf{M})^{-1} \mathbf{M}^T I_{TL}. \tag{4.18}$$

The determination of the vector $n_0$ requires at least two TL glow curves recorded at two different heating rates, referred as $q_1$ and $q_2$ with $q_1 < q_2$ (experimental vectors $I_{TL1}$ and $I_{TL2}$). From the calculation of matrices corresponding to these rates, $\mathbf{M}(\mathbf{1})$ and $\mathbf{M}(\mathbf{2})$, it is possible to obtain the associated populations, $n_{01}$ and $n_{02}$, by solving equation (4.18). We then have by construction $I_{TL1} = \mathbf{M}(\mathbf{1})n_{01}$ and $I_{TL2}$=$\mathbf{M}(\mathbf{2})n_{02}$. Since the filling states $n_{01}$ and $n_{02}$ probed by the TL readout results from the same irradiation conditions and is independent of the value of $q$, they must obey $n_{01} = n_{02}$ so the relationship $I_{TL1} = \mathbf{M}(\mathbf{1})n_{02}$ and $I_{TL2} = \mathbf{M}(\mathbf{2})n_{01}$ must also be verified.
The adjustment of the 3 parameters C, W, $w_0$ and of the energy interval within which the energies $E_k$ are located, consists in finding the values leading to the best agreement between: $n_{01}$ and $n_{02}$; or between measured $I_{TL1}$ and the curve calculated thanks to $\mathbf{M}(\mathbf{1})$ $n_{02}$ on one hand and $I_{TL2}$ (measured) and $\mathbf{M}(\mathbf{2})$ $n_{01}$ (calculated) on the other hand.
To conclude this section it is worth to note few remarks about this procedure.

1 The theoretical TL intensity is expressed as the number of radiative recombination per unit volume and temperature ($cm^{-3}K^{-1}$). The experimental TL intensity is recorded by means of a PM tube whose output signal is an electric current expressed in Amperes (see 2.6). So this signal is proportional to the theoretical intensity:

$$I_{TL}^{Exp}(T) = K I_{TL}^{theor}(T) \tag{4.19}$$

However, the conversion factor K is unknown. Therefore, the direct application of the analysis proposed to the experimental curves actually provides the vector $K\mathbf{n_0}$ rather than $\mathbf{n_0}$. The populations of levels contained in this vector are not the directly densities of trapped carriers but rather quantities proportional to them. Moreover, since we make the approximation of a single capture cross section for all trap levels, these quantities are also proportional to the density of traps $N_k$ for all levels $E_k > E_D(T_0, t_{TL})$, where to $t_{TL}$ is the $t_{irr} + t_{relax}$.

2 The value of the Mott-Seitz coefficient W (see eq.(4.5)) extracted from the analysis makes the exponential term in the denominator of $\eta(T)$ (see eq.(2.12)) very large for all physically plausible values of C (generally $10^8$ in our results). So from eq. (2.12) one has: $Cexp(-W/k_BT) \gg 1$, that leads to:

$$\eta(T) \approx C^{-1} \times exp(-W/k_BT) \tag{4.20}$$

If we use this exponential equivalent of the yield in the expression of the TL intensity (2.13) and (4.5), we notice that the parameter $C$ play only the

role of a global multiplicative factor, without impacting the characteristics of thermal extinction which is therefore exclusively adjusted by $W$. The order of magnitude of $C$ just affects the order of magnitude of the elements of the vector $K\mathbf{n_0}$ extracted from the analysis.

3 Finally, whereas the use of 2 heating rates is in principle enough to extract the DOTS $\mathbf{n_0}$, the procedure carried out in this thesis work uses in practice 4 heating rates. We thus conduct the analysis on all of the 6 possible combination of curve pairs. This makes it possible to check that the 6 sets of parameters and the 6 DOTS $\mathbf{n_0}$ obtained following the above protocol are comparable. By doing so, we shown that the extraction procedure is robust and that the results are fully consistent and reliable. This procedure is illustrated below for pure silica.

**Parameters determination and application on pure silica** The calculation of the matrix elements defined by equation (4.15) requires knowing the thermal quenching parameters $C$ and $W$ that appear in the luminescence yield $\eta(T)$ and, most importantly, the frequency factor $w_0$. The importance of the $w_0$ value of the extracted DOTS $\mathbf{n_0}$ is highlighted below for pure silica sample. The matrix M(0.5) (so it means that the equation (4.18) has been solved based on the TL measured at $q$ = 0.5 °C $s^{-1}$, i.e. $I_{TL}(0.5)$ ) has been calculated for 3 different values of the frequency factor $w_0$ within its plausible variation range, namely $w_0 = 5 \times 10^9$, $10^9$ and $5 \times 10^8$ $s^{-1}$ (the other parameters being $C = 10^8$ and $W$ = 0.072 eV). The DOTS K$\mathbf{n_0}$ given by equation (4.18) is plotted in Figure 4.3a for these 3 values. It is normalized in % of the total DOTS obtained for the M = 60 energy levels considered in the calculation. Figure 4.3b compares the experimental TL curve (black line) to those rebuilt according to ITL = KM(0.5)$\mathbf{n_0}$ for these 3 frequency factors (color lines).
By construction, the 3 rebuilt TL curves merge and are in perfect agreement with the experimental plot. However, these identical TL curves are produced by 3 different DOTS. This example well shows the crucial importance of the $w_0$ value on the energy scaling of the DOTS. The order of magnitude of the frequency factor must be properly estimated to ensure that the depths of trapped states are correctly returned by the analysis model. In order to choose the correct $w_0$ value, one must consider an additional TL plot (at least) acquired after an identical irradiation but at a different heating rate. The 3 DOTS of Fig.4.3a corresponding to $q$ = 0.5 °C $s^{-1}$ and now noted $\mathbf{n_0}(0.5)$, were used to predict the TL curve they would produce at $q$ = 2 °C $s^{-1}$ by calculating $I_{TL}(2)$ = $\mathbf{M}(2)$ $\mathbf{n_0}(0.5)$ (one matrix M(2) for each $w_0$ value; $C$ and $W$ remained unchanged).
This prediction was then compared to the curve $I_{TL}(2)$ measured at 2°C $s^{-1}$, as shown in Fig.4.3c.
A too small frequency factor produces a too large temperature shift of the TL peak (compare fig.). Conversely, a too large value would lead to a too small temperature shift, with a consequent bad prediction of the TL peak. In the case of pure silica, the value of $w_0 = 5 \times 10^9$, leads to the best agreement with the experimental shift of the TL peak between q=0.5 and 2°C$s^{-1}$. The same procedure was made for each possible combination of heating rate pairs in order to obtain the best frequency factor value. Of course, it is important to obtain the best choice for the thermal

quenching parameters too. They are determined in a similar way to produce the same TL response lowering as that observed experimentally.

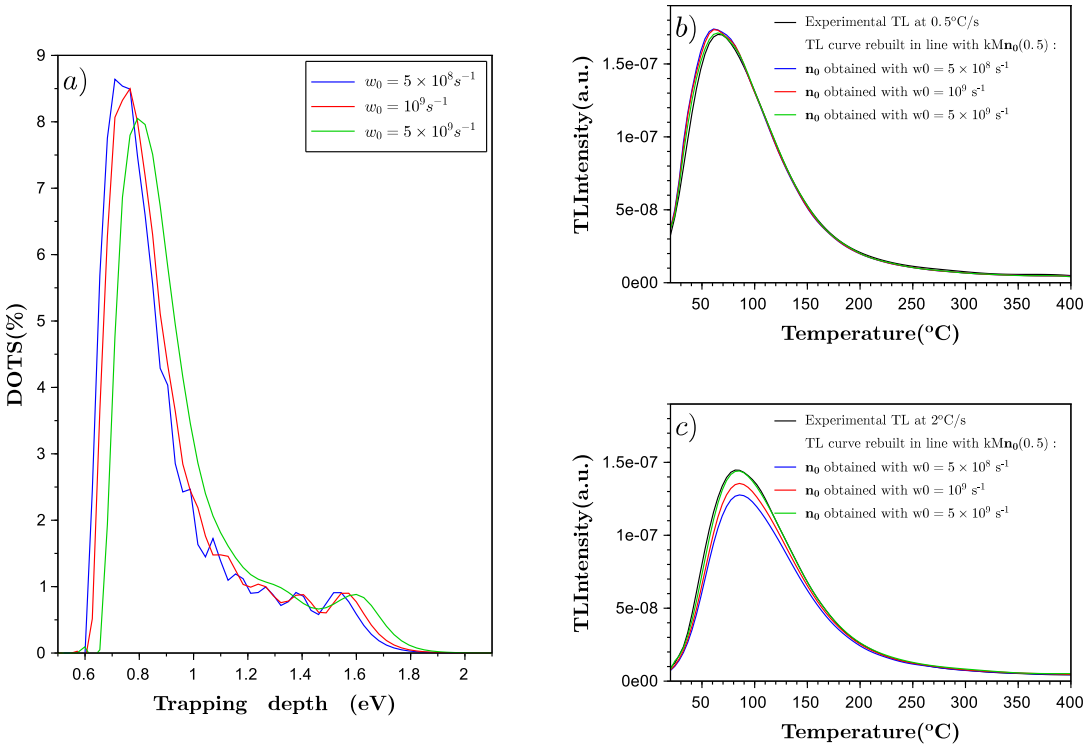


**Figure 4.3:** a) DOTS $K\mathbf{n_0}$ extracted from equation (4.18) from the TL curve measured at 0.5 °C $s^{-1}$ for pure silica sample L02. (b) Experimental TL curve used for the DOTS extraction (black line) and the TL curves rebuilt according to $I_{TL}(0.5)$ = KM(0.5)$\mathbf{n_0}$ for the 3 $\mathbf{n_0}$ vectors plotted in (a). c) Experimental TL curve at 2°C $s^{-1}$ and the TL curves rebuilt according to $I_{TL}(2)$ = KM(2)$\mathbf{n_0}$ for the 3 $\mathbf{n_0}$ vectors plotted in (a)

Generally, once the frequency factor is determined, a wrong value of non-radiative de-excitation barrier $W$ would lead to a bad prediction of the lowering of the TL intensity (when increasing the heating rate) compared with experimental data. An example is reported in fig. 4.4, where a barrier of $W$ = 0.05 eV and $W$=0.1 eV are used to simulate the TL at 0.5 and 2 °C $s^{-1}$ with the same frequency factor $w_0$ and C values, namely $5 \times 10^9$ $s^{-1}$ and $10^8$, respectively. For each $W$ value:

- The matrix M(0.5) was first calculated to extract the DOTS K$\mathbf{n_0}$(0.5) from the TL curve measured at q=0.5 °C $s^{-1}$. Then, the matrix M(2) was calculated for q=2 °C $s^{-1}$ to predict the TL curve at this heating rate, i.e. KM(2)$\mathbf{n_0}$(0.5).
- The DOTS K$\mathbf{n_0}$(2) was extracted from the TL curve measured at q=2 °C $s^{-1}$ (using M(2)). This DOTS are used to predict the TL curve at q=0.5 °C $s^{-1}$ by calculating KM(0.5)$\mathbf{n_0}$(2).
- Both predicted curve (KM(2)$\mathbf{n_0}$(0.5) and KM(0.5)$\mathbf{n_0}$(2)) were compared to experimental ones ($I_{TL}(2)$ and $I_{TL}(0.5)$, respectively).

The comparison with data is shown in Figure 4.4 for $W$ = 0.05 eV(a) and 0.1 eV (b), respectively. A barrier of $W$ = 0.05 eV is too small to explain the TL intensity loss between the two considered heating rates. On the contrary, a barrier of $W$=0.1 eV is too large. The value giving the best agreement is intermediate, equal to 0.072 eV (fig.4.4c).

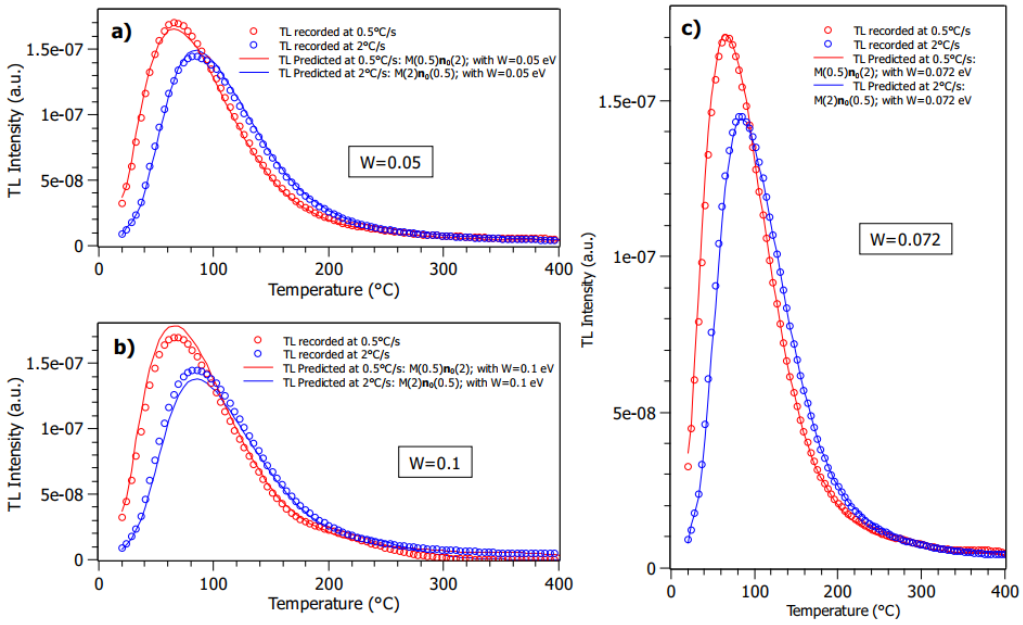


**Figure 4.4:** TL curves recorded (symbols) at heating rates q = 0.5 and 2 °C$s^{-1}$ for the pure silica sample (L02) after irradiation in standard conditions. The predicted TL (solid lines) at 0.5 and 2 °C$s^{-1}$ are calculated from KM(0.5)$\mathbf{n_0}$(2) and KM(2)$\mathbf{n_0}$(0.5), respectively.

We proceeded in this way with all the possible combination of 2 heating rates out of the 4 used. We obtain a good overall agreement with the same parameters $w_0$ and $W$ for all of them. The results obtained from the correct parameter values for all calibrations of heating rates are reported in fig.4.5 for the pure silica sample (L02). The parameters are given in table 4.2. This cross-checking made between the other TL curve combination confirms that these values always anticipate correctly the TL peak shift and lowering.
The corresponding DOTS obtained with this procedure for each couple of TL curves reported in fig.4.5, are superimposed in figure 4.6. As one can see, they are well superimposed showing that the best parameter values are found. In practice, we retain the average of these 6 energy distributions as the best DOTS estimate.

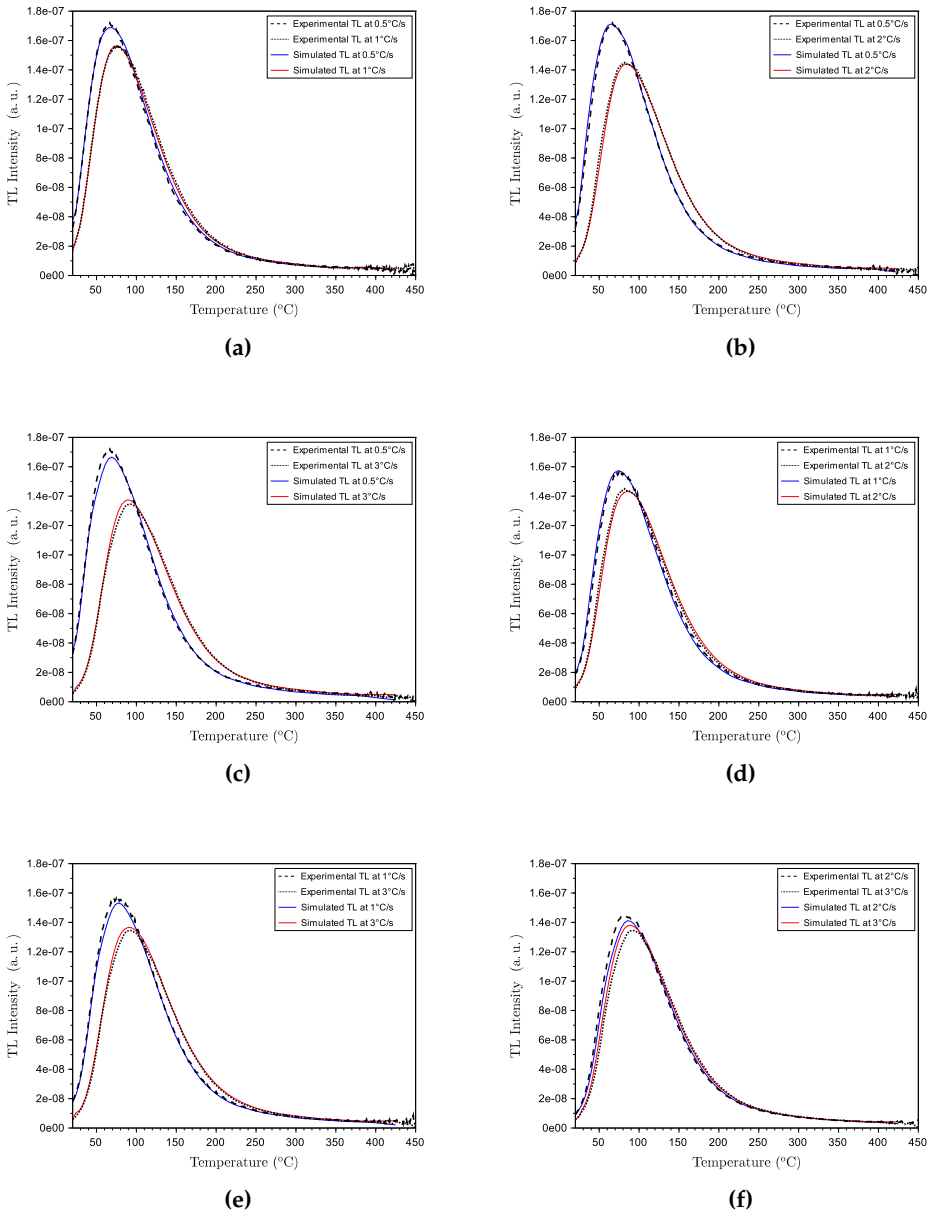


**Figure 4.5:** Experimental TL and simulated TL curves obtained from the first order kinetics simulations for the pure silica sample (L02) after irradiation in standard conditions. The TL curves recorded at heating rates q1 (blue line) and q2 (red line). The predicted TL (dashed line) at q1 and q2 (dotted line) are calculated from KM(q1)$\mathbf{n_0}$(q2) and KM(q2)$\mathbf{n_0}$(q1), respectively. For each subfigure, the heating rates q1-q2 corresponds respectively to: 0.5-1 °C $s^{-1}$ a) 0.5-2 °C $s^{-1}$ b) 0.5-3 °C $s^{-1}$ c) 1-2 °C $s^{-1}$ d) 1-3 °C $s^{-1}$ e) 2-3 °C $s^{-1}$ f). The values of the main parameters used for these simulations are reported in table 4.2.

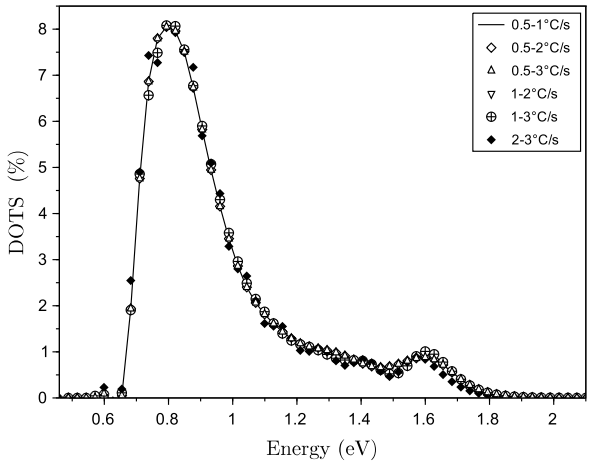


**Figure 4.6:** DOTS generated by a "standard" irradiation in the pure silica (L02) sample, as extracted from each pair of TL curves.

Fig.4.7 reports the DOTS extraction results on Q25 sample (see table.4.2 for the parameters). TL curves are recorded (symbols) at two heating rates (q = 1 and 2 °C $s^{-1}$) after irradiation in standard conditions. Cross-checking by predicting TL (solid lines) at 1 and 2 °C$s^{-1}$, calculated from KM(1)$\mathbf{n_0}$(2) and KM(2)$\mathbf{n_0}$(1), respectively. The couple of DOTS extracted are not well superimposed such as the ones obtained for L02 sample. This is ,most probably, a consequence of the quality of the TL curves on Q25, which are quite noisy. Indeed F-doped silica is "radiation-resistant " and the TL intensity from such doped silica is weak.

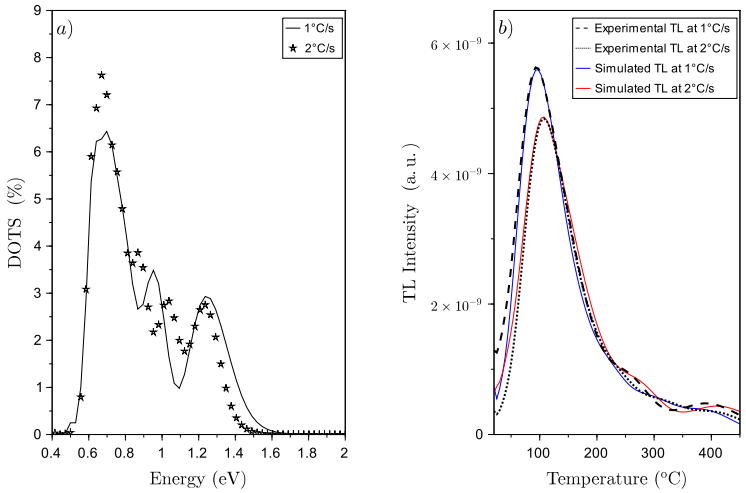


**Figure 4.7:** DOTS a) extracted from the TL curves in b) (dashed line) recorded at heating rates q = 1 and 2 °C$s^{-1}$ for the F-doped silica sample (Q25) after irradiation in standard conditions. The predicted TL in a) (solid lines) at 1 and 2 °C$s^{-1}$ are calculated from M(1)$\mathbf{n_0}$(2) and M(2)$\mathbf{n_0}$(1), respectively.

| | L02 | Q25 |
|---|---|---|
| Frequency factor $w_0$ ($s^{-1}$) | $5 \times 10^9$ | $5 \times 10^9$ |
| Mott-Seitz factor $C$ | $10^8$ | $10^8$ |
| energy barrier $W$ (eV) | 0.072 | 0.12 |

**Table 4.2:** Parameters obtained from the DOTS extraction for L02 and Q25 samples reported in fig.4.6-4.7a and the simulated TL of fig.4.5-4.7b.

**Discussion on the applicability of the first order approximation** The pure silica sample L02 were also irradiated in IRMA conditions. The $\gamma$-irradiation was performed using a total dose and an irradiation time ($t_{irr}$) much higher respect to one used in standard conditions (such as to perform the TL measurements of fig.4.5). Moreover, the time spent between the end of the irradiation and the TL readout ($t_{relax}$) is much longer respect to the one usually spent during our experiment. A comparison of both conditions is reported in table.4.3.

| | standard | IRMA |
|---|---|---|
| irradiation time (min) | 15 | $2 \times 10^4$ |
| time relax (min) | 1.5 | $3.7 \times 10^4$ |
| Dose (Gy($SiO_2$)) | $3 \times 10^3$ | $10^6$ |
| Dose rate (Gy($SiO_2$)/min) | 200 | 50.3 |

**Table 4.3:** Details of experimental conditions: standard and IRMA ones.

We want to highlight the difference of these conditions to support the application of the DOTS extraction on the TL measured from IRMA experiment. The TL measurements on L02 sample irradiated at 1MGy at IRMA facility were performed at 1°C/s. The corresponding DOTS have been extracted with the same parameters adopted to extract the DOTS in standard conditions summarized above in table 4.2. The results of both TL recorded in standard and IRMA conditions are reported in fig. 4.8a. The extracted DOTS from both TL curves are then displayed in fig.4.8b. The DOTS obtained for such different irradiation conditions contain similar structures, but the intensity and the demarcation energy is different, due to the total dose and the much longer $t_{relax}$ respect to the standard case. Due to the much intense irradiation, the DOTS extracted from the TL following the IRMA irradiation are 10 times more intense than the standard DOTS, whereas the demarcation energy $E_D$ is increased from 0.74 to 0.94 eV from standard to IRMA conditions. Since the populated levels probed by TL have shifted toward deeper states, the IRMA glow curves raise from a higher temperature and reach their main peak around 160 °C instead of 75 °C.
The TL recorded in these two different conditions, present a different intensity ratio between the peak and the shoulder at 350°C. The relative intensity of this shoulder, with respect to the main peak intensity, is significantly increased in IRMA TL. The TL shoulder, being above the TL peak, is due to deeper trapped states.

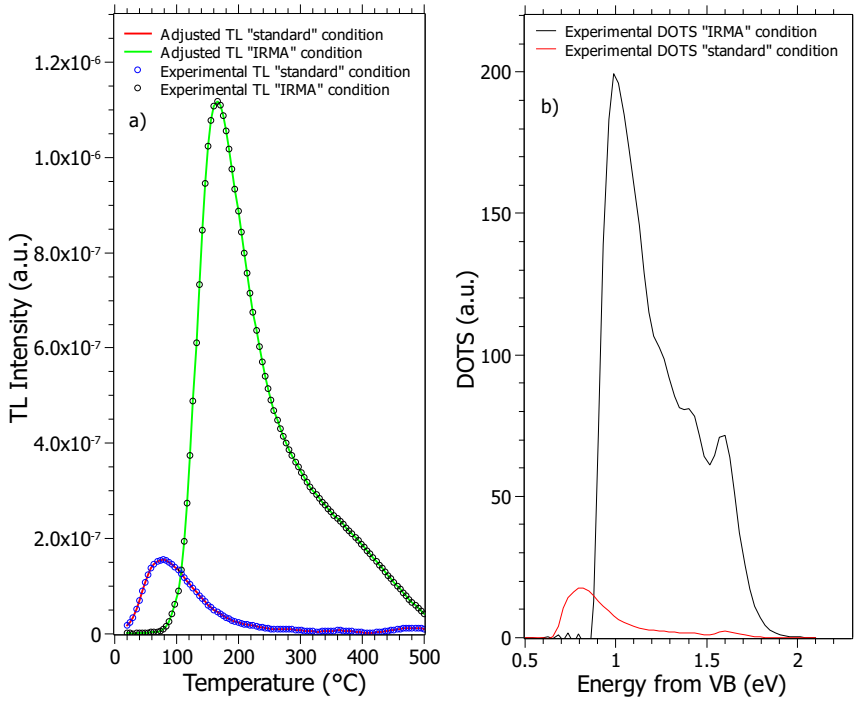


**Figure 4.8:** TL curves and DOTS from undoped sample L02 measured at q = 1°C/s in standard and IRMA condition a) Experimental TL and TL re-built from the DOTS $n_0$ in b) according to K**M**$n_0$ at 1°C/s.

This is directly explained by the fact that deep trapped states responsible for these high-temperature TL components are relatively more populated with respect to the maximum of the DOTS [174]. Under IRMA irradiation, the total density of trapped holes is increased respect to that obtained under standard irradiation, as a consequence of the higher dose given to the material. But since these levels remain much deeper, the continuously shifting demarcation energy only store up trapped holes whereas those crossing this energy are affected by a detrapping slowing down the filling. Because of this effect of time, the total density of the trapped states increases by favoring the relative fraction of carriers located in the deep states. In other words, the holes gradually condense into deep traps during irradiation [174]. This condensation effect could be reinforced by the post-irradiation time elapsed before the TL measurement. During this period, the demarcation energy is still progressing towards high activation energies and the population of deep traps could be further increased by the re-trapping of holes emitted from the shallow levels reached by $E_D$. This contribution may be significant if the re-trapping of released holes prevails over their recombination. In this case the basic hypothesis of first order kinetics on which we based the DOTS extraction procedure would fail. In most samples presented in this thesis there is however strong evidence that recombination well dominates re-trapping. The only case where this evidence is not obvious is that of Ge-doped silica. Anyway for this type of doped fiber we proceed with a particular modeling because of specific features that we will show ad the end of this chapter.

The first approximation seems to be consistent with these results. Considering the

higher delivered dose in the case of IRMA irradiation with respect to the standard one, we expect to observe more electron hole pairs created in a proportional way with the delivered dose. Contrary to what was expected, the maximum TL recorded after IRMA irradiation is just increased by a factor ∼7.3. Basically, despite the delivered dose (which we note is $\sim$ 300 times higher than that given in standard irradiation), most of excess pairs have disappeared by recombination, which therefore prevails over trapping. The total trapped-hole density overall increased but the DOTS following standard and IRMA irradiations are not simply proportional [174]. We can note that respect to the DOTS left by standard irradiation (red line in fig.4.8b, the DOTS maximum left by IRMA irradiation (black line in fig.4.8b is increased by a factor $\sim$ 10, whereas at higher energies such as the DOTS peak at 1.6 eV, just by a factor $\sim$ 30. The main change introduced by IRMA is related to a time effect reflected in the increase of the demarcation depth and in the subsequent condensation of holes in deep levels. Another strong indication for prevailing recombination over trapping is the sub-linear dose dependence of the TL intensity, which will be observed below.

### 4.1.4 Dimensionless formulation

From the first order analysis we obtained the relative DOTS and reduced the number of unknown parameters of eq. (4.1)-(4.4) from 125 to only 5: N, H, $\gamma$, $\delta$ and $\beta$. At this point of the procedure, it is in principle possible to solve the system of differential equations.
But the modeling of radiation-induced processes can be further refined thanks to a new formulation which is based on the dimensionless treatment of equations (4.1)-(4.4).
The dimensionless equations are obtained dividing the equation (4.1)-(4.4) by $\beta N^2$ [182], always under the assumption that all traps have the same capture cross-section. $\beta N^2$ is a quantity measured in $cm^{-3}s^{-1}$, which corresponds to the maximum trapping rate $\beta N$ of each single free carrier multiplied by the density of trap N. It thus corresponds to the maximum trapping rate per unit volume in a case where the density of free carriers is equal to that of traps. With this normalization, one obtains:

$$\frac{du_c}{d\tau} = R - u_c \sum_{k=1}^{M} \xi_k(1-\varphi_k) - \frac{r}{\alpha} u_c \varphi_h + \psi \sum_{k=1}^{M} \xi_k \varphi_k exp\left(\frac{-E_k}{k_B T}\right) \tag{4.21}$$

$$\frac{d\varphi_k}{d\tau} = u_c(1-\varphi_k) - \sum_{k=1}^{M} \psi \varphi_k exp\left(\frac{-E_k}{k_B T}\right), k = 1...M \tag{4.22}$$

$$\frac{du_v}{d\tau} = \frac{R}{r} - \frac{\theta}{\alpha} r u_v (1-\varphi_h) \tag{4.23}$$

$$\frac{d\varphi_h}{d\tau} = \frac{\theta}{\alpha} u_v r (1-\varphi_h) - \frac{1}{\alpha} u_c \varphi_h \tag{4.24}$$

In (4.21), $\varphi_k = n_k/N_k$ is the trap filling rate of the $k^{th}$ trap. $r = H/N$ is the ratio of the density of hole traps to that of electron traps. $\psi = N_c/N$ where $N_c$ is the equivalent density of states in the CB, $\xi_k = N_k/N$ is the relative fraction coefficient

of each trap k, $R = g_0/\beta N^2$ is the dimensionless dose rate coefficient, $u_c = n_c/N$ and $u_v = h_v/H$ are the populations $n_c$ and $h_v$ normalized by the density of traps, as well as the RC occupancy rate $\varphi_h = h_v/H$; finally $\tau = \beta N t$ is the reduced time, $\alpha = \beta/\gamma$ and $\theta = \delta/\gamma$ are the coefficient representing the competition between electron trapping-recombination and hole trapping-recombination, respectively.
Contrary to what happens in the standard equations reported at the beginning of this chapter, the system described by these new equations is not determined by individual parameter, but by dimensionless ratios accounting for the main competition between transitions: $\alpha$= $\beta/\gamma$, $\theta$= $\delta/\gamma$ and accounting for the concentration of hole against electron traps.
This demonstrates that the system is not determined by individual parameters, but by the value of their ratios. Such ratios being given, we only need to define one density ($N$ or $H$), and one transition parameter ($\alpha$, $\delta$ or $\gamma$).
In this work, we used to set $\beta$ and $N$. Once $N$ and $\beta$ are set, the value of $\psi$ is known, since $\psi = N_c/N = w_0/\beta N$ where the frequency factor $w_0$ is known from the first order analysis. It is worth to remind that the thermal extinction parameters $C$ and $W$ involved in the simulation of TL, are also known from the first order analysis.
In practice, the choice of the transition parameter value ($\beta$), sets the kinetics of the simulated processes. The choice of a value for the density of traps ($N$) sets the saturation degree of the traps, given that the total density of the free electron-hole pairs $N_{EHP}$ injected by irradiation is fixed experimentally by the total dose given to the sample. Since this density is $N_{EHP} = g_0 t_{irr}$ ($cm^{-3}$), one has $\frac{N_{EHP}}{N} = \frac{g_0}{\beta N^2} \times \beta N t_{irr} = R\tau_{irr}$, a ratio which measures to the dose in a dimensionless form. $\frac{N_{EHP}}{N} \ll 1$ means that the system will remain far below saturation, and conversely.
In summary, the solutions of the equations (4.21) - (4.24) are only determined by 5 parameters: $\beta$, $N$, $\theta$, $\alpha$, $r$. In the next section it will be noted that these parameters are actually 4, because of the choice of a very small $\alpha$ value (and then set as a known parameter) according to the first order modeling. We argue in the next section that the first order approximation is justified for most of the samples tested in this thesis.

### 4.1.5 On the validity of the first order approximation of the TL processes in our materials.

This section discusses on the validity of the first order approximation of the TL processes in our samples. This choice, which is translated into adopting $\alpha \ll 1$ ($10^{-5}$ in our simulations), is well justified for all the samples tested in this thesis, exception made for Ge-doped ones, which always require a separate discussion because of the particularities that this element introduces. The technique of DOTS extraction presented above, has been demonstrated in [174] to apply very well to various silica-based fiber preforms with different core compositions (pure silica, silica doped with aluminum, phosphorus, erbium or ytterbium). Here we will keep to prove the solidity of this method showing other results concerning similar samples as those used in [174].
As it will be reported further, for such kind of doped silica, extracted DOTS always consist of a distribution of trapped-hole states. Before has been proven the consistency between the DOTS extracted after two different irradiation conditions: the

first one obtained in a standard configuration in our laboratory (X-rays irradiation at 200Gy($SiO_2$)/min at RT and TL recorded after 90s from the end of the irradiation), the second one by IRMA condition (see 2.6.3), as reported previously in the experimental results of this thesis. It has been found that the main change introduced by IRMA conditions is related to a time effect reflected in the increase of the demarcation depth and in the subsequent condensation of holes in deep levels.

**Simulation with the general model [eq.(4.21)-(4.24)]** In the previous section, the modeling procedure has been explained following a standard energy level scheme used to explain the TL phenomenon, such as the one represented by Fig. 4.2. This means that we reported eq. (4.21)-(4.24) considering that TL traps are electron traps and RCs are trapped holes. From the experimental results of chapter 3, we proposed a reverse scheme respect to this standard one and represented in Fig.4.9 for pure silica. We already argued that the recombination mechanism involves the recombination of thermally released holes at trapped electrons, such as the $SiODC^-$ center. This claim is also valid for all the doped silica samples investigated in this work.
The proposed energy level scheme needs new modified equations, which basically are similar to eq. (4.21)-(4.24) but in a "reversed"scheme, where the role of electrons and holes is simply switched. The same equations will be also used for radiation sensitive samples, whereas for Telecom grade samples a specific model with appropriate differential equations will be required.

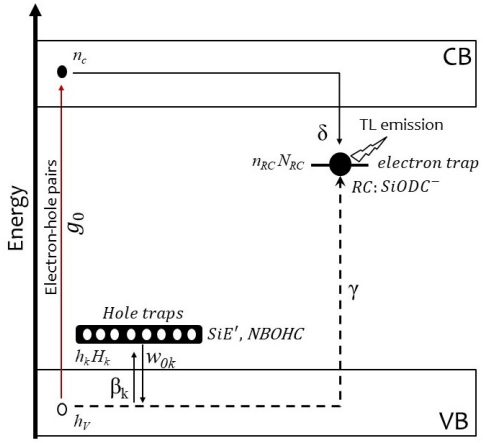


**Figure 4.9:** Diagram of trapping/recombination processes in silica samples.

The DOTS extraction protocol provided the DOTS reported in fig.4.6 and a starting set of $H_k$. This $H_k$ set is subsequently properly adjusted by simulating the DOTS formed under irradiation and by comparing the related TL (the theoretical TL corresponding to these DOTS) with experimental TL curves at different doses.
Then, using the parameters we obtained, we can also simulate the effect of the heating rate on the TL. We can also check the good agreement between simulated and experimental dots. This is basically an internal consistency because we simulate in the same irradiation conditions. We will show that anyway we can predict both DOTS and related TL in very different conditions.

The remaining parameters are: $\alpha$, $\theta$ ,r, N and $\beta$ and $\alpha$. How they are estimated is explained in what follow, where are also shown the results obtained from the simulation with the general model.

**Parameters estimation:TL simulation at different irradiation doses** The prediction of the TL at different doses is helpful to fix $\alpha$, stating whether re-trapping is negligible ($\alpha \ll 1$) or significant ($\alpha = 1$). The case of $\alpha \ll 1$ is in fact a strong precondition required by the first order approximation.
We argued that detrapping/recombination process well obey first order kinetics, that is $\alpha \ll 1$. Then, to meet this condition, we set the value of $\alpha = 10^{-5}$.
The other parameters $r$ and $\theta$ are found to have only a negligible impact on the simulation results across decades (between $10^{-3} - 10^{3}$). Then we choose for convenience the central values of $r = 1$ and $\theta = 1$.
The trapping coefficient $\beta$ and the trap density $N$ appear to be the most important parameters. In practice, $N$ sets the saturation degree, so is best estimated from the dose dependence of the TL response. $\beta$ is such that $w_0 = \beta N_c$, but it is well-known that the equivalent density of state $N_c$ is usually between $10^{18}$ and $10^{20}$ $cm^{-3}$. Considering that $w_0$ is known from DOTS extraction, we can deduce the order of magnitude of $\beta$, say at one decade. The values of ($\beta$, N) are also adjustable in such a way that the DOTS produced when simulating the trap filling during irradiation and after irradiation must be identical to that extracted directly from the TL curves (experimental DOTS). DOTS are now generated (or simulated, which means build by simulating the irradiation and trap filling), not extracted, We can use this simulation to predict the DOTS and the related TL in other conditions that differs from standard irradiation conditions. So we can simulated the dose dependence, from which we get a refined estimate of N and $\beta$. These determining parameters have been calibrated to make this experimental DOTS successfully reproduced by the general simulation of the irradiation and relaxation phase (trap filling state at $t_{irr} + t_{relax}$). Once all the other parameters are calibrated and validated in our standard irradiation conditions, we are able to predict the DOTS (and associated TL) in different experimental conditions. Notably those that are not achievable in laboratory, changing $t$, $T$, $D$ and $\dot{D}$. Precisely, the following results are obtained from the prediction of the DOTS at several $t_{irr} + t_{relax}$ (then at different doses) different from the ones used in the calibration procedure.
From these simulated DOTS we obtain the TL to compare with the experimental ones recorded at the same irradiation times and doses. These results are reported in Fig.4.10 and has been obtained by general model using the parameters reported in table 4.4. Figure shows the areas of the TL areas measured and simulated ine Q25 sample (1.19$at.$% of F in the core) as function of the irradiation dose.
The TL was recorded after each irradiation, at several doses, from 500 Gy to 3000 Gy, using a dose rate of 200Gy/min. Due to the low level of the TL intensity, the TL glow curves were very noisy and the calculated area from each curve was therefore characterized by a bigger error than usual. A power-law fit of the simulated points reveals a variation in $D^{0.8}$. As one can see, the agreement between the experimental points and the simulated ones is good. The simulated results are obtained from the parameter reported in table 4.4 changing the irradiation times, obtaining 6 irradiation doses from 500 Gy to $3 \times 10^3$ kGy.

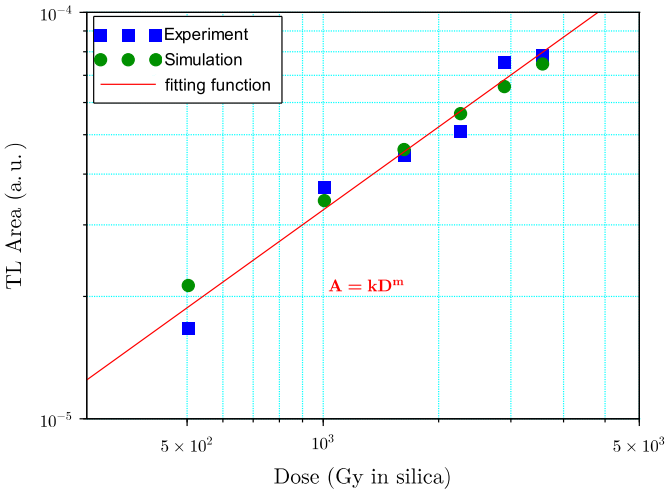


**Figure 4.10:** Experimental and simulated TL curve areas on the Q25 sample as a function of the dose and power-law fit $A = k * D^m$ (red line) of the simulated points, with $m = 0.8$.

| | Q25 |
|---|---|
| Trap density $N$ ($cm^{-3}$) | $1.3 \times 10^{22}$ |
| Trapping coefficient $\beta$ ($cm^3 s^{-1}$) | $10^{-10}$ |
| $\alpha = \beta/\gamma$ | $10^{-5}$ |
| $\theta = \delta/\gamma$ | 1 |
| $r = H/N$ | 1 |
| frequency factor $w_0$ ($s^{-1}$) | $5 \times 10^9$ |
| Mott-Seitz factor C | $10^8$ |
| Energy barrier W (eV) | 0.12 |

**Table 4.4:** Parameters used for general simulation to obtain the simulated DOTS and corresponding TL of fig. 4.10 in Q25 sample. $C$ and $W$ are just used to simulate the TL and are obtained from DOTS extraction, along with the frequency factor $w_0$. $N$ and $\beta$ are adjusted from the general simulation of the DOTS and dose dependence.

We now want to show how $\alpha$ selection is decisive in predicting the TL behavior as the dose varies. Using $\alpha = 1$, which then moves us away from the first order approximation, we get the TL simulated areas of figure 4.11 (with otherwise the same parameters of table 4.4). From a power-law fit revealing the dependence $D^{1.21}$, we see that the trend is markedly different from the experimental one, showing a super-linear increase with the total dose. This proves that the first order approximation (made a priori to stem the problem of an otherwise unsolvable model) is strongly supported by experimental data.

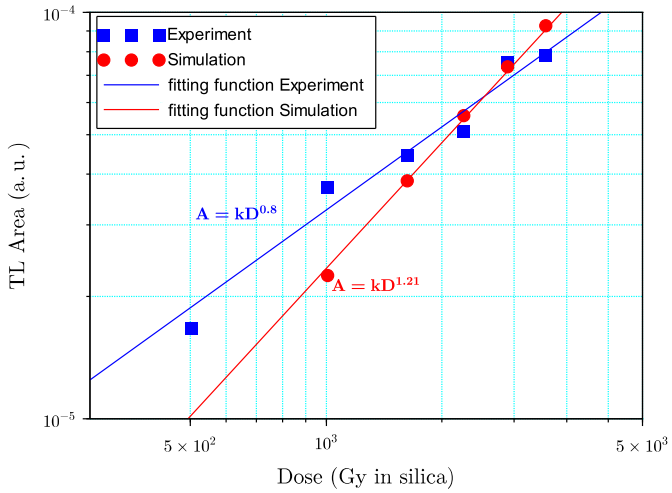


**Figure 4.11:** Experimental and simulated TL curve areas on the Q25 sample as a function of the dose obtained using $\alpha = 1$ in the simulation. The power-law fit $A = k * D^m$ (red line), reveals a super-linear increase, with a slope m=1.21.

The DOTS obtained from these simulations, giving the TL areas of fig. 4.10, are reported in fig. 4.12. One can see the occupancy states at different doses (black lines) and the density of trapping sites (red line).

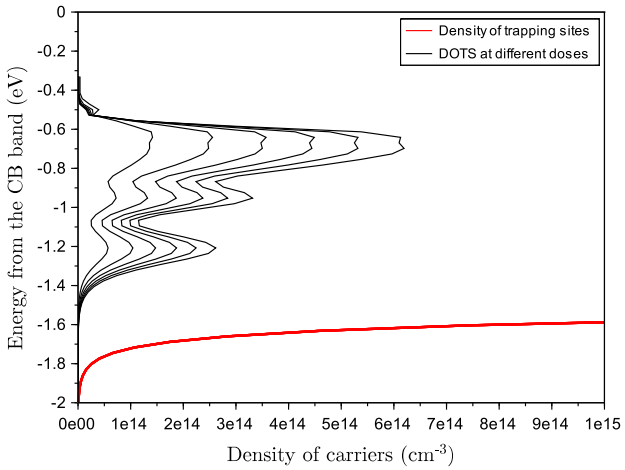


**Figure 4.12:** Trap filling states probed by TL reported in a representation where the ordinate is the energy from the CB and the abscissa the density of carriers ($cm^{-3}$). The black curve represents the occupancy states at different doses (from 500 Gy to $3 \times 10^3$ kGy) and the red one is the density of trapping sites, both simulated from the TL reported in fig.4.10 from the general order simulation.

As one can see from fig.4.12, the trap filling remains far from saturation, at the dose level used in fig.4.10 and 4.11. This is in agreement with results of chapter

3, where this was shown to be the case for all the tested samples. The TL studies as a function of the irradiation dose, indeed, indicated that at the maximum dose level delivered to the samples the TL, and therefore the trap sites, are still far from saturation. Therefore, the sublinear dose dependence of the TL response is not due to the fact that trap filling approaches saturation but well to the fact that $\alpha \ll 1$. If $\alpha$ was close to 1, the dose dependence would be closer to linearity as in fig.4.11. It however remains that the density of traps $N$ has been adjusted to reproduce at best the dose dependence of the TL response. This dose dependence is an important point for the calibration of $N$.
Finally, we want to observe that in fig.4.12 the density of states in x-axis is expressed in $cm^{-3}$, but its order of magnitude is not correctly calibrated. Also the value of the density of traps $N$ is not physically realistic; considering for example that in silica the density of Si atom is around $5 \times 10^{22} cm^{-3}$. This problem is due to the lack of the shallower levels in the DOTS. The density of trapping sites cannot be predicted for shallow states that are not probed by TL measurements in our experimental conditions. The density of trapping sites must be extrapolated between the demarcation energy $E_D(T_0,t_{TL})$ and a certain minimum depth considered in the simulation (between 0.5 and 0.6 eV). Unfortunately, this extrapolation takes the form on an exponential tail growing towards the VB edge, so it introduces an artificial, but very large density of trapping sites below $E_D$. This has two consequences: first, the total density of states $N$ is very large and then overestimated. Second, this leads to a large underestimate of the density of TL traps (those levels above $E_D$), and hence of the density of trapped carriers.
As the total density of considered traps is related to the all levels included in the simulation, this amount brings to an underestimation of the density of trap levels involved in the production of the TL (at an energy level deeper than the demarcation energy $E_D(T_0, t_{TL})$). Only a refined knowledge of the density of traps with energy smaller than the demarcation energy reached at the start of the TL reading would allow a correct quantitative reproduction of the density of traps and trapped carriers.

**Effect of the heating rate** Once all the parameters are found and validated, it is possible to simulate correctly the effect of the heating rate with the general simulations model. We expect that the DOTS simulated under standard conditions well predict the TL (in shape and position). As well as the simulated TL at different heating rates will predict the correct decrease in intensity and the shift of the peak using the Mott-Seitz factors $C$ and $W$ (already estimated from the DOTS extraction procedure). In Fig. 4.13a are reported the experimental TL curves (dashed line) acquired at 4 heating rates on L02 sample. Whereas fig.4.13b shows the comparison between the simulated DOTS and the re-normalized extracted DOTS, from the first order procedure. Both have been calculated in the standard condition used to acquire the TL: Xray radiation of 3kGy with a dose rate of 200Gy(SiO2)/min and a relaxation time between the end of the irradiation and the TL readout of 90 seconds. Of course the agreement between the experimental and simulated one is perfect by construction, since to simulate the DOTS are used the conditions on which our calibration procedure is based.

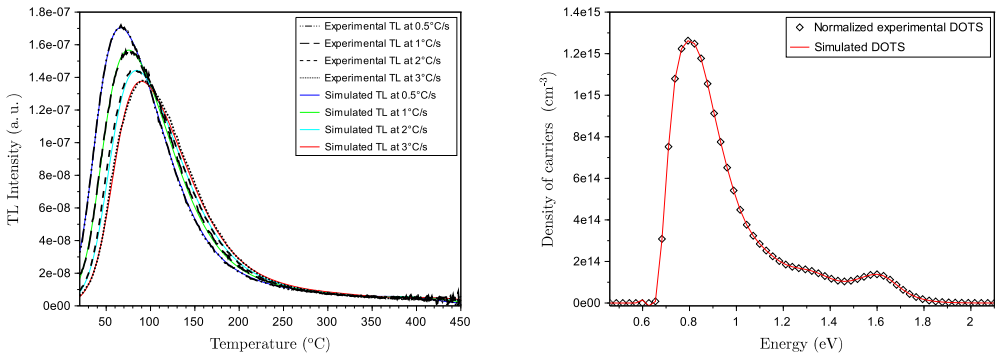


**(a)** **(b)**

**Figure 4.13:** a)Experimental and simulated glow curve at four heating rates: $0.5^oC/s$, $1^oC/s$, $2^oC/s$, $3^oC/s$ in the L02 sample (pure silica). b) Extracted DOTS (scatter graph) normalized with respect to the simulated one (red line) by general model in standard conditions.

From the simulated DOTS we obtained the theoretical TL in fig.4.13a (solid lines). The simulation parameters are summarized in table 4.5 for the L02 sample.

| | L02 |
|---|---|
| frequency factor $w_0$ $(s^{-1})$ | $5 \times 10^9$ |
| Trap density $N$ $(cm^{-3})$ | $4 \times 10^{21}$ |
| Trapping coefficient $\beta$ $(cm^3 s^{-1})$ | $10^{-10}$ |
| $\alpha = \beta/\gamma$ | $10^{-5}$ |
| $\theta = \delta/\gamma$ | 1 |
| $r = H/N$ | 1 |
| Mott-Seitz factor C | $10^8$ |
| Energy barrier W (eV) | 0.072 |
| r | 1 |

**Table 4.5:** Parameters used for general simulation to obtain the simulated DOTS and corresponding TL of fig.4.13a in the L02 sample. $C$ and $W$ are just used to simulate the TL and are obtained from DOTS extraction, along with the frequency factor $w_0$. $N$ and $\beta$ are adjusted from the general simulation of the DOTS.

The dashed black lines and the colored continuous ones represent the measured and the simulated TL curves respectively. The agreement between the experimental curves and the simulated ones is good. This result is obtained with $\alpha \ll 1$, i.e. in condition of a weak re-trapping where recombination is dominant. This condition is consistent with the fact that a first-order TL process is well the case for silica. Anyway the TL prediction at 4 heating rates is possible also in a non negligible re-trapping case (for example with $\alpha$=1) [174]. This confirms that the assumption of negligible re-trapping is certainly sufficient but not required to accurately account for the TL measured at different heating rates. This is therefore not this type of

measure that can provide a definite proof of the validity of the first-order approximation of the TL process, but the sublinear dose dependence of the TL response. The case of $\alpha \ll 1$ is in fact a strong requirement, in our general model, to reproduce correctly by simulation the experimental dependence of the TL response on the dose. Once all the other parameters are calibrated and validated in our standard irradiation conditions, we are able to predict the DOTS (and associated TL) in different experimental conditions. Notably those that are not achievable in laboratory (changing $t$, $T$, $D$ and $\dot{D}$).

**On the ability of the model to predict at different t, T, D and dose rate** This calibrated model is able to predict the DOTS and related TL curve in different experimental conditions, which therefore take into account the variability in time, temperature, dose and dose rate. To confirm this ability we present now the prediction of the DOTS and glow curve produced after irradiation in IRMA condition. The details of this experimental conditions are reported in table.4.3. It is worth to note that passing from standard to IRMA conditions means that the dose is multiplied by 333 to reach 1MGy, the irradiation time is multiplied by 1333 and the relaxation time by 24960.
Fig.4.14a shows a comparison between the experimental TL recorded on the L02 sample in standard and IRMA conditions, and the predicted ones. These latter are obtained from the DOTS simulated in the same conditions (standard and IRMA) reported in Fig.4.14b.

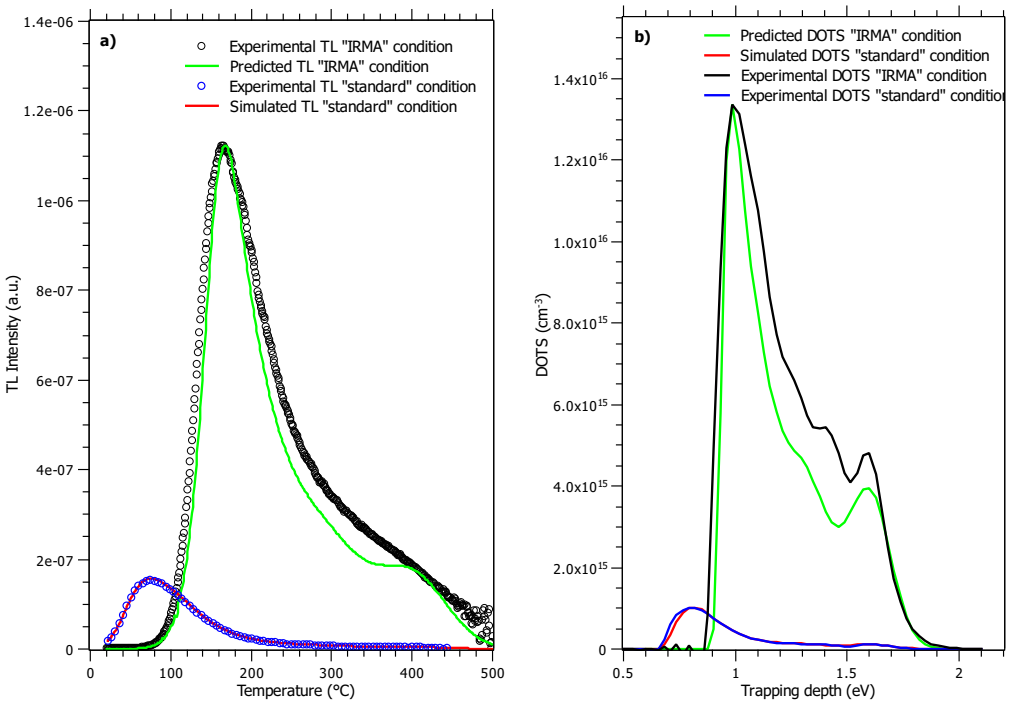


**Figure 4.14:** TL curves and DOTS from undoped sample L02 measured at $q$ = 1°C/s in standard and IRMA conditions a) TL experimental and predicted one from the simulated DOTS in b) using in the general model the parameters in table.4.5.

The simulated DOTS are compared to the experimental one obtained by DOTS extraction procedure, already shown in fig.4.8. Note that the model has been calibrated in standard laboratory conditions, and that no further adjustment has been made to obtain the DOTS and TL predictions in IRMA conditions. As one can see from the simulated TL, the peak shift is very well predicted (from 70°C to 130°C), whereas from the DOTS comparison (black and green line in fig.4.14b we can observe that the demarcation energy is shifted up to the same energy (which demonstrates clearly that kinetics are correctly rendered and anticipated). Moreover, the quantitative error in the intensity of the DOTS and TL is within the TL experimental error (between 5 and 10%). These results well support the validity of the model, since this prediction take into account experimental conditions very different from those on which the model is calibrated.

### 4.1.6 RIA modeling

The RIA observed in the UV-Visible range, due to the presence of color centers (CC), can be decomposed in optical absorption (OA) bands related to these CCs. From the well known Smakula formula for gaussian bands [183], it is possible to determine the density of CC ($N_k$ in $cm^{-3}$) knowing some physical parameters such as the amplitude ($a_k$) and the FWHM ($W_k$) of each $k^{th}$ OA band, its oscillator strength ($f_k$) and the refractive index $n$ of the medium. Conversely, if $N_k$ is known (for instance from the DOTS), it is possible to obtain one of the unknown parameters (for instance the OA band amplitude) from equation (4.25).

$$N_k \times f_k = 8.7 \times 10^{16} \times \frac{n}{(n^2+2)^2} \times W_k \times a_k \tag{4.25}$$

The amplitude and the FWHM of the gaussian band are expressed in $cm^{-1}$ and eV respectively. The settings $W_k$ and $f_k$ are easily found in the literature, but they may be marginally adjusted to best reproduce the measured spectrum.
Following this approach, we can reproduce the optical absorption band obtaining the value of their amplitude from the density of CC $N_k$ that can be found in the simulated DOTS. As seen before, from the TL simulation one can have access to the densities of trapped holes, according to their energy levels in the gap. As it will be shown further for pure silica and successively for other samples, these levels can be associated with some particular CCs.
So, once is known the density of each type of CC contributing to the RIA spectrum, it is possible to estimate the amplitude of their optical absorption band using equation (4.25) . Finally, the RIA spectrum is obtained from the superimposition of all calculated absorption bands.
The simulated DOTS are located within a 0.4-2.1 eV energy range above the VB. They show a main peak around 0.8 eV associated with that of the TL curve.
This value is reasonable since the one estimated experimentally from the initial rise method and represented in Fig.3.4 for an undoped silica sample, from which a depth of about 0.76 eV was estimated. This main peak most probably due to the truncation of the density of trapping sites existing between the valence band and $E_D$ by the occupation rate function at the beginning of the TL readout [174]. For deeper hole states, between 0.9 and 1.6 eV the DOTS can be considered the

result of the superimposition of several gaussian bands. Each one of them contains the depths associated with a particular CC, being the depth distribution for one CC due to some kind of in-homogeneous broadening. Some of these bands are always present in all our samples. It is the case for the components centered around 1.3 eV. In our RIA modeling, we tried to associate such bands to some radiation induced CC contributing to the RIA. Previous works by our team already demonstrated that one of the most important radiation-induced intrinsic trapped-hole centers in silica, the SiE' centers, release their holes in a temperature range around 250-275 °C during the TL process at $q$ = 1°C/s [77]. At this temperature we observed the bleaching of SiE' thanks to the thermal annealing protocol (bleaching map of fig.3.9). This observation proves the connection between the TL component at 250-275 °Cand the related energy in the DOTS. This energy component may be then associated to the SiE' center. In the framework of the first-order formalism of the TL peaks, differentiation of equation (4.13) gives the relationship between the depth $E_k$ and the temperature $T_k$ of the single TL peak it generates. It can be written as follow:

$$\frac{E_k + 2k_B T_k}{W} = \frac{Cexp(-W/k_B T_k)}{1 + Cexp(-W/k_B T_k)} + \frac{w_0}{q}\frac{k_B {T_k}^2}{W}\left(\frac{T_k}{300}\right)^2 exp\left(\frac{-E_k}{k_B T_k}\right) \tag{4.26}$$

According to equation (4.26) and given the values of $q$, $w_0$, $C$ and $W$ for L02 sample in table 4.5, TL components at 250 °C and 275 °C should correspond to holes trapped at 1.19 and 1.26 eV above the valence band, respectively [174]. Consequently, the holes trapped into levels between 1.2 and 1.4 eV in the DOTS of Fig.4.13b most likely correspond to holes forming the SiE' states.
In the DOTS of fig.4.13b is also present a band around 1.6 eV. Using again eq.(4.26) with the same parameters, one obtains that the temperature corresponding to this energy (1.6 eV) should be around 400°C, a temperature at which the annealing is almost complete both for TL and RIA spectra.
For completeness, we showed in fig. 4.14a the TL recorded in standard condition (3 kGy in 911 s, $t_{relax}$=90s) and the one at 1 MGy measured more than 26 days after the end of the $\gamma$ irradiation, already referred as "IRMA conditions"($\sim 1MGy$ in $\sim$ 14 days, $t_{relax} \sim$ 26 days, see table 4.3). In fig.4.15 are shown the DOTS extracted from these TL curve (experimental DOTS), together with the temperature correspondence (blue line) given by equation (4.26) for the L02 sample.
At 400°C the bleaching map resulting from the thermal annealing treatment reported in fig.3.9 does not report any particular feature. Anyway, considering the TL results in the same condition reported in fig. 4.15 (red line), we still have a shoulder at 400 °C (IRMA TL curve in fig. 4.14a). As already pointed out by our group [174], the relative intensity of this shoulder, which is increased by comparison with the case of a standard irradiation, can be explained by the fact that in IRMA irradiation conditions, the carriers localized in deep states are accumulated and such effect could be strengthened by the post-irradiation time that has elapsed before the TL measurement [174]. In fact, as the elapsed time between the irradiation and the TL readout ($t_{relax}$) was much more important in the case of " IRMA ", the demarcation energy has significantly progressed towards high activation energies and the population of deep traps has been further increases (beyond the

effect of a much more higher dose) by the re-trapping in deep states of holes emitted from the shallow levels reached by the demarcation energy [174]. Even if the re-trapping is weak compared to recombination, it does exist.

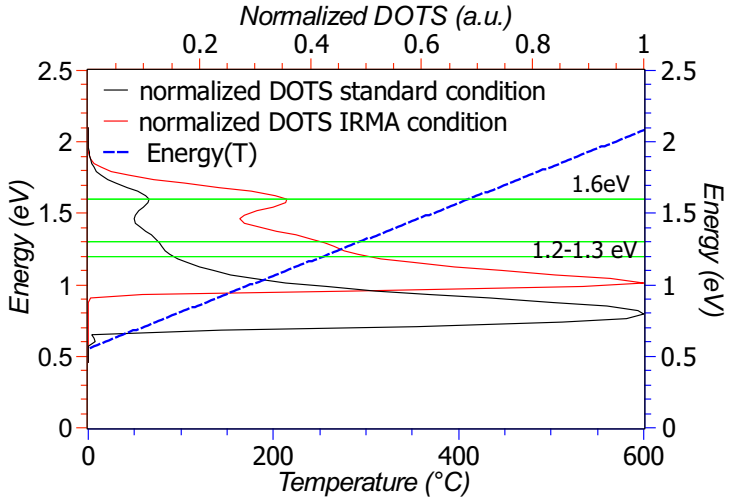


**Figure 4.15:** Comparison between the normalized DOTS extracted from the experimental TL in 4.14a. The blue line is the energy as a function of temperature obtained according to eq. (4.26) for the L02 sample.

A decomposition attempt of the DOTS obtained in standard conditions is reported in fig. 4.16. The exponential contribution (magenta line) corresponds to the intrinsic levels, that are the first to be depleted since they are the shallower with respect to the edge of the VB. The Gaussian band centered 1.3 eV (blue line) corresponds to the SiE' centers. The band centered at 1.6 eV corresponds to "other contributions"already explained above in this section. These two contributions were properly used in the RIA modeling as explained in what follows.

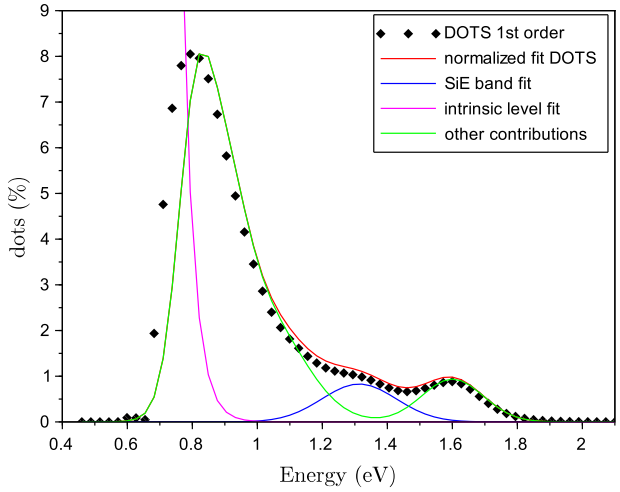


**Figure 4.16:** Attempt of DOTS decomposition of pure silica sample (L02).

From the experimental results reported in chapter 3, the processes of creation and destruction of color centers in pure silica were highlighted. As already said, the silica related CC present in the RIA spectrum were the trapping holes centers: NBOHC and SIE', whereas, from the TL and RIA annealing studies, it was demonstrated that were created also $SiODC : e^-$ centers upon electron trapping at SiODC (oxygen vacancies).
By summarizing, one can write a neutrality equation, stating that the amount of trapped $e^-$ and $h^+$ should be equal:

$$N_{intrinsic_{e^-}} + N_{SiODC:e^-} = N_{intrinsic_{h^+}} + N_{NBOHC} + N_{SiE'} \tag{4.27}$$

Where, in the left side we found the density of trapped electrons (which contribution is made by the intrinsic levels and the $SiODC : e^-$ density), and in the right side the density of trapped holes, composed by the densities of intrinsic levels, NBOHC and SiE'.
From the DOTS and their contribution we can obtain the concentration of the terms on the right hand side of this equation. The only term missing to be directly conducted to the DOTS decomposition is the NBOHC density. This center in fact contributes to the RIA, but they are not clearly associated with some levels present in the densities of states. But, knowing that SiE' centers and NBOHC can be produced in pairs from certain processes [34], we assumed that the NBOHC density is a fraction of that of SiE' centers. This fraction, being an adjustable parameter in the simulation of the RIA code, can be properly modified.
Concerning left hand side of the equation (4.27), we can get the $N_{SiODC:e^-}$ value from the TL simulations, given that the concentration of $SiODC : e^-$ is simply that of recombination centers (to one constant). The only missing contribution is that of the intrinsic levels below the CB ($N_{instrinsic:e^-}$). As already reported above, this problem is also responsible for a false quantification of the DOTS, due to the lack of TL information at temperatures lower than RT. From eq. (4.27) we can estimate this value since we have access to all the other terms, but we must to take into account that is an underestimation. As a consequence, we may apply a correction factor on the total trap density to make simulated RIA levels close to the experimental ones. In the resulting RIA in fig.4.17a, this corrective factor is 75.
Once the $N_k$ values calculated at all energies contained in each single DOTS contribution, we can use equation (4.25) to calculate the amplitude of the related OA band and simulate the RIA as explained above. The sum of each contribution (in this case 3 optical bands: 2 for NBOHC and 1 for SiE' centers) gives the total RIA spectrum. The RIA spectrum of the pure silica sample was reconstructed according to this approach. The calculation was based on the state distributions simulated for this sample at a dose of 10 kGy (SiO2), which result is shown in Fig. 4.17. The simulated spectrum in Fig.4.17a was optimized to reproduce the experimental spectrum of Fig.4.17b. The best agreement has been obtained for an NBOHC density equal to 33% of that of the SiE' centers. This value was estimated from gaussian fit of the experimental RIA, using the Smakula formula. We calculated the density of centers using an oscillator strength of SiE' and NBOHC of 0.14 and 0.05, respectively.
In figure 4.17 are reported the simulated and the experimental RIA on pure silica

sample. The characteristics of the simulated optical absorption bands of fig.4.17a, (which typical values of $x_c$, FWHM and oscillator strength drawn from literature [28, 46]), are reported in table 4.6. On the left of fig.4.17, the experimental curve (blackline) is normalized with respect to the simulated one (red line). As one can see from this comparison the simulated intensity predict quite well the experimental ones. Moreover the simulated bands are well located with respect to the fit made on the experimental curve and respect to the characteristic values found in literature. On the right side of fig.4.17b, the experimental curve (black line) is shown with its gaussian fit (red line) and the single absorption bands related to the characteristic color centers in silica: NBOHC and SiE' (blue and green lines respectively).

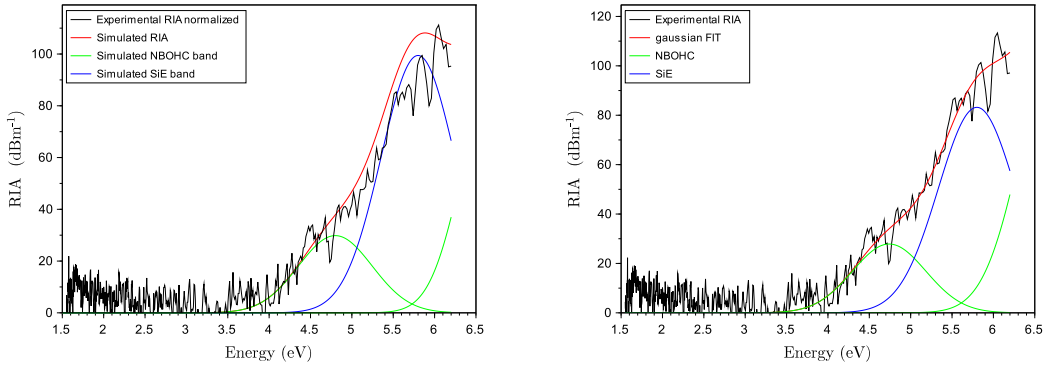


**Figure 4.17:** a) Simulated RIA and optical bands and experimental RIA normalized with respect to the simulated one for the L02 sample. b) Experimental RIA after X-ray irradiation at 10 kGy on pure silica sample and gauss fit.

| Defect | $x_c$ (eV) | FWHM (eV) | $f$ simulation | $f$ literature |
|---|---|---|---|---|
| NBOHC | 4.8 | 1.05 | 0.2 | 0.2 [32] |
| | 6.7 | 0.9 | 0.5 | 0.05 [35] |
| SiE' | 5.8 | 1.05 | 0.4 | 0.4 [32] |

**Table 4.6:** Characteristics of the simulated optical absorption bands of fig.4.17a. The bands centers and widths have been estimated from well-known admitted literature values [32, 35, 42].

This method will be properly adapted to all the other kind of samples tested in this thesis. The predictive capacity of our RIA simulations will be demonstrated through the anticipation of the RIA in IRMA conditions (for Al- and P-doped samples) and through the dependence of the RIA on temperature for Ge-doped samples (during annealing).

## 4.2 Radiation sensitive fibers

We now present the calibration of the simulation and their results for radiation sensitive fibers: Al- and P-doped silica samples, respectively labeled K04 and L28, (see table 4.7 for details). The results for these samples has been obtained following the procedure previously exposed for the pure silica and F-doped samples. We start showing the DOTS extraction procedure from the TL ("experimental DOTS"), from which we find the values for the frequency factor $w_0$ and the thermal quenching parameters $C$ and $W$. Then, we present the calibration of the general simulations of DOTS. As seen for radiation tolerant samples, this procedure allow us to find the unknown parameters necessary to the general model (the trap density N, the trapping coefficient $\beta$, the dimensionless competition rates $\alpha$ and $\theta$ and the ratio between hole and electron traps concentration$r = H/N$). This calibration is performed thanks to the study of the TL response changing the dose. The results predicted by these simulations, in terms of DOTS and TL, are validated against experimental data, showing the correct calibration of the model. Moreover, the DOTS simulated according to the irradiation conditions encountered in IRMA irradiation demonstrates the extrapolation capacity of our model. In fact, from the comparison between the experimental TL and the simulated one (obtained from the simulated DOTS), we can see whereas the simulated DOTS are well predicted or not. Finally, we present both the RIA modeling procedure the related results.

| sample name | doping | | characterization | |
|---|---|---|---|---|
| | Cladding | Core | *at.*% | Δn |
| K04 | Si | Al | 1.9 Al | $4.7 \cdot 10^{-3}$ |
| L28 | Si | P | 4 P | $4.5 \cdot 10^{-3}$ |

**Table 4.7:** Radiation sensitive fiber preforms under investigation.

In chapter 3 the process of creation and destruction of the radiation induced centers following the irradiation and the TL readout was described through a spectroscopic characterization of the samples. The energy level scheme in fig. 3.24 and 3.35, adopted respectively for P- and Al- doped silica, were reported in order to synthesize these processes, which are now expressed mathematically through the evolution of populations by a system of coupled non linear differential equations. The evolution of the electron population in the CB, in the RC and that of the hole population in the trap levels and VB is described by equations (4.1)-(4.4) or (4.21)-(4.24), previously reported for undoped silica. It is worth to remember that the role of electrons and holes in the equations is reversed also in this kind of samples, according to the scheme of fig. 3.24 and 3.35.

### 4.2.1 DOTS extraction

We now present the DOTS extraction results. The DOTS extraction procedure from the TL recorded at two heating rates, allows the access to the values for the frequency factor $w_0$ and the thermal quenching parameters: $C$ and the energy barrier $W$. These values are reported in table 4.8 for Al-doped (K04) and P-doped (L28) samples.

| | K04 | L28 |
|---|---|---|
| Frequency factor $w_0$ ($s^{-1}$) | $5 \times 10^9$ | $4 \times 10^7$ |
| Mott-Seitz factor C | $10^8$ | $10^8$ |
| Energy barrier W (eV) | 0.072 | 0.095 |

**Table 4.8:** Parameters used for 1st order kinetics simulation of fig.4.18 and 4.19 in K04 and L28 samples.

The DOTS reported in fig. 4.18a are extracted from the experimental glow curves of figure 4.18b on K04 sample. The TL measurements are recorded following the standard-laboratory conditions: irradiation dose D=3 kGy($SiO_2$), dose rate $\dot{D}$=200 Gy($SiO_2$)/min, irradiation time $t_{irr}$=15 min, relaxed time $t_{relax}$=90s (time spent between the end of the irradiation and the start of the TL readout).

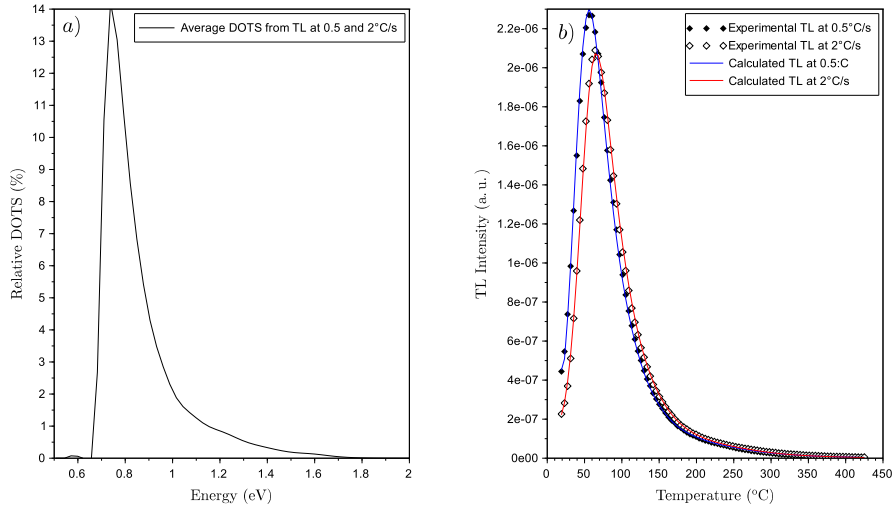


**Figure 4.18:** DOTS and TL curves of the Al-doped sample K04 measured in standard conditions. a) Average density of trapped states (DOTS) $n_0$ extracted from glow curves reported in (b) measured at 0.5 and 2 °C/s. The simulated TL curves in b) are re-built from the DOTS in a), according to $\mathbf{M}n_0$ at respective heating rates.

In these standard conditions, the DOTS is located within a 0.5-2 eV range above the VB. It shows a peak around 0.8 eV. This value is reasonable given the one estimated experimentally, as reported in Fig.3.29 for Al-doped sample, which shows the energy trap depths evaluated according to the initial rise (IR) method. In Fig.3.29 one can see that to the TL peak at 75 °C corresponds an activation energy level lying between 0.6 and 0.9 eV. This experimental range well correspond to that of the main DOTS peak in fig.4.18a, thus demonstrating that the DOTS extraction is correctly scaled in energy.
The DOTS reported in fig. 4.19a is extracted from the experimental glow curves of figure 4.19b measured in the P-doped sample L28. The DOTS are located within a 0.5-2 eV energy range above the VB. It has a main peak at about 0.7 eV. This value is consistent with the one estimated experimentally by the initial rise method

and represented in Fig.3.19 for P-doped silica sample, where the main peak were demonstrated to be associated with activation energy in the 0.6-1.2 eV range.

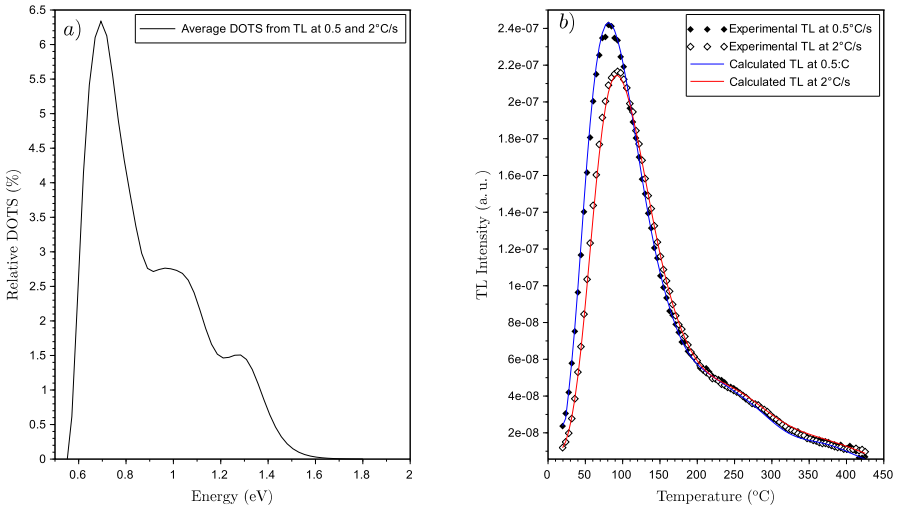


**Figure 4.19:** DOTS and TL curves of P-doped sample L28 measured in standard conditions. a) Average density of trapped states (DOTS) $n_0$ extracted from glow curves reported in (b) measured at 0.5 and 2 °C/s. The simulated TL curve in b) are re-built from the DOTS in a), according to $\mathbf{M}n_0$ at respective heating rates.

Both DOTS of Fig.4.18a-4.19a in the K04 and L28 samples, respectively, are located between 0.4 and 1.8 eV. Both present a main density peak extremely steep which is due to the truncation of the density of trapping sites existing between the valence band and $E_D$ by the occupation probability function [174] (this effect will be clearer further, when a DOTS fit will be shown in the RIA simulation results). The hole states above 0.9 eV are deeper and, from a gaussian decomposition, it is possible to see how these hole states are distributed within overlapping energy bands. Such as decomposition attempt will be shown below in fig.4.26 and 4.28. Some of these bands are always present in our samples. It is the case for the components centered at 1.2 eV, already found in pure silica sample (L02) and now in Al- and P-doped silica. For this latter, also a band around 1 eV is present, probably linked to a P-related trapped-hole defect. In the RIA modeling we tried to associate such bands to some radiation induced CC. All radiation-induced states are distributed within a rather narrow energy range (0.7 – 2 eV), so trapped-hole centers associated with silica or different dopants can be characterized by similar activation energies.
According to equation (4.26) and given the values of $q$, $w_0$, $C$ and $W$ for K04 and L28 samples, TL components at 250 and 275 °C should correspond to holes trapped at 1.19 and 1.26 eV above the valence band, respectively (according to eq.(4.26)). Consequently, the holes trapped on levels between 1.2 and 1.4 eV in the DOTS of Fig.4.18-4.19 again most likely correspond to holes forming the SiE' states.
As already reported in chapter 3 for P-doped sample L28, the irradiation exposure leads to the formation of the P-related radiation induced CC like POHC, P1 and

P4 centers, which are annealed during the TL readout. In the same sample, the TL spectra do not contain any P-related centers but only the typical emission of intrinsic oxygen vacancies (SiODCs). Thus, P-related hole centers do not act as recombination centers but as trapped states in the TL scheme (see fig.3.24). Consequently, the trapped-hole states forming the POHCs as well as P1 and P4 centers must be present in the DOTS of Fig. 4.19. In the RIA modeling section, this argument and the the DOTS components will be treated in detail.

### 4.2.2 Calibration of the general simulations of the DOTS

From the DOTS extraction procedure, using the 1st order kinetics simulation, we obtained the experimental DOTS, which is needed as an input in the general model, and some of the necessary parameters (reported in table.4.8) for solving the equation describing the trap filling (eq.(4.21)-(4.24) or (4.1)-(4.4)).
The passage from the experimental DOTS to the simulated one, needs the knowledge of the other parameters: $N$, $\alpha$, $\beta$, $\theta$, $r$. All the considerations made for the L02 sample remain valid here. So we refer to section 4.1.5 for the justification of the reasonable values range for the parameters and the choice of $\alpha$, $\theta$ and $r$ values. But we remind here that the estimation of $N$ and $\beta$ is the most important step.
N sets the saturation degree, so is best estimated from the dose dependence of the TL response. $\beta$ is such that $w_0 = \beta N_c$, where $N_c$ lies between $10^{18}$ and $10^{20}$ $cm^{-3}$ typically. $w_0$ is known from DOTS extraction so we can deduce the order of magnitude of $\beta$. To determine these last parameters we use the general model to simulate the TL response as a function of the dose. The dose dependence of the TL response and the DOTS predicted by simulating irradiation and relaxation phases best reproduce the experimental dose dependence and the experimental (extracted) DOTS by setting $\beta = 10^{-10}$ $cm^{-3}s^{-1}$ and $N$=2 $\times$ $10^{20}$ $cm^{-3}$ for K04, and 1.4 $\times$ $10^{20}$ $cm^{-3}$ for L28 (see table 4.9).

| | K04 | L28 |
|---|---|---|
| Trap Density N ($cm^{-3}$) | $2 \times 10^{20}$ | $1.4 \times 10^{20}$ |
| $\beta$ ($cm^{-3}s^{-1}$) | $10^{-10}$ | $10^{-10}$ |
| $\alpha$ | $10^{-5}$ | $10^{-5}$ |
| $\theta$ | 1 | 1 |
| $r$ | 1 | 1 |
| Frequency factor $w_0$ ($s^{-1}$) | $5 \times 10^{9}$ | $4 \times 10^{7}$ |
| Mott-Seitz factor C | $10^{8}$ | $10^{8}$ |
| Energy barrier W (eV) | 0.072 | 0.095 |

**Table 4.9:** Parameters determined for the general model for Al- and P-doped samples K04 and L28, respectively. $C$ and $W$ factors, found from the 1st order kinetics simulation, are used just in the TL simulations.

Table 4.9 summarizes the best parameters used for the general model to simulate the DOTS and the related TL response changing the dose for Al- and P-doped samples (fig.4.20 and 4.21, respectively). It is worth to remind that the Mott-Seitz parameters $C$ and $W$, found from the 1st order kinetics simulation, are used in the general model just in the TL simulations, not for the DOTS.

In Fig.4.20 is reported the area of the TL curves as a function of the dose for K04 sample. The measurements are carried out for several irradiation at a fixed dose rate of (200 Gy(SiO2)/min) but changing the irradiation time. The TL readout were then performed at 1°C/s. The TL areas shows a power-law dependency of $D^{0.45}$ on the dose, as highlighted from red line fit in figure. The simulated areas follow perfectly the experimental ones. Similar considerations are made for the P-doped sample (fig.4.21). The TL response reported in figure is found to increase according to a power-law ($D^{\alpha}$) with an exponent of 0.65.

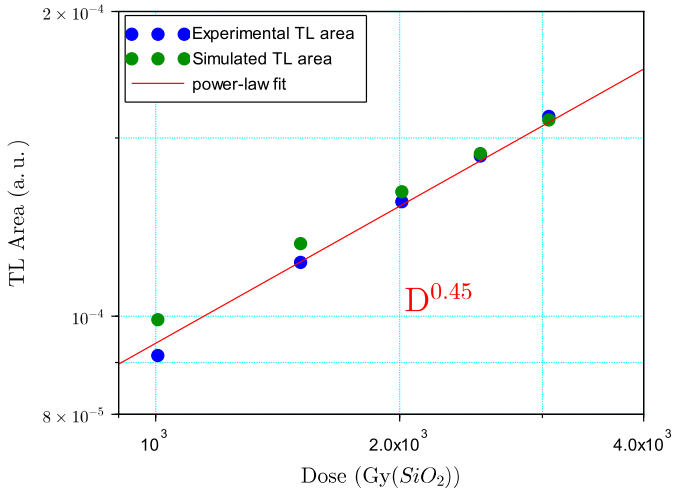


**Figure 4.20:** Areas of experimental TL glow curve (blue) and simulated ones (green) as a function of the dose for Al-doped silica (K04 sample).

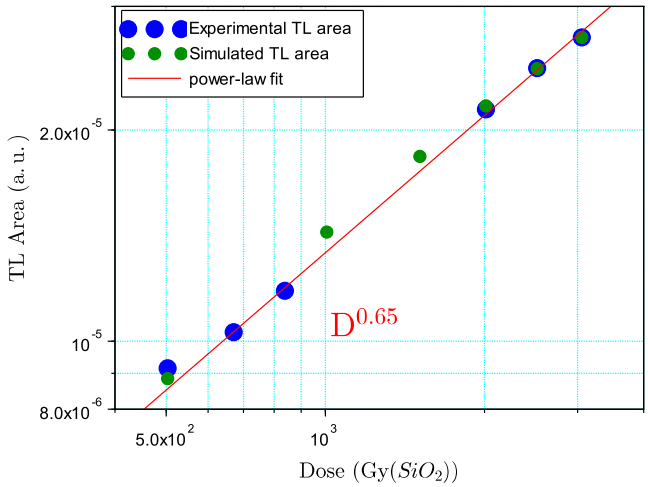


**Figure 4.21:** Areas of experimental TL glow curve (blue) and simulated ones (green) as a function of the dose for P-doped silica (L28 sample).

At this point, we found all the parameters necessary for the general model. Now we want to check if the parameters reported in table 4.9 allows us to predict the TL

response correctly, notably upon changing the heating rate. In Fig.4.22 and 4.23 are reported the superimposition of the experimental and simulated TL curves at four heating rates (0.5, 1, 2 and 3°C/s) adopting the general modeling, for the K04 and L28 samples respectively. Considering an error of 5% on the measured intensity, we can conclude that the agreement is good.

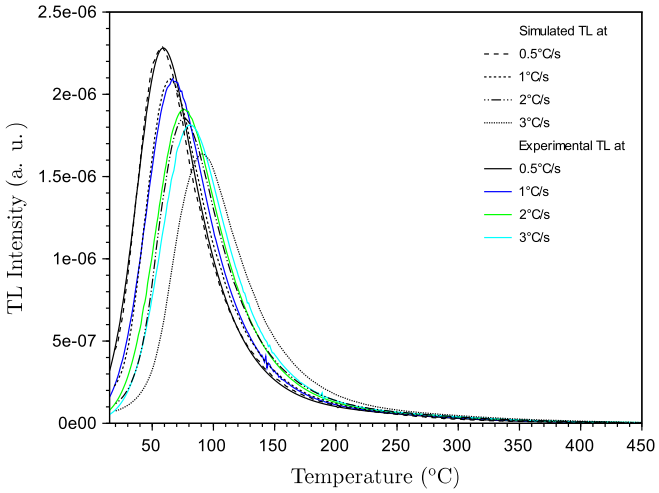


**Figure 4.22:** Superimposition of the experimental TL glow curves (solid lines) and simulated ones (dotted lines) at $0.5^oC/s$, $1^oC/s$, $2^oC/s$, $3^oC/s$ for the K04 sample, after standard irradiation.

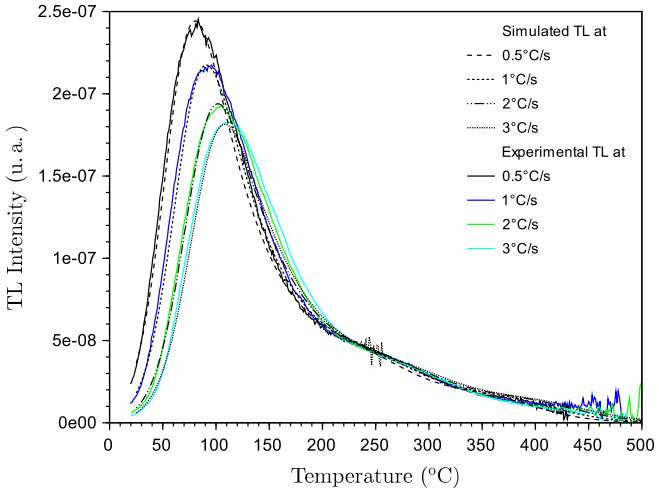


**Figure 4.23:** Superimposition of the experimental TL glow curves (solid lines) and simulated ones (dotted lines) at $0.5^oC/s$, $1^oC/s$, $2^oC/s$, $3^oC/s$ for the L28 sample, after standard irradiation.

### 4.2.3 Validation of the DOTS simulation by IRMA prediction

The general method, calibrated to simulate the DOTS and the TL recorded in standard-laboratory conditions, is able to predict the DOTS in conditions that markedly differ from the standard ones (extrapolation capacity). As shown for un-doped and F-doped silica (L02 and Q25 samples) in the introduction of our simulation procedure, we pass from the calibration procedure to the validation of the model. This means an available prediction of the DOTS confirmed by the simulation of the TL. We show now how the calibrated model well predict the DOTS left by IRMA irradiation, trough the TL. We used the parameters reported in table 4.9 to simulate the DOTS left by the IRMA irradiation in Al- and P-doped silica samples. From these simulations, we obtain the DOTS in IRMA conditions. These DOTS are well predicted because the simulated TL recorded in IRMA condition is well superimposed to the experimental one. These results are shown in fig.4.24 for K04 sample and in fig.4.25 for L28 sample. Once again, it is worth noting that once the model is calibrated in standard conditions, the simulation is made in IRMA conditions without any further adjustment.

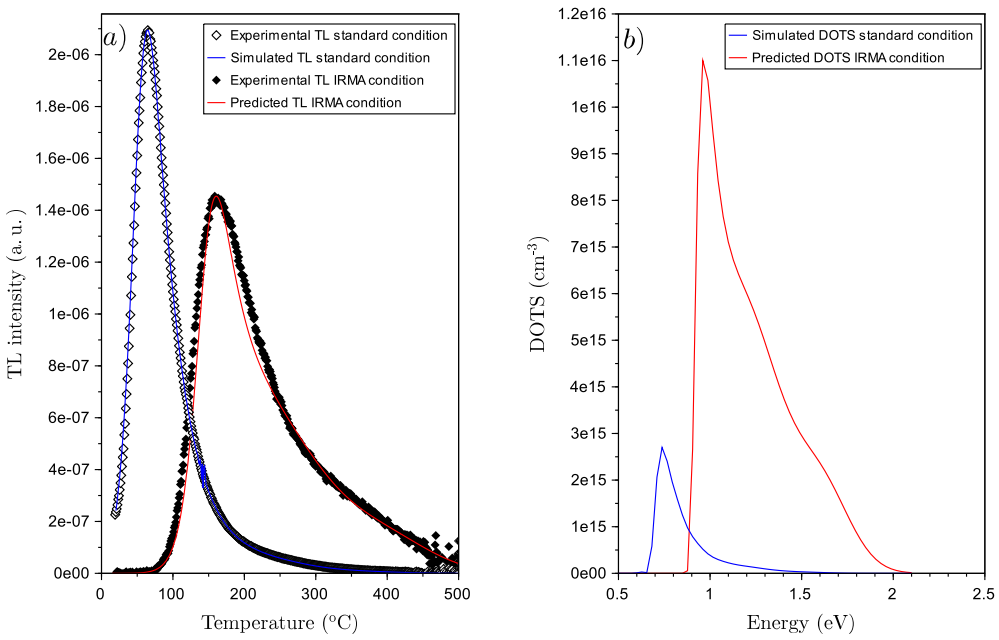


**Figure 4.24:** TL curves and DOTS from Al-doped sample K04 measured at q = 1°C/s in standard and IRMA conditions.

In fig. 4.24 the TL following standard irradiation conditions is more intense than the one obtained in IRMA conditions. Compared to other tested samples, the Al-doped one, such as K04, presents the highest TL intensity (at least one order of magnitude higher than other doped silica samples). Then, despite the high dose delivered during IRMA irradiation (1MGy), the time $t_{relax}$ between the end of the irradiation and the beginning of the TL readout, causes a significant fading effect. The DOTS simulated in standard condition are reported in blue in fig.4.24b,

whereas the one in IRMA condition are in red. One can say that these DOTS are well predicted since the simulated TL obtained from these DOTS, are well superimposed to the experimental one. If this result is obvious for the TL recorded in standard condition (being the parameters calibrated on these TL curves), it is at least a non-trivial result for the IRMA TL curves. These last are in fact recorded in irradiation and post irradiation conditions significantly different from the standard one (remind to table 4.3): compared with the standard conditions, the dose was multiplied by 333 to reach 1MGy, the irradiation time was multiplied by 1333 and the relaxation time by 24960.
In the same way, we obtained the DOTS and the simulated TL in standard and IRMA condition for the P-doped silica sample L28 (fig.4.25).

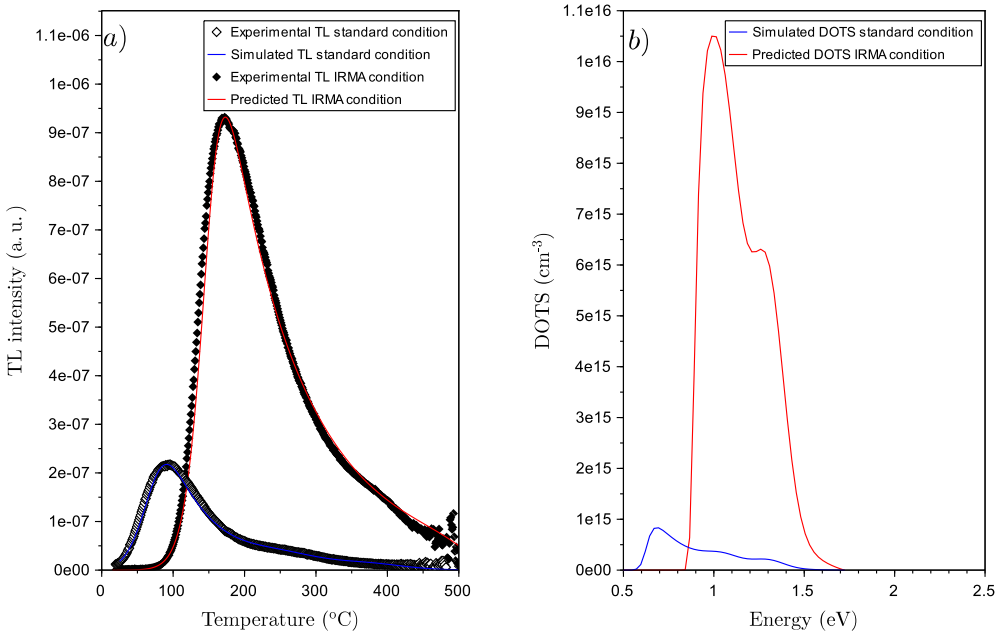


**Figure 4.25:** TL curves and DOTS from P-doped sample L28 measured at $q = 1°C/s$ in standard and IRMA conditions.

### 4.2.4 Simulation of the RIA

Before presenting the RIA simulation we need to analyze the DOTS decomposition. Once the DOTS contribution at each energy was reconducted to the formation of a particular CC (thanks to the annealing protocol correlates TL and the RIA annealing), the connection between the DOTS and the optical absorption bands in the RIA allows to calculate the amplitude of the CC absorption bands and simulate the RIA spectrum in the visible range.
As it was done for the undoped silica (section 4.1.6), we now present a discussion on the connection between the DOTS features of Al- and P-doped samples and the radiation induced CC to simulate the RIA.

The results are presented for the Al-doped sample K04 and for the P-doped sample L28.
As shown by the experimental results, the CC present in the RIA spectrum of K04 sample were the trapped holes centers NBOHC, SIE', AlOHC and the trapped-electron center AlE' (Fig.3.30). From the TL and the RIA annealing study, it was proposed that were created also $SiODC : e^-$ centers upon electron trapping. Considering the total density of trapped electrons and holes, the charge conservation equation for an Al-doped silica sample such as K04, can be written as:

$$N_{intrinsic_{e^-}} + N_{SiODC:e^-} + N_{AlE'} = N_{intrinsic_{h^+}} + N_{NBOHC} + N_{SiE'} + N_{AlOHC} \quad (4.28)$$

As one can see from the DOTS fit reported in fig.4.26 for the Al-doped sample K04, it is easy to recognize the contribution already proposed in the DOTS of the L02 sample: the exponential tail for the intrinsic levels and the SiE' contribution centered at 1.3 eV. As regards the NBOHC centers we can again assume that their density is a fraction of that SiE' centers, because these two types of defects can be produced in pairs [34]. The DOTS presents a main density peak extremely steep starting from 0.6 eV due to the truncation of the density of trapping sites existing between the valence band and $E_D$ by the occupation probability function (or the occupancy rate here shown in blue line). The DOTS fit is calculated by multiplying each contribution of the fit (exponential tail and the gaussian bands) by the occupancy rate, given by the simulation at the onset of the TL readout (estimated by the simulation at RT and $t = t_{irr} + t_{relax}$).

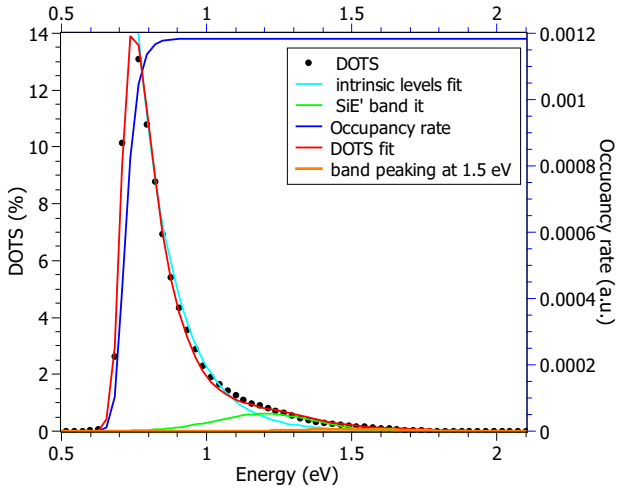


**Figure 4.26:** Decomposition attempt on the DOTS reported in fig.4.18 for K04 sample. The occupancy rate at the onset of the TL readout is given by the general simulation at RT and $t = t_{irr} + t_{relax}$.

On the left side of equation (4.28), in addition to the $N_{SiODC:e^-}$ already encountered in L02, is also present the term $N_{AlE'}$. The density of electron centers AlE' represents a certain part of the total density of trapped electrons, being proportional to the number of RC ($SiODC : e^-$), which density is given by the simulation. This fraction is a parameter that can be suitably adjusted in order to obtain the best result for the RIA. For our results, considering the proportional rule between the

density of AlE' and that of RCs as $N_{AlE'}$=$\alpha$ $N_{RC}$, we use a factor $\alpha$ equal to 0.365. This value was found to provide us the with the best agreement between measured and simulated RIA spectra.
In chapter 3, it has been shown, from the thermal annealing results on K04, that the radiation-induced Al-related AlOHC centers release their holes around 375-400 °C during the TL process. In the works by Mady *etal*. [77, 174] it was highlighted that the holes released from AlOHCs were shown to be the main contributors to the restoration of $Yb^{3+}$ ions in Al:Yb doped sample. It was then proposed that for this kind of sample the TL components between 275 and 300 °C are associated with holes trapped between 1.42 and 1.5 eV [174], and that the DOTS levels around these values might be attributed to holes trapped into the form of AlOHCs. In our results, this contribution between 1.4 and 1.5 eV is barely visible. Anyway, a small contribution is still present, and from the results previously carried out by our team in [77, 174], we assigned these levels to AlOHC centers in the RIA simulation.
The RIA spectrum of the K04 sample was reconstructed according to the approach explained for the sample L02: calculation of the intensities of the optical absorption bands of the main CC based in the Smakula's formula. The central energy of these OA bands being known from literature, FWHM and oscillator strengths were adjusted to produce the best agreement between simulated and measured RIA spectra. The result is shown in Fig. 4.27. The simulated OA bands are related to the following radiation induced CC: the AlOHC, peaking at 2.3 eV, the AlE' peaking at 4.08 eV, the NBOHC, at 4.9 and 6.8 eV, and finally the SiE' center at 5.7 eV. The simulated OA band parameters are reported in table 4.10. In addition to the oscillator strength characterizing the simulated gaussian bands, the reproduction of the RIA spectrum is obtained adjusting other factors, such as:

- The proportionality factor between the recombination Centers and the AlE' centers: $RatioAlE' = \frac{Density_{AlE'}}{Density_{RC}} = 0.365$
- The proportionality factor between the densities of NBOHC and SiE' centers which gives the estimation of the density of NBOHC centers: NBOHC=0.66 $\times \frac{f(SiE')}{f(NBOHC)*N_{SiE'}}$ ($f$ is the oscillator strength);
- Total trap density value $N = 10^{22}\ cm^{-3}$

The agreement is quite good but it should be noted that using the trap density N value obtained from the calibration procedure (table4.9) the simulated RIA would be one order of magnitude lower. This quantitative discrepancy is the directly consequence quantitative problem of density of states already explained for L02. As written, this difference in magnitude compared to the physical one is due to the lack of knowledge about the density shallow states that are not probed by TL (already emptied at the beginning of the TL readout). This also implies a non negligible difference in the calculation of the RIA. Although sometimes this problem does not persist, and the calculated and experimental intensities are ultimately quite close, it seems not negligible for the present Al-doped samples. In order to obtain the same intensity, one choice is to arbitrarily change the total number of the density of traps $N$ in the simulation.

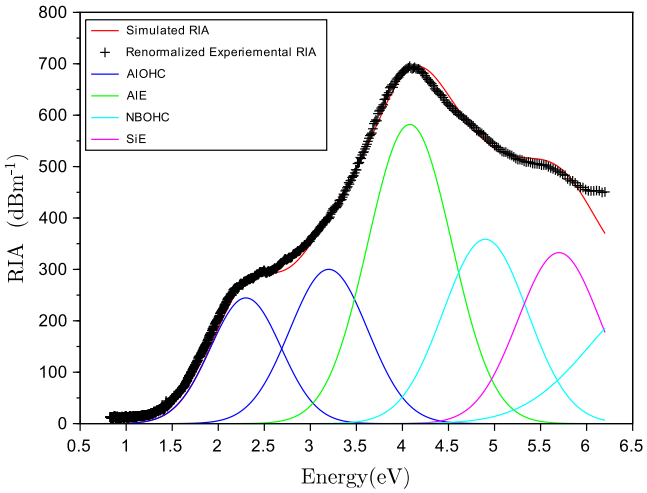


**Figure 4.27:** Simulated OA bands and RIA spectrum and normalized experimental RIA on K04 sample after irradiation of a dose of 3 kGy in standard conditions.

| Defect | $x_c$ (eV) | FWHM (eV) | $f$ simulation | $f$ literature |
|---|---|---|---|---|
| AlOHC | 2.2 | 0.9 | 0.11 | 0.06 [59] |
| | 3.2 | 1 | 0.15 | 0.12 [59] |
| AlE' | 4.08 | 1.07 | 0.21 | 0.214 [59] |
| NBOHC | 4.9 | 1.08 | 0.6 | 0.2 [32] |
| | 6.8 | 1.76 | 0.7 | 0.05 [35] |
| SiE' | 5.7 | 1.0 | 0.5 | 0.4 [32] |

**Table 4.10:** Parameters of the OA bands used in the RIA simulation of fig.4.27.

Concerning the L28 sample, a decomposition attempt of the DOTS is reported in fig.4.28. The exponential contribution (cyan line) corresponds to the intrinsic levels, the energy distribution centered at 1.3 eV (green line) corresponds to SiE' centers, in accordance with what explained above, whereas a band at around 1 eV is also present. This contribution is mostly likely associated with P-related trapped-hole states since it appears to be specific to the P-doped sample. In fact, from the experimental results on L28, we argued in chapter 3, that all radiation-induced trapped-hole P-related centers should act as TL traps and not as recombination centers. The annealing of POHC centers, found to take place between 200 and 250 °C (see fig.3.23), is therefore most probably due to the release of their holes that subsequently recombine at $SiODC : e^-$ centers to contribute to the TL curve between 200 and 250 °C. This region is precisely the one where a shoulder appears in TL curves at the higher P concentration. To this temperature range, corresponds a demarcation energy of about 1 eV, calculation obtained from eq. 4.26. This analysis suggests that the band in the DOTS at around 1 eV is due to the POHCs.

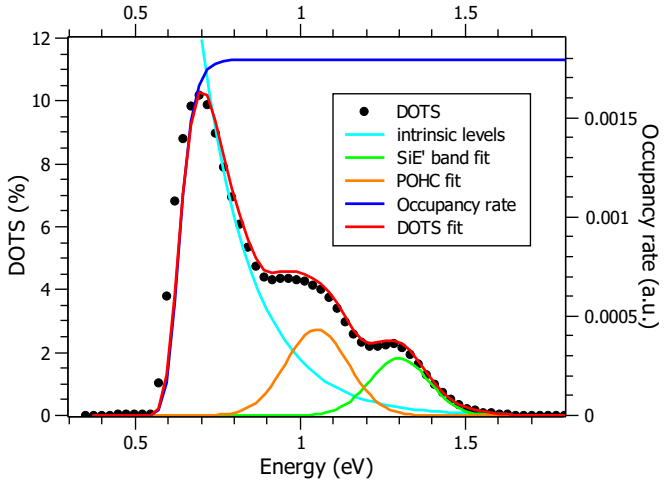


**Figure 4.28:** Decomposition attempt on the DOTS reported in fig.4.19 for the L28 sample. Blue line: occupancy rate at the onset of the TL readout given by the general simulation at RT and $t = t_{irr} + t_{relax}$.

The RIA spectrum of the L28 sample shown in fig.3.20b with the appropriate fit, revealed the presence of some P-related CCs such as POHC and P2, respectively trapped hole and a trapped electron centers. According to what has been already reported for undoped silica, considering also the presence of P-related CCs, one can write the charge conservation equation for the P-doped silica sample such as follows:

$$N_{intrinsic_{e^-}} + N_{SiODC:e^-} + N_{P2} = N_{intrinsic_{h^+}} + N_{NBOHC} + N_{SiE'} + N_{POHC} \quad (4.29)$$

The RIA spectrum of the L28 sample was reconstructed according to the usual approach considering that the densities of trapped-hole CCs is given by the DOTS, following the decomposition shown in fig. 4.28. The P2 center does not act as a recombination center, but its contribution in the RIA spectrum has been calculated by assuming that $N_{P2}$ is a fraction of the total density of electron centers $N_{e^-}$ in the left side of this equation. Precisely we set $N_{P2} = 0.35 N_{e^-}$. This parameter, together with the ones describing the ratio between NBOHC and SiE′ centers concentration, are adjustable. This latter was set considering the NBOHC=0.33 $\times \frac{f(SiE')}{f(NBOHC)*N_{SiE'}}$, where $f$ is the oscillator strength of the 4.75 eV NBOHC band.
The simulated and experimental RIA are compared in fig. 4.29, where the simulated RIA (red line) is well superimposed to the experimental RIA one (scattered line). The energy location, the FWHM and the oscillator strength of the simulated gaussian bands are reported in table 4.11.
As one can see the agreement between the experimental and the simulated RIA is quite good for both Al-doped and P-doped silica samples (K04 and L28, respectively). Starting from their DOTS in fig.4.26 and 4.28, it was possible to build the RIA in the visible part of the spectrum.

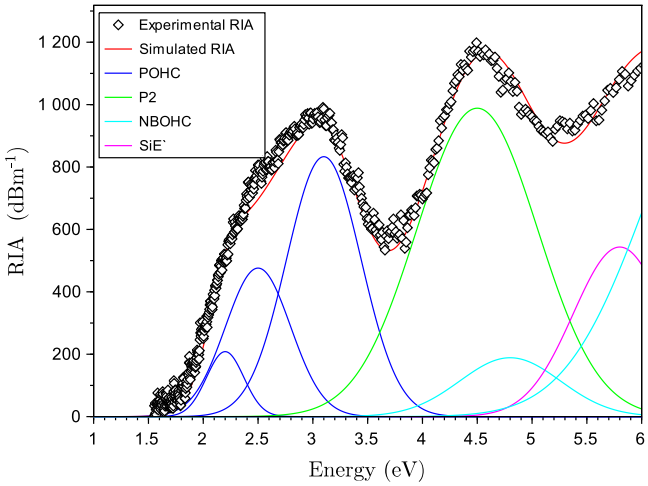


**Figure 4.29:** Simulated and normalized experimental RIA on L28 sample after irradiation of a dose of 6 kGy.

| Defect | $x_c$ (eV) | FWHM (eV) | $f$ simulation | $f$ literature |
|---|---|---|---|---|
| POHC | 2.2 | 0.4 | 0.1 | 0.5 [84] |
| | 2.5 | 0.7 | 0.4 | 0.5 [84] |
| | 3.1 | 0.8 | 0.8 | 0.5 [84] |
| P2 | 4.5 | 1.3 | 0.53 | 0.035 [84] |
| NBOHC | 4.8 | 1.08 | 0.15 | 0.2 [32] |
| | 6.8 | 1.76 | 1.5 | 0.05 [35] |
| SiE' | 5.8 | 1.0 | 0.8 | 0.4 [32] |

**Table 4.11:** Parameters of the OA bands used in the RIA simulation of fig.4.29.

To support the method and check the predictive capacity of our model, we now report the RIA simulated with the parameters calibrated in laboratory conditions (those used above), but applied to very different irradiation conditions, namely those of the IRMA experiments. The details of this irradiation have been reported in section 2.6.3 and has been summarized in table4.3; we refer to them here as "IRMA conditions". The simulated DOTS and the related TL in these conditions has been reported in fig.4.24-4.25 together with the standard results. We report again here just the results by IRMA condition to show them in a clearly way.
In fig.4.30 are reported the experimental TL curves recorded in the IRMA conditions and the simulated ones for Al- doped sample, predicted from the DOTS simulated in the same experimental conditions, reported in b). One can see how the model can predict very well the TL behavior and hence, more importantly, the DOTS existing on the moment of the TL readout. The main goal is not just the prediction of the DOTS (and related TL) but the ability to simulate the RIA at 1MGy from the simulated DOTS. From the DOTS and the protocol explained before, it was possible to calculate the optical absorption bands due to the radiation induced

CCs, following the same connection reported above for the standard DOTS of fig. 4.26. The comparison between the experimental RIA and its simulation at 1MGy is reported in fig. 4.31. As one can see the agreement is quite good.

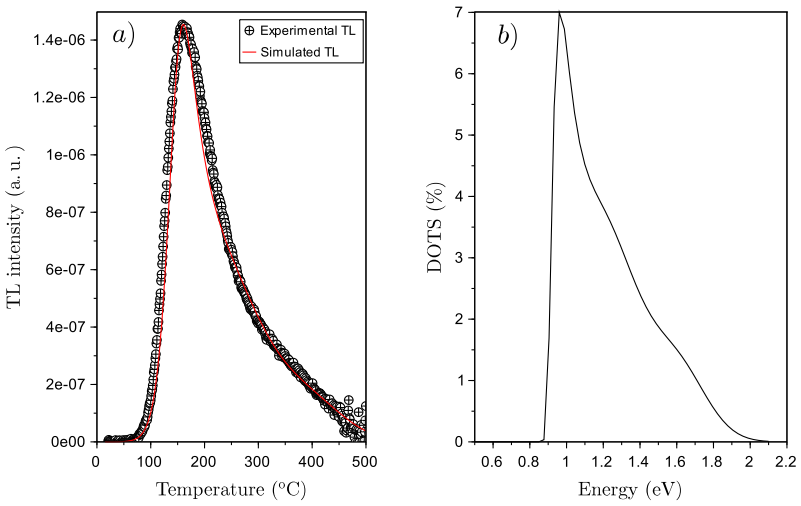


**Figure 4.30:** a) Comparison between the TL curve predicted from the DOTS simulated in IRMA conditions (in (b)) and the TL curve actually measured in such condition on K04 sample. b) DOTS simulated in IRMA conditions.

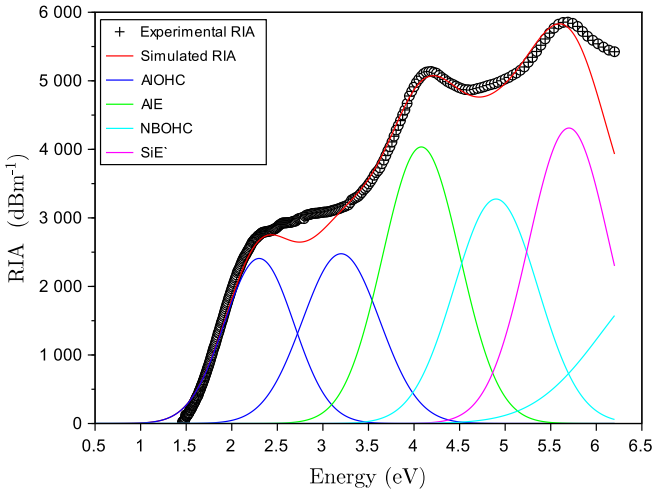


**Figure 4.31:** Comparison between the experimental and the predicted RIA in IRMA condition on K04 sample.

As presented above for K04, we report the same results for the P-doped sample L28. In fig. 4.32 are reported the experimental TL curves and the simulated ones predicted from the DOTS simulated according to IRMA conditions, reported in b). The results for P-doped sample (L28) showed that the DOTS obtained for such

different irradiation conditions contain similar structures. Due to the much longer irradiation and delay before the TL readout, the demarcation energy is increased from 0.7 to 0.9 eV for the P-doped sample in IRMA conditions. The delay in the TL readout brings to a shift of the populated levels probed by TL towards deeper states, consequently the TL glow curves by IRMA conditions reach their main peak at around 160 °C instead of 70-90 °C (in the standard condition which leads to the TL shown in fig. 4.23 at 1 °C/s). A similar discussion is valid for Al-doped sample (K04). In this sample the TL glow curves by IRMA conditions shown in fig. 4.30, reach their main peak at around 170 °C, while the TL recorded in standard condition at 1°C/s presents a peak around 65 °C (fig. 4.22).

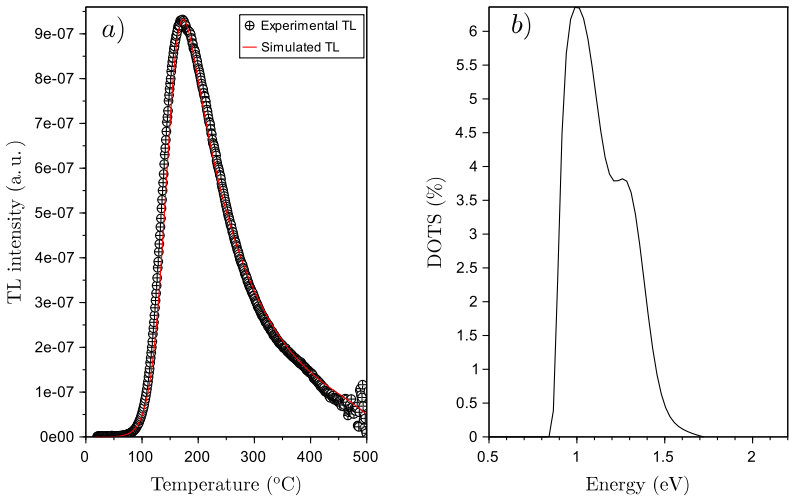


**Figure 4.32:** a) Comparison between the TL curve predicted from the DOTS simulated in IRMA conditions and the TL curve actually measured in such condition on L28 sample. b) DOTS simulated in IRMA conditions.

Using the same DOTS decomposition as in fig. 4.28 and the parameters calibrated in laboratory conditions for the RIA simulation, we can predict the RIA recorded following IRMA irradiation. The comparison between the RIA actually measured in those conditions to that predicted by our laboratory calibrated physical model is reported in fig. 4.33. This agreement is obtained without additional adjustment in IRMA conditions. This results clearly demonstrate that the physical model we propose to anticipate the DOTS, related TL and the corresponding RIA, has well a predictive capacity to perform dose, temporal or dose rate extrapolation.
To conclude, in this section it has been shown how the TL technique has been successfully used to extract the DOTS in Al- and P-doped silica and anticipate the RIA in these materials. This was possible once the specific radiation-induced mechanisms associated with the presence of Al and P in silica were elucidated (see section 3.2). Then these mechanisms were put into equations whose determining parameters were calibrated against experimental data in standard conditions.

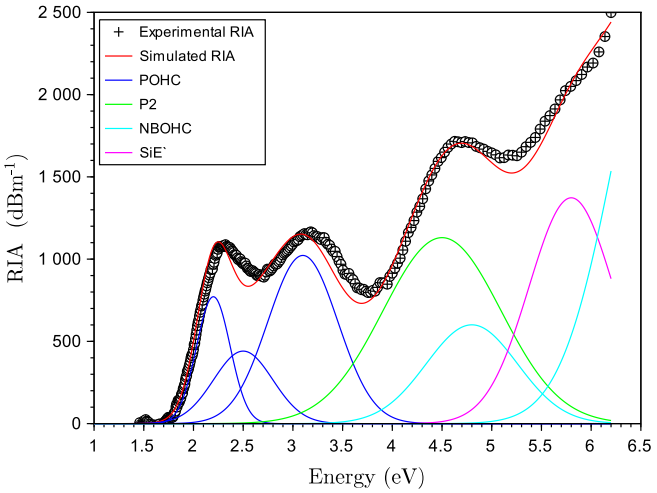


**Figure 4.33:** Comparison between the experimental and the predicted RIA in IRMA condition on the L28 sample.

The main determining parameters of the model are calibrated so as to reproduce the experimental DOTS (extracted from TL curves) as well as its dose dependence (experimentally probed by TL measurements). Not only the theoretical TL responces, associated with simulate DOTS, was proved to have a similar dose dependence as experimental ones, but they also deproduce the impact of the TL heating rate on TL curves.
Thanks to this calibrated model, the DOTS can be predicted in conditions that differ from those of laboratory test to allow the extrapolation of the DOTS and RIA behavior. These DOTS present activation energies distribution confirmed by experimental measurements using the 'Initial Rise' method. For K04 and L28 samples, these DOTS show a peak at a depth of 0.8-0.9 eV above the VB edge (in standard conditions) .
Finally, the connection between the DOTS and the optical absorption bands in the RIA allows to calculate the amplitude of the CC absorption bands and simulate the RIA spectrum in the visible range. The obtained results present a good agreement with data. This goal supports the hypotheses reported on the mechanisms of creation/destruction of the radiation induced point defects and the relevance of our approach. Extrapolation capacities, both for the DOTS and the RIA, have been demonstrated for pure, Al- and P-doped silica.

## 4.3 Telecom-grade fibers

We now present the results concerning Telecom-grade fibers containing germanium. The samples belonging to this category are the Ge-, GeP- and GeF- doped silica samples, named respectively Q01, Q07 and Q09 (see table 4.12 for sample details). The main discussion concerning the creation and annealing mechanisms is focused on the Q01 samples, but what is deduced on this sample is also true for Q07 and Q09, since they present the sample TL features which are mainly related to the presence of germanium. To show this, a comparison between Q01, Q07 and Q09 will be reported.

| sample name | doping | | characterization | |
|---|---|---|---|---|
| | Cladding | Core | *at.*% | $\Delta$n |
| Q01 | Si | Ge | 2.88 Ge | $3.5 \cdot 10^{-3}$ |
| Q07 | P | Ge | 4.46 Ge, 0.89 P | $3 \cdot 10^{-3}$ |
| Q09 | F | Ge | 1.01 Ge | $7 \cdot 10^{-3}$ |

**Table 4.12:** Telecom-grade fiber preforms under investigation.

The procedure proposed in the previous sections for pure, Al-, P-doped silica allows extracting the energy distribution of the Density of Trapped States (DOTS) induced by ionizing irradiation from TL experiments. This knowledge is of first importance to understand and predict the temporal and thermal stability of the optical degradation, since the DOTS notably contains the energy levels of color centers that contribute to the RIA. Unfortunately, the formalism introduced for pure, Al-, P-doped silica, does not work in the case of Ge-doped glasses due to their "anomalous" TL features, namely an increase of the TL intensity with the increasing of the heating rate. It is precisely the first goal of this section to extend the model and capability of the DOTS extraction technique to Ge-doped glasses.
The objective is primarily to elucidate the specific radiation-induced mechanisms associated with the presence of Ge in silica, that notably induce the anomalous TL response. We already showed in section 3.4 the experimental study of the RIA thermal annealing during the TL readout, and its correlation with the TL glow curve. We proposed that ODCs centers, trapping electrons during irradiation, form deep states ($SiODC : e^-$ and $GeODC : e^-$) which act as recombination center (RCs) in the TL process (fig.3.51).
In this chapter we propose a specific model that predicts the anomalous TL features and how they are arise from two specific properties of the annealing processes of Ge-related radiation-induced centers: the presence of "thermally disconnected traps " (TDT) and a temperature dependent recombination cross section.
This model built "ad hoc" for Germanium doped samples, consists of a " modified first order kinetic" used to extract the experimental DOTS and of a general model, described by eq.(4.30)-(4.34) below, able to simulate the DOTS and from them, predict the TL and the RIA.
The good prediction of the simulated DOTS in the laboratory experimental condition and then of the simulated TL at different heating rate, would prove the validity of our model. The prediction of the TL through this calibrated model is the way to validate the model, since the increasing of the TL intensity with the increasing

heating rate is the anomalous feature that the "classic " model previous reported cannot account for.
Once the DOTS simulation is validated, the RIA simulation will be introduced. The validation of the RIA model will be finally presented through the simulation of the RIA during the thermal annealing treatment. This last result is obtained thanks to a specific TL measurement from which it was possible to simulate the DOTS at several heating steps. The details of this procedure will be explained below.

### 4.3.1 Specific TL model and DOTS extraction

The evolution of the electron population in the CB, in the RC and the evolution of hole population in the trap levels, in the thermally disconnected trap (TDT) (see sec.3.4) and VB is described by a system of coupled-non linear-differential equations (4.30)-(4.34):

$$\frac{dh_V}{dt} = g_0 - \sum_{k=1}^{M} \frac{dh_k}{dt} - \frac{dh_{TDT}}{dt} - \gamma n_{RC} h_V \tag{4.30}$$

$$\frac{dh_k}{dt} = h_V \beta_k \left(H_k - h_k\right) - w_{0k} exp\left(-\frac{E_k}{k_B T}\right) h_k \quad (k = 1...M) \tag{4.31}$$

$$\frac{dh_{TDT}}{dt} = \beta_{TDT} h_V \left(H_{TDT} - h_{TDT}\right) \tag{4.32}$$

$$\frac{dn_{RC}}{dt} = \delta n_c \left(N_{RC} - n_{RC}\right) - \gamma n_{RC} h_V \tag{4.33}$$

$$\frac{dn_c}{dt} = g_0 - \delta n_c \left(N_{RC} - n_{RC}\right) \tag{4.34}$$

In (4.30) the right-hand side term represents the generation, the trapping on the M-levels, thermal de-trapping from the same levels, and recombination.
Pair generation takes place at a constant rate $g_0$ per unit volume and time which is representative of the dose rate absorbed by the material during the irradiation process. Electrons generated in the conduction band (CB) in concentration $n_c$ can be trapped by a set of shallow trapping levels (not included in these equations) or captured at SiODCs and GeODCs to form the RC with an electron trapping coefficient $\delta$. The densities of electron traps and of trapped electrons are referred to as $N_{RC}$ and $n_{RC}$, respectively. Holes generated in the valence band (VB) are in concentration $h_v$. The hole trap concentration is defined by $H_k$, the density of trapped holes is $h_k$ and the hole trapping coefficient is $\beta_k = \sigma_k v_{th}$ for the $k^{th}$ trapping level, where $\sigma_k$ is the capture cross-section and $v_{th}$ the thermal velocity in the VB. Holes captured in these levels can be released thermally at a rate $w_{0_k} \times exp\left(-E_k/k_b T\right)$, where $E_k$ is the trapping depth measured with respect to the VB edge and the pre-exponential factor $w_{0_k} = \sigma_k v_{th} N_V$ is the frequency factor. TDT are in concentration $H_{TDT}$. They are populated by a density $h_{TDT}$ of trapped holes, representing the concentration of GeE' centers, and characterized by the trapping coefficient $\beta_{TDT}$ characterized by the energy barrier $E_{TDT}$ ($\beta_{TDT} = \sigma exp\left(-E_{TDT}/k_b T\right) v_{th}$). Holes in VB can also recombine at RC consisting of electrons trapped into the form of SiODC:e- and GeODC:e- centers. The recombination coefficient is $\gamma = \sigma_r v_{th}$ where $\sigma_r$ is the re-

combination cross-section, which expression is given by $\sigma_r = \sigma_{r0} e^{-E_b/k_B T}$. The stability of the traps induced by irradiation is determined by their thermally activation energy $E_k$.
The evolution of the trapped hole density in (4.31) is assumed to result from trapping and de-trapping. The population of holes in TDT, described by (4.32), has just a positive term due to the hole trapping since we are considering that we do not have de-trapping from the such deep trapped states. The population of electrons on RC evolves due to electron trapping and holes recombination according to (4.33). The electron population in the CB varies according to the generation and trapping on RC and hence obeys (4.34).
The coupled-non linear-differential equations (4.30)-(4.34) can be solved numerically, and as already mentioned, it is useful to reduce the amount of parameters. First of all, we make the assumption of a same trapping cross section $\sigma$, so in equations (4.30)-(4.34) $\beta_k$ and $w_{0k}$ are the same for all the traps [182]. Its direct consequence is the proportionality between the density $h_k$ of trapping carriers and the density of sites $H_k$ at any energy level $E_k$ provided this level is thermally stable.
As already explained in section 4.1.6, equations (4.30)-(4.34) describe all the experimental phase characterizing the TL measurements: the irradiation stage ($t_{irr}$), the relaxation post irradiation stage ($t_{relax}$) and finally the TL readout (when the temperature increases from $T_0$ to $T_f$ linearly with time at a heating rate $q$ ).
The RCs have the characteristic to be stable during the TL readout. This means that RCs do not undergo to de-trapping but they can be depleted only by recombination processes. This implies that the trapping of electrons rifle quickly the CB during the relaxation phase and this band stay empty during the TL readout. Thus the TL readout is described by the equations (4.30)-(4.34) with the condition $n_c = 0$ and solving these equation the TL intensity can be calculated, as given by the equation $I_{TL} = -\eta(T) \frac{dn_{RC}}{dt}$ [164, 165]. The main difference between the model previously presented and this new model adopted for Ge-doped samples, is the temperature dependence of the recombination cross section and the presence of the TDT in competition with the RC. The carriers trapped by the TDT cannot be thermally released during the TL readout, at least up to the experimental temperature of 550°C.
As already seen for other kinds of doped silica presented in this work, the model described by equations (4.30)-(4.34) presents also the issue that the DOTS, represented by the set of trapped-hole populations $h_k$ in the above equations, depends on the density of trap states $H_k$ that are also unknown.
To overcome this problem, we adopted the useful strategy based on the DOTS extraction from the TL curves (named experimental DOTS). This experimental DOTS gives the relative distribution of trap densities above the VB for depth $E > E_D$ ($T_0$, $t_{irr} + t_{relax}$) that are probed by TL. DOTS extraction is made under the assumption that the TL process obeys first-order kinetics. Normally, as said in section 4.1.6, this approximation implies that carriers thermally released from traps can only recombine with the RCs and they cannot be re-trapped on deeper levels. In this specific TL model for Ge-doped sample, we need to imply the possibility that carrier released thermally from traps can be re-trapped on the TDT. We refer to this new DOTS extraction strategy as a "modified first order approximation".
Due to the very large recombination cross-section ($\gamma = \sigma_r v_{th}$), the lifetime of re-

leased carriers in the VB is also considered to be negligible (it is even more negligible that it is further reduced by the trapping of released holes on TDT). Thus, the density of the free charges in the VB remains negligible in front of trapped populations and the rates of de-trapping equals the rate of trapping on TDT plus the rate of recombination. At given trap depths, the temperature of TL peaks and the amplitude of their shift upon varying the heating rate are then only determined by the frequency factor $w_0$ of TL traps (trapped-hole levels in silica). This factor can be estimated from TL curves acquired at several heating rates (at least 2, commonly 4) following a procedure similar to that described in detail in section 4.1.6 and in [174]. This finally provides us with the DOTS, i.e. the distribution of energy levels $E_k$ within the bandgap with their relative populations $h_k$, at the onset of the TL readout. As far as all hole trapping levels share the same capture cross-section, this DOTS is simply parallel to the density of trapping states: the $h_k$ are proportional to the $H_k$ for all levels that are thermally stable at RT, at the beginning of the TL heating. This provides a very good starting set of $H_k$ to initiate the optimization of the general model in equations (4.30)-(4.34) and fit it correctly to experimental glow curves. In particular, the depths of trapping levels are correctly located in the gap thanks to the DOTS extraction made from a modified first-order analysis, which will be presented in detail below.
We now summarize briefly the strategy adopted to find the best results which are presented below. In the following subsections, we explain in detail the modified first-order analysis and the simulations results with the general model.
From the first order modified kinetics we obtain the experimental DOTS (extracted from the TL curves at two heating rates) and some of the parameters we need in the general model: $w_0(300)$ (already discussed for pure silica), $\alpha_{TDT}$, $\xi_{TDT}$, $E_b$ and $u_0$. Where $\alpha_{TDT} = \beta_{TDT}/\gamma$, $\xi_{TDT} = H_{TDT}/H$ is the proportion of TDT respect to the total density of hole traps (TL traps and TDTs), and $u_0 = n_{RC}(T_0)/H$ is the initial filling rate. Note that at this step, in the TL re-built from experimental DOTS, we are assuming the effect of Mott-Seitz parameters negligible, then $C = 0$. One of the assumption of the first-order method is that recombination prevails over trapping, which means $\beta_{TDT} \ll \gamma$ ($\alpha_{TDT} = \beta_{TDT}/\gamma \ll 1$). In our modified model, the best agreement is with $0.4 < \alpha_{TDT} < 10$. We start using $\alpha_{TDT} = 1$, which assigns the same importance at both mechanisms: $\beta_{TDT} = \gamma$.
Once we have the DOTS we keep to find the parameters for the general through the study of the experimental TL recorded at different doses and at different heating rates. The remaining unknown parameters are: $\alpha = \beta/\gamma$, $\theta = \delta/\gamma$, $r = H/N$, $H$.
Once the DOTS has been extracted and $\alpha_{TDT}$, $\xi_{TDT}$ and $E_b$ values are estimated, we keep to find the rest of unknown parameters. These are estimated from two different studies: the dose dependence on the TL response and the TL recorded at different heating rates. From the first study we were able to find the values for: $\alpha = \beta/\gamma$, $\theta = \delta/\gamma$, $r = H/N$, $N$, whereas from the last one we found the value for $E_{TDT}$, and, if necessary, refine the values of the other parameters previously found, such as $\alpha_{TDT}$.

**modified first order kinetics** In the description of the DOTS extraction protocol (section 4.1.6), we assumed that the TL process was obeying to a first order kinetics. This assumption implies that the carriers cannot be re-trapped by traps (no re-

trapping) during the TL readout; but they recombine with the RC immediately upon their thermal release from traps. Concerning the Ge-doped silica samples, we assume the presence of TDTs. The presence of this deep trap in competition with the RC, is one of the crucial point in the trap filling model built for this kind of sample (the other point is the recombination cross section depending from the temperature). Since trapping on TDTs compete with recombination, the first order kinetics is no longer valid. In fact, the basic assumption of no re-trapping is no longer true because we are assuming now the possibility for holes released from TL traps of re-trapping on the TDT. We therefore need a specific modified description of trap filling and recombination in Ge-containing silica; both for the general model razionalized by equations (4.30)-(4.34) and for the DOTS extraction.
We report here the description of the so-called "modified first order " kinetics used for DOTS extraction in Ge-doped silica samples, which energy level scheme is represented in fig.4.34.

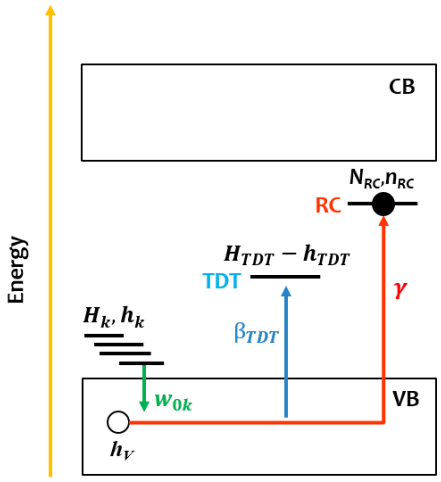


**Figure 4.34:** Energy level scheme.

The "modified first order " kinetics model is based on the following assumptions:

- The recombination of de-trapped carriers is the predominant process ($\beta_{TDT} \ll /\gamma$);
- holes released from TL traps cannot re-trap on other TL traps, they immediately recombine at RC or get trapped by the TDTs (competition between RCs and TDT);
- Carriers trapped in the TDT cannot be released (no de-trapping from very deep TDT states);
- The recombination cross section is related to the temperature and to the activation energy in the form: $\sigma_r = \sigma_{r0} e^{-E_b/k_B T}$.

During the TL readout, the population of holes stores in the $k^{th}$ TL trap varies according to:

$$\frac{dh_k}{dt} = -w_{0k} e^{-E_k/k_B T} h_k \tag{4.35}$$

where the de-trapping frequency factor from $k^{th}$ level is $w_{0k} = w_{0k}(300)(T/300)^2$. $w_{0k}(300)$ is the value of $w_{0k}$ at room temperature (T=300K), (see appendix 4.3.4). Using the change of variable $dh_k/dt = 1/q dh_k/dT$ and with the single cross section assumption, which leads to the same frequency factor value for all traps ($w_{0k} = w_0$), we can write eq.(4.35) as follow:

$$\frac{dh_k}{dT} = -\frac{w_0(300)}{q}\left(\frac{T}{300}\right)^2 e^{-E_k/k_B T} h_k \tag{4.36}$$

As a result of integration from $T_0$ to $T$ we have:

$$h_k(T) = h_k(T_0) exp\left[-\frac{w_0(300)}{q}\int_{T_0}^{T}\left(\frac{T'}{300}\right)^2 e^{-E_k/k_B T'} dT'\right] \tag{4.37}$$

Once the carriers are de-trapped, they can be trapped by the TDT or recombine with the RC. On one hand, the rate of hole trapping in TDTs (per unit time and volume) is: $\beta_{TDT} h_V (H_{TDT} - h_{TDT})$. On the other hand, the recombination rate is $\gamma h_V n_{RC}$. If we assume that these processes happen instantaneously upon detrapping, the recombination rate $\gamma h_V n_{RC}$ can be written as:

$$\gamma h_V n_{RC} = \sum_k \frac{dh_k}{dt}\frac{\gamma n_{RC} h_V}{\gamma h_V n_{RC} + \beta_{TDT} h_V (H_{TDT} - h_{TDT})} = \sum_k \frac{dh_k}{dt}\frac{1}{1 + \frac{\beta_{TDT}(H_{TDT} - h_{TDT})}{\gamma n_{RC}}} \tag{4.38}$$

We rewrite the equation above having made explicit the dependence from the temperature of the thermal velocity $v_{th}$ in $\beta_{TDT}$ and $\gamma$. The thermal velocity can be written as $v_{th} = v_{th}(300)(T/300)^{1/2}$, where $v_{th}(300)$ is the velocity at room temperature (T = 300K). The expression of $\beta_{TDT}$ and $\gamma$ become then: $\beta_{TDT} = \sigma_{TDT} v_{th} = \sigma_{TDT} v_{th}(300)(T/300)^{1/2} = \beta_{TDT}(300)(T/300)^{1/2}$. In the same way, $\gamma$ may be made explicit as follow: $\gamma = \sigma_r v_{th} = \sigma_{r0} e^{-E_b/k_B T} v_{th} = \sigma_{r0} e^{-E_b/k_B T} v_{th}(300)(T/300)^{1/2}$. Finally, by placing $\alpha_{TDT} = \beta_{TDT}(300)/\gamma(300)$, and assuming that the TDT is far from saturation ($n_D \ll N_D$), the $\sum_k \frac{dh_k}{dt} = \sum_k \frac{1}{q}\frac{dh_k}{dT}$, can be written from eq.(4.38) as:

$$\sum_k \frac{dh_k}{dT} = \gamma n_{RC} h_V \left[1 + \frac{\alpha_{TDT} H_{TDT}}{n_{RC}}\left(e^{E_b/k_B 300}\right)^{300/T - 1}\right] \tag{4.39}$$

We already reported in section 4.1, that the theoretical TL intensity is expressed as the number of radiative recombination per unit volume and temperature ($cm^{-3}K^{-1}$). The experimental TL intensity is recorded by means of a PM tube whose output signal is an electric current expressed in Amperes (see section 2.6). So this signal is proportional to the theoretical intensity:

$$I_{TL}^{Exp}(T) = K I_{TL}^{theor}(T) = -K\frac{dn_{RC}}{dt}, \tag{4.40}$$

where the population $n_{RC}$ of RC only varies due to recombination during the TL readout. By integrating equation (4.40) from the initial temperature $T_0$ to the final

one $T_{fin}$ of the TL readout, we obtain:

$$n_{RC}(T_{fin}) - n_{RC}(T_0) = -\frac{1}{K}\int_{T_0}^{T_{fin}} I_{TL}^{Exp}(T')dT' \tag{4.41}$$

which can be rearranged in order to obtain the following expression:

$$n_{RC}(T) = n_{RC}(T_0)\left[1 - \frac{\int_{T_0}^{T} I_{TL}^{Exp}(T')dt'}{\rho\int_{T_0}^{T_{fin}} I_{TL}^{Exp}(T')dt'}\right] \tag{4.42}$$

where $\rho = 1 - \frac{n_{RC}(T_{fin})}{n_{RC}(T_0)}$ ($\rho \geq 1$).
By inserting equation (4.42) in (4.39) we obtain the following expression

$$\sum_k \frac{dh_k}{dT} = -\frac{1}{K} I_{TL}^{Exp}\left[1 + \frac{\alpha_{TDT}\xi_{TDT}\left(e^{E_b/k_B 300}\right)^{300/T-1}}{u_0\left[1 - \frac{\int_{T_0}^{T} I_{TL}^{Exp}(T')dt'}{\rho\int_{T_0}^{T_{fin}} I_{TL}^{Exp}(T')dt'}\right]}\right] \tag{4.43}$$

where $u_0 = n_{RC}(T_0)/H$ and $\xi_{TDT} = H_{TDT}/H$ (proportion of TDT with respect to the total density of hole traps, then TL traps and TDTs).
By inserting (4.36) and (4.37) into (4.43) we obtain the "first order modified TL" equation, which modifies eq.(4.14) and (4.15):

$$I_{TL}\left[1 + \frac{\alpha_{TDT}\xi_{TDT}\left(e^{E_b/k_B 300}\right)^{300/T-1}}{u_0\left[1 - \frac{\int_{T_0}^{T} I_{TL}^{Exp}(T')dt'}{\rho\int_{T_0}^{T_{fin}} I_{TL}^{Exp}(T')dt'}\right]}\right] =$$
$$K\frac{w_0(300)}{q}\left(\frac{T}{300}\right)^2 \sum_k h_k(T_0)e^{-E_k/k_B T} exp\left[-\frac{w_0(300)}{q}\int_{T_0}^{T}\left(\frac{T'}{300}\right)^2 e^{-E_k/k_B T'}dT'\right] \tag{4.44}$$

The main difference between this modified first order equation and the "classic " one is the presence of the modified factor F:

$$F = \left[1 + \frac{\alpha_{TDT}\xi_{TDT}\left(e^{E_b/k_B 300}\right)^{300/T-1}}{u_0\left[1 - \frac{\int_{T_0}^{T} I_{TL}^{Exp}(T')dt'}{\rho\int_{T_0}^{T_{fin}} I_{TL}^{Exp}(T')dt'}\right]}\right] \tag{4.45}$$

Which depends by the parameters $\alpha_{TDT}$, $\xi_{TDT}$, $E_b$ and $u_0$. Since the temperature measurements are made at discrete points $T_l$ ($l = 1 \ldots N$) (whereas we considered M traps labeled by the index $k$); eq.(4.44) can be written in matricial form as follow:

$$\mathbf{I_{TL}} \times F = K\mathbf{M}\mathbf{n_0} \tag{4.46}$$

where the $N \times M$ matrix $\mathbf{M}$ is made of elements:

$$M_{l,k} = \frac{w_0(300)}{q}\left(\frac{T_l}{300}\right)^2 \times \\ \times \sum_k e^{-E_k/k_B T_l} exp\left[-\frac{w_0(300)}{q}\int_{T_0}^{T_l}\left(\frac{T'}{300}\right)^2 e^{-E_k/k_B T'} dT'\right] \tag{4.47}$$

From the experimental TL one can calculate the integrals $\int_{T_0}^{T} I_{TL}(T')dt'$ and $\rho\int_{T_0}^{T_{fin}} I_{TL}(T')dt'$ (at each $T$) in eq.(4.45). Then, it is possible to calculate the right hand side of eq. (4.44) or (4.46).
The vector $K\mathbf{n_0}$ is obtained by applying the matricial inversion rule on eq.(4.46):

$$K\mathbf{n_0} = (\mathbf{M}^T\mathbf{M})^{-1}\mathbf{M}^T(\mathbf{I_{TL}} \times F) \tag{4.48}$$

The determination of the vector $n_0$ requires at least two TL glow curves recorded at two different heating rates, referred as $q_1$ and $q_2$ with $q_1 < q_2$ (experimental vectors $I_{TL1}$ and $I_{TL2}$). From the calculation of matrices corresponding to these rates, $\mathbf{M}(\mathbf{1})$ and $\mathbf{M}(\mathbf{2})$, it is possible to obtain the associated populations, $n_{01}$ and $n_{02}$, by solving equation (4.46).
We then have by construction $I_{TL1}$ =K $\mathbf{M}(\mathbf{1})n_{01}/F$ and $I_{TL2}$=K$\mathbf{M}(\mathbf{2})n_{02}/F$. Since the filling states $n_{01}$ and $n_{02}$ probed by the TL readout results from the same irradiation conditions and is independent of the value of $q$, they must obey $n_{01} = n_{02}$ so the relationship $I_{TL1}$ = K$\mathbf{M}(\mathbf{1})n_{02}/F$ and $I_{TL2}$ =K $\mathbf{M}(\mathbf{2})n_{01}/F$ must also be verified.
The adjustment of the parameters $w_0(300)$, $\alpha_D$, $\xi_D$, $E_b$ and $u_0$ and of the energy interval within which the energies $E_k$ are located, consists in finding the values leading to the best agreement between: $n_{01}$ and $n_{02}$; or between measured $I_{TL1}$ and the curve calculated thanks to $\mathbf{M}(\mathbf{1})$ $n_{02}$ on one hand and $I_{TL2}$ (measured) and $\mathbf{M}(\mathbf{2})$ $n_{01}$ (calculated) on the other hand. In what follows, we report the best DOTS extraction results using this modified analysis formalism.

**DOTS extraction results with modified first order kinetics** In addition to the frequency factor parameter which has been already introduced for the other samples in the DOTS extraction procedure, we need an estimation of $\alpha_D$, $\xi_D$, $E_b$ and $u_0$, present in the factor $F$. We then proceed in the adjustment of these parameters which lead to the best agreement between the measured TL and the calculated one from $\mathbf{M}$ $n_0$ at two heating rates. We proceed describing the way we choose the parameter values (at least in a possible reasonable range), then we show the best results giving the best parameter values found.
The modified first order equation is obtained in the approximation of not saturated TDT, which means $\varphi_{TDT} = h_{TDT}/H_{TDT} \ll 1$. This assumption also means that we should have $\beta_{TDT} \ll \gamma$, or $\alpha_{TDT} \ll 1$. Anyway a small value of $\alpha_{TDT}$ does not predict correctly the increasing if the TL rebuilt form the extracted DOTS. We then started using the value of $\alpha_{TDT} = 1$ (the case where trapping on TDT and

recombination at RCs have the same cross-section). We remind that the DOTS extraction is a first attempt which intent is to extract the DOTS and obtain the parameters necessary to the general model. We will find from the general model, that the approximation of TDT far from saturation does not predict correctly the TL curves from the simulated DOTS.
Concerning the estimation of $u_0$ and $\xi$ it was necessary to use a comparison between a first attempt of the results by DOTS extraction and a feedback from the simulations made by the general model. We proceed with this double check to refine the parameter choice. The initial filling rate $u_0 = n_{RC}(T_0)/H$, may depend on the dimensionless rate $\alpha = \beta/\gamma$, $\alpha_{TDT}$ and $\xi_{TDT}$ by the following relation (obtained under the assumption of $n_D \ll N_D$):

$$u_0 = \frac{h_{TDT}(T_0)}{H}\left[1 + \frac{\alpha}{\alpha_{TDT}}\left(\frac{1-\xi_{TDT}}{\xi_{TDT}}\right)\right] \tag{4.49}$$

where the term $\frac{h_{TDT}(T_0)}{H}$ is related to the reduced dose $D$ and $\alpha_{TDT}$ by [182]:

$$\frac{h_{TDT}(T_0)}{H} = \alpha_{TDT}\left[\sqrt{1 + \frac{2D}{\alpha_{TDT}}} - 1\right] \tag{4.50}$$

The relation in (4.50) was proved in the work by Mady *et al*. [182], where they shown how the filling of traps ruled by the trapping coefficient $\beta_{TDT}$ under the case of very low dose rate and direct recombination obeys to relation:

$$D = \alpha_{TDT}\left(1 - \frac{1}{\alpha_{TDT}}\right)\varphi_D - \frac{\ln(1-\varphi_D)}{\alpha_{TDT}} \tag{4.51}$$

Eq.(4.51) is approximated to (4.50) in the case of negligible saturation of traps ($\varphi_D = n_D/N_D \ll 1$).
By using a value of reduced dose $D$ and $\alpha$ already refined for the other samples, and choosing the arbitrary condition of $\xi_{TDT} = 60\%$ with respect to the total density of traps, we obtain a first estimation of the initial trap filling $u_0$.
Results of the "first order modified kinetics" are shown Fig.4.35-4.36 for the Q01 sample (Ge-doped core). These results are obtained using the parameters reported in table 4.13.
Fig.4.35 reveals that trapped states extend up to 2 eV in the bandgap from the VB edge. The DOTS extracted from the experimental TL curves at two heating rates are in good agreement each other and are both centered at an activation energy of 1.2 eV. This value is reasonable given the one estimated experimentally and represented in Fig.3.47; where is shown the trap depth (red scattered lines) evaluated according to the initial rise (IR) method [165, 184]. One can see that to the TL peak at 250°C corresponds an activation energy level lying between 1.2 eV and 1.4 eV, and that the energy range of the DOTS is correctly scaled.
In Fig.4.36 is reported the superimposition of the experimental TL curves (solid lines) and the theoretical ones (dashed lines), at two heating rates (0.5 °C/s and 2°C/s). These theoretical TL curves are generated by the DOTS displayed in Fig.4.35 from M(0.5)$\mathbf{n_0}$(2) to check the prediction of the TL at 0.5°C/s and from M(2)$\mathbf{n_0}$(0.5) to check the prediction of the TL at 2°C/s.

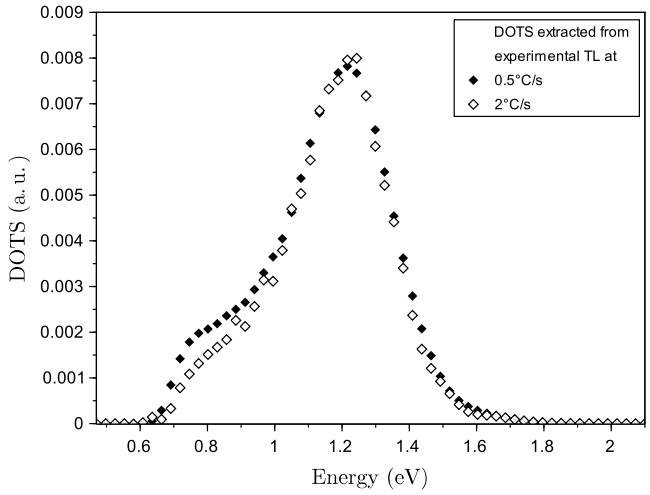


**Figure 4.35:** Density of trapped states (DOTS) extracted from glow curves of Fig. 4.36 measured for Q01 sample at 0.5 and 2 $^oC/s$. The extraction is made assuming the TL obeys a "modified " first-order kinetic process (due to TDT). These distributions of trapped holes give the theoretical TL curve of Fig. 4.36.

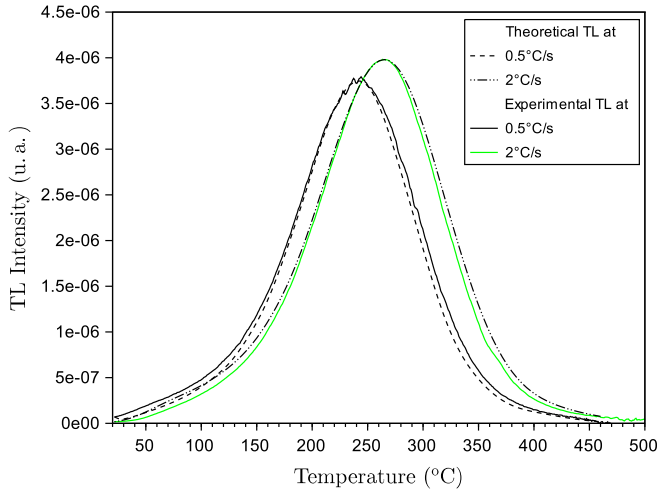


**Figure 4.36:** Comparison between the experimental TL glow curves (solid lines) of Q01 sample recorded at 0.5 and 2 $^oC/s$ and the ones rebuilt with extracted DOTS of fig.4.35 (dotted lines). These latter (theoretical TL) are calculated from M(0.5)$\mathbf{n_0}$(2) to check the prediction of the TL at 0.5°C/s and from M(2)$\mathbf{n_0}$(0.5) to check the prediction of the TL at 2°C/s.

This modified DOTS extraction protocol considers the presence of a TDT and a

recombination cross section depending on the temperature. As far as we tried to account for the " anomalus" increase of the TL response with the heating rate, this combination is the only one that proved to reproduce experimental behaviors. The ability of this protocol to extract similar DOTS from the TL curves at 2 heating rates, strongly supports the relevance of our proposal concerning the specific features of TL processes in Ge-containing samples.

| | Q01 |
|---|---|
| Frequency factor $w_0$ ($s^{-1}$) | $1.5 \times 10^{10}$ |
| $\alpha_{TDT}$ | 1 |
| Initial filling rate $u_0$ | 0.005 |
| Proportion of TDT $\xi_{TDT}$ (%) | 60 |
| Energy barrier $E_b$ (eV) | 0.12 |

**Table 4.13:** Simulation parameters used for the DOTS extraction of fig. 4.35 and the relatives TL curves in Fig. 4.36 rebuilt from these DOTS . $E_b$ is the energy barrier of the recombination cross section.

### 4.3.2 Simulations with the general model.

In the study of the TL response as a function of the dose, the best agreement with extrapolated DOTS and simulated ones and from the TL responses (peak areas) and experimental ones, we refine the choice of the following parameters: $\alpha = \beta/\gamma$, $\theta = \delta/\gamma$, $r = H/N$, $N$, $C$ and $W$. Basically we put all the parameters related to the TDT at zero, such as in the "classical general model" adopted for all the other samples. This choice does not effect the results since the anomaly characterizing the Ge-doped silica samples is related to the TL response with the increasing heating rate. The "classical general model" can predict well the TL response when changing the dose but not the heating rate. The procedure used in the search for these parameters is therefore similar to that observed in the other samples. We refer to section 4.1.5 for the justification of the reasonable values range for the parameters and the choice of $\alpha$, $\theta$ and $r$ values. The TL response as a function of the dose allows us to estimate $N$, which sets the saturation degree and $\beta$. $\beta$ is such that $w_0 = \beta N_c$, where $N_c$ lies between $10^{18}$ and $10^{20}$ $cm^{-3}$ typically. $w_0$ is known from DOTS extraction so we can deduce the order of magnitude of $\beta$.
Finally, from the simulated DOTS obtained with the general model we can well predict the increasing TL with the increasing heating rate. From this last study we found $E_{TDT}$ and refine the values of the other parameters previously found, such as $\alpha_{TDT}$. The value of $\alpha_{TDT}$ was found to be a very important parameter in the effect of the decreasing or increasing of the TL with the heating rate. If in the first order modified model, the choice of $\alpha_{TDT}$ between 0.4 and 10 does not change the results, in the general one, $\alpha_{TDT}$ must be between 1 and 0.1. A too small value of $\alpha_D$ does not predict the correct TL. Moreover, using a small value of $\alpha_{TDT}$ (i.e. $10^{-5}$), with a small percentage of TDT (10%), the simulated TL predict a decreasing of the TL. Then the choice of $\xi_{TDT} = 60\%$ previously used in the DOTS extraction is confirmed by the general model.
In what follows we report the best results of the simulated TL at several doses and at four heating rates. We present the results showing the comparison between the

samples Q01 (Ge), Q07 (GeP) and Q09 (GeF). All of these samples present the same TL features, then the simulations are obtained using the same parameters.

**TL response as a function of the irradiation dose** The determining parameters estimated from the TL response changing the irradiation dose are the dimensionless ratios rationalizing the competitions between the various transitions ($\beta/\gamma$, $\delta/\gamma$), the ratio between the total densities of hole and electron traps ($H/N$).
In Fig.4.37 is reported the area of the TL curves as a function of the dose of Q01 (Ge), Q07 (GeP) and Q09 (GeF) samples. The parameters used to obtain these results are reported in table 4.14.

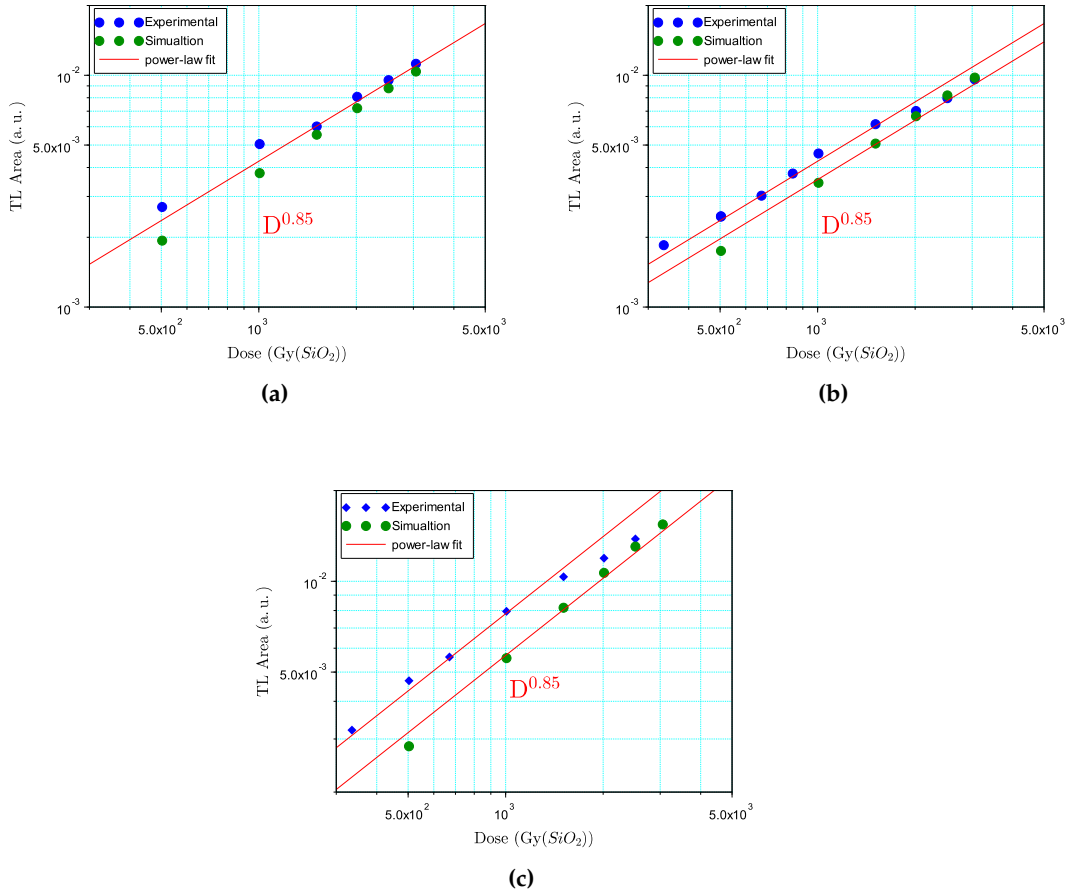


**Figure 4.37:** Areas of Experimental TL glow curve and simulated ones as a function of the dose using a dose rate of 200Gy/min(SiO2), for Q01 (a), Q07 (b) and Q09 (c) samples. The power-law fit (red line) to experimental points reveals a power dependence from the dose of $D^{0.85}$.

The measurements were performed using several irradiation times at a fixed dose rate (200 Gy($SiO_2$) $min^{-1}$) and changing the irradiation time. TL readout were performed at 1°C/s. The TL areas show a power-law behavior with the dose with

exponent 0.85, highlighted in the figure by the red line. Simulated TL responses with parameter values of Table 4.14 follow quite well the experimental ones, even if they are underestimated at low doses. As seen for the other samples previously reported in this chapter, the TL dose dependence prediction set the correct value of $\alpha$. Also for Ge-doped silica sample we found a small value of $\alpha$ ($10^{-5}$), meaning that the re-trapping is negligible (at TL traps).

| | Q01-Q07-Q09 |
|---|---|
| Trap Density H ($cm^{-3}$) | $1.6 \times 10^{18}$ |
| $\beta$ ($cm^3 s^{-1}$) | $10^{-10}$ |
| $\alpha = \beta/\gamma$ | $10^{-5}$ |
| $\theta = \delta/\gamma$ | $10^{-5}$ |
| $r = H/N$ | $10^{-5}$ |

**Table 4.14:** Simulation parameters used for the results reported in Fig. 4.37. The proportion of TDT(%) is set in relation to the total hole trap density $H$.

In order to obtain the best agreement, we played with the ratio between hole trap density and electron traps density $r = H/N$. This parameter affects the prediction of the TL intensity and the temperature of the peak. For a small value of r ($< 1 \times 10^{-5}$) the peak is shifted to higher temperature when decreasing of the dose, whereas for value of r=1 the TL intensity is overestimated. For this reason, this study is useful to understand the effect of some parameters and find the best ones.

**TL response changing the heating rate** Note that the only determining parameters are the energy Barrier for trapping cross-section on TDT ($E_{TDT}$), $C$ and $W$. Fig. 4.38 shows the superimposition of the experimental and simulated TL at four heating rates (0.5, 1, 2 and 3°C/s) adopting the general model described by equations (4.30)-(4.34) for the Ge sample (Q01).

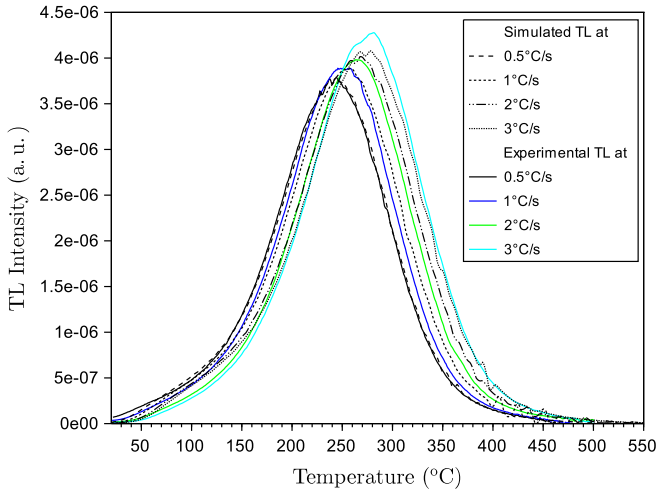


**Figure 4.38:** The superimposition of the experimental TL glow curves (solid lines) and simulated ones (dotted lines) in Q01 sample, at $0.5^oC/s$, $1^oC/s$, $2^oC/s$, $3^oC/s$.

The experimental curves were recorded after a dose of 1kGy, at $t_{relax} = 120s$ from the end of the irradiation. Simulations have been done with the parameters given in Table 4.15, with the same irradiation and relaxation times as those used in experiments. Using these parameters, the reproduction of the TL response dependence on the heating rate is quite good. The correct location of the peak with the good prediction of the TL intensity increase with the increasing heating rate, validate the simulated DOTS from which these TL curves are calculated.
Considering an error of 5% in the measured intensity, the agreement between experimental and simulated curves is good, proving that the proposed model well explains the increase of the TL peak area observed in Ge-doped silica samples when increasing the heating rate. The presence of the TDT combined with the temperature dependence of the recombination cross-section $\sigma_r$ (see eq. (3.12)) are crucial in this respect. To fit the experimental difference in intensity at various heating rates, we can adjust the parameters already estimated such as the percentage of TDT among hole traps or the ratio $r = H/N$. But the most determinant factor in the increasing of the TL intensity with the heating rate is the ratio between $\beta_{TDT}$ and $\gamma$ (then $\sigma_r$). This factor describes the competition between the trapping of holes in the TDT and their recombination at RCs. If this ratio tends to zero we approach a process where all free holes recombine (as if there was no TDTs). From this study we found that the best choice for $\alpha_{TDT}$ is 0.1.

| | Q01 |
|---|---|
| Trap Density H ($cm^{-3}$) | $10^{18}$ |
| $\beta$ ($cm^3s^{-1}$) | $10^{-10}$ |
| $\beta/\gamma$ at 300 K | $10^{-5}$ |
| $\delta/\gamma$ at 300 K | $10^{-5}$ |
| $H/N$ | $10^{-5}$ |
| $C$ | $10^8$ |
| $W$ (eV) | 0.05 |
| $E_{TDT}$(eV) | 0.007 |
| Proportion of TDT (%) | 60 |
| $\beta_{TDT}/\gamma$ at 300 K | 0.1 |
| $E_b$ | 0.17 |

**Table 4.15:** Simulation parameters used for the results reported in Fig. 4.38.The proportion of TDT(%) is set in relation to the total hole trap density $H$.

From parameters of table 4.16 we obtained the results of Fig.4.39a and 4.39b from the general simulation model, where is reported a comparison between the simulated curves obtained for a GeP doped silica preform (Ge in the core and P in the cladding), and a P-doped core preform (L28). The results on P-doped sample were obtained using the "normal" simulation model already presented in 4.2.4 based on equations similar to (4.30)-(4.34) without the population on TDT and for a temperature-independent recombination cross-section.

| | Q07-Q09 | L28 |
|---|---|---|
| Trap Density H ($cm^{-3}$) | $10^{18}$ | $1.4 \times 10^{20}$ |
| $\beta$ ($cm^3 s^{-1}$) | $10^{-10}$ | $10^{-10}$ |
| $\beta/\gamma$ at 300 K | $10^{-5}$ | $10^{-5}$ |
| $\delta/\gamma$ at 300 K | $10^{-5}$ | 1 |
| $H/N$ | $10^{-5}$ | 1 |
| $C$ | $10^{8}$ | $10^{8}$ |
| $W$ (eV) | 0.05 | 0.095 |
| $E_{TDT}$(eV) | 0.007 | - |
| Proportion of TDT (%) | 60 | - |
| $\beta_{TDT}/\gamma$ at 300 K | 0.1 | - |
| $E_b$ | 0.17 | - |

**Table 4.16:** Simulation parameters used for the results reported in Fig.4.39.The proportion of TDT(%) is set in relation to the total hole trap density $H$.

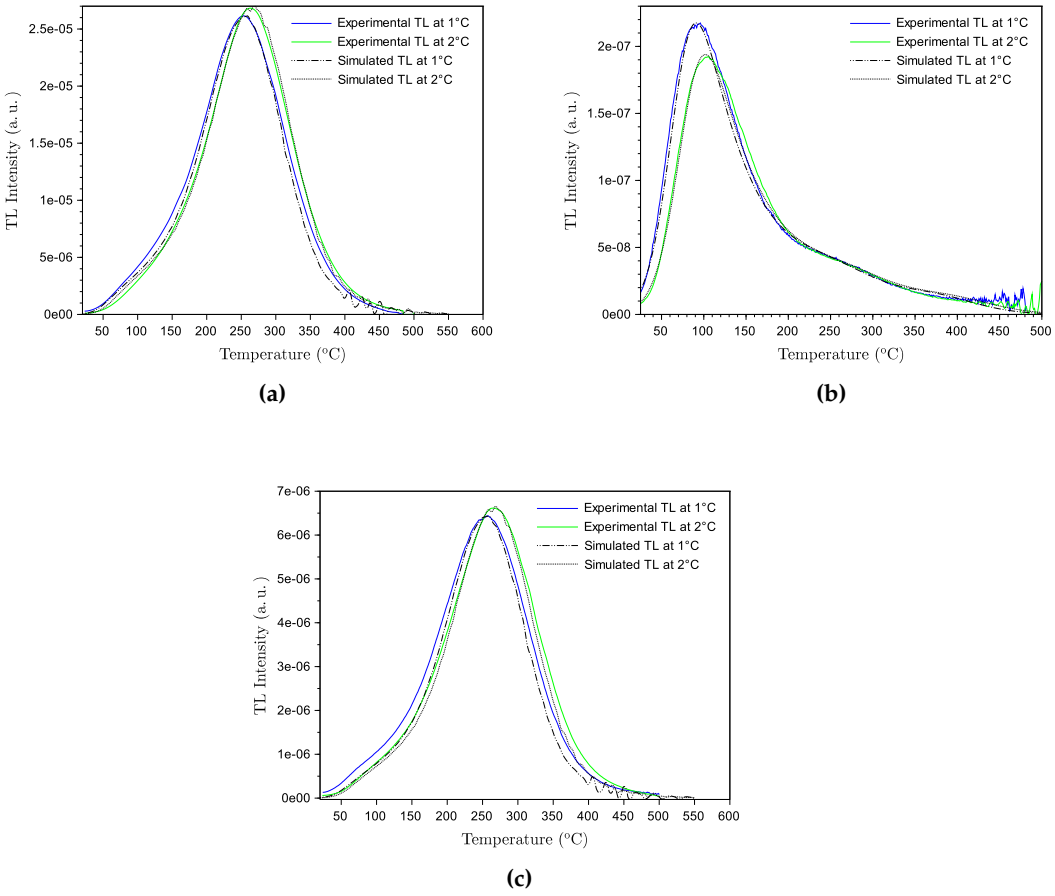


**Figure 4.39:** TL glow curves at $1^oC/s$ and $2^oC/s$ on a) GeP- (Q07), b) P-doped silica preform (L28), and c) GeF (Q09) doped silica sample.

The GeP-doped sample shows the same TL features than the Ge-doped one. The effect of Phosphorous doping is negligible since the TL intensity due to Germanium is much higher than that of pure silica or P-doped silica. Even if germanium doping is focused in the core of the preform while phosphorous spreads over all the cladding, in Q07 sample the P content is just 0.89 at.%, whereas the Ge content is 4.46 at.% (see table 2.1). In fig.4.39c is reported the results for GeF doped silica (Q09). The considerations made for Ge sample are valid also for GeF. Although this sample contains F, it does not involve any new characteristics in the TL features compared to the germano-silicate sample and exhibits the same TL features as the Ge-doped sample Q01.

### 4.3.3 RIA simulation during thermal annealing

The model exposed above was built specifically for Ge-doped silica in order to describe an anomalous feature characterizing the TL on this kind of doped silica. Such model allowed us to extract the DOTS. As seen previously for other kinds of tested samples, the final goal of the modeling procedure exposed in this work is to predict the RIA from the assignment of color centers, whose optical absorption bands contribute to RIA to some of the trapped states present in the DOTS.
This subsection presents such RIA modeling for Ge-doped samples. After calibrating the RIA model (from DOTS simulation) against the RIA spectrum measured at RT, we will show that the simulation is capable of predicting the RIA spectra obtained at the various temperatures of the RIA thermal annealing protocol. These results will demonstrate that the thermal effects are well accounted by the proposed model.
In order to predict the RIA during the thermal annealing procedure, we must simulate the DOTS at each "stopping temperature" of this protocol. The experimental procedure performed to get the TL curves of these temperatures steps is explained below. It was performed in the same heating conditions as those of RIA during the thermal annealing.
The experimental results obtained from this experiment are reported below. Then, the section continues by assigning the DOTS to the color centers causing RIA in the visible, as shown for the other samples. Finally, the simulation of the RIA bleaching during the thermal annealing will be presented as well as a comparison with the experimental spectra.

**Experimental details** The studied fiber preform presented here, named GeD2, is produced by iXFiber SAS by MCVD process. The Ge content and the doping profile are already reported elsewhere [96]. Germanium doping levels are designed to follow a two-step distribution: the first step is doped with $\sim 4.5 wt.\%$, whereas the second with $9 \sim wt.\%$. The preform slice sample has a thickness of about 0.6 mm. This sample presents a germanium content lower than Q01, which presents an in-core Ge concentration as high as 10 wt.%. This high amount of Ge leads to problems in the simulation of the RIA, since the GLPC absorption band recorded before the irradiation, is saturated. In order to have a clear gaussian band we have chosen to do the study on another sample with less Ge content such as the GeD2 one. The use of a sample from a different manufacture will be the opportunity to

show that our simulation model are not just adapted for the particular sample fabricated in Nice for the *CERTYF* project. By contrast, in includes sufficiently basic physics, common to all Ge-doped silica, to offer the required universality.
The RIA thermal annealing experiment (see section 4.3.4) was performed on the GeD2 sample after a dose exposure of 4.6 kGy at a dose rate of 150 Gy($SiO_2$)/min. The thermoluminescence annealing treatment or "pre-heating protocol" was performed on GeD2 sample from RT to stopping temperature $T_{stop}$, which was increased from 50 °C to 500 °C by step of 50 °C , i.e. according to the same scheme as for the RIA thermal annealing protocol (appendix 4.3.4).
Once the sample has been exposed to radiation (at a dose of 330 Gy($SiO_2$) and using a dose rate of 200 Gy($SiO_2$)/min), it was heated up to the temperature $T_{stop}$ by means of the TL setup. Then the sample temperature was brought back to RT and the TL measurement was recorded at 1 °C/s from RT to 500 °C. This process, consisting in (i) irradiation, (ii) heating up to $T_{stop}$ and (iii) TL readout, has repeated for several $T_{stop}$ values; namely at 50°C , 100°C 150°C , 200°C , 250°C , 300°C , 350°C , 400°C , and 450 °C . With this procedure we empty progressively traps of increasing depths and the TL readout probes the DOTS starting from deeper and deeper levels (increasing $E_D$ values). The important point here is that we can get the simulated DOTS from which calculate the TL curves. These TL curves can be compared with the experimental one to prove that the simulated DOTS are well predicted. Once obtained the DOTS, we can then simulate the RIA spectra at each step of the thermal annealing.

**Experimental results** Fig.4.40 shows the RIA obtained at RT on the GeD2 sample at a dose of 4.6 kGy($SiO_2$). Decomposition attempt of this RIA into Gaussian bands have been done to comply with usual bands attributed to well identified Ge-related centers: Ge1 at 4.25 eV and silica related ones such as NBOHC (4.8 eV)) [46] (see tab.4.17).

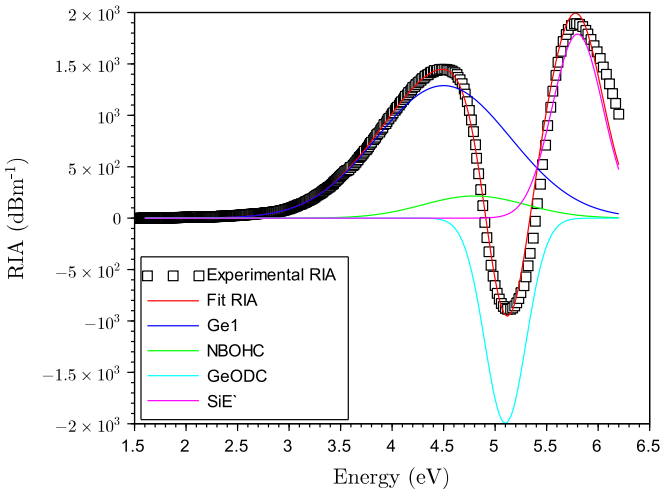


**Figure 4.40:** RIA of a Ge-doped sample GeD2 after 4.6 kGy($SiO_2$) X-ray irradiation at RT.

One can note that the main contribution to this observed RIA is largely due to Ge1 centers. The band at 5.8 eV corresponds to the intrinsic SiE' centers and to Ge(2) centers, both centers being most probably present [46, 78, 94, 98, 185]. The optical absorption by the Germanium lone-pair centers (GLPC), a variety of Ge-related oxygen deficient centers (GeODC), clearly appears as a band centered around 5.1 eV in the absorption spectrum of the pristine sample. In agreement with previous observations [94], we found that this band is reduced by irradiation. The decomposition attempt of the RIA in Fig.4.40 therefore includes this band at 5.1 eV with a negative amplitude.

| Defect | $x_c$(eV) | FWHM (eV) |
|---|---|---|
| Ge1 | 4.25 | 1.5 |
| NBOHC | 4.8 | 1.17 |
| GeODC | 5.1 | 0.46 |
| 5.8eV/SiE' | 5.8 | 0.6 |

**Table 4.17:** Characteristics of the optical absorption bands used for the Gaussian decomposition of fig.4.40.

The thermal annealing results are reported in Fig. 4.41, where the RIA curves at all the temperature steps are superimposed. The RIA progressively decreases as the stopping temperature increases as a result of CC annealing. One can observe on one hand the decrease of the RIA at energies related to the Ge1, SiE' and NBOHC centers, and on the other hand the increase of the band related to GeODC. The latter starts from a negative amplitude up to almost zero at 500 °C.

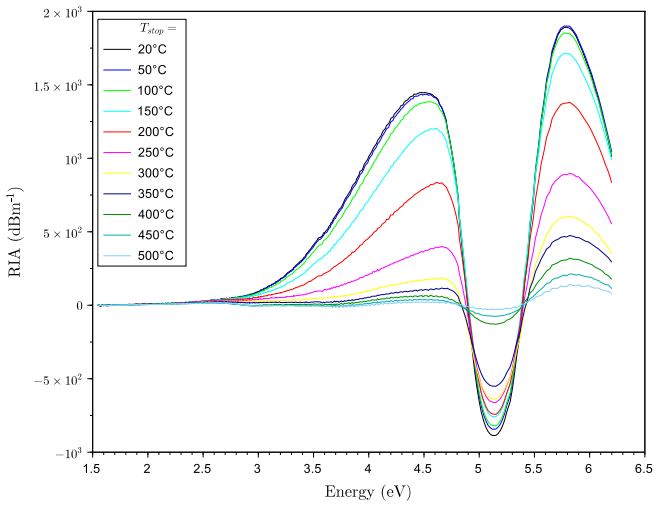


**Figure 4.41:** RIA recorded during the thermal annealing treatment.

To better analyze the bleaching of defects, we plotted in Fig.4.42 the evolution of the different band areas (optical intensities) at each stopping temperature ($T_{stop}$) of the annealing protocol. We observe an important decrease of the optical intensities between 150 and 400°C, exception made for GeODC centers, which are reformed

during annealing. The band intensities at RT and 50°C are pretty close. This result is observed for all the thermal annealing measurements made in this work. The temperature of 50°C is not high enough to observe a change in the RIA intensity, at least under our experimental condition.

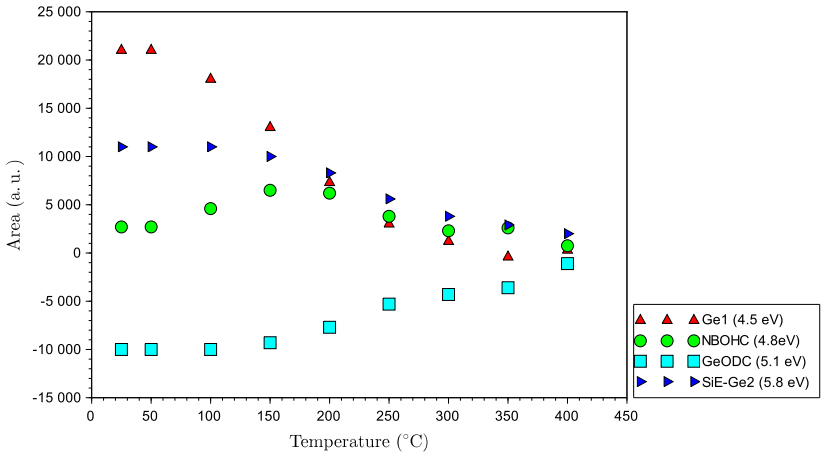


**Figure 4.42:** Optical intensities (areas) of the various gaussian bands used in the decomposition reported in fig.4.41 as a function of $T_{stop}$ of the thermal annealing step.

The TL curves measured along the "pre-heating protocol" is reported in fig.4.43. The TL glow curves show a decrease of the intensity with the increasing $T_{stop}$. One can note that up to ∼100°C, the temperature of the main TL peak and its intensity remains more or less the same, while lower temperature components are logically extinguished.

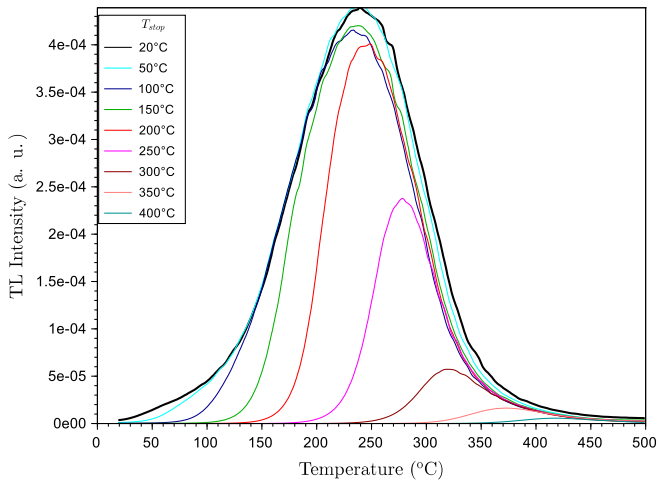


**Figure 4.43:** TL glow curves recorded after an irradiation dose of 330 Gy($SiO_2$) and after pre-heating up to $T_{stop}$, from 20 to 400°C.

This is due to the fact that in that range of temperature we are depleting the shal-

lower traps. When the stopping temperature $T_{stop}$ exceeds the peak temperature, the intensity of the peak decreases significantly up to the total annealing at 500 °C. This behavior is an obvious result, that one may expect from the way on which the experiment is carried out, since the temperature of the readout increases at each step. But what is important for us is the possibility to simulate the DOTS from these experimental curves which will be used in the RIA modeling to simulate the RIA spectra bleached shown in fig.4.41 at the various $T_{stop}$.

**Simulation results** In order to predict the RIA at RT and during the thermal annealing procedure, we must simulate the DOTS at each "stopping temperature" of this protocol (note that the RIA at RT (fig.4.40) will be obtained from the DOTS at $T_{stop}$=20°C). The simulated DOTS at each pre-heating is the results of a prediction which must take into account the irradiation time ($t_{irr}$) and $t_{relax}$ between the end of the irradiation and the TL reading, but also the pre-heating phase of the sample before the TL readout. During this phase, when the temperature increases with a constant heating rate, holes trapped in the shallower levels are progressively released, as one can see on the TL curves of fig.4.43 which low-temperature side is more and more depleted as the $T_{stop}$ increases.
The experimental condition characterizing the "pre-heating" TL experiment, need a specific procedure in the simulation, composed by the following steps:

1 DOTS extraction from TL curves using the "first order modified kinetics" ;

2 Simulation with the general model of the DOTS under the irradiation and post-irradiation condition before the "pre-heating" protocol (Dose = 330 Gy($SiO_2$), Dose rate = 200 Gy($SiO_2$/min), $t_{relax}$ = 120 s). This DOTS at $T_{stop}$ = 20 °C gives us the simulated TL at the same $T_{stop}$, which is the TL curve recorded just after the end of the irradiation and without the "pre-heating " treatment.

3 Simulation of the DOTS under the post-irradiation conditions of the "pre-heating" protocol and of the related TL at each $T_{stop}$. The comparison between these simulated TL with the experimental one of fig.4.43 would confirm whether the DOTS prediction is good or not.

This first step has been obtained in a similar way to that of Q01 sample. After the extraction of dots from the experimental curves it was possible to simulate dots under the above experimental conditions. The DOTS extraction and the research of the parameters has been rendered simple once the model has been calibrated for Q01 sample. Both samples, although with a different concentration of germanium, have the same TL, which differs only in intensity. Then we just report the simulation results obtained following the steps 2-3 above, explaining in detail the procedure and summarizing the parameters found for the results.
Fig.4.44 reports the comparison between the experimental TL curves and the simulated ones during the "pre-heating" protocol. These latter curves (dashed lines in figure) are obtained from the simulated DOTS reported in fig.4.45.

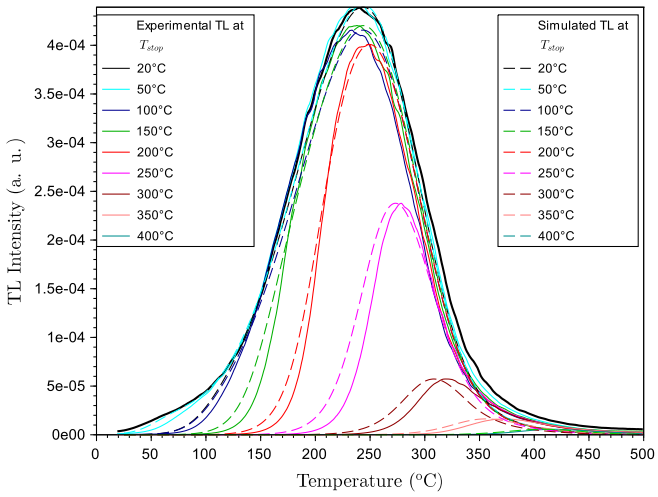


**Figure 4.44:** Experimental (continuous lines) and simulated (dashed lines) TL glow curves, during the thermal annealing treatment at the same $T_{stop}$ values.

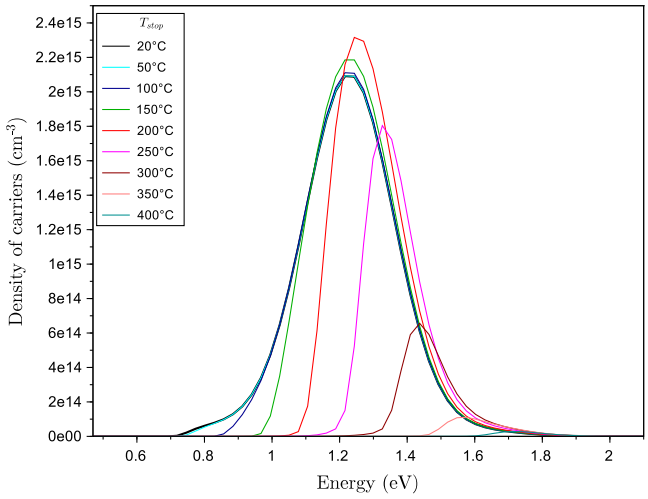


**Figure 4.45:** Simulated DOTS during the thermal annealing treatment which produce the calculated TL curves of fig.4.44.

The simulated DOTS at each $T_{stop}$ step of the "pre-heating protocol " are obtained from the general model considering an irradiation and post irradiation condition in accordance to the cit pre-heating protocol " and a TL readout phase carried up to $T_{stop}$. From this step we obtain the population of the traps ($n_k(T_{stop})$) after the irradiation and the heating up to $T_{stop}$. Then, we perform the TL simulation readout using $n_k(T_{stop})$ as initial condition of the trap filling. From this last step we obtain the simulated TL at $T_{stop}$.
This procedure has been made for all the heating steps from RT to 400°C. One

can see from the results of fig.4.44 that the agreement from the experimental TL and the simulated one is quite good. The model for trap filling is well capable of rendering the effect of pre-heating treatment. One can see that the position of the peak at each $T_{stop}$ is well located. The intensity during the simulation procedure is normalized just to the TL recorded right after the radiation ($T_{stop}$=20°C). Then the relative TL intensities at teach $T_{stop}$ are also well predicted. The agreement between experimental and simulated TL obtained from the simulated DOTS of fig.4.45, strongly support that the DOTS simulation is reliable.
The results reported here have been obtained by varying some parameters previously reported for Q01. The main difference concern the general model parameters, namely the percentage of TDT, $H$ and the values of Mott Seitz for the TL simulation. The parameters used to obtain the simulated DOTS and the related TL are reported in table 4.18.

| | GeD2 |
|---|---|
| Trap Density H ($cm^{-3}$) | $3.1 \times 10^{18}$ |
| $\beta/\gamma$ at 300 K | $10^{-5}$ |
| $\delta/\gamma$ at 300 K | $10^{-5}$ |
| $H/N$ | $10^{-5}$ |
| $C$ | $10^{8}$ |
| $W$ (eV) | 0.095 |
| $E_{TDT}$(eV) | 0.007 |
| Proportion of TDT (%) | 30 |
| $\beta_{TDT}/\gamma$ at 300 K | 0.1 |
| $E_b$ | 0.17 |

**Table 4.18:** Simulation parameters used for the results reported in fig.4.44 and 4.45.

Once the simulated DOTS are validated, we can proceed to the RIA simulation at RT and during the thermal annealing treatment. First of all, we start with the usual assignment of each component of the DOTS at RT ($T_{stop}$=20°C) to CCs involved in the RIA, from which it is possible to calculate the optical absorption produced by the densities of the radio-induced centers. As adopted for all the other doped samples, we report the charge conservation equation which in the case of Germanium, can be written as:

$$N_{intrinsic_{e^-}} + N_{SiODC:e^-} + N_{GeODC:e^-} + N_{Ge1} = \\ = N_{intrinsic_{h^+}} + N_{NBOHC} + N_{SiE'/Ge2} \quad (4.52)$$

As seen from the experimental results (fig.4.40), the radiation-induced CC are the trapped holes centers such as NBOHC, SiE', and Ge2 if we consider its structure as an ionized GLPC, and the trapping electrons centers such as the $SiODC : e^-$ and $SiODC : e^-$, Ge1 (and Ge2 if we consider its structure as the Ge1 similar one).
In the exploitation of the charge conservation equation, the usual difficulty concerns the NBOHC centers. The latter contribute to the RIA, but it have not yet been associated with any particular level of the DOTS. We always assume the NBOHC density as a fraction of the SiE' centers concentration, because these two types of

defects are produced in pairs [34]. This fraction is an adjustable parameter of the RIA simulation.
In the same way, the estimation of Ge1 and Ge2 concentration a priori is not independent, as it will be explained in what follows. In Ge-doped silica the absorption band at 5.8 eV is usually related to Ge2, but SiE' centers are also characterized by an absorption band centered at the same energy. One can consider that the main contribution to the RIA at that energy is due to Ge2. Anyway, in our RIA model, we considered just one band centered at 5.8 eV. This lack of separation is unfortunately present also in the DOTS. In the DOTS decomposition attempt reported in fig.4.46, we notice the presence of a wide band around 1.2-1.3 eV. In silica this band undoubtedly contained to the levels of the SiE' centers.

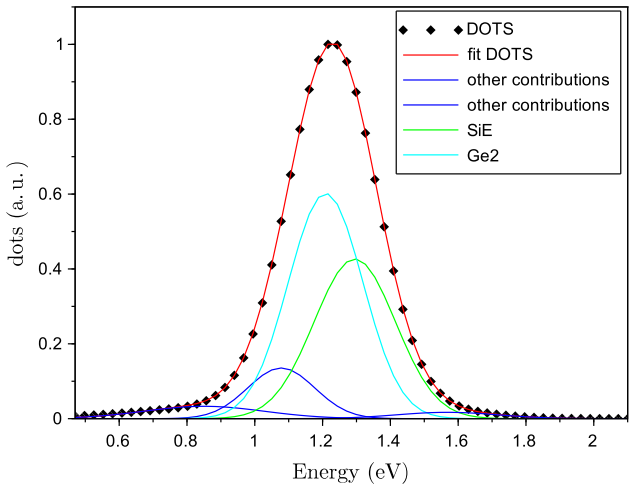


**Figure 4.46:** Simulated DOTS at RT and its decomposition.

In the DOTS of GeD2, this band is very high and wide. This feature can be interpreted into two different ways:

1 The presence of Ge strongly enhanced the formation of trapped-hole centers, including SiE' centers.

2 Ge2 centers are trapped-hole states that share the same activation energy as SiE' (and not only the same optical absorption energy), thus giving rise to an additional contribution to the DOTS around 1.2-1.3 eV.

In both cases, we can just consider the DOTS contribution centered at 1.2-1.3 eV, related to a CC absorbing around 5.8 eV. This is basically what we made. The problem consists now in the calculation of the Ge1 band. The relationship between the production of Ge1 and Ge2 centers is indeed not obvious. In literature, the nature of Ge2 is still questionable. If it is considered as a kind of Ge1, is it a trapped electron. If it is, conversely, considered an ionized GLPC, it is a trapped hole center. In the first case we cannot calculate it from the DOTS since it is a trapped electron. In the latter one, we can find a correlation in the DOTS as we made for SiE'. Moreover, once is found the Ge2 contribution in the DOTS and is calculated the amplitude of his gaussian band, we can obtain an estimation of Ge1 centers because it is known

that both are created in pairs. Since this description works and is quite accessible from our model, we followed this way and we assumed the Ge1 concentration as a fraction of that of Ge2 ones, as made previously for NBOHC and SiE'.
The simulated DOTS for each heating step can be fitted properly thanks to the occupancy state information obtained from the simulation procedure. The simulations give the occupancy rate of hole traps at any step of the protocol. Thanks to this occupancy rate, we were able to follow the "truncation " of the DOTS at each step, and, as a consequence, also the components of the fit.
As an example, we report in fig 4.47 the DOTS at RT (circles), the DOTS at $T_{stop}$ = 150 °C (blue line) and the normalized occupancy state at $T_{stop}$ = 150 °C (red line). Basically, the DOTS at $T_{stop}$ = 150 °C is the results of the DOTS at RT multiplied by the occupancy state at $T_{stop}$ = 150 °C. We obtain the truncation of the gaussian components of the DOTS multiplying all the contributions by the occupancy state.

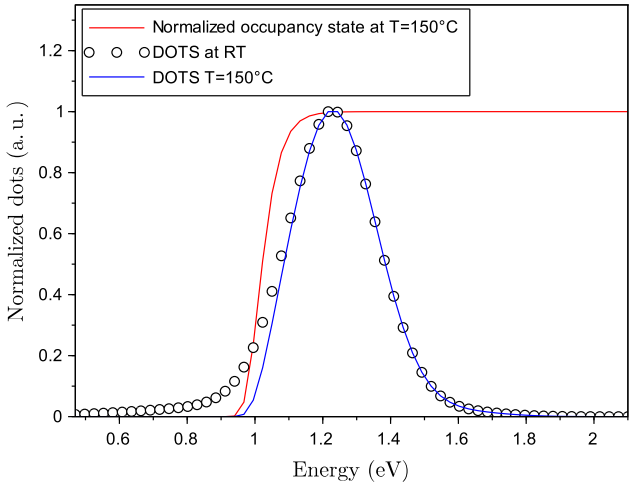


**Figure 4.47:** DOTS at RT (circles), at $T_{stop}$ = 150 °C (blue line) and the normalized occupancy state at $T_{stop}$ = 150 °C (red line).

To follow the DOTS composition at each $T_{stop}$, we use exactly the same bands (centers and FWHM) as for the decomposition of the RIA at RT. But now, knowing the occupancy rate of levels (from DOTS simulation) at each step of the protocol, we truncate the gaussian components by adjusting not with pure gaussian functions, but with gaussian multiplied by the occupancy rate. In this way we can use the analytical functions of the DOTS bands at each heating step for the RIA modeling, in the same way as made for the RIA at RT. The fit of the DOTS at all the temperature annealing steps are reported in fig.4.48.
Once the density of each type of CC contributing to the RIA spectrum is known, it is possible to estimate the amplitude of their optical absorption band using Smakula's formula for Gaussian bands as explained before. The RIA spectrum of the Ge sample was reconstructed according to this approach.

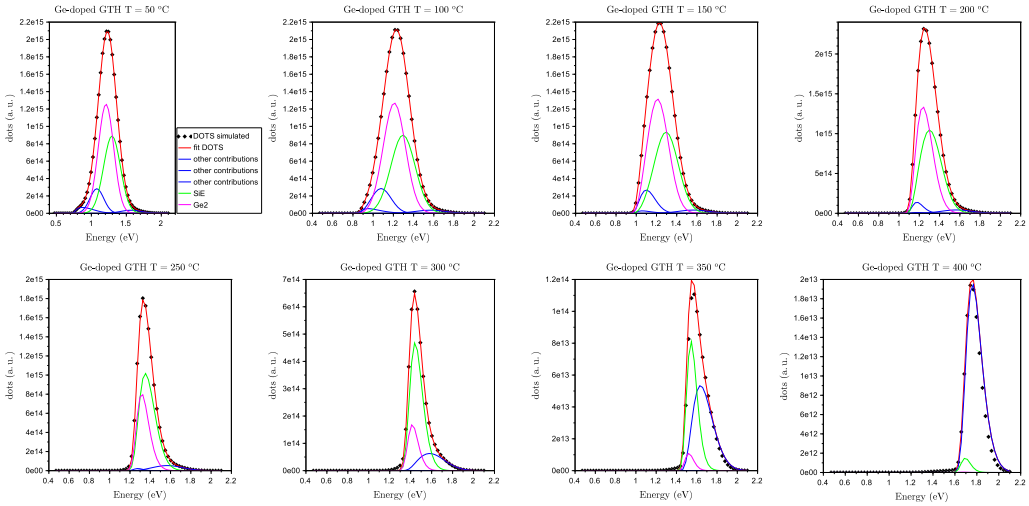


**Figure 4.48:** Fit of the simulated DOTS reported in fig.4.45 at all steps of the annealing along the "pre-heating" protocol.

The simulation of the RIA at RT is shown in Fig. 4.49, where the half-height widths and the band position used are given in tab. 4.19. The NBOHC concentration was set at 33% respect to SiE', whereas the Ge1 concentration is 66% of that of Ge2. Concerning the oxygen-deficiency centers centers, we considered GeODC represent 80% of the total ODC concentration.

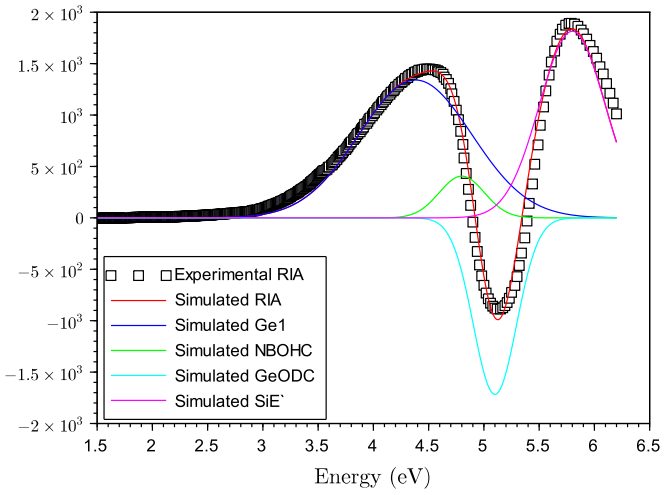


**Figure 4.49:** Experimental (scatter graph) and simulated (red line) RIA on Ge sample after a dose of 4.6 kGy($SiO_2$). In the figure are also reported by colored lines the simulated gaussian bands which parameters are reported in table 4.19.

| Defect | $x_c$ (eV) | FWHM (eV) | $f$ simulation | $f$ literature |
|---|---|---|---|---|
| Ge1 | 4.38 | 1.2 | 0.19 | 0.28 [117] |
| NBOHC | 4.8 | 0.48 | 0.05 | 0.05 [36] |
| GeODC | 5.1 | 0.46 | 0.3 | 0.4 [186] |
| 5.8eV/SiE′ | 5.8 | 0.7 | 0.14 | 0.14 [32] |

**Table 4.19:** Characteristics of the RIA simulated bands.

The RIA simulation was also performed at all temperature steps of the RIA annealing (fig. 4.41). We used the DOTS in fig.4.48 to calculate the RIA at each thermal annealing step with the same parameters as those found at RT. In order to show the comparison between the experimental and simulated curves, we compare in fig.4.50 the optical intensities (areas) of the simulated gaussian bands to the fit of the experimental ones. As one can see the agreement is quite good.

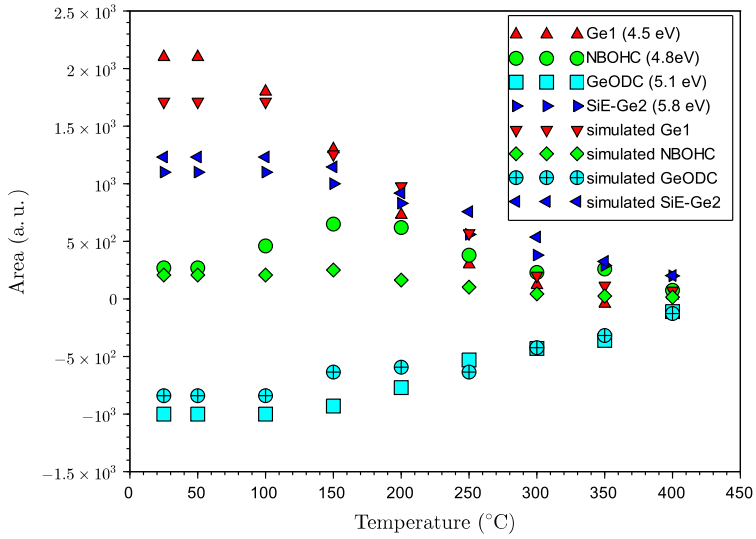


**Figure 4.50:** Optical intensities of the gaussian bands used for the fit of each RIA curve reported in fig.4.41 as a function of $T_{stop}$ of the thermal annealing step. Comparison between simulation and experiment.

### 4.3.4 Summary of the results for Ge-doped silica.

To summarize on Ge-doped silica results, we can say that from TL, we are able to investigate the radiation-induced mechanisms and estimate activation energies of these radiation-induced trapped-hole centers governing the temporal and thermal stabilities of the RIA. As already used to extract the DOTS in pure, Al-, P-doped silica (in addition to Er- and Yb-doped silica made elsewhere [174]), it could not be applied to Ge-doped fibers due to an "anomalous" increase of the TL response with the heating rate. However, Ge-doped silica fibers are of obvious technological importance and they well deserve a special treatment. The objective of this section

was thus: (i) to elucidate the specific radiation-induced mechanisms associated with the presence of Ge in silica, that notably induces the anomalous TL response; (ii) to put these mechanisms in equations to allow their validation and calibration against experimental data. Our experimental study of the thermal annealing of the RIA during the TL readout, and its correlation with the TL glow curve, made it possible to conclude that ODCs centers (both SiODC and GeODC) trap electrons during irradiation to form deep Si- and GeOCD:e- states which act as recombination center in the TL process. Part of native ODCs are thus destroyed. They can only be restored upon recombination of trapped ODC:e- states by free holes. This process is at the origin of the TL emission. The recovery of color centers associated with trapped electrons, as the Ge1 centers, takes place below 250 °C during the TL readout. The main TL peak around 225-275 °C was found to follow the release of holes from SiE´centers. The anomalous TL response was argued to be due to the combination of two specific properties. First, the cross-section characterizing the recombination of free holes with RCs, i.e. Si- and GeODC:e- trapped electron centers, must increase with temperature. We used a thermally activated cross-section (Arrhenius law) in our model, considering that it was a simple and reasonable assumption for demonstrative purposes. Second, a process of hole capture on very deep hole traps (TDT) must compete with that of recombination at RCs and the related capture cross-section must be less sensitive to temperature than that of recombination. The presence of such competing deep traps is specific to Ge-doped glasses since holes trapped in TDT were associated with the thermally-stable GeE´ centers [4].

When rationalized into a set of coupled non-linear ordinary differential equations, our model well reproduces the increase of the TL response with the heating rate as well as its dependence on the total dose. This twofold validation strongly supports the model and its parameters. Thanks to this new validated model, the DOTS could be extracted from TL curves. The activation energies were confirmed by the 'Initial Rise' method, the most basic physical approach. This DOTS shows a peak around a depth of 1.22 eV (above the VB edge). According to the RIA bleaching map (Fig. 3.50), this level most probably corresponds to holes trapped into the form of intrinsic SiE´ centers. This location of SiE' states in the bandgap is in fair agreement with that we estimated in [174] from Ge-free silica samples. Once the DOTS are obtained from the TL modeling, it is possible to correlate the band present in the DOTS to the CC responsible of the RIA. As reported above, it was possible to get a comparison between the experimental thermal annealing RIA and the simulated ones using this method. The agreement between the fit on the experimental band and the simulated ones is good considering the repeteability error of the experiment.

One can conclude that the method created starting from the DOTS is well capable of predicting the annealing of the RIA, after the thermal treatment at various temperature. Therefore, we now have a predictive model to simulate the RIA in Ge-doped glasses, with extrapolation capacities.

# Conclusions

Silica-based optical fibers have a broad range of use in harsh or severe environment applications with radiation constraints. The exposure of optical fibers to ionizing radiation involves damage to optical properties and contributes to the degradation of the fiber performances. This phenomenon is the direct effect of the Radiation Induced Attenuation (RIA): the attenuation of the transmitted light intensity due to the radiation exposure. The degradation of optical properties of the silica-based materials can be explained by the structural adjustments in the silica lattice with the creation of point defects. The nature of the defects depends on the chemical composition of the glass. The knowledge of the creation and annealing mechanisms after radiation of these defects is important in the RIA control. For these reasons, in optical fibers application fields with radiation constraints, such as high-energy physics facilities, waste depositories and nuclear power plants, there is a strong interest in improving knowledge about the degradation processes through the RIA. It is in this context that the CERTYF project fits. The project aims to improve the knowledge about the basic mechanisms leading to the degradation through the radiation-induced attenuation (RIA) of silica-based materials and optical fibers in harsh or severe environments encountered by ANDRA, combining temperature, radiations and hydrogen (R-H-T) constraints. By RIA control can be developed radiation tolerant systems able to operate in the radioactive waste storage facilities; or enhance the fiber radiation sensitivity in order to design radiation detectors and dosimeters able to detect the radiation dose or dose rate present in the radiative environment. The RIA control is achieved by being able to predict its trend in this harsh environment, namely building a physical model able of prediction. We proposed a model able to simulate the RIA in the visible part of the spectrum. The ability of prediction of this model considers the experimental conditions that induce the degradation inside silica based optical fibers, such as time, temperature, dose and dose rate. This model is based on the connection between the color centers (CC) and the density of trapped states (DOTS), through the thermal annealing protocol. The thermal annealing of the RIA allowed us to assign the main color centers to energy levels present in the DOTS. The knowledge of the DOTS is the first step to get a model capable of reproducing and predicting the evolution of the radiation-induced states over different external conditions. The obtain DOTS we used complex procedure based on simulations and experiments. The experiments aimed to provide an analysis of the mechanisms of the RIA development and its annealing in silica-based fiber preforms by exploring the main dopants characterizing our samples: Al, P and Ge. The study carried out according to the thermal annealing protocol, gave a mapping of defect destruction with the increasing tem-

perature. This last point is crucial in our analysis, since it gave access to the correlation between CC bleaching and energy depth of the trapping levels. From the bleaching map results, we were able to relate the bleaching of a center at a certain temperature, to the energy depth of a trapping level through the DOTS revealed by the thermoluminescence (TL). Our experimental study of the thermal annealing of the RIA during readout, and its correlation with the TL curve, made it possible to conclude that ODC centers trap electrons during irradiation to form deep Si-/Ge-/Al-ODC:e- states which act as recombination centers in the TL process. Part of native ODCs are thus destroyed. They can only be restored upon recombination of trapped ODC:e- states by free holes. Common to all samples is the fact that the TL emission is due to the release of trapped holes that subsequently recombine on RC formed by trapped electron states. As a consequence, the extracted DOTS always correspond to distributions of trapped holes in the bandgap, near by the valence band. The DOTS are obtained through a modeling of trap filling and recombination, under and after irradiation. To predict the RIA, we simulated the DOTS in several conditions as those encountered in the RIA experiences. To get a correct prediction of the DOTS, these must be validated by strong evidence. In this sense, it is needed a strategy to calibrate the DOTS under a certain condition (the laboratory standard) and to assure their validity by simulating them in any condition (such as the IRMA irradiation conditions at 1MGy). We showed that our model is well capable of prediction thanks to the comparison between the simulated TL, obtained from the simulated DOTS, and the experimental one. Once the DOTS were obtained, it was possible to correlate the components of the DOTS to the CC responsible of the RIA through the thermal annealing protocol. The agreement between the fit of the experimental gaussian band and the simulated ones was revealed good for all the sample tested. Moreover, we can strengthen the robustness of the model thanks to the simulations of the RIA annealing on Ge-doped silica samples. We showed how our model, starting from the DOTS and without any adjustment, is well capable of predicting the annealing of the RIA, after the thermal treatment at various temperatures. Therefore, we now have a predictive model to simulate the RIA in Ge-doped glasses, with extrapolation capacities. Both DOTS extraction and simulation procedures were successfully conducted using the same modeling for pure, Al-, P-doped silica samples. For Ge-doped fibers we needed to build a model ad hoc. We presented the anomalous increase of the TL response with the heating rate in this kind of samples, which makes impossible the DOTS extraction procedure. Elucidating the specific radiation-induced mechanisms associated with the presence of Ge in silica, we argued that the anomalous TL response is due to the combination of two specific properties: (i) the cross-section characterizing the recombination of free holes with RCs, i.e. Si- and Ge-ODC:e- trapped electron centers, must increase with temperature; (ii) a process of hole capture on very deep hole traps (thermally disconnected trap, TDT) must compete with that of recombination at RCs and the related capture cross-section must be less sensitive to temperature than that of recombination. The presence of such competing deep traps is specific to Ge-doped glasses since holes trapped in TDT were associated with the thermally-stable GeE´ centers. When rationalized into a set of coupled non-linear ordinary differential equations, our model well reproduces the increase of the TL response with the heating rate as well as its dependence on the total dose.

Thanks to this new validated model, the DOTS could be extracted from TL curves also in Ge-doped silica samples.

# Density state equations. Fermi level approximation.

The rate equation governing the electron population in the conduction band ($n_c$) is composed by a positive contribution describing the trapping of the electrons by the traps located below the CB (at $E_0$ energy), and a negative contribution describing the de-trapping of the electrons from the traps to the CB.

$$\frac{dn_c}{dt} = \beta n_c(N-n) - wn \tag{53}$$

where $\beta = \sigma v_t h$ is the trapping fluence rate expressed in $cm^{-3}s^{-1}$ that depends by the electron cross section ($\sigma$) and the thermal velocity ($v_{th}$), $w$ is the detrapping frequency, expressed in $s^{-1}$ and n is the electron density in the trap levels N, expressed in $cm^{-3}$, see fig.51.
At equilibrium $\frac{dn}{dt} = 0$, so we have:

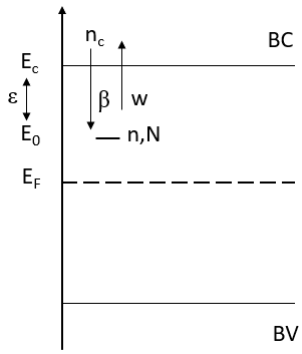


**Figure 51:** Energy level scheme.

$$\beta n(N-n) = wn$$
$$w = \beta \frac{n_c}{n}(N-n)$$

At equilibrium we can use the Fermi-Dirac statistic to calculate $n_c$, $n$, $(N-n)$ in order to obtain an expression for $w$. We will obtain at the end of the following steps the expression 60 while in the appendix 4.3.4 we will see that the frequency factor $w_0$ is not a constant but is a function of the temperature by a power law

dependence.
From the well known Fermi energy function

$$f(E) = \frac{1}{1 + e^{(E-E_F)/k_B T}} \tag{54}$$

we can calculate the density of electrons in BC solving the expression:

$$n_c = \int_{E_c}^{\infty} N_c(E) F(E) dE \tag{55}$$

we can use the approximation:

$$f(E) \simeq exp\left[-\frac{(E - E_F)}{k_B T}\right]$$

for $E - E_F \gg k_B T$.
Using this approximation we can calculate 55:

$$\begin{aligned} n_c &= \int_{Ec}^{\infty} N_c(E) exp\left[\frac{E - E_c + E_c - E_F}{k_B T}\right] dE \\ &= \int_{Ec}^{\infty} N_c(E) exp\left[\frac{E - E_F}{k_B T}\right] dE \cdot exp\left[-\frac{E_c - E_F}{k_B T}\right] \\ &= N_c \cdot exp\left[-\frac{E_c - E_F}{k_B T}\right] \end{aligned} \tag{56}$$

where for the integral we substitued $N_c = 2(2\pi m^* k_0 T/h)^{3/2}$ the known effective density states from physics of semiconductors[187]
For the calculus of n we use the same approximation for the Fermi-Dirac function for the energies $E_0 - E_F \gg k_B T$[1], where $E_0$ is the energy at the $N^{th}$ level (see fig. 51). In this approximation we can write:

$$n \backsim N exp\left[-\frac{E_0 - E_F}{k_B T}\right] \tag{57}$$

and

$$\begin{aligned} N - n &= N - n f(E) \\ &= N(1 - f(E)) \\ &\backsim N\left(1 - exp\left[-\frac{E_0 - E_F}{k_B T}\right]\right) \\ &\backsim N \end{aligned} \tag{58}$$

[1] it is worth to note that if $E_0 \backsim 1eV$, $E_0 - E_F \backsim 5eV$; and if $T = 600^o C = 873K$, then $k_B T = 0.0035eV$. So we can always make the assumption that $E_0 - E_F \gg k_B T$.

Substituting 56,57, 58 in 4.11, we obtain:

$$w = \beta n_c \left( \frac{N-n}{n} \right) \tag{59}$$

$$= \sigma v_{th} N_c exp \left[ -\frac{E_c - E_F}{k_B T} \right] \frac{N}{N} exp \left[ \frac{E_0 - E_F}{k_B T} \right]$$

$$= \sigma v_{th} N_c exp \left[ -\frac{E_c - E_0}{k_B T} \right]$$

$$= \sigma v_{th} N_c exp \left[ -\frac{\epsilon}{k_B T} \right]$$

$$= w_0 exp \left[ -\frac{\epsilon}{k_B T} \right] \tag{60}$$

# Temperature effect

The trapping frequency obeys to a Arrhenius type law (see 4.11). In this equation, $w_0 = \sigma v_{th} N_c$ is actually a function of the temperature and of the cross section:

$$w_0 = T^2 \cdot \sigma \tag{61}$$

In fact $w_0$ has a dependence from T being a function of $v_{th}$, $N_c$ and $\sigma$. Exploiting the T dependence of these therms we have:

$v_{th} = \sqrt[2]{\frac{3kT}{m^*}}$, this expression is obtained from the equivalence between the average translation kinetic energy of the particles in thermal motion ($\overline{E_{CT}} = 3/2 k_B T$) and the translational kinetic energy of a particle ($E_{CT} = 1/2 m^* v_{th}^2$)[2];

$N_c = 2(2\pi m^* k_0 T/h)^{3/2}$[187].

Handling these expressions we can write the equation for $w_0$ 61 as:

$$w_0 = \sigma \frac{16\pi m^*}{h^3} (k_B T)^2 \tag{62}$$

where $m^*$ is the reduced mass.
Considering $w_0(300)$ as the trapping frequency value at room temperature (T=300 K), the expression for $w_0$ can be written as $w_0 = w_0(300)(T/300)^2$.
To give some estimations, $w_0(300)$, varies between $10^8$ - $10^{21}$ $s^{-1}$ , considering that at this temperature $\sigma_k \sim 10^{18}$ - $10^{14}$ $cm^2$, $v_{th} \sim 10^7$ cm $s^{-1}$ and $N_c \sim 10^{19}$ $cm^{-3}$.

[2] Actually is possible to prove that the right expression is $v_{th} = (8k_B T/\pi m^*)^{1/2}$.

# Experimental conditions

**TL conditions** In the experimental results will be reported for each sample, the dependence of the TL on the heating rate and the dependence of the TL on the dose.
For the first experiment, the TL is recorded at four heating rates ($0.5^oC/s$, $1^oC/s$, $2^oC/s$ and $3^oC/s$) at the same irradiation and post-irradiation condition, generally using a dose rate of $200Gy/min(SiO_2)$ and waiting 90s between the irradiation and the TL readout ($t_{relax}$).
For the TL dose and dose rate dependence, the TL curves were recorded at several irradiation doses, which are reached changing the irradiation time (at fixed dose rate of $200Gy/min(SiO_2)$) or changing the dose rate turning the current. The procedure used is reported in table 20.

| Intensity current | Irradiation time | dose rate | dose |
|---|---|---|---|
| mA | s | $Gy(SiO_2)/min$ | $Gy(SiO_2)$ |
| 5 | 40 | 34 | 22 |
| 2.5 | 300 | 17 | 84 |
| 5 | 300 | 33 | 168 |
| 10 | 300 | 67 | 335 |
| 15 | 300 | 101 | 503 |
| 20 | 300 | 134 | 671 |
| 30 | 25 | 200 | 84 |
| 30 | 60 | 200 | 201 |
| 30 | 150 | 200 | 503 |
| 25 | 300 | 168 | 838 |
| 30 | 300 | 200 | 1006 |
| 30 | 450 | 200 | 1509 |
| 30 | 600 | 200 | 2012 |
| 30 | 750 | 200 | 2515 |
| 30 | 911 | 200 | 3055 |

**Table 20:** Experimental procedure adopted to investigate the TL dependency from the dose and dose rate.

The experiments were expected to reveal weather the TL intensity or TL area is linear with the dose and if there are any dose rate effects. For the last intention, we found no significant effect from the dose rate. This is supported by the fact that the TL areas recorded by the procedure exposed in table 20, lay in the same line,

and some point recorded after the same total dose but using a different dose rate are almost superimposed. In the results we just report a singular line to show the dependence of the TL from the dose.
A deep explanation of the initial rise technique and how it is performed is reported in 2.5.2. Experimentally, the procedure require to measure a TL curve, then is performed again the measure, but stopping it when the TL reach $1/10^{th}$ of the intensity of the peak. When the sample is cooled back to RT the measurement is relaunched and this step is repeated until the peak will remains less intense of 1/10 of the intensity. From all these curves is obtained a distribution of energies as shown in fig.2.13 (red scatters).

**Optical absorption and RIA measurements** The optical absorption measurements were made by a UV-VIS-NIR spectrophotometer (Perkin-Elmer) with a resolution of 0.16 nm in the spectral range (200nm-850nm). We used a perforated plate as sample holder in order to leave the light passing only through the Ge-doped core of the preform. The RIA was deducted from absorbances A measured before ($A_b$) and after ($A_a$) irradiation, as referred in (63) [118]

$$RIA(dBm^{-1}) = \frac{10}{d}(A_a - A_b) \tag{63}$$

where d is the thickness of the preform sample. Equation (63) is directly obtained by the relation between the attenuation ($\alpha$), the optical input power ($P_{in}$), optical output power ($P_{out}$) and the fiber length (L) given by 1.8 [118].
To make the sought connection between TL mechanisms and RIA, the thermal annealing experiment was performed. It consist of several steps [77]:

1 Recording the OA of the pristine sample;

2 Recording the OA of the sample after exposure to X-rays at RT, thus giving the RIA;

3 heating the sample up to $T_{stop}$=50 on the TL reader at the same heating rate as the TL readout (generally 1°C/s)

4 The new core OA was measured after cooling at RT, thus giving the RIA at $T_{stop}$=50°C

5 by repeating the steps 3 and 4 each 50°C up to 500°C , we obtain the RIA after heating in TL condition up to $T_{stop}$=50, 100, 150, 200, 250, 300, 350, 400, 450, 500°C.

With this procedure, the partial RIA recovery within 50°Cintervals could be followed correlatively to TL peaks and their emissions. From these measurements, we build a thermal bleaching map by differentiating RIA spectra with respect to $T_{stop}$.
From these measurements, we built thermal bleaching maps by differentiating RIA spectra with respect to $T_{stop}$. At any wavelength, the absolute RIA variation around $T_{stop}$ values were normalized to the total RIA to obtain the relative bleaching in

each 50°C interval (in % of the RIA at the considered wavelength) [77]. Treated into the form of a color contour plot, these data are interpolated to provide an overview of the RIA annealing as a function of both temperature and wavelength along the TL readout. Color levels give an estimate of the percentage of the RIA (at wavelengths in the vertical axis) that is bleached at temperatures in the horizontal axis [77]. Sometimes, because of the low RIA level, the bleaching map is built without differentiation respect to the total one, this choice anyway does not compromise the physical interpretation. This is the case of L02 and Q01 samples (fig.3.9 and 3.50 respectively).

# Experimental errors

The experimental error in the TL measurements by means of the PM tube is around 5% of the measured intensity. This typical value was estimated once several measurements were made under the same conditions. In fig 52 is reported a TL glow curve (red line) with the error bars (blue lines) along the y-axes. The error bars are not reported in the result plots to lighten the graphs, but one should keep in mind this error especially in the fourth chapter, where the experimental TL curves are superimposed to the simulated ones.

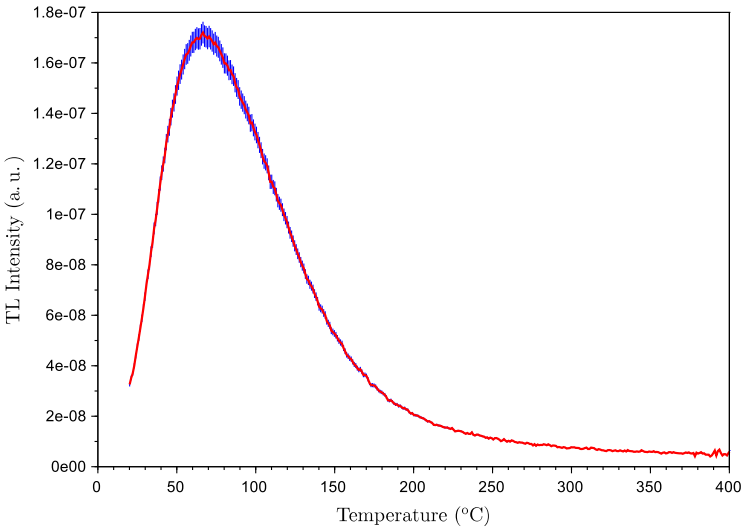


**Figure 52:** Typical TL glow curve on pure silica sample with the error bars corresponding to 5% of the intensity.

The indeterminacy of the RIA results is mainly due to the lack of precision in placing the sample in exactly the same position in the sample holder during the optical absorption measurements. In order to have an estimation of the error due to this inaccuracy, several spectra were recorded under the same experimental conditions The estimated error is estimated at 3-5% of the measured absorption (Fig.53), which then bring to a relative error on the RIA spectra of about 10%.

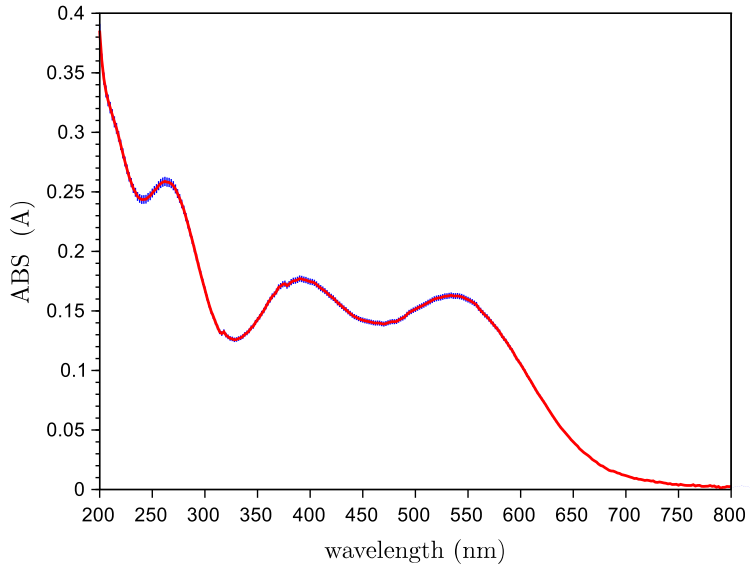


**Figure 53:** Absorption spectrum after an irradiation of 1MGy on P-doped silica sample showing the error bars corresponding to 3% of the measurements.

# Bibliography


[1] S. Girard, A. Morana, A. Ladaci, T. Robin, L. Mescia, J.-J. Bonnefois, M. Boutillier, J. Mekki, A. Paveau, B. Cadier, E. Marin, Y. Ouerdane, A. Boukenter, *J. Opt.* **2018**, *20*, 093001, DOI 10.1088/2040-8986/aad271.

[2] E. J. Friebele, *Optical Engineering* **1979**, *18*, 186552, DOI 10.1117/12.7972434.

[3] J. E. Golob, P. B. Lyons, L. D. Looney, *IEEE Transactions on Nuclear Science* **1977**, *24*, 2164–2168, DOI 10.1109/TNS.1977.4329184.

[4] D. L. Griscom in Radiation Effects on Optical Materials, *Vol. 541*, International Society for Optics and Photonics, **1985**, pp. 38–59.

[5] E. J. Friebele, K. J. Long, C. G. Askina, et al. in Radiation Effects on Optical Materials, *Vol. 0541*, International Society for Optics and Photonics, **1985**, pp. 70–88, DOI 10.1117/12.975360.

[6] G. P. Agrawal, *Fiber-Optic Communication Systems*, *Vol. 222*, John Wiley & Sons, **2012**.

[7] J. L. Bourgade, et al., *Review of Scientific Instruments* **2008**, *79*, 10F301, DOI 10.1063/1.2991161.

[8] K. Roeed, M. Brugger, G. Spiezia, *CERN Document Server* **2011**.

[9] S Yamamoto, T Shikama, V Belyakov, *Journal of Nuclear Materials*, 9th Int. Conf. on Fusion Reactor Materials **2000**, *283-287*, 60–69, DOI 10.1016/S0022-3115(00)00157-4.

[10] P. Ferdinand, S. Magne, G. Laffont in Fourth Asia Pacific Optical Sensors Conference, *Vol. 8924*, International Society for Optics and Photonics, **2013**, 89242G, DOI 10.1117/12.2033922.

[11] S. Delepine-Lesoille, S. Girard, M. Landolt, J. Bertrand, I. Planes, A. Boukenter, E. Marin, G. Humbert, S. Leparmentier, J.-L. Auguste, Y. Ouerdane, *Sensors* **2017**, *17*, 1377, DOI 10.3390/s17061377.

[12] S O'Keeffe, D McCarthy, P Woulfe, *The British Journal of Radiology* **2015**, *88*, 20140702, DOI 10.1259/bjr.20140702.

[13] S. Girard, J. Kuhnhenn, A. Gusarov, B Brichard, M. Van Uffelen, Y. Ouerdane, A. Boukenter, C. Marcandella, *IEEE Transactions on Nuclear Science* **2013**, *60*, 2015–2036.

[14] W. Primak, *Physical Review* **1958**, *110*, 1240–1254, DOI 10.1103/PhysRev.110.1240.

[15] NASA Technical Reports Server (NTRS), https://ntrs.nasa.gov/citations/20180001142.

[16] M. S. Longair, *High Energy Astrophysics*, 3rd ed, Cambridge University Press, Cambridge ; New York, **2011**.

[17] M. J. Berger, J. S. Coursey, M. A. Zucker, **1999**.

[18] R. A. B. Devine, J. P. Duraud, E. Dooryhée, *Structure and Imperfections in Amorphous and Crystalline Silicon Dioxide*, John Wiley & Sons Inc, **2000**.

[19] S. T.Pantelides, *The Physics of $SiO_2$ and Its Interfaces*, pergamon press, **1978**.

[20] J.C.Lagomancini, D.Bravo, A.Martin, F.J.Lopez, P.Martin, A.Ibarra, *Journal of non crystalline solids* **2014**, *403*, 5–8.

[21] H.Rawson, *Glasses and Their Application*, the institute of metall, **1991**.

[22] G. Pacchioni, L. Skuja, D. L. Griscom, *Defects in SiO2 and Related Dielectrics*, Dordrecht:Kluwer Academic, **2000**.

[23] J. a.Weil, *Phys Chem Minerals* **1984**, *10*, 149–165.

[24] W. H. Zachariasen, *Journal of the American Chemical Society* **1932**, *54*, 3841–3851, DOI 10.1021/ja01349a006.

[25] A. C. Wright, *Journal of non-crystalline solids* **1994**, *179*, 84–115.

[26] A. Pasquarello, R. Car, *Physical Review Letters* **1998**, *80*, 5145–5147, DOI 10.1103/PhysRevLett.80.5145.

[27] F. L. Galeener, A. E. Geissberger, *Physical Review B* **1983**, *27*, 6199–6204, DOI 10.1103/PhysRevB.27.6199.

[28] L Skuja, M Hirano, H Hosono, K Kajihara, *physica status solidi (c)* **2005**, *2*, 15–24.

[29] D. L. Griscom, *Nuclear Instruments and Methods in Physics Research Section B: Beam Interactions with Materials and Atoms* **1984**, *1*, 481–488, DOI 10.1016/0168-583X(84)90113-7.

[30] G. Buscarino, Phd Thesis, Università degli Studi di Palermo, **2006**.

[31] A. Alessi, S. Agnello, G. Buscarino, Y. Pan, R. Mashkovtsev, *Applications of EPR in Radiation Research Anders Lund*, (Ed.: M. Shiotani), Springer International Publishing, **2014**.

[32] L. Skuja, *Journal of Non-Crystalline Solids* **1998**, *239*, 16–48.

[33] S Agnello, R Boscaino, M Cannas, F. Gelardi, *Applied Magnetic Resonance* **2000**, *19*, 579–585.

[34] L. Skuja, K. Kajihara, M. Hirano, H. Hosono, *Physical Review B* **2011**, *84*, 205206, DOI 10.1103/PhysRevB.84.205206.

[35] H. Hosono, K. Kajihara, T. Suzuki, Y. Ikuta, L. Skuja, M. Hirano, *Solid State Communications* **2002**, *122*, 117–120, DOI 10.1016/S0038-1098(02)00118-7.

[36] T. Suzuki, L. Skuja, K. Kajihara, M. Hirano, T. Kamiya, H. Hosono, *Physical Review Letters* **2003**, *90*, 186404, DOI 10.1103/PhysRevLett.90.186404.

[37] L. Skuja, *Journal of Non-Crystalline Solids* **1994**, *179*, 51–69, DOI 10.1016/0022-3093(94)90684-X.

[38] K. Kajihara, et al., *Phys. Rev. Lett.* **2004**, *92*, 015504, DOI 10.1103/PhysRevLett.92.015504.

[39] H. Nishikawa, R. Tohmon, Y. Ohki, K. Nagasawa, Y. Hama, *Journal of Applied Physics* **1989**, *65*, 4672–4678, DOI 10.1063/1.343242.

[40] N. Kuzuu, H. Horikoshi, *Journal of Applied Physics* **2005**, *97*, 093508, DOI 10.1063/1.1883307.

[41] K. Awazu, H. Kawazoe, K.-i. Muta, *Journal of Applied Physics* **1991**, *69*, 1849–1852, DOI 10.1063/1.348753.

[42] D. L. Griscom, *Physics Research International* **2013**, *2013*.

[43] D. L. Griscom, *Journal of Non-Crystalline Solids* **2006**, *352*, 2601–2617, DOI 10.1016/j.jnoncrysol.2006.03.033.

[44] Y. Sasajima, K. Tanimura, *Phys. Rev. B* **2003**, *68*, 014204, DOI 10.1103/PhysRevB.68.014204.

[45] J. Stone, G. E. Walrafen, *The Journal of Chemical Physics* **1982**, *76*, 1712–1722, DOI 10.1063/1.443210.

[46] S. Girard, A. Alessi, N. Richard, L. Martin-Samos, V. De Michele, L. Giacomazzi, S. Agnello, D. Di Francesca, A. Morana, B. Winkler, et al., *Reviews in Physics* **2019**, 100032.

[47] B Brichard, A Fernandez Fernandez, H Ooms, et al., *Journal of Nuclear Materials*, Proceedings of the 11th International Conference on Fusion Reactor Materials (ICFRM-11) **2004**, *329-333*, 1456–1460, DOI 10.1016/j.jnucmat.2004.04.159.

[48] B. Brichard, A. L. Tomashuk, V. A. Bogatyrjov, A. F. Fernandez, S. N. Klyamkin, S. Girard, F. Berghmans, *Journal of Non-Crystalline Solids*, SiO, Advanced Dielectrics and Related Devices 6 **2007**, *353*, 466–472, DOI 10.1016/j.jnoncrysol.2006.10.039.

[49] A. L. Tomashuk, M. Y. Salgansky, P. F. Kashaykin, V. F. Khopin, A. I. Sultangulova, K. N. Nishchev, S. E. Borisovsky, A. N. Guryanov, E. M. Dianov, *Journal of Lightwave Technology* **2014**, *32*, 213–219, DOI 10.1109/JLT.2013.2285157.

[50] P. F. Kashaykin, A. L. Tomashuk, M. Y. Salgansky, A. N. Abramov, K. N. Nishchev, A. N. Guryanov, E. M. Dianov, *Journal of Lightwave Technology* **2015**, *33*, 1788–1793.

[51] E. Regnier, I. Flammer, S. Girard, F. Gooijer, F. Achten, G. Kuyt, *IEEE Transactions on Nuclear Science* **2007**, *54*, 1115–1119, DOI 10.1109/TNS.2007.894180.

[52] A. L. Tomashuk, M. Y. Salgansky, P. F. Kashaykin, V. F. Khopin, A. I. Sultangulova, K. N. Nishchev, S. E. Borisovsky, A. N. Guryanov, E. M. Dianov, *Journal of Lightwave Technology* **2014**, *32*, 213–219, DOI 10.1109/JLT.2013.2285157.

[53] G. Cheymol, H. Long, J. F. Villard, B. Brichard, *IEEE Transactions on Nuclear Science* **2008**, *55*, 2252–2258, DOI 10.1109/TNS.2008.924056.

[54] E. Regnier, I. Flammer, S. Girard, F. Gooijer, F. Achten, G. Kuyt, *IEEE transactions on nuclear science* **2007**, *54*, 1115–1119.

[55] P. V. Chernov, L. S. Kornienko, I. O. Morozova, A. O. Rybaltovskii, E. M. Dianov, V. N. Karpechev, V. O. Sokolov, V. B. Sulimov, *Physica Status Solidi B* **1989**, *156*, 663–675.

[56] S. Girard, C. Marcandella, A. Alessi, A. Boukenter, Y. Ouerdane, N. Richard, P. Paillet, M. Gaillardin, M. Raine, *IEEE Transactions on Nuclear Science* **2012**, *59*, 2894–2901, DOI 10.1109/TNS.2012.2222440.

[57] P. F. Kashaykin, A. L. Tomashuk, I. S. Azanova, O. L. Vokhmyanina, T. V. Dimakova, I. A. Maltsev, Y. O. Sharonova, E. A. Pospelova, O. M. Tatsenko, A. V. Filippov, N. S. Kuzyakina, O. V. Zverev, E. M. Dianov, *Journal of Non-Crystalline Solids* **2019**, *508*, 26–32, DOI 10.1016/j.jnoncrysol.2018.12.016.

[58] V. D. Michele, C. Marcandella, D. D. Francesca, P. Paillet, A. Alessi, M. Cannas, Y. Ouerdane, A. Boukenter, S. Girard, *physica status solidi (a)* **2019**, *216*, 1800487, DOI 10.1002/pssa.201800487.

[59] H. Hideo, K. Hiroshi, *Nuclear Instruments and Methods in Physics Research Section B: Beam Interactions with Materials and Atoms* **1994**, *91*, 395–399.

[60] J. H. Mackey, J. W. Boss, D. E. Wood, *Journal of Magnetic Resonance* **1970**, *3*, 44–54.

[61] M. C. O'Brien, *Proceedings of the Royal Society of London. Series A. Mathematical and Physical Sciences* **1955**, *231*, 404–414.

[62] S. Girard, B Tortech, E Regnier, M Van Uffelen, A Gusarov, Y Ouerdane, J Baggio, P Paillet, V Ferlet-Cavrois, A Boukenter, et al., *IEEE transactions on nuclear science* **2007**, *54*, 2426–2434.

[63] G. Williams, M. Putnam, C. Askins, M. Gingerich, E. Friebele, *Electronics Letters* **1992**, *28*, 1816, DOI 10.1049/el:19921158.

[64] S. Girard, B. Tortech, E. Regnier, M. Van Uffelen, A. Gusarov, Y. Ouerdane, J. Baggio, P. Paillet, V. Ferlet-Cavrois, A. Boukenter, J.-P. Meunier, F. Berghmans, J. R. Schwank, M. R. Shaneyfelt, J. A. Felix, E. W. Blackmore, H. Thienpont, *IEEE Transactions on Nuclear Science* **2007**, *54*, 2426–2434, DOI 10.1109/TNS.2007.910859.

[65] B. Brichard, A. F. Fernandez, E. Fern, H. Ooms, F. Berghmans, *Gamma Dose Rate Effect in Erbium-Doped Fibers for Space Gyroscopes*, **2003**.

[66] A. Alessi, A. Guttilla, S. Girard, S. Agnello, M. Cannas, T. Robin, A. Boukenter, Y. Ouerdane, *physica status solidi (a)* **2018**, DOI 10.1002/pssa.201800485.

[67] G. M. Williams, M. A. Putnam, E. J. Friebele in Photonics for Space Environments IV, *Vol. 2811*, International Society for Optics and Photonics, **1996**, pp. 30–37, DOI 10.1117/12.254052.

[68] R. S. Quimby, W. J. Miniscalco, B. Thompson, *Journal of Applied Physics* **1994**, *76*, 4472–4478, DOI 10.1063/1.357278.

[69] K. Arai, H. Namikawa, K. Kumata, *Journal of Applied Physics* **1986**, *59*, 3430–3436, DOI 10.1063/1.336810.

[70] M. Leon, M Lancry, N Ollier, B. H. Babu, L Bigot, H. E. Hamzaoui, I Savelii, A Pastouret, E Burov, F Trompier, B Poumellec, M Bouazaoui, *Journal of Materials Science* **2016**, *51*, 10245–10261.

[71] R Schnadt, A Räuber, *Solid State Communications* **1971**, *9*, 159–161.

[72] H. Hideo, K. Hiroshi, *Nuclear Instruments and Methods in Physics Research Section B: Beam Interactions with Materials and Atoms* **1994**, *91*, 395–399.

[73] A. Trukhin, J. Teteris, A. Fedotov, D. Griscom, G. Buscarino, *Journal of Non-Crystalline Solids* **2009**, *355*, 1066–1074.

[74] N. Koumvakalis, *Journal of Applied Physics* **1980**, *51*, 5528–5532.

[75] Brower, K. L, *Physical Review Letters* **1978**, *41*, 879.

[76] K. Brower, *Physical Review B* **1979**, *20*, 1799.

[77] F. Mady, A. Guttilla, M. Benabdesselam, W. Blanc, *Optical Materials Express* **2019**, *9*, 2466–2489.

[78] D. L. Griscom, *Journal of Non-Crystalline Solids* **2011**, *357*, 1945–1962.

[79] A. S. Zyubin, A. M. Mebel, S. H. Lin, *J. Chem. Phys.* **2003**, *119*, 11408–11414, DOI 10.1063/1.1622660.

[80] A. N. Trukhin, J. L. Jansons, K. Truhins, *Journal of Non-Crystalline Solids* **2004**, *347*, 80–86.

[81] S. Girard, D. Di Francesca, A. Boukenter, T. Robin, E. Marin, A. Ladaci, I. Reghioua, A. Morana, S. Rizzolo, C Cangialosi, et al., *IEEE Transactions on Nuclear Science* **2015**, *62*, 2941–2947.

[82] S. Girard, C. Marcandella, A Morana, *IEEE Trans. Nucl. Sci.* **2013**, *60*, 4305–4313.

[83] E. Regnier, I. Flammer, S. Girard, F. Gooijer, F. Achten, G. Kuyt, *IEEE transactions on nuclear science* **2007**, *54*, 1115–1119.

[84] D. L. Griscom, E. J. Friebele, K. J. Long, J. W. Fleming, *Journal of Applied Physics* **1983**, *54*, 3743–3762, DOI 10.1063/1.332591.

[85] D. di Francesca, S. Girard, S. Agnello, A. Alessi, C. Marcandella, P. Paillet, Y. Ouerdane, Y. Kadi, M. Brugger, A. Boukenter, *physica status solidi (a)* **2019**, *216*, 1800553, DOI 10.1002/pssa.201800553.

[86] G Origlio, A Boukenter, S. Girard, N Richard, M. Cannas, R Boscaino, Y Ouerdane, *Nuclear Instruments and Methods in Physics Research Section B: Beam Interactions with Materials and Atoms* **2008**, *266*, 2918–2922.

[87] J. W. Chan, T. Huser, J. S. Hayden, S. H. Risbud, D. M. Krol, *Journal of the American Ceramic Society* **2002**, *85*, 1037–1040, DOI 10.1111/j.1151-2916.2002.tb00219.x.

[88] D. L. Griscom, E. J. Friebele, K. J. Long, J. W. Fleming, *Journal of Applied Physics* **1983**, *54*, 3743–3762, DOI 10.1063/1.332591.

[89] S. Girard, A. Boukenter, Y. Ouerdane, J. P. Meunier, J. Keurinck, *Journal of Non-Crystalline Solids*, Proceedings of the 4th Franco-Italian Symposium on SiO2 and Advanced Dielectrics **2003**, *322*, 78–83, DOI 10.1016/S0022-3093(03)00179-0.

[90] M. Benabdesselam, F. Mady, S. Girard, *Journal of Non-Crystalline Solids* **2013**, *360*, 9–12.

[91] M. Benabdesselam, F. Mady, S. Girard, Y. Mebrouk, J. B. Duchez, M. Gaillardin, P. Paillet, *IEEE Trans. Nucl. Sci.* **2013**, *60*, 4251–4256, DOI 10.1109/TNS.2013.2284289.

[92] A.Alessi, Phd Thesis, Università degli Studi di Palermo, **2010**.

[93] H. S. Nalwa, *Silicon-Based Material and Devices, Two-Volume Set: Materials and Processing, Properties and Devices*, *Vol. 1*, Academic Press, **2001**.

[94] M. Fujimaki, T. Watanabe, T. Katoh, T. Kasahara, N. Miyazaki, Y. Ohki, H. Nishikawa, *Physical Review B* **1998**, *57*, 3920.

[95] M. Cannas, G. Origlio, *Physical Review B* **2007**, *75*, 233201, DOI 10.1103/PhysRevB.75.233201.

[96] A. Alessi, S. Girard, C. Marcandella, S. Agnello, M. Cannas, A. Boukenter, Y. Ouerdane, *Journal of Non-Crystalline Solids*, SiO2, Advanced Dielectrics and Related Devices **2011**, *357*, 1966–1970, DOI 10.1016/j.jnoncrysol.2010.10.038.

[97] V. Neustruev, *Journal of Physics: Condensed Matter* **1994**, *6*, 6901.

[98] L. Giacomazzi, L. Martin-Samos, A. Boukenter, Y. Ouerdane, S. Girard, N. Richard, *Optical Materials Express* **2015**, *5*, 1054–1064.

[99] M. M. Bubnov, E. M. Dianov, O. N. Egorova, S. L. Semjonov, A. N. Guryanov, L. A. Ketkova, V. F. Khopin in Optical Devices for Fiber Communication II, *Vol. 4216*, International Society for Optics and Photonics, **2001**, pp. 164–173, DOI 10.1117/12.414112.

[100] M. M. Bubnov, A. N. Guryanov, E. M. Dianov, L. A. Ketkova, M. E. Likhachev, M. Y. Salganskii, V. F. Khopin, *Inorganic Materials* **2010**, *46*, 556–562, DOI 10.1134/S0020168510050213.

[101] A. Abramov, M. Bubnov, E. Dianov, L. Kol'Chenko, S. Semjonov, A. Shchebunjaev, A. Gurjanov, V. Khopin, *Electronics Letters* **1993**, *29*, 1977–1978, DOI 10.1049/el:19931316.

[102] S. Shibata, M. Nakahara, *Journal of Lightwave Technology* **1985**, *3*, 860–863, DOI 10.1109/JLT.1985.1074253.

[103] T. Wei, M. P. Singh, W. J. Miniscalco, P. I. K. Onorato, J. A. Wall in Fiber Optics Reliability: Benign and Adverse Environments, *Vol. 0842*, International Society for Optics and Photonics, **1987**, pp. 169–173, DOI 10.1117/12.968190.

[104] D. Di Francesca, A. Boukenter, S. Agnello, S. Girard, A. Alessi, P. Paillet, C. Marcandella, N. Richard, F. Gelardi, Y. Ouerdane, *Optical Materials Express* **2014**, *4*, 1683, DOI 10.1364/OME.4.001683.

[105] A. Alessi, S. Girard, M. Cannas, S. Agnello, A. Boukenter, Y. Ouerdane, *Optics Express* **2011**, *19*, 11680–11690, DOI 10.1364/OE.19.011680.

[106] D. Di Francesca, PhD thesis, univertity of Palermo and university of Saint Etienne, Saint Etienne, **2015**.

[107] E. Anoikin, V. Mashinsky, V. Neustruev, Y. Sidorin, *Journal of non-crystalline solids* **1994**, *179*, 243–253.

[108] S. Girard, J. Baggio, J. Bisutti, *IEEE Transactions on Nuclear Science* **2006**, *53*, 3750–3757, DOI 10.1109/TNS.2006.886222.

[109] J. W. Fleming, D. L. Wood, *Applied optics* **1983**, *22*, 3102–3104.

[110] S. Girard, C Marcandella, G Origlio, Y Ouerdane, A Boukenter, J.-P. Meunier, *Journal of non-crystalline solids* **2009**, *355*, 1089–1091.

[111] H. Hosono, M. Mizuguchi, L. Skuja, T. Ogawa, *Optics letters* **1999**, *24*, 1549–1551.

[112] R. E. Youngman, S. Sen, *Journal of non-crystalline solids* **2004**, *337*, 182–186.

[113] K. Kajihara, et al., *Nuclear Instruments and Methods in Physics Research Section B: Beam Interactions with Materials and Atoms*, Proceedings of the Twelfth International Conference on Radiation Effects in Insulators **2004**, *218*, 323–331, DOI 10.1016/j.nimb.2003.12.032.

[114] G.Origlioi, Phd Thesis, University Jean Monnet of Saint Etienne, **2010**.

[115] K. Arai, H. Imai, J. Isoya, H. Hosono, Y. Abe, H. Imagawa, *Physical Review B* **1992**, *45*, 10818.

[116] M Kyoto, Y Ohoga, S Ishikawa, Y Ishiguro, *Journal of materials science* **1993**, *28*, 2738–2744.

[117] D. L. Griscom, *Optical Materials Express* **2011**, *1*, 400–412.

[118] G.Keiser, *Optical Fiber Communications*, McGraw-Hill Series in Electrical Engineeringl, **1991**.

[119] A. A. GHATAK, A. Ghatak, K. Thyagarajan, K. Thyagarajan, *An Introduction to Fiber Optics*, Cambridge University Press, **1998**.

[120] J. B. MacChesney, D. J. DiGiovanni, *J.Am.Ceram.Soc.* **1990**, *73*, 3537–56.

[121] J. A. Buck, *Fundamentals of Optical Fibers*, John Wiley & Sons, **2004**.

[122] H Osanai, T Shioda, T Moriyama, S Araki, M Horiguchi, T Izawa, Takata, *Electronics Letters* **1976**, *12*, 549–550.

[123] M. Leone, S. Agnello, R. Boscaino, M. Cannas, F. Gelardi, *Silicon-Based Materilas and Devices*, *Vol. 2*, H.S Nalwa, Academic Press San Diego, **2001**.

[124] J. R. Lakowicz, B. R. Masters, *Journal of Biomedical Optics* **2008**, *13*, 029901.

[125] S.Agnello, PhD thesis, Università degli Studi di Palermo, **2000**.

[126] R. Brückner, *Journal of Non-Crystalline Solids* **1970**, *5*, 123–175, DOI 10.1016/0022-3093(70)90190-0.

[127] B. Bendow, *Fiber Optics: Advances in Research and Development*. Springer, Place of publication not identified, **2012**.

[128] L Cognolato, *Le Journal de Physique IV* **1995**, *5*, C5–975.

[129] N. Broll, P. D. Chateaubourg, *Spectral Distribution from End Window X-Ray Tubes*.

[130] H. Berger, *X-Ray Spectrometry* **1986**, *15*, 241–243, DOI 10.1002/xrs.1300150405.

[131] J. H. Hubbell, S. M. Seltzer, *X-Ray Mass Attenuation Coefficients*, Radiation Physics Division, PML, NIST, **1996**.

[132] I. Reghioua, S. Girard, M. Raine, *IEEE Transactions on Nuclear Science* **2017**, *64*, 2318–2324, DOI 10.1109/TNS.2016.2644981.

[133] A. Gusarov, S. K. Hoeffgen, *IEEE Transactions on Nuclear Science* **2013**, *60*, 2037–2053, DOI 10.1109/TNS.2013.2252366.

[134] A. Alessi, S. Agnello, S. Grandi, A. Parlato, F. M. Gelardi, *Physical Review B* **2009**, *80*, 014103, DOI 10.1103/PhysRevB.80.014103.

[135] R. Schenker, W. Oldham, *Journal of Applied Physics* **1997**, *82*, 1065–1071, DOI 10.1063/1.365872.

[136] D. Griscom, M. Gingerich, E. Friebele, *Physical Review Letters* **1993**, *71*, 1019.

[137] V. A. Mashkov, W. R. Austin, L. Zhang, R. G. Leisure, *Physical Review Letters* **1996**, *76*, 2926–2929, DOI 10.1103/PhysRevLett.76.2926.

[138] D. L. Griscom, *Physical Review B* **2001**, *64*, 174201.

[139] Y. Morita, W. Kawakami, *IEEE Transactions on Nuclear Science* **1989**, *36*, 584–590, DOI 10.1109/23.34505.

[140] G. M. Williams, B. M. Wright, W. D. Mack, E. J. Friebele in Optical Fiber Reliability and Testing, *Vol. 3848*, International Society for Optics and Photonics, **1999**, pp. 271–280, DOI 10.1117/12.372781.

[141] F. Xie, F. Xie, C. Shao, C. Shao, F. Lou, M. Wang, C. Yu, S. Feng, S. Feng, L. Hu, *Chinese Optics Letters* **2018**, *16*, 010603.

[142] O. Gilard, J. Thomas, L. Troussellier, M. Myara, P. Signoret, E. Burov, M. Sotom, *Applied optics* **2012**, *51*, 2230–2235.

[143] R. A. B. Devine, *Nuclear Instruments and Methods in Physics Research Section B: Beam Interactions with Materials and Atoms* **1990**, *46*, 261–264, DOI 10.1016/0168-583X(90)90709-4.

[144] H. Henschel, E. Baumann, *Journal of Lightwave Technology* **1996**, *14*, 724–731, DOI 10.1109/50.495151.

[145] H. Imai, H. Hirashima, *Journal of Non-Crystalline Solids*, Proceedings of the First PAC RIM Meeting on Glass and Optical Materials **1994**, *179*, 202–213, DOI 10.1016/0022-3093(94)90698-X.

[146] E. J. Friebele, M. E. Gingerich, D. L. Griscom in Optical Materials Reliability and Testing: Benign and Adverse Environments, *Vol. 1791*, International Society for Optics and Photonics, **1993**, pp. 177–188, DOI 10.1117/12.141177.

[147] R. Kohlrausch, *Annalen der Physik* **1854**, *167*, 179–214, DOI 10.1002/andp.18541670203.

[148] D. T. H. Liu, A. R. Johnston, *Opt. Lett. OL* **1994**, *19*, 548–550, DOI 10.1364/OL.19.000548.

[149] O. Gilard, M. Caussanel, H. Duval, G. Quadri, F. Reynaud, *Journal of Applied Physics* **2010**, *108*, 093115, DOI 10.1063/1.3503370.

[150] M. Caussanel, P. Signoret, J. Gasiot, O. Gilard, M. Sotom, *Electronics Letters* **2005**, *41*, 168–170, DOI 10.1049/el:20057704.

[151] A. Kimmel, P. Sushko, A. Shluger, *Journal of Non-Crystalline Solids* **2007**, *353*, 599–604.

[152] D. Sporea, A. Sporea, C. Oproiu, *Journal of nuclear materials* **2012**, *423*, 142–148.

[153] P. Lemaire, R. Atkins, V. Mizrahi, W. Reed, *Electronics Letters* **1993**, *29*, 1191–1193, DOI 10.1049/el:19930796.

[154] C. L. Liou, L. A. Wang, M. C. Shih, *Applied Physics A: Materials Science & Processing* **1997**, *64*, 191–197, DOI 10.1007/s003390050463.

[155] J. Crank, E. P. J. Crank, *The Mathematics of Diffusion*, Clarendon Press, **1979**.

[156] J. Shelby, *Journal of Applied Physics* **1977**, *48*, 3387–3394.

[157] J Stone, G. E. Walrafen, *The Journal of Chemical Physics* **1982**, *76*, 1712–1722.

[158] Y. Mita, S. Matsushita, T. Yanase, H. Nomura, *Electronics Letters* **1977**, *13*, 55–56.

[159] B Malo, J. Albert, F Bilodeau, T Kitagawa, D. Johnson, K. Hill, K Hattori, Y Hibino, S Gujrathi, *Applied physics letters* **1994**, *65*, 394–396.

[160] J. Canning, P.-F. Hu in Bragg Gratings, Photosensitivity, and Poling in Glass Waveguides (2001), Paper BThA6, Optical Society of America, **2001**, BThA6, DOI 10.1364/BGPP.2001.BThA6.

[161] D. Di Francesca, G. L. Vecchi, S Girard, A. Alessi, I Reghioua, A Boukenter, Y. Ouerdane, Y Kadi, M Brugger, *IEEE Transactions on Nuclear Science* **2017**, *65*, 126–131.

[162] H. Hosono, K. Kajihara, M. Hirano, M. Oto, *Journal of applied physics* **2002**, *91*, 4121–4124.

[163] S Girard, V De Michele, A Alessi, C Marcandella, D Di Francesca, P Paillet, A Morana, J Vidalot, C. Campanella, S Agnello, et al., *IEEE Transactions on Nuclear Science* **2019**.

[164] S. W. McKeever, *Thermoluminescence of Solids*, *Vol. 3*, Cambridge University Press, **1988**.

[165] R. Chen, S. W. McKeever, *Theory of Thermoluminescence and Related Phenomena*, World Scientific, **1997**.

[166] A. C. Coleman, E. G. Yukihara, *Radiation Measurements* **2018**, *117*, 70–79, DOI 10.1016/j.radmeas.2018.07.010.

[167] G. Kitis, V. Pagonis, S. E. Tzamarias, *Radiation Measurements* **2017**, *100*, 27–36, DOI 10.1016/j.radmeas.2017.03.047.

[168] P. Bräunlich, *Journal of Applied Physics* **1967**, *38*, 2516–2519, DOI 10.1063/1.1709939.

[169] T. S. C. Singh, P. S. Mazumdar, R. K. Gartia, *J. Phys. D: Appl. Phys.* **1988**, *21*, 1312–1314, DOI 10.1088/0022-3727/21/8/014.

[170] M. Benabdesselam, F. Mady, J. B. Duchez, Y. Mebrouk, S. Girard, *IEEE Transactions on Nuclear Science* **2014**, *61*, 3485–3490.

[171] J. B. Duchez, Theses, Univeristé Nice Sophia Antipolis, **2015**.

[172] J Auge, J. Pocholle, J Raffy, *Revue de physique appliquée* **1984**, *19*, 87–94.

[173] V. Shah, *Journal of lightwave technology* **1987**, *5*, 35–43.

[174] F. Mady, A. Guttilla, M. Benabdesselam, W. Blanc, S Girard, Y Ouerdane, A. Boukenter, H. Desjonquères, C. Monsanglant-Louvet in Fiber Lasers and Glass Photonics: Materials through Applications II, *Vol. 11357*, International Society for Optics and Photonics, **2020**, 113571B.

[175] A. Trukhin, J. Troks, D. Griscom, *Journal of Non-Crystalline Solids* **2007**, *353*, 1560–1566, DOI 10.1016/j.jnoncrysol.2007.01.028.

[176] G. Li Vecchi, D. Di Francesca, C. Sabatier, S. Girard, A. Alessi, A. Guttilla, T. Robin, Y. Kadi, M. Brugger, *Optical Fiber Technology* **2020**, *55*, 102166, DOI 10.1016/j.yofte.2020.102166.

[177] S Agnello, B Boizot, *Journal of non-crystalline solids* **2003**, *322*, 84–89.

[178] E. Friebele, Correlation of Single Mode Fiber Fabrication Factors and Radiation Response, tech. rep., NAVAL RESEARCH LAB WASHINGTON DC, **1992**.

[179] E. J. Friebele, C. G. Askins, C. M. Shaw, M. E. Gingerich, C. C. Harrington, D. L. Griscom, T.-E. Tsai, U.-C. Paek, W. H. Schmidt, *Applied optics* **1991**, *30*, 1944–1957.

[180] G Kitis, G. Polymeris, V Pagonis, N. Tsirliganis, *physica status solidi (a)* **2006**, *203*, 3816–3823.

[181] Y. Sakurai, *Journal of Non-Crystalline Solids* **2000**, *276*, 159–162, DOI 10.1016/S0022-3093(00)00276-3.

[182] F. Mady, M. Benabdesselam, J.-B. Duchez, Y. Mebrouk, S. Girard, *IEEE Transactions on Nuclear Science* **2013**, *60*, 4341–4348.

[183] A. Smakula, *Z. Physik* **1930**, *59*, 603–614, DOI 10.1007/BF01344801.

[184] N. Rawat, M. Kulkarni, D. Mishra, B. Bhatt, C. Sunta, S. Gupta, D. Sharma, *Nuclear Instruments and Methods in Physics Research Section B: Beam Interactions with Materials and Atoms* **2009**, *267*, 3475–3479.

[185] V. Neustruev, *Journal of Physics: Condensed Matter* **1994**, *6*, 6901.

[186] H. Hosono, Y. Abe, D. L. Kinser, R. A. Weeks, K. Muta, H. Kawazoe, *Phys. Rev. B* **1992**, *46*, 11445–11451, DOI 10.1103/PhysRevB.46.11445.

[187] S. M. Sze, K. K. Ng, *Physics of Semiconductor Devices*, John wiley & sons, **2006**.